

Ruprecht-Karls-Universität

***N*-Body Simulations of Multiplanetary Systems in  
Star Clusters:  
The Effect of External Perturbations on the  
Dynamical Evolution of Planets**

Katja Verena Stock

A thesis submitted in fulfillment of the requirements  
for the degree of Doctor of Natural Sciences

to the

Combined Faculty of Mathematics, Engineering and Natural Sciences

Oral examination: April 20, 2022



Dissertation

submitted to the  
Combined Faculty of Mathematics, Engineering and Natural Sciences  
of Heidelberg University, Germany  
for the degree of

Doctor of Natural Sciences

Put forward by

Katja Verena Stock  
born in Schwetzingen, Germany

Oral examination: April 20, 2022



***N*-Body Simulations of Multiplanetary Systems in Star Clusters:  
The Effect of External Perturbations on the Dynamical Evolution of  
Planets**

Referees: apl. Prof. Dr. Rainer Spurzem  
Prof. Dr. Cornelis Dullemond

**Katja Verena Stock**

*N-Body Simulations of Multiplanetary Systems in Star Clusters:*

*The Effect of External Perturbations on the Dynamical Evolution of Planets*

Ruprecht-Karls-Universität, April 20, 2022

Reviewers: apl. Prof. Dr. Rainer Spurzem and Prof. Dr. Cornelis Dullemond

Supervisors: apl. Prof. Dr. Rainer Spurzem and apl. Prof. Dr. Andreas Just

**Ruprecht-Karls-Universität**

*Computational Stellar Dynamics Group*

Astronomisches Rechen-Institut

Zentrum für Astronomie

Mönchhofstraße 12-14

69120 Heidelberg

# Abstract

Stars predominantly form in groups or clusters, which, however, only dissolve completely after hundreds of millions of years. Within such stellar overdensities, stars interact gravitationally with each other. On timescales of the order of millions of years, close flybys of neighbouring stars occur, which can significantly alter the orbital architecture of the planetary systems that have formed around the stars in the cluster. In this thesis, I simulate a total of four star cluster environments of different densities and subsequently numerically integrate different planetary system architectures over 100 million years, taking into account the gravitational forces that would have acted on them due to the motion of their central stars through the cluster. The results show that the gravitational perturbations from the birth environment can explain the large diversity in the orbital parameters of the observed exoplanet population. In particular, the simulation results show that about 1–2% of all planets adopt stable retrograde orbits due to external stellar perturbations or resulting interactions with other planets in the system. Furthermore, by taking into account tidal interactions between the host star and the planets, the formation of hot Jupiters can be observed in some systems as an indirect consequence of stellar encounters. Moreover, all simulated star cluster environments produce a significant percentage of unbound planets.



# Zusammenfassung

Sterne entstehen überwiegend in Gruppen oder Haufen, die sich jedoch erst nach Hunderten von Millionen Jahren vollständig auflösen. Innerhalb solch stellarer Überdichten wechselwirken Sterne gravitativ miteinander. Auf Zeitskalen in der Größenordnung von Millionen von Jahren kommt es zu nahen Vorbeiflügen benachbarter Sterne, welche die orbitale Architektur der Planetensysteme, die um die Sterne im Haufen entstanden sind, erheblich verändern können. In dieser Arbeit simuliere ich insgesamt vier unterschiedlich dichte Sternhaufenumgebungen und integriere anschließend numerisch verschiedene Planetensystemarchitekturen über 100 Millionen Jahre unter Berücksichtigung der gravitativen Kräfte, die aufgrund der Bewegung ihrer Zentralsterne durch den Haufen auf sie gewirkt hätten. Die Ergebnisse zeigen, dass die gravitativen Störungen aus der Geburtsumgebung die große Diversität in den Orbitalparametern der beobachteten Exoplaneten-Population erklären können. Insbesondere zeigen die Simulationsergebnisse, dass etwa 1–2% aller Planeten infolge von externen stellaren Störungen oder daraus resultierenden Interaktionen mit anderen Planeten im System stabile retrograde Umlaufbahnen einnehmen. Des Weiteren lässt sich unter Berücksichtigung von Gezeitenwechselwirkung zwischen Zentralstern und Planeten in einigen Systemen die Entstehung heißer Jupiter als indirekte Folge stellarer Begegnungen beobachten. Alle simulierten Sternhaufenumgebungen produzieren zudem einen signifikanten Prozentsatz ungebundener Planeten.



# Acknowledgements

Countless people have supported me during my PhD, both scientifically and in other ways. I would like to thank them all, even though I cannot list them individually.

First and foremost, I would like to thank my PhD supervisor, Prof. Dr. Rainer Spurzem, for the support as well as the scientific discussions during my PhD. In particular, the 2 months I spent at NAOC in Beijing and at XJTLU in Suzhou in China as well as at KASI in Daejeon in South Korea following Rainer's invitation remain an unforgettable experience for me.

A very special thanks goes to Dr. Maxwell Cai, who did an excellent job with the development of LPS! Without him, this PhD thesis would not have been possible in this form. I also greatly appreciate his support during the initial phase and his exceptional hospitality during my stays at Leiden Observatory.

In addition to Dr. Maxwell Cai, I would also like to thank Dr. Dimitri Veras, Prof. Dr. Simon Portegies Zwart, Prof. Dr. Thijs Kouwenhoven and my second and third supervisors, Prof. Dr. Andreas Just and Prof. Dr. Cornelis Dullemond, as well as all my colleagues from SPP1992, such as PD Dr. Sabine Reffert and Prof. Dr. Willy Kley, for all the scientific discussions that helped improving my work. Sabine in particular had a very positive influence on my way of working and thinking scientifically during my Bachelor's thesis, which was of great help during the PhD.

Many thanks also to Dr. Stephan Stock and Dr. Uwe Reichert for their thorough reading of the dissertation, their helpful suggestions for improvement and their professional and emotional support up to the very last minute! Also a big thanks to Dr. Branislav Avramov, PD Dr. Sabine Reffert, Dr. Markus Hundertmark, Dr. Oliver Völkel and Albrecht Kamlah for reading and commenting on individual chapters.

My thanks also go to all colleagues at ARI who accompanied me during this adventurous journey. In particular, I would like to mention Dr. Branislav Avramov and Dr. Matteo Mazzarini. You both put a smile on my face every day! Thanks also to Dr. Fabian Klein for being my contact person in all aspects during my initial phase at the ARI. And thanks also to my office mate Dr. Kseniia Sysoliatina for all the nice conversations I had with her during the first year. I would like

to sincerely thank Bhusan Kayasta, my colleague at the NAOC in Beijing, for his help with all the language barriers during my stay in China!

The support I received from my family was also huge. My husband, Stephan Stock, not only accompanied me through two years of working from home due to the pandemic, but also supported me in every way possible whenever necessary (and always cooked well!). Especially in the final phase of my PhD, he did an incredible job, although he himself was not short of work. Many thanks for that, I love you!

I would also like to take this opportunity to thank my parents for their support throughout my studies! A special thanks goes to my father, who read and corrected all my theses and always had suggestions for stylistic improvements.

Of course, I would also like to thank all my friends who have accompanied me during the last years! I especially appreciate that they have always been supportive during stressful times and have never held it against me when they haven't heard from me for a while. I am looking forward to spending more time with them again.

# Contents

<b>1</b>	<b>Introduction</b>	<b>1</b>
1.1	Star Clusters as a Birth Environment for Planetary Systems . . . . .	1
1.1.1	The Formation of Stars and Planets in Clustered Environments . . . . .	1
1.1.2	The Solar System’s Birth Environment . . . . .	3
1.1.3	Motivation for this Thesis . . . . .	4
1.2	Keplerian Motion and the Gravitational Two-Body Problem . . . . .	6
1.2.1	The Two-Body Problem . . . . .	6
1.2.2	Conservation Laws . . . . .	10
1.2.3	Elliptical Keplerian Orbits . . . . .	12
1.2.4	Keplerian Elements . . . . .	15
1.2.5	The Elliptical Kepler Orbit in Three Dimensions . . . . .	17
1.2.6	Conversion from Orbital State Vectors to Orbital Elements . . . . .	18
1.3	The Gravitational $N$ -Body Problem . . . . .	20
1.4	Star Clusters as Collisional Stellar Systems . . . . .	21
<b>2</b>	<b>Hybrid Approach for the Simulation of Planetary Systems in Star Clusters</b>	<b>27</b>
2.1	Previous Methods for Simulating Planetary Systems in Star Clusters . . . . .	27
2.2	Simulation of Star Clusters using NBODY6++GPU . . . . .	28
2.2.1	N-Body Units . . . . .	29
2.2.2	Hermite Integration Scheme . . . . .	30
2.2.3	The Individual Time-Step Criterion and the Block Time-Step Scheme . . . . .	31
2.2.4	The Ahmad-Cohen Neighbour Scheme . . . . .	34
2.3	Simulation of Planetary Systems Embedded in Star Clusters using LPS . . . . .	35
2.3.1	The LonelyPlanets Scheme . . . . .	35
2.3.2	REBOUND’s ias15 Integrator . . . . .	38
<b>3</b>	<b>On the Survival of Resonant and Non-Resonant Planetary Systems in Star Clusters</b>	<b>41</b>
3.1	Introduction . . . . .	41

3.2	Methods and Initial Conditions . . . . .	45
3.2.1	Computational Approach . . . . .	45
3.2.2	Star Cluster Simulations . . . . .	46
3.2.3	Planetary System Simulation . . . . .	48
3.3	Results . . . . .	51
3.3.1	Fractions of Surviving Planets . . . . .	51
3.3.2	Comparison of the Survival Fractions with Previous Studies . . . . .	54
3.3.3	Distribution in <i>a-e</i> Space . . . . .	57
3.3.4	Distribution in <i>a-i</i> Space . . . . .	62
3.3.5	Dynamical Evolution of a Planetary System in Different Initial Configurations . . . . .	63
3.4	Discussion and Conclusions . . . . .	66
<b>4</b>	<b>Birth Cluster Simulations of Planetary Systems with Multiple Super-Earths: Initial Conditions for White Dwarf Pollution Drivers</b>	<b>69</b>
4.1	Introduction . . . . .	70
4.2	Methods and Initial Conditions . . . . .	72
4.2.1	Computational Approach . . . . .	72
4.2.2	Initial Conditions for the Star Cluster Simulation . . . . .	73
4.2.3	Initial Conditions for the Planetary System Simulations . . . . .	74
4.3	Results and Discussion . . . . .	77
4.3.1	Fraction of Surviving Planets . . . . .	77
4.3.2	Semimajor Axis and Eccentricity Distribution and Possible Engulfment during Red Giant Phase . . . . .	79
4.3.3	Inclination and Retrograde Orbits . . . . .	82
4.3.4	Mean-Motion Resonances . . . . .	84
4.3.5	Long-term Stability . . . . .	89
4.4	Conclusions . . . . .	89
<b>5</b>	<b>The Effect of Stellar Encounters in Star Clusters on the Formation of Hot Jupiters</b>	<b>91</b>
5.1	Hot Jupiters . . . . .	91
5.2	Formation Scenarios for Hot Jupiters . . . . .	92
5.3	The Angular Momentum Deficit . . . . .	92
5.4	Modelling the Tidal Star-Planet Interaction . . . . .	94
5.5	Initial Conditions . . . . .	96
5.5.1	Test Runs of Short-Period Planets in Isolation . . . . .	96

5.5.2	Initial Conditions for the Planetary System Simulations including Stellar Perturbation . . . . .	98
5.6	Results . . . . .	99
5.6.1	Tidal Evolution and Hot Jupiter Candidate Criterion . . . . .	99
5.6.2	The Formation of Hot Jupiters through Stellar Encounters Based on Individual Systems . . . . .	102
5.6.3	Statistics and Comparison with Second Simulation Set . . . . .	104
5.7	Discussion . . . . .	111
<b>6</b>	<b>Discussion and Conclusion</b>	<b>117</b>
6.1	The Survival of Solar-System Analogues in Different Star Cluster Environments	118
6.2	The Birth Cluster as Potential Origin for White Dwarf Pollution Drivers . . . . .	121
6.3	Stellar Flybys as a Trigger for Hot Jupiter Formation . . . . .	124
6.4	Comparison of the Simulation Results with the Population of Detected Exoplanets	126
6.5	Conclusion and Outlook . . . . .	129
	<b>Bibliography of Own Publications</b>	<b>131</b>
	<b>Bibliography</b>	<b>133</b>
<b>A</b>	<b>Appendix for Chapter 1</b>	<b>145</b>
A.1	Additional Material for Sec. 1.2.2 . . . . .	145
A.2	Additional Material for Sec. 1.2.3 . . . . .	145
<b>B</b>	<b>Appendix for Chapter 3</b>	<b>147</b>
B.1	Additional Material . . . . .	147
<b>C</b>	<b>Appendix for Chapter 4</b>	<b>153</b>
C.1	Additional Material . . . . .	153
	<b>Declaration</b>	<b>163</b>



“*The Milky Way is nothing else but a mass of innumerable stars planted together in clusters.*”

— Galileo Galilei

## 1.1 Star Clusters as a Birth Environment for Planetary Systems

### 1.1.1 The Formation of Stars and Planets in Clustered Environments

The question of how the Earth, the Sun and our neighbouring planets in the Solar system came into being has fascinated mankind in all cultures for thousands of years. Besides several unsuccessful attempts to explain the formation of planets and stars independently, it was the *nebular hypothesis* that first suspected a close connection between the formation of a star and its planets (e.g. [Helled & Morbidelli 2021](#)). Among their first proponents were Immanuel Kant<sup>1</sup> ([Kant 1755](#)) and Pierre-Simon Laplace<sup>2</sup> ([Laplace & Fourier 1835](#)). This theory was based on the assumption that the Sun and its planets originated from the same nebula and forms the basis of today’s common theory of star and planet formation.

From today’s perspective, the formation of planets is inextricably linked to the formation of their host stars. Observations with space telescopes such as *Hubble*, *Spitzer* and *Herschel* have revealed impressive images of star-forming regions where young stars are deeply embedded in giant molecular clouds (e.g. [Lada & Lada 2003](#); [Parker 2020](#)). These molecular clouds are composed of gas (mainly molecular hydrogen and a small amount of helium) and silicate dust. Once a critical mass is reached (*Jeans instability*; [Jeans 1902](#)), the internal gas pressure is no longer strong enough to prevent the cloud’s gravitational collapse due to self-reinforcing contractions. During this process, the cloud breaks down hierarchically into fragments from which

---

<sup>1</sup>German philosopher (1724 – 1804)

<sup>2</sup>French mathematician, physicist and astronomer (1749 – 1827)

individual stars or multiple star systems are formed (e.g. [Parker 2020](#)). From the fragmentation of the cloud during its collapse, it can be concluded that stars are formed primarily in groups or clusters, which is indeed consistent with observations from the past decades (e.g. [Lada et al. 1993](#); [Clarke et al. 2000](#); [Lada & Lada 2003](#)).

Due to shearing, turbulence and collisions with other clouds, each interstellar cloud has an intrinsic angular momentum that is conserved during contraction. As a result, a strongly flattened accretion disc of gas and dust forms perpendicular to the rotation axis of the newly formed *protostar*, which in the early stages is called *protostellar disc* and which is the predecessor of the birthplace of planets, the *protoplanetary disc* (e.g. [Dullemond et al. 2008](#); [Weigert et al. 2010](#)). The *Atacama Large Millimeter Array* (ALMA; [ALMA Partnership et al. 2015b](#)) in particular has produced impressive images of protoplanetary discs in recent years (see e.g. fig. 3 in [Andrews et al. 2018](#)), including one of the most famous images of the disc around HL Tau ([ALMA Partnership et al. 2015a](#)).

The current predominant planet formation model is the *core accretion scenario*. In this scenario, dust from the primordial molecular cloud forms the basis of planet formation. The first growth phase in the micrometre and metre range is characterised by dust coagulation due to aerodynamic forces. From these dust grains, larger agglomerates of silicate and ice particles are formed ([Birnstiel et al. 2010](#)). Current studies suggest that planetesimals, the building blocks for planets, are formed by the collapse of large clouds of dust and pebbles due to instabilities in the disc ([Klahr & Schreiber 2020](#)). In the next growth phase, it is assumed that planetesimals grow into planet embryos through collisions, which increasingly gravitationally dominate their orbits. When the mass is sufficiently large, approximately equal to the mass of Earth's Moon, the object can additionally accrete pebbles ([Ormel & Klahr 2010](#)). This process can be more efficient than the accretion of planetesimals and is thus the second major mechanism in the formation of massive solid bodies, such as super-Earths and gas giant planet cores. In the case of giant planets, it is assumed that their cores succeed in becoming sufficiently massive to be able to accrete significant amounts of gas onto their cores (*runaway gas accretion* phase; [Pollack et al. 1996](#)) before the gas disc disperses after a few million years (e.g. [Seager & Lissauer 2010](#); [Emsenhuber et al. 2021](#), and references therein). In the standard model of planet formation, it is assumed that giant planets form beyond the *ice line* (sometimes referred to as snow line), at which it is sufficiently cold for volatiles to condense into icy materials, which can considerably accelerate planet formation due to their solid form (e.g. [Dawson & Johnson 2018](#); [Emsenhuber et al. 2021](#)).

Protoplanetary discs, and thus planet formation, can be significantly affected by the clustered environment into which the host star was born. If the stellar density in the star-forming region

is high enough ( $> 10^3 M_{\odot} \text{pc}^{-3}$ )<sup>3,4,5</sup>, such as in the nearby Orion Nebula Cluster (Parker 2014), protoplanetary discs can either be completely destroyed (Parker 2020) or truncated by the flyby of other cluster members (e.g. Portegies Zwart 2016) at radii that can be as small as 0.3–0.5 of the minimum encounter distance (Clarke & Pringle 1993; Hall et al. 1996). Another threat to the protoplanetary disc, which results from the high stellar density in a star cluster and which can also be observed in the Orion Nebula Cluster, is photoevaporation by massive stars in the vicinity (Störzer & Hollenbach 1999; Armitage 2000). In this process, O and B stars that are more massive than  $5 M_{\odot}$  emit high-energy photons (in the near as well as in the extreme ultraviolet range of the spectrum), which heat up the disc’s edges in particular, as a result of which gas can escape due to the thermal pressure, leading to a mass loss of the disc (Parker 2020). The loss of mass through photoevaporation can significantly shorten the lifetime of the protoplanetary disc to about  $10^6$  yr (Störzer & Hollenbach 1999), which in turn can affect the formation of gas giants, which is thought to take  $\geq 10^6$  yr (e.g. Pollack et al. 1996; Helled & Morbidelli 2021). This leads to the conclusion that the formation of massive planets in dense star cluster environments is presumably hampered (Armitage 2000).

## 1.1.2 The Solar System’s Birth Environment

On closer inspection, there are features in the Solar system that provide evidence for a formation in a clustered environment. The Kuiper belt, a remnant of the Sun’s protoplanetary disc, ends abruptly at about 50 au (Kenyon & Bromley 2004). In addition, the orbits of some Kuiper-belt objects, such as the dwarf planet Sedna, are strongly inclined to the plane of the remaining Solar system. Both features indicate that there was at least one close flyby of a neighbouring star at a distance of the order of 100 au (Ida et al. 2000; Kenyon & Bromley 2004).

According to Portegies Zwart et al. (2018a), an alternative theory for the truncation of the Solar system’s protoplanetary disc is a nearby supernova at a distance of about 0.15 pc–0.40 pc. Assuming that this supernova occurred at an angle of  $35^{\circ}$ – $65^{\circ}$ , this theory also explains the tilt of the ecliptic with respect to the Sun’s equatorial plane by  $6^{\circ}$ – $7^{\circ}$  (Beck & Giles 2005; Portegies Zwart et al. 2018a) as well as the Solar protoplanetary disc’s enrichment with short-lived radioisotopes (such as  $^{26}\text{Al}$ ) and its multiple shock heating events, for which there is evidence in chondrules (see Portegies Zwart et al. 2018a, and references therein). In this scenario, Sedna could have been captured by the Solar system from a passing star at a later time. This flyby

<sup>3</sup>Solar Mass:  $1 M_{\odot} = (1.988475 \pm 0.000092) \text{ kg}$  (Prša et al. 2016)

<sup>4</sup>Parsec:  $1 \text{ pc} = 648000\pi^{-1} \text{ au}$  (Prša et al. 2016)

<sup>5</sup>Astronomical unit:  $1 \text{ au} = 149597870700 \text{ m}$  (XXVIII General Assembly of the IAU)

could have additionally truncated the disc and led to a scattering of the Kuiper-belt objects (Portegies Zwart et al. 2018a). In this model, the Sun’s birth cluster contained on the order of  $\sim 10^3$  stellar members and had a half-mass radius of  $\sim 1$  pc (Portegies Zwart 2009; Portegies Zwart et al. 2018a). About 10–60 stars from the Solar birth cluster can still be found in the stellar neighbourhood within a distance of about 100 pc (Portegies Zwart 2009).

### 1.1.3 Motivation for this Thesis

Once the planet formation phase is over and planets have successfully formed in the plane of the dissolved protoplanetary disc, the birth environment of the central star can still play a crucial role in the subsequent dynamical evolution of a planetary system. Especially in regions of high stellar density ( $\geq 100 M_{\odot} \text{pc}^{-3}$ ), gravitational perturbations caused by single or multiple close encounters with neighbouring stars can significantly change the dynamical architecture of planetary systems, as has been shown in several studies in recent years (e.g. Smith & Bonnell 2001; Davies & Sigurdsson 2001; Hurley & Shara 2002; Malmberg et al. 2007; Spurzem et al. 2009; Malmberg et al. 2011; Parker & Quanz 2012; Hao et al. 2013; Cai et al. 2017, 2018; van Elteren et al. 2019; Fujii & Hori 2019; Cai et al. 2019; Flammini Dotti et al. 2019; Glaser et al. 2020). In case of sufficient energy exchange, planets can also completely escape the gravitational field of the host star and either move through the cluster as *free-floating planets* (see e.g. Smith & Bonnell 2001; Parker 2020) — as detected in star clusters such as the  $\sigma$  Orionis cluster (Zapatero Osorio et al. 2000) or the Pleiades (Zapatero Osorio et al. 2014) — or be captured by the intruder or another cluster member (Gouliniski & Ribak 2018; van Elteren et al. 2019). With sufficient escape velocities or through further gravitational interactions with other stars, free-floating planets can even be ejected from the star cluster itself long before the cluster dissolves (Wang et al. 2015b).

The destructive effects of the star cluster environment on forming or already formed planets could also be one of the possible reasons why, of more than 4900 exoplanets found to date<sup>6</sup>, less than 1 per cent have been found in *open clusters* and an even significantly lower fraction in the larger and denser *globular clusters* (see table 1 in Cai et al. 2019), despite several specific attempts to find some in clusters like the Hyades (Guenther et al. 2005), NGC 2362 (Miller et al. 2008) and 47 Tucanae (47 Tuc; Weldrake 2008, and references therein). In old globular clusters like 47 Tuc, the low metallicity may have additionally suppressed planet formation (see e.g. Spurzem et al. 2009, and references therein).

---

<sup>6</sup>As of January 2022, according to the [NASA Exoplanet Archive](#).

In this thesis, only the gravitational effect of the star cluster on already formed planetary systems is studied, starting from the time when the gas has completely escaped from the system. The dynamical evolution of planetary systems in clusters, however, strongly depends on the exact architecture of the planetary system and the cluster environment (especially the stellar density along the trajectory of the host star), giving the initial conditions a crucial role in the simulations. Furthermore, each simulation method has advantages and disadvantages (see Sec. 2.1 and 3.4 for a discussion). In this thesis, I use more realistic and varying initial conditions and longer simulation times than in previous studies, analyse the dynamical evolution of individual planetary systems, and compare the results of simulations with slightly different initial conditions. The simulations are based on the method of Cai et al. (2017, 2018, 2019), which is explained in more detail in Chapter 2 and which offers several important advantages over previous methods. The aim of this thesis is to answer the question of how exactly planetary systems are shaped by the star cluster into which they are born, and whether this birth environment can explain the remarkable diversity of planetary systems detected over the last three decades.

Since this thesis focuses mainly on the dynamics of planets, the two-body problem is examined in the following (Sec. 1.2) based on the motion of a planet around a central star. All equations and quantities relevant for this thesis are derived and introduced. This mathematical basis is particularly important for Chapter 4, where resonances are systematically searched for and investigated. Based on the close examination of the two-body problem and the Keplerian motion of a planet around a star, the generalisation to the  $N$ -body problem follows in Sec. 1.3.

Chapter 2 describes the methodology of numerical  $N$ -body simulations and the hybrid approach used in this thesis. Chapter 3 simulates Solar system-like planetary systems in slightly different initial conditions in four different star cluster environments. While Chapter 3, like most previous studies, is limited to Solar-like host stars, Chapter 4 uses host stars with higher masses ( $1.5 M_{\odot}$ – $2.5 M_{\odot}$ ). All planets in the systems simulated in Chapter 4 have the same mass to be able to work out the effect of the cluster independently of the mass distribution in the system. Chapter 5 takes the tidal interaction between star and planet into account for the first time. I present first simulations, which will be extended at a later stage, to investigate whether hot Jupiters can form as a result of encounters with neighbouring stars.

I put the results from Chapters 3, 4 and 5, which are already discussed in the respective chapter in the context of the slightly different underlying questions, into the general context in Chapter 6 and, in particular, relate them to the population of exoplanets observed in recent decades.

## 1.2 Keplerian Motion and the Gravitational Two-Body Problem

### 1.2.1 The Two-Body Problem

In 1543, Nicolaus Copernicus<sup>7</sup> fundamentally revolutionised mankind’s conception of the universe with his work “*De revolutionibus orbium coelestium*” and the heliocentric model postulated therein, thus replacing the geocentric world view of Claudius Ptolemy<sup>8</sup> that had been valid until then (e.g. [Toomer 1998](#)). This conception was expanded a few decades later by Johannes Kepler<sup>9</sup>, who was hired by Tycho Brahe<sup>10</sup> as his assistant in 1601, shortly before Brahe’s death, to analyse the huge amounts of precise observational data Brahe had accumulated (e.g. [Bate et al. 2020](#); [Carroll & Ostlie 2007](#); [Hintz 2015](#)). From 1601 to 1606, Kepler tried to describe the motion of Mars using various geometric curves and eventually discovered that an ellipse was a possible solution that described the data with sufficient accuracy (e.g. [Bate et al. 2020](#)). In 1609 he published the first two laws named after him, the third followed in 1619 (e.g. [Bate et al. 2020](#)). These *Kepler’s laws of planetary motion* are as follows:

1. The orbit of each planet is an ellipse, with the Sun at a focus.
2. The line joining the planet to the Sun sweeps out equal areas in equal times.
3. The square of the orbital period of a planet is proportional to the cube of its mean distance from the Sun.

They describe the *Keplerian motion* of two bodies without further perturbation, for example due to the presence of another planet in the system. However, at that time Kepler’s laws were only a description of two-body motion — the physical explanation for these laws was provided by Isaac Newton<sup>11</sup> not until 1687 with his work “*Philosophiae Naturalis Principia Mathematica*” ([Newton 1687](#)). In this work, he introduced the three *laws of motion* named after him, which are ([Bate et al. 2020](#)):

1. Every body continues in its state of rest or of uniform motion in a straight line unless it is compelled to change that state by forces impressed upon it.

---

<sup>7</sup>Royal Prussian mathematician and astronomer (1473 – 1543)

<sup>8</sup>Alexandrian mathematician, geographer, astronomer and astrologer (ca. 100 A.D. – ca. 175 A.D.)

<sup>9</sup>German astronomer, physicist, mathematician and philosopher (1571 – 1630)

<sup>10</sup>Danish astronomer (1546 – 1601)

<sup>11</sup>English mathematician, physicist and astronomer (1642 – 1726<sup>jul.</sup>/1727<sup>greg.</sup>)

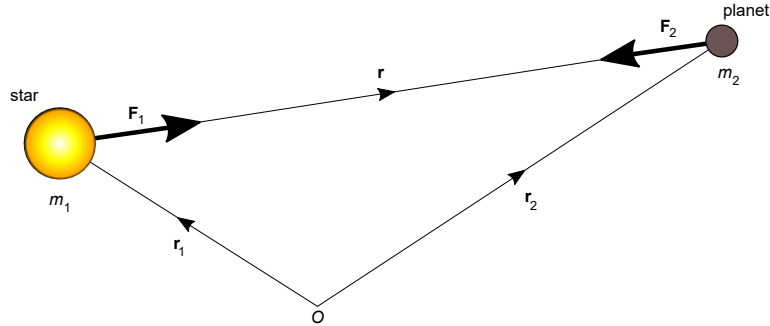


**Fig. 1.1.:** A two-body problem consisting of a star (with mass  $m_1$  and position vector  $\vec{r}_1$ ) and a planet (with mass  $m_2$  and position vector  $\vec{r}_2$ ), as well as the forces acting on each body.

2. The time-rate change of momentum is proportional to the force impressed and is in the same direction as that force.
3. To every action there is always opposed an equal reaction.

However, in this work, he also formulates his universal law of gravity, which states that the force between two bodies of masses  $m_1$  and  $m_2$  with distance  $r$  is

$$F = G \frac{m_1 m_2}{r^2}, \quad (1.1)$$

where  $G$  is the universal gravitational constant<sup>12</sup>.

If we have a planet with mass  $m_2$  in orbit around a star with mass  $m_1$ , as shown in Fig. 1.1, the position of both bodies with respect to the origin of the coordinate system can be described with the position vectors  $\vec{r}_1$  (for the star) and  $\vec{r}_2$  (for the planet). The separation of both objects is equal to the length of the distance vector

$$\vec{r} = \vec{r}_2 - \vec{r}_1, \quad (1.2)$$

and is therefore  $r = |\vec{r}|$ .

Using Newton's second law (the sum of all forces acting on a mass  $m$  is proportional to its acceleration), which is formulated mathematically as

$$\sum \vec{F} = m\vec{a} = m\ddot{\vec{r}}, \quad (1.3)$$

<sup>12</sup>Gravitational constant:  $G = (6.67408 \pm 0.00031) \cdot 10^{-11} \text{ m}^3\text{kg}^{-1}\text{s}^{-2}$  (Prša et al. 2016; Mohr et al. 2016)

and Eq. 1.1, we obtain for the forces acting on the star and the planet respectively,

$$\vec{F}_1 = m_1 \ddot{\vec{r}}_1 = G \frac{m_1 m_2}{r^2} \frac{\vec{r}}{r} \quad (1.4)$$

$$\vec{F}_2 = m_2 \ddot{\vec{r}}_2 = -G \frac{m_1 m_2}{r^2} \frac{\vec{r}}{r} \quad (1.5)$$

and see that Newton's third law ( $\vec{F}_1 = -\vec{F}_2$ ) is valid.

To solve this *two-body problem*, it can be transformed into two independent one-body problems by replacing one mass with the sum of the masses of both bodies ( $M = m_1 + m_2$ ) and replacing the other mass with the *reduced mass*

$$\mu = \frac{1}{1/m_1 + 1/m_2} = \frac{m_1 m_2}{m_1 + m_2} = \frac{m_1 m_2}{M}, \quad (1.6)$$

which is always  $\mu \leq m_1$  and  $\mu \leq m_2$ .

The underlying idea is to find equations of motion for the centre of mass as well as for the distance vector  $\vec{r}$ , so that the force between two objects is only a function of their separation, but not their positions  $\vec{r}_1$  and  $\vec{r}_2$ . Both equations of motion can be derived from Eqs. 1.4 and 1.5. To find the equation of motion for the centre of mass whose position vector corresponds to

$$\vec{R} = \frac{m_1 \vec{r}_1 + m_2 \vec{r}_2}{m_1 + m_2}, \quad (1.7)$$

we add Eqs. 1.4 and 1.5 and obtain

$$\vec{F}_1 + \vec{F}_2 = m_1 \ddot{\vec{r}}_1 + m_2 \ddot{\vec{r}}_2 = (m_1 \ddot{\vec{r}}_1 + m_2 \ddot{\vec{r}}_2) \frac{M}{m_1 + m_2} = M \ddot{\vec{R}} \stackrel{\text{Newton's 3. law}}{=} 0. \quad (1.8)$$

This equation is satisfied when

$$\ddot{\vec{R}} = \frac{m_1 \ddot{\vec{r}}_1 + m_2 \ddot{\vec{r}}_2}{m_1 + m_2} = 0, \quad (1.9)$$

which means that the centre of mass is either stationary (if  $m_1 \dot{\vec{r}}_1 + m_2 \dot{\vec{r}}_2 = 0$ ) or moving with a constant velocity in a constant direction<sup>13</sup>. Equation 1.9 is the *equation of motion for the centre of mass*.

---

<sup>13</sup>A constant motion of the centre of mass also implies that the total momentum  $m_1 \dot{\vec{r}}_1 + m_2 \dot{\vec{r}}_2$  is constant and conserved.

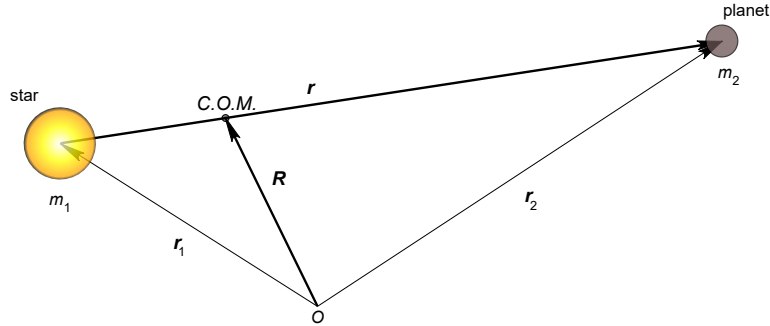


**Fig. 1.2.:** The Jacobi coordinates  $\vec{R} = \frac{m_1\vec{r}_1}{M} + \frac{m_2\vec{r}_2}{M}$  and  $\vec{r} = \vec{r}_2 - \vec{r}_1$  for the two-body problem and the centre of mass (C.O.M.).

We obtain a second-order ordinary differential equation for the motion of the distance vector  $\vec{r}$  by rewriting and subtracting Eq. 1.4 from Eq. 1.5, which results in

$$\ddot{\vec{r}} + \frac{GM}{r^2} \frac{\vec{r}}{r} = 0. \quad (1.10)$$

This *equation of relative motion* describes the motion of the planet around the star.

Equations 1.2 and 1.7 are the *Jacobi coordinates* for the two-body problem and are depicted in Fig. 1.2. Jacobi coordinates are commonly used for simulating planetary systems as they facilitate dealing with hierarchical structures such as those present in a planetary system.

Now that the one-body problem is solved by the trajectory  $\vec{r}(t)$  and the motion of the centre of mass  $\vec{R}$  is also known, we can convert back from the Jacobi coordinates to the original coordinates. For this purpose, we introduce two further position vectors  $\vec{R}_1$  and  $\vec{R}_2$  that describe the position of the star and the planet in relation to the centre of mass. As can be seen in Fig. 1.3,

$$\vec{R}_1 = \vec{r}_1 - \vec{R} \quad (1.11)$$

$$\vec{R}_2 = \vec{r}_2 - \vec{R} \quad (1.12)$$

It follows from Eq. 1.7 that  $m_1\vec{R}_1 + m_2\vec{R}_2 = 0$ , so by rewriting Eqs. 1.11 and 1.12 we obtain the expressions:

$$\vec{r}_1(t) = \vec{R}(t) - \frac{m_2}{m_1 + m_2} \vec{r}(t), \quad \vec{r}_2(t) = \vec{R}(t) + \frac{m_1}{m_1 + m_2} \vec{r}(t). \quad (1.13)$$

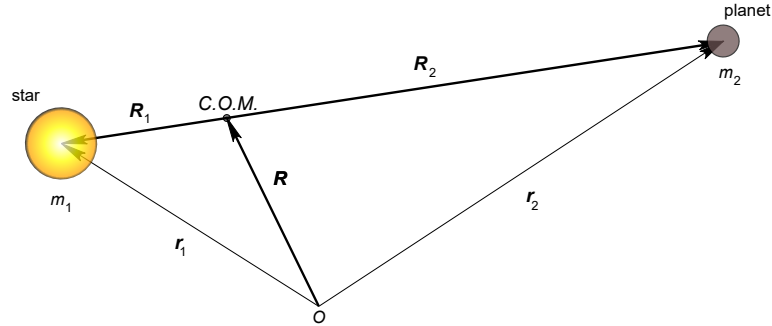


**Fig. 1.3.:** Position vectors for the star ( $\vec{r}_1$ ), the planet ( $\vec{r}_2$ ) and the centre of mass ( $\vec{R}$ ) with respect to the origin  $O$ , as well as the position vectors for the star ( $\vec{R}_1$ ) and the planet ( $\vec{R}_2$ ) with respect to the centre of mass (C.O.M.).

## 1.2.2 Conservation Laws

By taking the cross product of  $\vec{r}$  with Eq. 1.10, we get

$$\vec{r} \times \ddot{\vec{r}} = 0, \quad (1.14)$$

because  $\vec{r} \times \dot{\vec{r}} = 0$ . This can be integrated, which yields

$$\vec{r} \times \dot{\vec{r}} = \vec{r} \times \vec{v} = \vec{h}, \quad (1.15)$$

where  $\vec{h}$  is a constant vector. Since the angular momentum is defined as  $\vec{L} = \vec{r} \times \vec{p}$ , where  $\vec{p} = \mu \dot{\vec{r}}$  is the generalised momentum, we can relate  $\vec{h}$  to the angular momentum as follows:

$$\vec{h} = \frac{\vec{L}}{\mu}. \quad (1.16)$$

The vector  $\vec{h}$  is called the *specific angular momentum* and is always perpendicular to the orbital plane. As  $\vec{h}$  is constant,  $\vec{L}$  must also remain constant. The (specific) angular momentum is therefore one of a total of three conserved quantities in the two-body problem.

The second quantity which is conserved along the trajectories of  $m_1$  and  $m_2$  can be obtained by multiplying Eq. 1.10 by  $\dot{\vec{r}}$ :

$$\dot{\vec{r}} \cdot \ddot{\vec{r}} + \dot{\vec{r}} \cdot \frac{GM \vec{r}}{r^2} = 0. \quad (1.17)$$

If we consider that  $\frac{d}{dt}\left(\frac{v^2}{2}\right) = v\dot{v}$  and  $\frac{d}{dt}\left(-\frac{GM}{r}\right) = \frac{GM}{r^2}\dot{r}$ , we obtain:

$$\frac{d}{dt}\left(\frac{v^2}{2} - \frac{GM}{r}\right) = 0. \quad (1.18)$$

The integration of this equation yields the second constant (and thus conserved) quantity, the *specific mechanical energy*:

$$\frac{v^2}{2} - \frac{GM}{r} = \epsilon. \quad (1.19)$$

Alternatively, we can consider the total energy of the system as a conserved quantity, which we obtain by multiplying the specific mechanical energy by the reduced mass:

$$E = T + U = \frac{\mu v^2}{2} - \frac{GM}{r}\mu, \quad (1.20)$$

where  $T$  is the kinetic energy and  $U$  the potential energy.

To obtain the third conserved quantity, we first take the cross product of Eq. 1.10 with the specific angular momentum  $\vec{h}$ :

$$\ddot{\vec{r}} \times \vec{h} = -\frac{GM}{r^3}(\vec{r} \times \vec{h}). \quad (1.21)$$

The right side of this equation can be rewritten (see Eq. A.1 in Sec. A.1 in the appendix for a full derivation) to

$$-\frac{GM}{r^3}(\vec{r} \times \vec{h}) = GM \frac{d}{dt}\left(\frac{\vec{r}}{r}\right). \quad (1.22)$$

We can therefore write Eq. 1.21 as

$$\frac{d}{dt}(\dot{\vec{r}} \times \vec{h}) = GM \frac{d}{dt}\left(\frac{\vec{r}}{r}\right), \quad (1.23)$$

which we can integrate so that we obtain

$$\dot{\vec{r}} \times \vec{h} = GM \frac{\vec{r}}{r} + \vec{B}, \quad (1.24)$$

where  $\vec{B}$  is a constant vector. It is related to the *Laplace-Runge-Lenz vector*

$$\vec{e} = \vec{B}/(GM) = \frac{\vec{v} \times \vec{h}}{GM} - \frac{\vec{r}}{r}, \quad (1.25)$$

which is the third conserved quantity in the two-body problem.

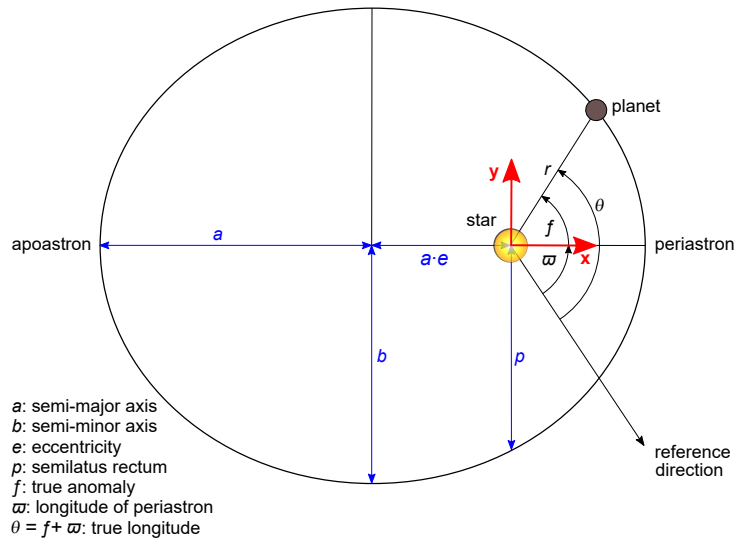


**Fig. 1.4.:** The semimajor axis  $a$ , the semiminor axis  $b$ , the eccentricity  $e$  and the semilatus rectum  $p$  of an elliptical Keplerian orbit. The longitude of periastron  $\varpi$  is an angular parameter defining the position of the periastron with respect to a certain reference direction ( $\theta = 0^\circ$ ). The true anomaly  $f$  gives the current angular position of the planet with respect to the periastron. Consequently, the true longitude  $\theta = f + \varpi$  is the planet's current angular position with respect to the reference direction.

### 1.2.3 Elliptical Keplerian Orbits

The Laplace-Runge-Lenz vector is closely related to the eccentricity of the ellipse, which describes the shape of the planet's orbit around the star, and is therefore also called *eccentricity vector*. The vector  $\vec{e}$  is always parallel to the semimajor axis  $a$  of the ellipse. The semimajor axis corresponds to half of the longest diameter of the ellipse, i.e. the line that passes through both foci and connects the apoastron with the periastron. Apoastron and periastron<sup>14</sup> are the farthest and nearest points of the planet's orbit with respect to the central star. Both points are depicted in Fig. 1.4, which shows a schematic view of an elliptical orbit of a planet around a star including the most relevant quantities and angles.

<sup>14</sup>These terms vary depending on the primary and secondary object. For the orbits of the planets in the Solar system, they are called ap-/perihelion, whereas in the Moon-Earth system they are called apo-/perigee. More generally, they are often referred to as apo-/pericentre or apo-/periapsis, whereas the terms apo-/periastron are used specifically for exoplanets around stars other than the Sun.

Multiplying Eq. 1.24 by  $\vec{r}$  yields a scalar equation,

$$\vec{r} \cdot \dot{\vec{r}} \times \vec{h} = \vec{r} \cdot \text{GM} \frac{\vec{r}}{r} + \vec{r} \cdot \vec{B}, \quad (1.26)$$

which, using Eq. 1.15, can be rewritten as

$$h^2 = \text{GM}r + rB \cos f, \quad (1.27)$$

where  $f$  is the angle between the vectors  $\vec{B}$  and  $\vec{r}$ . The angle  $f$  is called the *true anomaly* and defines the current orbital position of the planet with respect to the periastron, as shown in Fig. 1.4, wherefore the components of the position vector  $\vec{r}$  in Fig. 1.4 are a function of the true anomaly:

$$x = r \cos f, \quad y = r \sin f. \quad (1.28)$$

By solving Eq. 1.27 for  $r$ , we get

$$r = \frac{h^2 / (\text{GM})}{1 + B / (\text{GM}) \cdot \cos f} = \frac{p}{1 + e \cos f}, \quad (1.29)$$

where

$$p = a(1 - e^2) \quad (1.30)$$

is the *semilatus rectum* of the ellipse (see Fig. 1.4 for its geometrical definition).

The area enclosed by an ellipse is  $A_{\text{ellipse}} = \pi ab$ , where

$$b^2 = a^2(1 - e^2) \quad (1.31)$$

is the *semiminor axis* of the ellipse and, like the semimajor axis, corresponds to half the length of one of the two axes of symmetry of the ellipse (see Fig. 1.4). The area  $A_{\text{ellipse}}$  is swept out by the distance vector  $\vec{r}$  in one *orbital period*,  $T$ . The differential element of area,  $dA$ , swept out by  $\vec{r}$  as the planet moves through an angle  $d\theta$  along its elliptical orbit, as shown in Fig. 1.5, is:

$$dA = \int_0^r r \, dr \, d\theta = \frac{1}{2} r^2 d\theta. \quad (1.32)$$

From this follows a mathematical expression for Kepler's second law,

$$\dot{A} = \frac{1}{2} r^2 d\dot{\theta} = \frac{1}{2} h = \text{const.}, \quad (1.33)$$

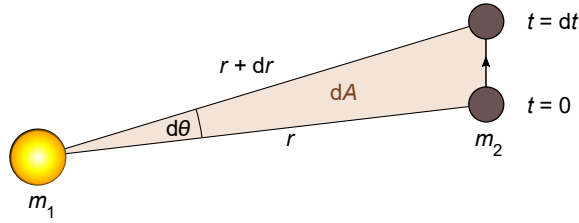


**Fig. 1.5.:** The differential element of area,  $dA$ , swept out by  $\vec{r}$  as it moves through an angle  $d\theta$ . Adapted from fig. 2.3 in Murray & Dermott (1999).

where we use the expression  $h = r^2\dot{\theta}$  that follows from converting Eq. 1.15 into polar coordinates (see Sec. A.2 in the appendix).

Our goal is to find an expression for the orbital period,  $T$ , with which both bodies orbit the mutual centre of mass. By integrating Eq. 1.33 for one orbital period  $T$  it follows that the area of the ellipse can also be expressed by  $A_{\text{ellipse}} = hT/2$ , which can then be rewritten as:

$$T = \frac{2\pi ab}{h} \quad \Rightarrow \quad T^2 = \frac{4\pi^2 a^3}{GM} = \frac{4\pi^2 a^3}{G(m_1 + m_2)}. \quad (1.34)$$

Equation 1.34 confirms the proportionality between the square of the planet's orbital period and the cube of its mean distance in Kepler's third law since the planet's semimajor axis  $a$  is a quantity for the mean distance between planet and star.

Now that we know the orbital period of the planet, we introduce another useful quantity, the mean motion

$$n = \frac{2\pi}{T}, \quad (1.35)$$

with the help of which we transform Eq. 1.34 into the following form<sup>15</sup>:

$$GM = n^2 a^3. \quad (1.36)$$

<sup>15</sup>The quantity  $GM$  is called the *standard gravitational parameter* and is usually also referred to as  $\mu$ , like the reduced mass. To avoid confusion with the reduced mass, the standard gravitational parameter is not further defined in this thesis.

Since the longitude of periastron  $\varpi$  (angle between the reference direction and the periastron) is a constant angle, we know that  $\dot{\theta} = \dot{f}$ . Using this relationship, Eq. 1.36 and  $A_{\text{ellipse}} = \pi ab = hT/2$ , the specific angular momentum in polar coordinates can be put into the following form:

$$h = r^2 \dot{f} = \sqrt{a(1 - e^2)GM} = na^2 \sqrt{1 - e^2}. \quad (1.37)$$

Using Eq. 1.37, we can now take the time derivative of Eq. 1.29 and obtain the following expression for the velocity of the planet as a function of its true anomaly:

$$\dot{r} = \frac{r \dot{f} e \sin f}{1 + e \cos f} = \frac{na}{\sqrt{1 - e^2}} e \sin f. \quad (1.38)$$

## 1.2.4 Keplerian Elements

The size, shape and orientation of an elliptical orbit is sufficiently defined by five parameters. However, to define the position of the planet along its orbit, a sixth parameter is needed. The classical six orbital parameters are:

1. **Semimajor axis** ( $a$ ) — defines the size of the orbit.
2. **Eccentricity** ( $e$ ) — defines the shape of the orbit.
3. **Inclination** ( $i$ ) — the tilt angle between orbital and reference plane, measured at the ascending node (the point where the planet crosses the reference plane in the upward direction).
4. **Longitude of the ascending node** ( $\Omega$ ) — the angle between the reference direction and the line connecting star and ascending node, measured counter-clockwise.
5. **Argument of periastron** ( $\omega$ ) — the angle between ascending node and periastron, defines the orbit's orientation in the orbital plane.
6. **True anomaly** ( $f$ ) — the position of the planet along the orbit at a specific epoch.

The geometric definitions of the latter three parameters are shown in Fig. 1.6. The sixth orbital element is substitutable with other associated quantities, such as the *time of periastron passage*,  $t_0$ , or the *mean anomaly*,  $M$ , at a specific epoch. The mean anomaly is a theoretical quantity and describes the position relative to the periastron that the planet would have on a circular orbit at the same epoch. It is defined as:

$$M = n(t - t_0). \quad (1.39)$$

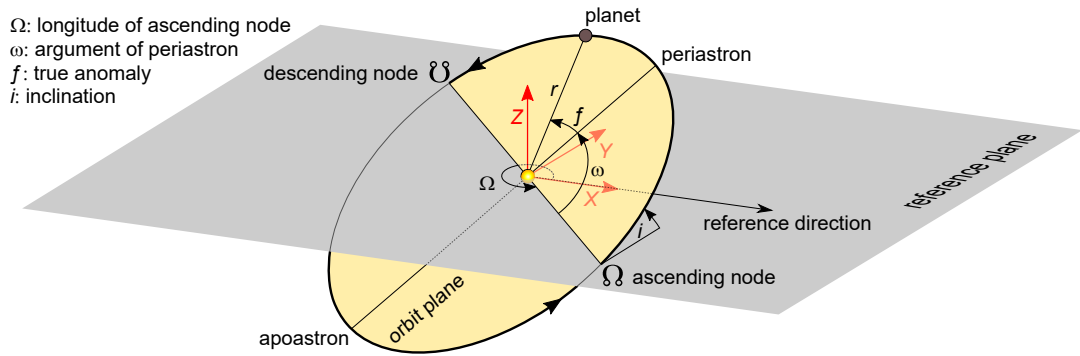


**Fig. 1.6.:** Definition of the orbital parameters  $i$ ,  $\omega$  and  $\Omega$ . The three-dimensional  $(X, Y, Z)$  coordinate system, which will be introduced in Sec. 1.2.5 is additionally shown. Adapted from fig. 2.2 in Perryman (2011).

Furthermore, it is closely linked to the Kepler problem, finding  $r$  as a function of time instead of an angle (such as  $f$ , as in Eq. 1.29).

To solve the Kepler problem, the *Kepler equation*,

$$M = E - e \sin E, \quad (1.40)$$

must be solved, which relates the mean anomaly,  $M$ , to the *eccentric anomaly*,  $E$ . The Kepler equation is a transcendental equation, thus it cannot be solved algebraically for  $E$  and must therefore be solved numerically. Since a description of numerical methods for the solution of the Kepler equation exceeds the purpose of this thesis, reference is made to relevant literature, such as Danby (1988) or Murray & Dermott (1999).

The relationship between the angles  $E$  and  $f$  is shown schematically in Fig. 1.7, where we use the Cartesian coordinates  $\bar{x}$  and  $\bar{y}$  (note that they are not the same as in Fig. 1.4 as they are centred on the centre of the ellipse).

From Fig. 1.7, we see that  $\bar{x} = a \cos E$ . Using the equation for an ellipse,  $(\bar{x}/a)^2 + (\bar{y}/b)^2 = 1$ , as well as Eq. 1.31, we obtain  $\bar{y}^2 = b^2 \sin^2 E$  and therefore  $\bar{y} = a \sqrt{1 - e^2} \sin E$ . Since the coordinate systems in Figs. 1.4 and 1.7 are only shifted by the value  $a \cdot e$  in horizontal direction, one can rewrite the components of the position vector  $\vec{r}$  from Eq. 1.28 to:

$$x = a(\cos E - e), \quad y = a \sqrt{1 - e^2} \sin E. \quad (1.41)$$

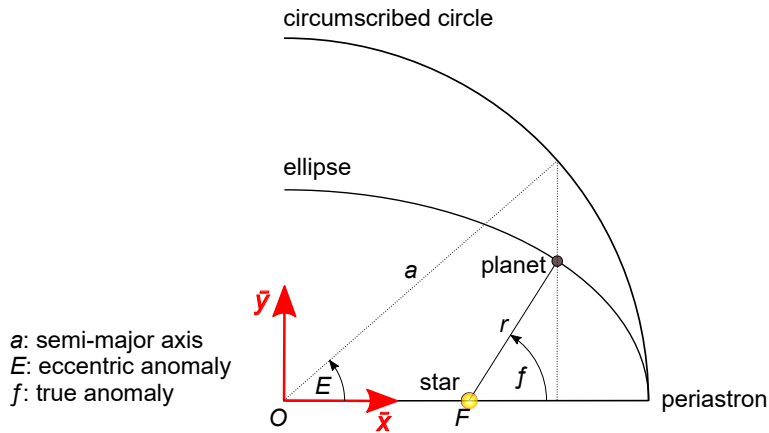


**Fig. 1.7.:** The geometric interpretation of the eccentric anomaly,  $E$ , and its relation to the true anomaly,  $f$ . Adapted from fig. 2.7 in Murray & Dermott (1999).

As an alternative expression for the length of  $\vec{r}$ , we therefore obtain

$$r = a(1 - e \cos E) \quad (1.42)$$

using the Pythagorean identity,  $\sin^2 E + \cos^2 E = 1$ .

## 1.2.5 The Elliptical Kepler Orbit in Three Dimensions

So far, we have only considered the motion of the planet in the two-dimensional orbital plane. However, we need a general three-dimensional description for simulating multiple planets in a system, which should be independent of the orbital plane of an individual planet.

As a first step, we extend the two-dimensional coordinate system from Fig. 1.4 to three dimensions and obtain:

$$\vec{r} = \begin{pmatrix} x \\ y \\ z \end{pmatrix} = \begin{pmatrix} r \cos f \\ r \sin f \\ 0 \end{pmatrix}. \quad (1.43)$$

Then we introduce the Cartesian coordinates  $X$ ,  $Y$  and  $Z$ , which also have their origin in the centre of the star, and define the direction of  $X$  as the reference direction (see Fig. 1.6).  $Y$  is to be perpendicular to  $X$ , and  $Z$  in turn perpendicular to  $X$ ,  $Y$  and the reference plane.

To obtain the intended  $(X, Y, Z)$  coordinate system, the  $(x, y, z)$  coordinate system from Eq. 1.43 needs to be

- rotated through an angle  $\omega$  about the  $z$ -axis,
- rotated through an angle  $i$  about the  $x$ -axis,
- rotated through an angle  $\Omega$  about the  $z$ -axis.

This is achieved by using the rotation matrices  $\vec{P}_1$ ,  $\vec{P}_2$  and  $\vec{P}_3$ , which are as follows (Murray & Dermott 1999):

$$\vec{P}_1 = \begin{pmatrix} \cos \omega & -\sin \omega & 0 \\ \sin \omega & \cos \omega & 0 \\ 0 & 0 & 1 \end{pmatrix}, \quad (1.44)$$

$$\vec{P}_2 = \begin{pmatrix} 1 & 0 & 0 \\ 0 & \cos i & -\sin i \\ 0 & \sin i & \cos i \end{pmatrix}, \quad (1.45)$$

$$\vec{P}_3 = \begin{pmatrix} \cos \Omega & -\sin \Omega & 0 \\ \sin \Omega & \cos \Omega & 0 \\ 0 & 0 & 1 \end{pmatrix}. \quad (1.46)$$

The general  $(X, Y, Z)$  reference system for the position of a planet is thus:

$$\begin{pmatrix} X \\ Y \\ Z \end{pmatrix} = \vec{P}_3 \vec{P}_2 \vec{P}_1 \begin{pmatrix} r \cos f \\ r \sin f \\ 0 \end{pmatrix} = r \begin{pmatrix} \cos \Omega \cos(\omega + f) - \sin \Omega \sin(\omega + f) \cos i \\ \sin \Omega \cos(\omega + f) + \cos \Omega \sin(\omega + f) \cos i \\ \sin(\omega + f) \sin i \end{pmatrix}. \quad (1.47)$$

## 1.2.6 Conversion from Orbital State Vectors to Orbital Elements

To study the dynamical evolution of the planetary systems in detail, we need to be able to derive all orbital parameters and related angles from the orbital state vectors (Cartesian vectors of position  $\vec{r} = (X \ Y \ Z)^T$  and velocity  $\vec{v} = (V_X \ V_Y \ V_Z)^T$ ). Therefore, a short procedure for the conversion is given below:

1. Calculate  $\vec{h}$  from the orbital state vectors:

$$\begin{pmatrix} h_X \\ h_Y \\ h_Z \end{pmatrix} = \begin{pmatrix} X \\ Y \\ Z \end{pmatrix} \times \begin{pmatrix} V_X \\ V_Y \\ V_Z \end{pmatrix} = \begin{pmatrix} \pm h \sin i \sin \Omega \\ \mp h \sin i \cos \Omega \\ h \cos i \end{pmatrix}. \quad (1.48)$$

2. Calculate  $e$  using Eq. 1.25:

$$e = |\vec{e}|. \quad (1.49)$$

3. Calculate  $a$  using  $p = h^2/(GM)$  and Eq. 1.30:

$$a = \frac{h^2/(GM)}{(1 - e^2)}. \quad (1.50)$$

4. Calculate  $i$  from Eq. 1.48:

$$i = \cos^{-1} \left( \frac{h_Z}{h} \right). \quad (1.51)$$

5. Calculate  $\Omega$  from Eq. 1.48 and use upper sign if  $h_Z > 0$  and lower sign if  $h_Z < 0$  (Murray & Dermott 1999):

$$\sin \Omega = \frac{\pm h_X}{h \sin i}, \quad (1.52)$$

$$\cos \Omega = \frac{\mp h_Y}{h \sin i} \quad (1.53)$$

$$. \quad (1.54)$$

6. Calculate  $r$ :

$$r = |\vec{r}| = \sqrt{X^2 + Y^2 + Z^2}. \quad (1.55)$$

7. Calculate  $\omega + f$  from Eq. 1.47 and subsequently  $f$  and  $\omega$  using Eqs. 1.38 and 1.29 (Murray & Dermott 1999):

$$\sin(\omega + f) = \frac{Z}{r \sin i}, \quad (1.56)$$

$$\cos(\omega + f) = \sec \Omega \left( \frac{X}{r} + \sin \Omega \sin(\omega + f) \cos i \right), \quad (1.57)$$

$$\sin f = \frac{h}{GM_e} \dot{r}, \quad (1.58)$$

$$\cos f = \frac{h^2/(GM) - r}{er}. \quad (1.59)$$

8. Calculate  $M$  by first calculating  $E$  from Eq. 1.42:

$$M = E - e \sin E. \quad (1.60)$$

### 1.3 The Gravitational $N$ -Body Problem

As soon as there is more than one planet in a planetary system, the system can no longer be considered a pure two-body problem and needs to be treated as an  $N$ -body problem. Another classic example of an  $N$ -body problem is star cluster dynamics, where the gravitational forces of all other  $N - 1$  stars in the cluster have an effect on the motion of each individual star.

The force acting on a single particle of index  $i$  is thus the sum of the gravitational forces of all other  $N - 1$  particles in the system:

$$\vec{F}_i = -Gm_i \sum_{j=1, j \neq i}^N m_j \frac{\vec{r}_i - \vec{r}_j}{|\vec{r}_i - \vec{r}_j|^3}. \quad (1.61)$$

The equations of motion for particle  $i$  are therefore:

$$\ddot{\vec{r}}_i = -G \sum_{j=1, j \neq i}^N m_j \frac{\vec{r}_i - \vec{r}_j}{|\vec{r}_i - \vec{r}_j|^3}. \quad (1.62)$$

The simulation of an  $N$ -body system thus requires the solution of  $N$  second-order differential equations, leading to a computational complexity of order  $O(N^2)$ . For the simulation of systems with small  $N$ , such as planetary systems, these calculations can be executed sequentially on general-purpose CPUs (central processing unit). For systems with large  $N$ , this leads to a quadratic

increase in computing time if the calculation of the acceleration for all  $N$  particles is executed sequentially and required (see Sec. 2.2.4 for the description of a method to avoid the full computation of all forces). For this reason, in order to keep the computational costs for those simulations within reasonable limits, GPUs (graphics processing units) are used for systems with large  $N$ , as GPUs enable a more efficient parallelisation of the computing processes due to their highly parallel structure.

Since the initial conditions consist of  $6N$  values ( $3N$  for positions and  $3N$  for velocities), the  $N$ -body problem can be specified by  $3N$  second-order or  $6N$  first-order differential equations (Aarseth 2003). The  $N$ -body problem can no longer be solved analytically for more than two bodies (except for a few special configurations in the case of  $N = 3$ )<sup>16</sup>. During numerical integration, due to the chaotic nature of the  $N$ -body problem in the case of  $N > 2$ , the smallest integration errors can grow exponentially with time (see also Miller 1964; Quinlan & Tremaine 1992, for a discussion on the reliability of gravitational  $N$ -body integrations).

## 1.4 Star Clusters as Collisional Stellar Systems

Different definitions exist for star clusters. Portegies Zwart et al. (2010), for example, consider a cluster to be a group of stars that are gravitationally bound to each other. Lada & Lada (2003), on the other hand, define a cluster as a collection of stars whose mass density is large enough to resist tidal disruption from the Galaxy in a state of *virial equilibrium*, defined by:

$$\langle T \rangle = -\frac{1}{2} \langle U \rangle. \quad (1.63)$$

Additionally, according to Lada & Lada (2003), the cluster must contain a sufficiently large number of stellar members so that it takes more than  $10^8$  yr for the cluster to evaporate through internal stellar encounters. Traditionally, star clusters have mostly been classified as *open clusters* and *globular clusters*. Open clusters consist of a few dozen to a few thousand stars and are generally found in the discs of spiral galaxies (see Fig. 1.8 for an image of the famous Pleiades open cluster). Globular clusters, on the other hand, are dense collections of up to several millions of stars and are found mostly in galactic halos. Moreover, the stellar population in globular clusters tends to be older and more metal-poor than in open clusters. Fig. 1.9 shows the second brightest globular cluster in the night sky, 47 Tuc.

---

<sup>16</sup>Karl Fritiof Sundman, a Finnish mathematician, found an analytical solution in 1913 in the form of a power series, which, however, converges too slowly to be of any practical use (Gurfil & Seidelmann 2016).



**Fig. 1.8.:** The Pleiades open star cluster. Image: Courtesy of Uwe Reichert.

The evolution of a star cluster can be simulated using Eq. 1.62. Star clusters are generally collisional systems, whereby the term “collisional” does not refer to an actual physical collision, but to the long-term effect of distant stellar encounters. For a given critical distance  $b_{\text{crit}}$ , the cross-section is  $\sigma = \pi b_{\text{crit}}^2$  and the mean free path is  $l \approx 1/(\pi b_{\text{crit}}^2 n_{\star})$ , where  $n_{\star}$  is the stellar number density. The typical timescale between two encounters with a distance smaller than  $b_{\text{crit}}$  is

$$\tau_{\text{enc}} \approx \frac{1}{\pi b_{\text{crit}}^2 n_{\star} \bar{v}_{\star}}, \quad (1.64)$$

where  $\bar{v}_{\star}$  is the typical relative velocity of the stars with respect to each other.

By inserting a typical stellar radius for  $b_{\text{crit}}$ , we obtain the event rate of physical collisions, which, however, is negligible. Instead, the rate for strong encounters between a test particle of mass  $m$  and a star of mass  $M_{\star}$  can be derived. An encounter is considered strong if the change in the particle’s potential energy  $U$  with respect to  $M_{\star}$  is greater or equal to the particle’s initial kinetic energy:

$$\Delta U = \frac{GM_{\star}m}{r} \geq \frac{m\bar{v}_{\star}^2}{2}. \quad (1.65)$$



**Fig. 1.9.:** The globular cluster 47 Tuc. Image: Courtesy of Uwe Reichert.

The critical distance for a strong encounter is then:

$$b_{\star} = \frac{2GM_{\star}}{\bar{v}_{\star}^2}. \quad (1.66)$$

Substituting  $b_{\text{crit}}$  in Eq. 1.64 with  $b_{\star}$  from Eq. 1.66 yields the following expression for the timescale between two strong encounters:

$$\tau_{\text{enc}} = \frac{\bar{v}_{\star}^3}{4\pi G^2 M_{\star}^2 n_{\star}} = 4 \cdot 10^9 \left( \frac{\bar{v}_{\star}}{\text{kms}^{-1}} \right)^3 \left( \frac{M_{\star}}{M_{\odot}} \right)^{-2} \left( \frac{n_{\star}}{\text{pc}^{-3}} \right)^{-1} \text{ yr}. \quad (1.67)$$

When we use the Solar neighbourhood values for the stellar number density and relative velocity,  $n_{\star} \approx 0.1 \text{ pc}^{-3}$  and  $\bar{v}_{\star} \approx 40 \text{ kms}^{-1}$  (Weigert et al. 2010), we obtain a timescale for strong encounters of  $\tau_{\text{enc}} > 2.5 \cdot 10^{15} \text{ yr}$  for the Sun, which exceeds the age of the Universe. The Solar neighbourhood, as well as the Milky Way disc, can thus be considered a collisionless system. However, the dependence of the encounter timescale on  $\bar{v}_{\star}^3$  and  $1/n_{\star}$  shows that the timescale for strong encounters is considerably shorter for dense stellar systems such as star clusters, where the

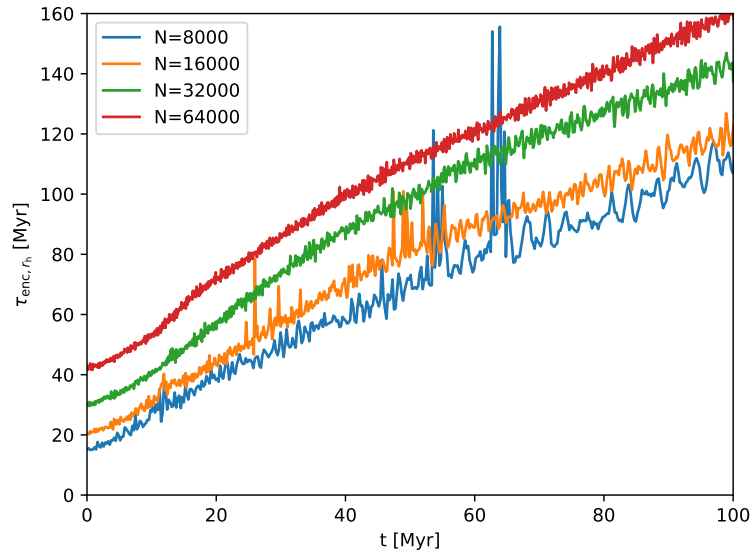


**Fig. 1.10.:** The strong encounter timescales according to Eq. 1.67 for Solar-mass stars located at the half-mass radius  $r_h$  for the four star clusters simulated in Chapter 3. The different colours correspond to different numbers of stars in the simulated cluster. The initial half-mass radius for all clusters is  $r_h = 0.78$  pc and increases with time.

velocity dispersion is typically a factor of 2–5 smaller than in the Solar neighbourhood (Weigert et al. 2010). Figure 1.10 shows the evolution of the timescales for strong encounters for stars with  $1 M_\odot$  at the half-mass radius  $r_h$  of the star clusters simulated in Chapter 3. For example, at the end of the simulation, after 100 Myr, the encounter timescale for the cluster with the lowest velocity dispersion (represented by the blue line) reaches a value that would correspond to the order of magnitude of the entire simulation time. For a star close to the half-mass radius, a strong encounter would no longer be expected in this cluster, even if the simulation time were extended.

However, strong encounters are not the only relevant process for the dynamical evolution of the stars in the cluster. Momentum is also transferred from one star to another during weak encounters, which are much more common and can slightly change the velocity component and thus the trajectory of both stars. The kinetic energy transferred during the encounter is conserved. After some time, however, the kinetic energy acquired through encounters is larger than the star’s

initial kinetic energy, resulting in the loss of information about its original motion. The timescale for the redistribution of kinetic energy through weak encounters is called the *relaxation time*,

$$\tau_{\text{relax}} = \frac{\bar{v}_\star^3}{8\pi G^2 M_\star^2 n_\star \ln(b_{\text{max}}/b_{\text{min}})}, \quad (1.68)$$

where  $b_{\text{min}}$  and  $b_{\text{max}}$  are the minimum and maximum impact parameters (see e.g. [Weigert et al. 2010](#)).

We can substitute  $b_{\text{min}}$  with  $b_\star$  from Eq. 1.66. The maximum impact parameter is more difficult to determine, but usually the total size of the system can be used for  $b_{\text{max}}$ . The relaxation timescale and the strong encounter timescale from Eq. 1.67 are related as follows:

$$\tau_{\text{relax}} = \frac{\tau_{\text{enc}}}{2 \ln(b_{\text{max}}/b_{\text{min}})}. \quad (1.69)$$

Star clusters thus evolve dynamically through weak encounters, which is called two-body relaxation. During a two-body interaction, the kinetic energy distribution of both stars is equalized. Stars with lower masses therefore gain velocity through multiple two-body interactions and can migrate to the outer regions of the cluster. Higher-mass stars, in contrast, lose kinetic energy, causing them to sink towards the centre. This process is called *mass segregation*. The evolution towards energy equipartition causes the core of the cluster to collapse (see e.g. [Lynden-Bell & Wood 1968](#); [Cohn 1979](#); [Lynden-Bell & Eggleton 1980](#); [Antonov 1985](#)). This *core collapse* can be stopped by binary stars in the centre, which can release energy by becoming more gravitationally bound, a process called *hardening* (e.g. [Bettwieser & Sugimoto 1984](#); [Makino 1996](#)).

Stellar systems with a relaxation timescale shorter than their age are considered collisional systems<sup>17</sup>. The evaporation timescale for a star cluster can be estimated from its relaxation timescale and is of order  $\tau_{\text{ev}} \approx 10^2 \tau_{\text{relax}}$  ([Lada & Lada 2003](#)). A simpler estimate for the relaxation timescale is obtained using the dynamical *crossing time*. The crossing time for a cluster with radius  $R_{\text{cl}}$  can be calculated using the cluster's velocity dispersion  $\sigma$  ([Krumholz et al. 2019](#)):

$$\tau_{\text{cross}} = R_{\text{cl}}/\sigma. \quad (1.70)$$

The relaxation timescale is then estimated to be ([Lada & Lada 2003](#)):

$$\tau_{\text{relax}} \approx \frac{0.1N}{\ln N} \tau_{\text{cross}}. \quad (1.71)$$

---

<sup>17</sup>However, the term “collisional” is not consistently defined in relevant literature, as it is sometimes also used for star clusters in which stars have direct physical collisions.

For the four clusters presented in Chapter 3, these approximations would result in evaporation timescales of the order of  $10^{10}$  yr.

# Hybrid Approach for the Simulation of Planetary Systems in Star Clusters

” *I can calculate the motions of the heavenly bodies, but not the madness of the people.*

— Isaac Newton

## 2.1 Previous Methods for Simulating Planetary Systems in Star Clusters

The dynamical evolution of planetary systems and star clusters is fundamentally different. While planetary systems typically evolve on secular rather than orbital timescales, the evolution of star clusters is mainly characterised by two-body relaxation, close few-body encounters and deterministic chaos. Although the long-term behaviour of planetary systems as well as that of star clusters can be studied using  $N$ -body simulations, the requirements for accuracy in the numerical integration of the orbits are significantly higher for planetary systems than for star clusters (Spurzem 1999). Furthermore, integration is complicated by the different timescales, which range from days (in planetary systems) to millions of years (in star clusters), so that the required time-step sizes would differ by several orders of magnitude (e.g. Hao et al. 2013). The simulation of planetary systems embedded in star clusters thus poses a major difficulty. There are approaches, such as in Spurzem et al. (2009), to treat single-planet systems around single stars like binary systems using two-body regularisation, such as the Kustaanheimo-Stiefel (KS) method (Kustaanheimo et al. 1965; Aarseth 2003; Aarseth et al. 2008), where both bodies are replaced by the common centre of mass and integrated as a combined system. However, resolving secular or resonance effects is not feasible with this approach.

With the help of Monte Carlo models, such as those used in [Hao et al. \(2013\)](#) or [Li & Adams \(2015\)](#), a relatively large number of encounters between stars and multiplanetary systems can be easily realised due to the low computational costs, but this method also has disadvantages. In most studies which use Monte Carlo models, as in [Li & Adams \(2015\)](#), only the effect of a single encounter on a dynamically stable planetary system is investigated and the simulation time of the planetary system is limited in favour of a larger number of realisations, which means that instabilities occurring after several million years are not detected. Additionally, the random selection of equally distributed phase-space parameters in Monte Carlo simulations does not reflect the physical reality in star clusters (for a comparison with a realistic distribution, see figs. 1 and 2 in [Spurzem et al. 2009](#)).

Another approach is used by [van Elteren et al. \(2019\)](#), who integrate planetary systems and stars together within the AMUSE framework ([Portegies Zwart 2011](#); [Portegies Zwart & McMillan 2018](#)), but use a fourth-order integrator for the equations of motion of the stars and an eighth-order symplectic integrator for the planetary systems. The Nemesi's module they use divides the entire cluster into subsystems that can contain both stars and planets. These subsystems are integrated separately, taking into account the mutual gravitational forces of the other objects in the star cluster.

The hybrid approach used in this thesis is based on splitting the integration of the star cluster and the planetary systems into two different codes that are executed sequentially. It was first used in [Cai et al. \(2017, 2018, 2019\)](#) and continued in [Flammini Dotti et al. \(2019\)](#), [Veras et al. \(2020\)](#), [Stock et al. \(2020\)](#) and [Stock et al. \(2022\)](#) (the latter two papers are part of this thesis). The division into two codes is possible due to the valid assumption that the star cluster environment affects the dynamical evolution of the planetary systems, but not vice versa.

## 2.2 Simulation of Star Clusters using NBODY6++GPU

The decoupling of the motion of the stars in the cluster from the dynamics of the planetary systems allows the simulation of the cluster without including the planets as a first step in our approach. For the simulation of the star cluster, NBODY6++GPU ([Wang et al. 2015c](#)) is used, a GPU-optimised version of NBODY6++ ([Spurzem 1999](#); [Spurzem et al. 2008](#)), which was specially developed for the simulation of large numbers of star cluster members on supercomputers and enables a parallelised calculation of the particles' equations of motion. NBODY6++ itself is based on the direct  $N$ -body code NBODY6, the penultimate version<sup>1</sup> from the well-known NBODY code

<sup>1</sup>The latest code in the series is NBODY7 ([Banerjee et al. 2020](#)).

series (Aarseth 1999). The most important properties of NBODY6++GPU that are relevant for the work presented in this thesis are introduced in the following sections.

## 2.2.1 N-Body Units

For astrophysical  $N$ -body simulations of self-gravitating systems, such as star clusters, dimensionless units are commonly used. These units are called  $N$ -body units and form a self-contained system of units that normalises the gravitational constant, the total mass of the system and the initial total energy as follows:

$$G = 1, \quad (2.1)$$

$$M_{\text{tot}} = 1, \quad (2.2)$$

$$E = -\frac{1}{4}. \quad (2.3)$$

The latter normalisation corresponds to a virial radius, defined by

$$r_{\text{vir}} = \frac{GM_{\text{tot}}^2}{2|U|}, \quad (2.4)$$

equal to unity for a system in virial equilibrium (see Eq. 1.63 in Sec. 1.4).

These normalisations create  $N$ -body units for mass, length and time (Heggie & Mathieu 1986), which are:

$$U_m = M_{\text{tot}}, \quad (2.5)$$

$$U_l = -\frac{GM_{\text{tot}}^2}{4E}, \quad (2.6)$$

$$U_t = \frac{GM_{\text{tot}}^{5/2}}{(4|E|)^{3/2}}. \quad (2.7)$$

The physical scaling of the star cluster must be taken into account for the creation of the initial conditions of the planetary systems as well as their subsequent integration and converted to astrophysical units to machine precision.

## 2.2.2 Hermite Integration Scheme

As described in Sec. 1.3, the  $N$ -body problem can only be solved numerically. For this purpose, the Hermite integration method (Makino & Aarseth 1992; Spurzem 1999; Aarseth 2003; Aarseth et al. 2008) is used in the software NBODY6++GPU, which is also successfully applied in many other simulation codes (Aarseth et al. 2008). From Eq. 1.62 we know that the equation of motion for particle  $i$  at an initial time  $t_0$  is as follows:

$$\vec{a}_{0,i} = -G \sum_{j=1, j \neq i}^N m_j \frac{\vec{r}_{0,i} - \vec{r}_{0,j}}{|\vec{r}_{0,i} - \vec{r}_{0,j}|^3}. \quad (2.8)$$

By taking the time derivative, we obtain the  *jerk*, the rate at which the acceleration changes in time:

$$\dot{\vec{a}}_{0,i} = -G \sum_{j=1, j \neq i}^N m_j \left( \frac{\vec{v}_{0,i} - \vec{v}_{0,j}}{|\vec{r}_{0,i} - \vec{r}_{0,j}|^3} + \frac{3(\vec{r}_{0,i} - \vec{r}_{0,j})[(\vec{v}_{0,i} - \vec{v}_{0,j}) \cdot (\vec{r}_{0,i} - \vec{r}_{0,j})]}{|\vec{r}_{0,i} - \vec{r}_{0,j}|^5} \right). \quad (2.9)$$

This expression for the first time derivative of the acceleration allows us to use a Taylor series<sup>2</sup> to predict the position of particle  $i$  at the next time step  $t_1$  up to the third order and its velocity up to the second order:

$$\vec{r}_{1,i,\text{pred}} = \vec{r}_{0,i} + \vec{v}_{0,i}(t_1 - t_0) + \frac{1}{2}\vec{a}_{0,i}(t_1 - t_0)^2 + \frac{1}{6}\dot{\vec{a}}_{0,i}(t_1 - t_0)^3, \quad (2.10)$$

$$\vec{v}_{1,i,\text{pred}} = \vec{v}_{0,i} + \vec{a}_{0,i}(t_1 - t_0) + \frac{1}{2}\dot{\vec{a}}_{0,i}(t_1 - t_0)^2. \quad (2.11)$$

However, these predicted values for position and velocity at time  $t_1$  do not fulfil the requirements for an accurate high-order integrator, since a very small time step  $t_1 - t_0$  would have to be chosen (which in turn would require unreasonable computational effort). As this would require more steps for a fixed time interval, a significant global integration error would occur relatively quickly. A high-order integrator thus reduces the local integration error, as well as the global integration error through a larger step size.

<sup>2</sup>The Taylor series of an infinitely differentiable function  $f(x)$  is the power series  $\sum_{n=0}^{\infty} \frac{f^{(n)}(a)}{n!} (x - a)^n$ .

To achieve better accuracy in the integration, the expressions

$$\vec{a}_{1,i} = \vec{a}_{0,i} + \dot{\vec{a}}_{0,i}(t_1 - t_0) + \frac{1}{2}\ddot{\vec{a}}_{0,i}^{(2)}(t_1 - t_0)^2 + \frac{1}{6}\ddot{\vec{a}}_{0,i}^{(3)}(t_1 - t_0)^3 \quad (2.12)$$

$$\dot{\vec{a}}_{1,i} = \dot{\vec{a}}_{0,i} + \ddot{\vec{a}}_{0,i}^{(2)}(t_1 - t_0) + \frac{1}{2}\ddot{\vec{a}}_{0,i}^{(3)}(t_1 - t_0)^2 \quad (2.13)$$

can be used for acceleration and jerk, which are formed using two further Taylor series and where the superscripts (2) and (3) represent the second and third time derivative of the acceleration.

However, since the derivation of the two missing orders  $\ddot{\vec{a}}_{0,i}^{(2)}$  and  $\ddot{\vec{a}}_{0,i}^{(3)}$  using Eq. 2.9 is quite cumbersome, we perform a *Hermite step*. For this purpose, we use the circumstance that both  $\vec{a}_{1,i}$  and  $\dot{\vec{a}}_{1,i}$  can be expressed equivalently to Eq. 2.8 and Eq. 2.9 for time step  $t_1$  and thus replace the left part of Eq. 2.12 and Eq. 2.13. This yields an expression for the third time derivative of the acceleration

$$\ddot{\vec{a}}_{0,i}^{(3)} = 12 \frac{\vec{a}_{0,i} - \vec{a}_{1,i}}{(t_1 - t_0)^3} + 6 \frac{\dot{\vec{a}}_{0,i} + \dot{\vec{a}}_{1,i}}{(t_1 - t_0)^2} \quad (2.14)$$

from Eq. 2.13, which we can then insert into Eq. 2.12 to obtain the second time derivative

$$\ddot{\vec{a}}_{0,i}^{(2)} = -6 \frac{\vec{a}_{0,i} + \vec{a}_{1,i}}{(t_1 - t_0)^2} - 2 \frac{2\dot{\vec{a}}_{0,i} + \dot{\vec{a}}_{1,i}}{(t_1 - t_0)}. \quad (2.15)$$

Finally, Eqs. 2.10 and 2.11 can now be extended by the two missing orders, yielding the corrected position and velocity for particle  $i$  at time  $t_1$ :

$$\vec{r}_{1,i,\text{cor}} = \vec{r}_{1,i,\text{pred}} + \frac{1}{24}\ddot{\vec{a}}_{0,i}^{(2)}(t_1 - t_0)^4 + \frac{1}{120}\ddot{\vec{a}}_{0,i}^{(3)}(t_1 - t_0)^5 \quad (2.16)$$

$$\vec{v}_{1,i,\text{cor}} = \vec{v}_{1,i,\text{pred}} + \frac{1}{6}\ddot{\vec{a}}_{0,i}^{(2)}(t_1 - t_0)^3 + \frac{1}{24}\ddot{\vec{a}}_{0,i}^{(3)}(t_1 - t_0)^4. \quad (2.17)$$

The integration cycle for all further steps of particle  $i$  can now be repeated from Eqs. 2.8 and 2.9. A simplified illustration of the Hermite integration scheme is shown in Fig. 2.1.

### 2.2.3 The Individual Time-Step Criterion and the Block Time-Step Scheme

To avoid that integration errors grow too much, time steps should be chosen sufficiently small to obtain acceptable integration results. For an unperturbed two-body system, such as a planetary system, usually one-hundredth of the orbital period is considered as a reference value for the

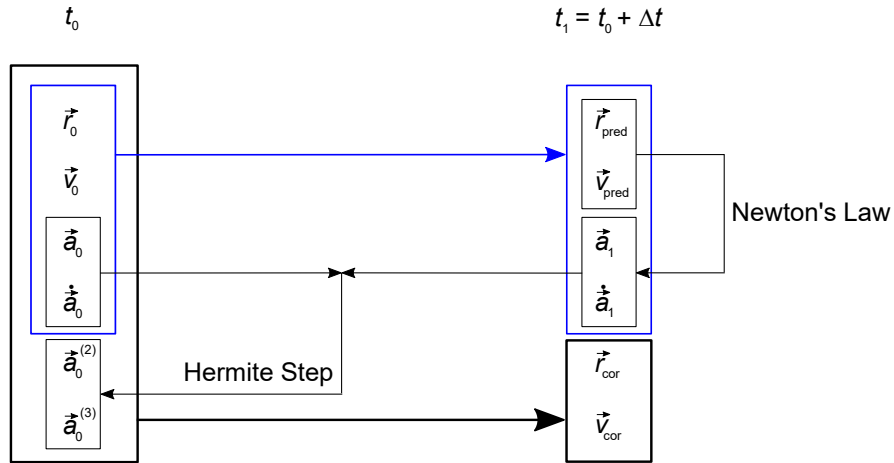


**Fig. 2.1.:** Illustration of the prediction-correction scheme used in the Hermite integration method.

step size<sup>3</sup> (e.g. Sheldon et al. 1957). However, this benchmark only works for a nearly circular orbit, since on an elliptical orbit the planet's velocity depends on its true anomaly, i.e. the current position along the orbit. At periastron, where the planet's velocity is highest, the time steps would have to be chosen smaller than at apoastron, the point with the lowest velocity.

In a star cluster, the search for adequate time-step sizes is even more complex, as there is usually neither an unperturbed two-body problem nor circular orbits. Apart from binary systems that may form in the cluster, the velocity of one star is larger than the escape velocity of the gravitational field of another star, so that the star will only pass the other star on a hyperbolic orbital curve (with  $e > 1$ ). A better criterion would therefore be the rate of change of the gravitational forces acting on a particle, or equivalently the rate of change of its acceleration. However, it would be computationally expensive and cumbersome if the same time-step size were chosen for all particles in the system, since all time steps would then have to be adjusted to the smallest required time-step size of a single particle. For reasons of efficiency, each particle in the system is therefore assigned an individual time step.

As a first estimate in this *individual time-step scheme*, the rate of change of the acceleration of particle  $i$  appears to be a suitable quantity for the choice of the individual time-step size  $\Delta t = t_1 - t_0$ :

$$\Delta t_i \propto \sqrt{\frac{\dot{\vec{a}}_i}{\vec{a}_i}}. \quad (2.18)$$

<sup>3</sup>It should be noted that this strongly depends on the order of the integrator used. Lower-order schemes generally require more steps with smaller step sizes to achieve the same accuracy as a higher-order integration scheme.

However, encounters between stars cannot be detected early enough with such a simple relation, so that the size of the time steps cannot be adjusted in time (Aarseth et al. 2008). To avoid such numerical errors, the expression

$$\Delta t_i = \sqrt{\eta \frac{|\vec{a}_{1,i}| |\vec{a}_{1,i}^{(2)}| + |\dot{\vec{a}}_{1,i}|^2}{|\vec{a}_{1,i}| |\vec{a}_{1,i}^{(3)}| + |\vec{a}_{1,i}^{(2)}|^2}}. \quad (2.19)$$

was determined experimentally as a criterion for the time-step size of an individual particle  $i$  (Aarseth 2003), where  $\eta$  is a dimensionless accuracy parameter that shows reasonable behaviour for  $\eta \approx 0.02$  (Aarseth et al. 2008).

However, this individual time-step scheme, which was used in the predecessor code NBODY5, has the disadvantage that the recomputation for each particle would take place in an unordered manner at arbitrary points in time. This would significantly hamper the possibility of parallelising the calculations and speeding up the simulation. Therefore, this concept was improved in NBODY6, NBODY6++ and NBODY6++GPU by introducing hierarchical block steps. In this *block time-step scheme*, first suggested by McMillan (1986), the time steps are quantised so that the recomputation of the forces for a group of particles can take place at the same point in time.

By predetermining a maximum time-step size  $\Delta t_{\max}$ , the hierarchical block time steps are defined as

$$\Delta t_n = \frac{\Delta t_{\max}}{2^{n-1}}, \quad (2.20)$$

where  $n > 0$  and  $n \in \mathbb{Z}$  (Aarseth 2003; Cai et al. 2015).

If the time step for a particle calculated using Eq. 2.19 is between two block time steps, the particle is assigned to the block with the smaller time-step size. This method allows the blocks of particles to be distributed across a large number of available GPU processors, resulting in a significant speed-up of the simulation due to the efficient parallelisation.

Figure 2.2 illustrates the block time-step scheme using four particles which are integrated for an arbitrary time unit. At the beginning of the integration, particle  $l$  has the smallest time step, whereby its phase-space coordinates are redetermined at every possible time step (up to the 12th step). The phase-space coordinates of the other particles are only completely redetermined using a full force calculation as soon as they encounter the dotted line. In the case of particle  $k$ , which initially has a time step twice as large as particle  $l$ , this occurs at time step 2, for particle  $j$  at time step 4 and for particle  $i$  not before time step 8. In between, only an extrapolation of their coordinates takes place at each time step using the predicted positions and velocities from Eqs. 2.10 and 2.11. The time-step size can be adjusted according to the hierarchical block

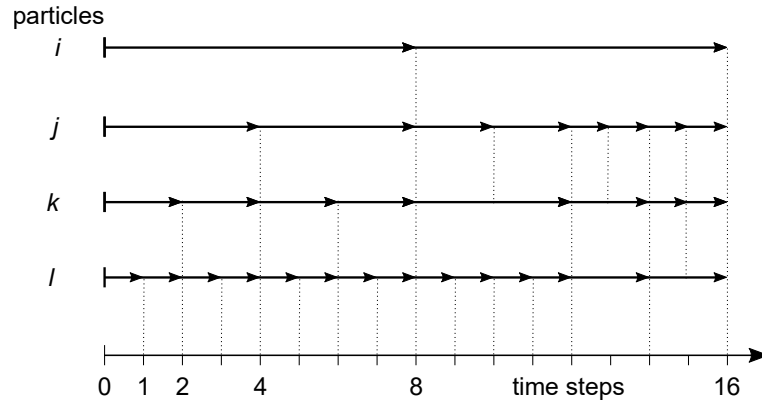


**Fig. 2.2.:** The block time-step scheme for four particles with indices  $i$ ,  $j$ ,  $k$  and  $l$ .

time-step scheme from Eq. 2.20 after each even multiple of the smallest time step, as is the case for particles  $k$  and  $j$  after time step 8 and for particle  $l$  after time step 12.

## 2.2.4 The Ahmad-Cohen Neighbour Scheme

Another approach used in codes such as NBODY5, NBODY6, NBODY6++ and NBODY6++GPU to achieve an additional speed-up in simulations of large numbers of particles is to distinguish between direct and distant neighbours. This is achieved by using the *Ahmad-Cohen neighbour scheme* (Ahmad & Cohen 1973), which is visualized in Fig. 2.3.

Neighbouring stars that lie within a certain radius  $r_S$  are considered direct neighbours, whose gravitational forces on particle  $i$  change on short timescales and must therefore be recalculated more frequently, whereas the gravitational influence of stars outside this sphere changes on longer timescales. For this purpose, the polynomial from Eq. 2.12 for particle  $i$  is split into an *irregular* and a *regular* component:

$$\vec{a}_i = \vec{a}_{i,\text{irr}} + \vec{a}_{i,\text{reg}}. \quad (2.21)$$

The irregular component results from the direct neighbours that lie within the radius  $r_S$  around particle  $i$  and must accordingly be calculated more frequently than the regular component from the more distant neighbours. This is why a differentiation is made between irregular and regular

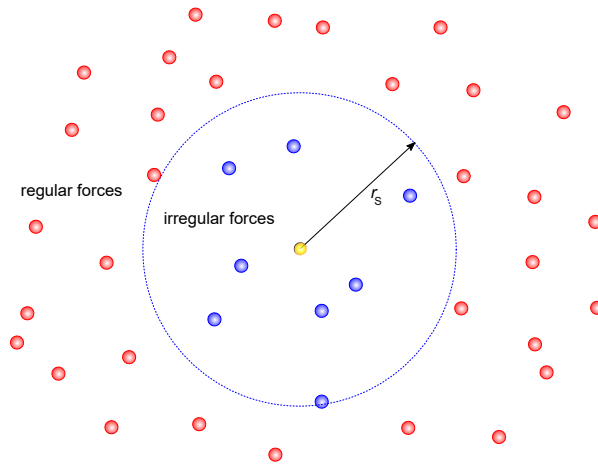


**Fig. 2.3.:** Illustration of the Ahmad-Cohen neighbour scheme for an individual particle (marked in yellow). The (irregular) gravitational forces of the particles inside the neighbour sphere with radius  $r_S$  (marked in blue) are recalculated more frequently than the (regular) forces from the particles outside the sphere (marked in red).

time steps ( $\Delta t_{\text{irr}}$  and  $\Delta t_{\text{reg}}$ ). As a first step in the Ahmad-Cohen Neighbour scheme, a list of neighbours that lie within  $r_S$  is generated for particle  $i$ , so that irregular and regular components of the acceleration can be determined. The actual value of  $r_S$  is based on a predefined optimal number of neighbours that can be passed to the simulation as an input parameter, which should typically be between 50 and 200, regardless of the total number of particles in the simulation (Khalisi et al. 2016). Once  $\vec{a}_{i,\text{irr}}$  and  $\vec{a}_{i,\text{reg}}$  are determined, the Hermite method from Sec. 2.2.2 and Eq. 2.19 can be used to calculate  $\Delta t_{\text{irr}}$  and  $\Delta t_{\text{reg}}$ , which must also follow the hierarchical block time-step scheme from Sec. 2.2.3.

## 2.3 Simulation of Planetary Systems Embedded in Star Clusters using LPS

### 2.3.1 The LonelyPlanets Scheme

The second code used for the hybrid simulation of planetary systems in star clusters is the LonelyPlanets Scheme (LPS; Cai et al. 2017, 2018, 2019). The functionality of LPS is il-

illustrated by a simplified flowchart in Fig. 2.5. LPS is based on two widely-used open-source codes, the astrophysical simulation framework AMUSE (Portegies Zwart & McMillan 2018) and REBOUND (Rein & Liu 2012), a multi-purpose  $N$ -body code for collisional dynamics. AMUSE is required for the proper coupling of LPS with the simulation data from NBODY6++GPU and thus enables, for example, the correct physical scaling between the star cluster simulation and the planetary system simulations. REBOUND, on the other hand, is used for the actual integration of the planetary systems under the gravitational influence of the host stars' neighbour stars from the NBODY6++GPU simulation.

Similar to NBODY6++GPU, LPS also uses a neighbour scheme, which is illustrated in Fig. 2.4. The number of neighbouring stars to be considered is variable and can be adapted to the density in the cluster environment. For all planetary system simulations presented in this thesis, the gravitational forces of the nearest five neighbouring stars (which change continuously) are taken into account. Although even a massive star rarely has a significant effect on the planetary system if it is not the nearest neighbour, due to the proportionality of the gravitational force with  $1/r^2$ , the cumulative effect of all perturbers can have an impact on planetary systems that are close to instability. Therefore, taking the five nearest neighbouring stars into account appears to be a suitable compromise between simulation accuracy and required computational costs.

The individual steps in the hybrid approach can be described as follows:

1. The star cluster is simulated using NBODY6++GPU according to the predefined initial conditions from an input file. Information about the  $N$ -body units used and thus about the physical scaling of the cluster, among other things, is stored in a log file in text format. Snapshots containing all relevant information (such as mass, position, velocity, acceleration and all required time derivatives of the acceleration of all stars) are stored according to the block time-step storage scheme (BTS; see Cai et al. 2015) in an HDF5 file during the simulation.
2. The initial conditions for the planetary systems are subsequently defined using LPS' `i.c.py` module, which determines those stars from the star cluster simulation whose mass is closest to the predefined host star mass using `h5nb6xx.py` and AMUSE. The initial conditions for the planetary systems can either be created with the `i.c.py` module, in which a predefined number of planets with optional masses are placed according to a certain number of mutual Hill radii<sup>4</sup>, defined by

$$r_{H,m} = \frac{a_1 + a_2}{2} \left( \frac{m_{pl,1} + m_{pl,2}}{3M_\star} \right)^{1/3}, \quad (2.22)$$

---

<sup>4</sup>The Hill radius of a single planet is defined as  $r_H = (m_{pl}a^3/(3M_\star))^{1/3}$  and contains the region around a planet within which the gravitational force from the planet dominates that of the star (Raymond 2015).

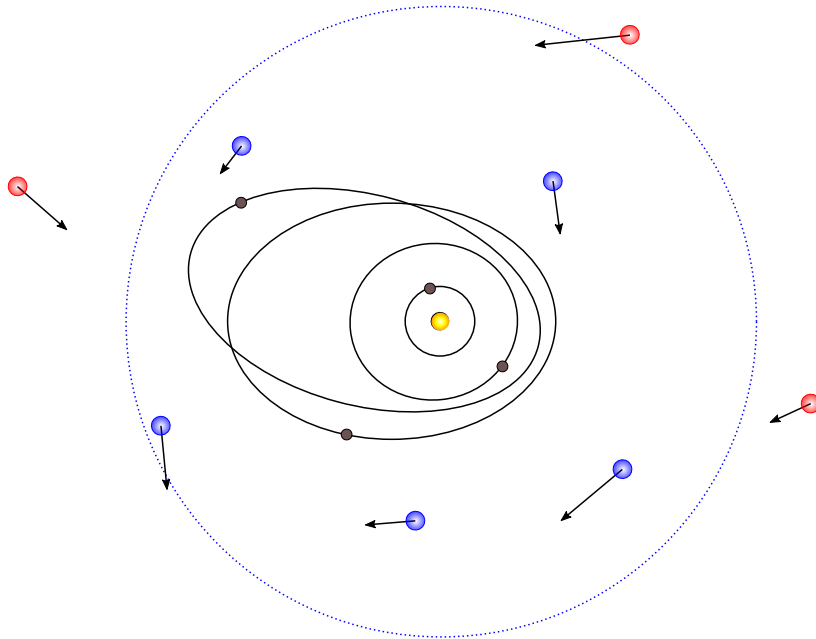


**Fig. 2.4.:** The neighbour scheme used in LPS. The gravitational forces of a definable number of neighbouring stars (here  $n = 5$ ) are taken into account for the integration of the planetary systems. The perturbers are updated in a definable interval (every 1000 years in this thesis).

between the planets. Alternatively, a planetary system with unequal mass distribution and arbitrary architecture can be created and stored as binary file using REBOUND, which can serve as input for `ic.py`.

3. Using the initial conditions for the planetary systems, `encounters.py` reconstructs the trajectories of the stars selected as host stars and interpolates their motions, as well as the motions of a definable number of neighbouring stars to be considered, using the time derivatives of the acceleration.
4. The simulation of the planetary systems, taking into account the encounter information calculated in the previous step, is carried out with `lps.py`. This is achieved by iteratively creating a REBOUND simulation, integrating it for a specified time period (typically 1000 years) and updating the perturber information.

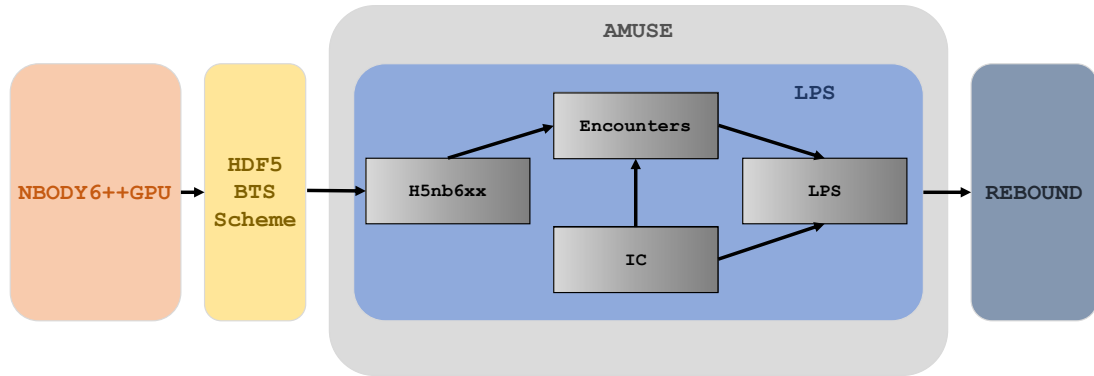


**Fig. 2.5.:** Flowchart describing the hybrid approach for the simulation of planetary systems in star clusters used in this thesis.

### 2.3.2 REBOUND's `ias15` Integrator

The integrator used in this thesis for the planetary system simulations is IAS15 (Rein & Spiegel 2015), a non-symplectic, 15th-order REBOUND-internal integrator with adaptive time stepping. *Symplectic* integrators are often used for the long-term integration of Hamiltonian systems and usually show good energy conservation properties (Gladman et al. 1991; Rein & Spiegel 2015). However, the necessity of describing the system in Hamiltonian formulation makes them unsuitable for non-conservative forces (Rein & Spiegel 2015). The considerably more important feature for this work, which the `ias15` integrator possesses in contrast to symplectic integrators, is the possibility of adjusting the step size. While most symplectic integrators are only suitable for moderately eccentric systems due to the lack of possibility to change the step size<sup>5</sup> if necessary (Gladman et al. 1991), the `ias15` integrator offers precise integration results even for very eccentric systems ( $e > 0.9$ ). Due to its high order, it also shows conservation properties that are equal or even superior to classical symplectic integrators. According to Rein & Spiegel (2015), errors in energy conservation are well below machine precision for the `ias15` integrator.

<sup>5</sup>Note that there are symplectic integrators with multiple time-step algorithms, such as SyMBA (Duncan et al. 1998).

The `ias15` integrator is an improved version of the Gauß-Radau integration scheme of [Everhart \(1985\)](#) and is described in detail in [Rein & Spiegel \(2015\)](#). The algorithm is based on the expansion of the acceleration term as a series. By integrating this series twice, one obtains an estimate for the velocity and position, respectively (at the end of the time step, as well as at any arbitrary time in between). The distance between the substeps is chosen according to the Gauß-Radau spacing, which is similar to the Gauß quadrature. A prediction-correction scheme (similar to the one described in [Sec. 2.2.2](#)) is iterated until convergence is reached (the convergence criterion is based on the magnitude of change of a coefficient in the series). Based on the number of iterations required until convergence, conclusions can be drawn about the suitability of the selected time-step size, which is then accepted or rejected by evaluating a precision parameter in relation to the parameter used for the convergence criterion.



# On the Survival of Resonant and Non-Resonant Planetary Systems in Star Clusters

” *When you look at the stars and the galaxy, you feel that you are not just from any particular piece of land, but from the Solar system.*

— **Kalpana Chawla**  
(Indian-American astronaut)

**Details of authorship:** *The content of this chapter is entirely based on the publication of [Stock et al. \(2020\)](#). The manuscript as well as all scientific work, calculations and conclusions contained therein have been prepared by me. Before submission and during the review process, I incorporated suggestions for improvement and corrections from the co-authors and the reviewer. For this thesis, I have slightly adjusted the format of the figures and tables to better fit the single-column layout of this thesis. A small correction and addition was made in the discussion of the encounter timescales. The appendix of this publication has been moved to the appendix of this thesis.*

## 3.1 Introduction

Studies of nearby giant molecular clouds by [Lada et al. \(1993\)](#) suggest that stars generally do not form in isolation but also in groups or stellar associations. If clustered star formation is the rule rather than the exception, there is reason to believe that star clusters are promising targets for the detection of newborn planetary systems because star and planet formation are closely connected to each other.

Despite the large number of 4158 extrasolar planets<sup>1</sup> which were detected in the last 25 yr, only around 30 planets (< 1%) have been detected in star clusters so far, and only one of them has been detected in a globular cluster (see table 1 in [Cai et al. 2019](#), for a complete list of planet detections in star clusters and their corresponding references). Among those planets detected in star clusters are, for example, 13 planets around 11 stars in the Praesepe (M44) cluster ([Quinn et al. 2012](#); [Malavolta et al. 2016](#); [Obermeier et al. 2016](#); [Gaidos et al. 2017](#); [Mann et al. 2017](#); [Rizzuto et al. 2018](#); [Livingston et al. 2019](#)), six planets in four systems in the Hyades cluster ([Sato et al. 2007](#); [Quinn et al. 2014](#); [Mann et al. 2016](#)) with one three-planet system ([Mann et al. 2018](#)), and five single-planet systems in the M67 cluster ([Brucalassi et al. 2014, 2016, 2017](#)). The origin for the periodic RV variations in the giant stars IC 4651 No. 9122, NGC 2423 No. 3, and NGC 4349 No. 127, which are all located in an open cluster, is still under debate ([Delgado Mena et al. 2018](#)). [Brucalassi et al. \(2017\)](#) find a comparable fraction of giant planets around stars in the cluster M67 than around field stars but a significantly higher fraction of Hot Jupiters in the cluster compared to the field (see also [Brucalassi et al. 2016](#)). Although the sample size in these studies is very small and statistics should therefore be interpreted with caution, the “excess” of Hot Jupiters found in M67 is an indication for significant dynamical perturbations from neighbouring stars on the planets in the cluster.

Clustered environments pose a threat already for the early phases of planet formation. Protoplanetary discs may be photoevaporated by the radiation of nearby massive stars (e.g. [Störzer & Hollenbach 1999](#); [Armitage 2000](#); [Anderson et al. 2013](#); [Facchini et al. 2016](#)) or truncated due to close encounters (e.g. [Clarke & Pringle 1993](#); [Olczak et al. 2006](#); [Portegies Zwart 2016](#); [Concha-Ramírez et al. 2019](#)). But even when a planetary system has successfully formed without major perturbations, its dynamical fate will still be determined by the host star’s position and motion inside the cluster and the properties of the cluster itself like its density (denser clusters, and especially globular clusters, tend to have a more destructive effect on planetary systems than loosely bound open clusters). Numerous studies have analysed the effect of cluster environments on planetary systems beyond the protoplanetary disc phase (e.g. [Malmberg et al. 2007](#); [Spurzem et al. 2009](#); [Malmberg et al. 2011](#); [Parker & Quanz 2012](#); [Hao et al. 2013](#); [Cai et al. 2017, 2018, 2019](#); [Flammini Dotti et al. 2019](#); [Fujii & Hori 2019](#); [van Elteren et al. 2019](#); [Glaser et al. 2020](#)).

[Spurzem et al. \(2009\)](#) presented a set of dynamical star cluster models with a large number of planetary systems (consisting of one planet) fully included into the model; they showed that there is a constant rate of planets liberated as a result of stellar encounters; they also showed that stellar encounters act like a diffusive process on planetary systems, where changes of semimajor axis

---

<sup>1</sup>As of May 2020, according to the [NASA Exoplanet Archive](#).

**Tab. 3.1.:** Initial conditions for the star cluster simulations.

Star cluster	8k	16k	32k	64k
Number of stars	8 000	16 000	32 000	64 000
Total mass ( $M_{\odot}$ )	4073	7939	16 302	32 619
Half-mass radius (pc)	0.78	0.78	0.78	0.78
Central density ( $M_{\odot}\text{pc}^{-3}$ )	3906	6813	13 852	25153
Initial tidal radius (pc)	22.58	28.20	35.84	45.16

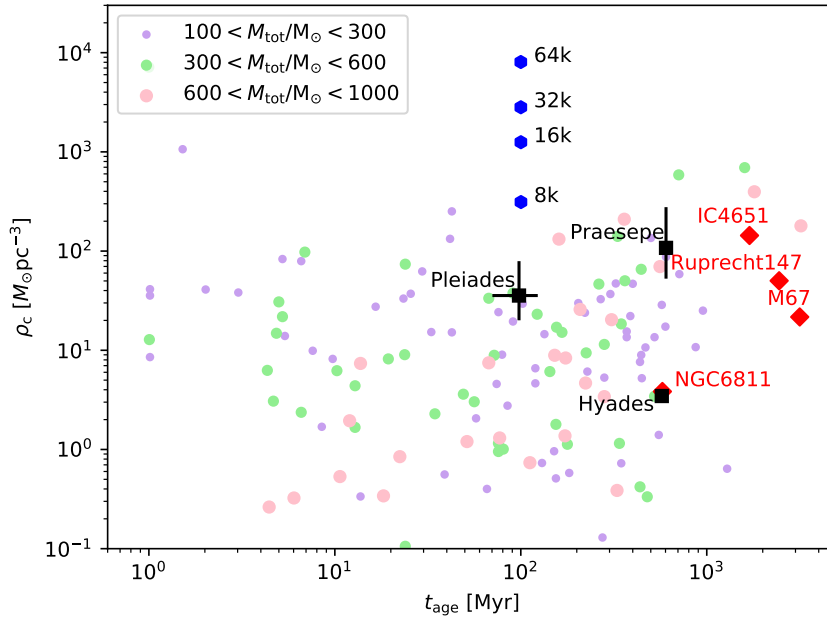


**Fig. 3.1.:** Central density ( $\rho_c$ ) as a function of the cluster age  $\tau_{\text{age}}$ , for our four simulated clusters (blue hexagons) at a simulation time of 100 Myr and the observed clusters from fig. 1 in Fujii & Hori (2019).

and angular momentum may be directed in both ways. Depending on the details of the encounter, there is a net flux outward, giving the rate at which free-floating planets are created. There could also be a net flow to the inner boundary, i.e. planets accreted onto the central star, which was not discussed in their paper. Li & Adams (2015) followed another approach — a Monte Carlo model, in which many thousands of encounters of single objects (single and binary stars) with planetary systems were modelled. They were able to cover a parameter space substantially larger than that of Spurzem et al. (2009). However, Monte Carlo models suffer from the inaccuracy in the stochastic selection of encounter parameters (the impact parameter and the velocity at infinity). In figs. 1 and 2 in Spurzem et al. (2009) one can see that the real distribution of these parameters in a star cluster differs from a random selection, covering the available phase space equally.

In the work of [van Elteren et al. \(2019\)](#), they adopted a different approach, in which planetary systems were integrated together with the stars in the cluster. To reduce the computational burden, planets in one system were not affecting the orbits of planets in another system. This still led to an enormous computational burden, which resulted in a rather limited parameter study.

Note that also very low-mass particles, such as planetesimals (asteroids and Kuiper belt objects) or comets (Oort cloud objects) are subject to these encounters (see e.g. [Veras et al. 2020](#)). A characterization of the importance of such close encounters on planetary systems with debris discs is presented in [Portegies Zwart & Jílková \(2015\)](#). This process can lead to flybys of interstellar objects ([Torres et al. 2019](#)) or to the capture of cometary objects into young planetary systems (e.g. [Kouwenhoven et al. 2010](#); [Perets & Kouwenhoven 2012](#); [Wang et al. 2015b](#)). This work is also closely related to a — somewhat less comprehensive — study by [Hands et al. \(2019\)](#). It was suggested that the extraordinary asteroid 90377 Sedna was abducted from the debris disc of another star in such a close encounter ([Jílková et al. 2016](#)). The identification of ‘Oumuamua and 2I/Borisov as possible interstellar objects in our Solar system has received much attention recently, and is connected to the idea that young planetary systems are sources of free-floating comets or planetesimals (see e.g. [Zheng et al. 2015](#); [Portegies Zwart et al. 2018b](#); [Hands et al. 2019](#); ‘Oumuamua ISSI Team et al. 2019; [Pfalzner & Bannister 2019](#), and references therein).

In this work, we study the effect of close stellar encounters on the dynamical architectures of planets that are born around stars in star clusters. We pay particular attention to the dependence on the initial orbital configuration of a planetary system before the first encounters with neighbouring stars take place. Our work differs from earlier works in several aspects. (i) We do not only focus on the effect of one single encounter on planetary systems but instead investigate the cumulative effect of several encounters on planetary systems by following their dynamical evolution during a significant fraction of time which they spend in the cluster. This again allows us to compare the distribution of orbital parameters at the end of our simulations with actual observed properties of planetary systems that are in conflict with current planet formation theories (e.g. eccentric or retrograde orbits). (ii) Our  $N$ -body approach enables a realistic representation of encounters between cluster members, while many previous works use a Monte Carlo approach which typically suffer from inaccuracy by randomly selecting encounter parameters equally from the available parameter space. (iii) Using a hybrid  $N$ -body code allows us to put every planetary system in different initial configurations while the host star’s trajectory through the cluster and thus also all external perturbations on the planetary system are the same for the different system architectures.

This paper is organized as follows. Section [3.2](#) describes the computational approach of the simulation of planetary systems embedded in star clusters and specifies the initial conditions for

the star cluster simulation and the simulation of the planetary systems. In Sec. 3.3 we present the results of our simulations which are then discussed and summarized in Sec. 3.4.

## 3.2 Methods and Initial Conditions

### 3.2.1 Computational Approach

Planetary systems evolve through secular evolution, the orbits of planets being relatively stable for millions, and sometimes tens of billions of orbits. Secular evolution is provided by mutual gravitational interaction between the planets, as well as by external perturbation through passing stars, in a star cluster or in the Galaxy. However, stellar clusters evolve differently, namely through two-body relaxation and few-body encounters. Orbits of stars in the system are changed by these processes in less than a single orbital timescale. The dynamical evolution of star clusters also exhibits deterministic chaos, so that slightly different initial conditions can lead to exponentially diverging outcomes in phase space within less than one orbital time (see e.g. [Miller 1964](#); [Quinlan & Tremaine 1992](#); [Boekholt et al. 2020](#)).

Therefore, a combined simulation of planetary systems in star clusters is a challenge. The challenge lies not so much in the different timescales or hierarchical nature of some objects (in this sense, close stellar binaries and planetary system are quite similar); rather the problem is to accurately follow resonant and secular effects in the internal evolution of planetary systems. This is why we simulate star cluster and planetary systems using different simulation codes. This is feasible because we assume that the neighbouring stars in the cluster affect the planets, but the planets have a negligible influence on the stellar kinematics.

Although currently the decoupled, combined simulations of planetary systems and star clusters as described earlier are state of the art, and fully coupled dynamical simulations of planetary systems in star clusters have only been carried out for single planetary systems (e.g. [Spurzem et al. 2009](#)), in the future more development on that side would be important. Using the current LPS algorithm (see below) neglects the potential effect of more distant perturbers and also tidal forces of the entire star cluster on the planetary system. Also very massive bodies being further away (e.g. stellar or intermediate mass black holes) could have an impact on planetary systems which are not taken into account here.

We first simulate the stellar population in the star cluster using NBODY6++GPU ([Wang et al. 2015c, 2016](#)) and integrate the motion of its members inside the cluster using the Hermite scheme.

NBODY6++GPU is a follow-up version of NBODY6 (Aarseth 1999) and NBODY6++ (Spurzem 1999), and has a significant speedup due to the usage of graphical processing units (GPUs) and parallelization of tasks through a message passing interface (MPI). All required information such as mass, position, velocities, acceleration, and the first time derivative of the acceleration of all cluster members in our simulation are stored at a high time resolution using the “block time-step” (BTS) storage scheme (Faber et al. 2010; Farr et al. 2012; Cai et al. 2015). This scheme allows the reconstruction of stellar encounters in details when planetary systems are assigned to single stars in the cluster at a subsequent step (see Sec. 3.2.3). The data are stored in HDF5<sup>2</sup> format to enable high-performance parallel access to the data.

The dynamical evolution of the planetary systems is simulated using the LonelyPlanets Scheme (LPS). It is based on the AMUSE framework (Portegies Zwart 2011; Portegies Zwart & McMillan 2018) and uses rebound (Rein & Liu 2012) to integrate the planets. Before integrating the planets using the IAS15 integrator (Rein & Spiegel 2015), all encounters with the next five neighbouring stars are derived by interpolating the data of the corresponding stars from the BTS data (see Cai et al. 2017, 2019, for further explanations).

### 3.2.2 Star Cluster Simulations

The simulated star clusters in this work contain 8 000, 16 000, 32 000, and 64 000 stars. We adopt the Kroupa (2001) initial mass function in the mass range of 0.08-100  $M_{\odot}$ . The stars have an expected average mass of 0.509  $M_{\odot}$ . We draw the initial positions and velocities for the stars in our clusters from the Plummer (1911) model. The initial half-mass radius for all clusters is  $r_{\text{hm}} = 0.78$  pc. We do not include primordial mass segregation and we do not include primordial binary systems. All initial parameters for the star cluster simulations are listed in Tab. 3.1. It should be noted that these values are initial cluster properties. After a short phase of core collapse the clusters rapidly expand and the central densities decrease significantly. Simulating the clusters for 100 – 250 Myr leads to central densities that correspond to those of observed star clusters. Figure 3.1 shows the central density of our simulated clusters after a simulation time of 100 Myr in comparison to the actual observed clusters from fig. 1 in Fujii & Hori (2019). The central density is not comparable to the typical density our planetary systems experience during their life in the cluster, and due to the onset of mass segregation it is unlikely that our 1  $M_{\odot}$  host stars remain in the small but dense core of a Plummer model cluster for a long time. The vast majority of all systems experience moderate stellar densities of up to a few hundred  $M_{\odot} \text{pc}^{-3}$ .

---

<sup>2</sup><https://www.hdfgroup.org/>

To calculate the encounter timescales for our simulated clusters, we use eq. 3 from [Malmberg et al. \(2007\)](#). Instead of using  $m_t = 1 M_\odot$  for the total mass of the stars involved in the encounter as [Malmberg et al. \(2007\)](#) do, we use a value of  $m_t = 1.5 M_\odot$  based on the assumption that our  $1 M_\odot$  host stars encounter stars with the average mass of  $\sim 0.5 M_\odot$ . We set  $r_{\min} = 1000$  au as the encounter distance. For the smallest cluster, we obtain a value of  $\tau_{\text{enc}} \approx 1.4$  Myr, and  $\tau_{\text{enc}} \approx 0.5$  Myr for the largest cluster. This corresponds to encounter rates of 0.7 (smallest cluster) and 2.0 (largest cluster) encounters per star per Myr. The encounter timescales determined for our clusters, taking into account the much less massive cluster in [Malmberg et al. \(2007\)](#), are comparable to the order of  $\tau_{\text{enc}} \approx 2.4$  Myr given there. However, these values only reflect the order of magnitude of the timescales for encounters below 1000 au. These encounters mostly have only a weak impact on the central star and its planetary system. The timescales for strong encounters (see Eq. 1.67 and Fig. 1.10 in Sec. 1.4) are significantly larger and of the order of  $\tau_{\text{enc,st}} > 20$  Myr.

The Lagrangian radii containing different fractions of the total cluster mass as a function of time are shown in Fig. 3.2 for the 8k cluster and give an overview of the evolution of the entire star cluster. For comparison, the initial tidal radius  $r_{\text{tid}}$  is plotted as well. The half-life of the cluster is defined as the time at which the 50% Lagrangian radius (half-mass radius) and the tidal radius are equal.

We use the standard definition<sup>3</sup> of the tidal radius as

$$r_{\text{tid}} = R_G \left( \frac{M_{\text{cl}}}{M_G} \right)^{\frac{1}{3}}, \quad (3.1)$$

where  $R_G$  and  $M_G$  are the distance to the Galactic centre and the mass of the Galaxy contained inside  $R_G$ ;  $M_{\text{cl}}$  is the star cluster mass. Our star clusters gradually lose mass over time due to stellar evolution (see below) which results in a shrinking tidal radius over time.

Near the tidal radius stars are typically only marginally bound to the cluster, and may escape from the cluster into the tidal tails. In reality the situation is much more complex, since stars escape through Lagrangian points, and not all stars with positive energy (or outside  $r_{\text{tid}}$ ) escape immediately, some of them may be retained by the cluster. This process is neatly described in the study of [Ernst et al. \(2008\)](#).

Our star clusters are assumed to orbit the Galactic centre in the solar neighbourhood, wherefore the tidal forces of the galaxy on the cluster are the same as for the solar neighbourhood ([Heisler](#)

---

<sup>3</sup>Note that this definition of the tidal radius is an operational one, used for example in our  $N$ -body code; other definitions use the truncation of the density profile ([King 1962](#)) or the distance between the Lagrange point and the cluster centre (see e.g. [Just et al. 2009](#)). These definitions differ from ours by a numerical factor of order unity.

& Tremaine 1986). The formation of tidal tails is observed in our simulations. We do not remove stars from our simulations even when their position is  $r \gg r_{\text{tid}}$ . Therefore, we still keep track of the motion of stars in our simulation that have physically already left the cluster. Hence, the cluster dissolves faster than Fig. 3.2 suggest. We assume that the clusters will have reduced their central density significantly after roughly 100 Myr. For example, in the 8k cluster, almost 20% of the stars are already beyond the tidal radius after 100 Myr and can be considered to have left the cluster. Therefore, we simulate the cluster environment of our planetary systems only for this time span as most strong encounters will have occurred by that time.

The star cluster simulations with NBODY6++GPU include stellar evolution of single and binary stars — they follow the evolution of masses and radii of all objects according to the recipes described in Hurley et al. (2005, and earlier citations of Hurley therein). Since we start without primordial binary stars, binary systems are rare — only a few dynamically formed binaries are found. The stellar evolution is implemented in the form of parametrized lookup tables; any mass-loss of stars or from binaries is assumed to leave the cluster instantaneously; mass transfer in a binary is approximately followed. The reader interested in more details could have a look into the DRAGON (million body) simulations (Wang et al. 2016). In recent years the stellar evolution prescriptions for  $N$ -body simulations are undergoing considerable changes, see for example Khalaj & Baumgardt (2015), Spera et al. (2015), and Banerjee et al. (2020) for an overview. The updates according to that paper are now also available in NBODY6++GPU, but have not yet been used for the simulations of this paper. Note that we select in the LPS scheme only host stars for planets which are close to one solar mass – therefore these systems are not subject to any changes due to stellar evolution, given the relatively short time of simulation used here. In future models, we could also initialize planets around more massive stars, which would undergo changes due to stellar evolution (mass-loss due to expansion of the host star on the AGB leads to a loss of planets or wider orbits of those remaining).

### 3.2.3 Planetary System Simulation

We aim to investigate how the initial configuration of the planetary systems affects the dynamical evolution of the planets that are born around stars in clustered environments and how it affects the likelihood of the individual planets to survive the first tens of millions of years in such a destructive environment. For this purpose, we adopt the six different initial configurations of Li & Adams (2015) as starting positions for the planets in our simulations (see Tab. 3.2).

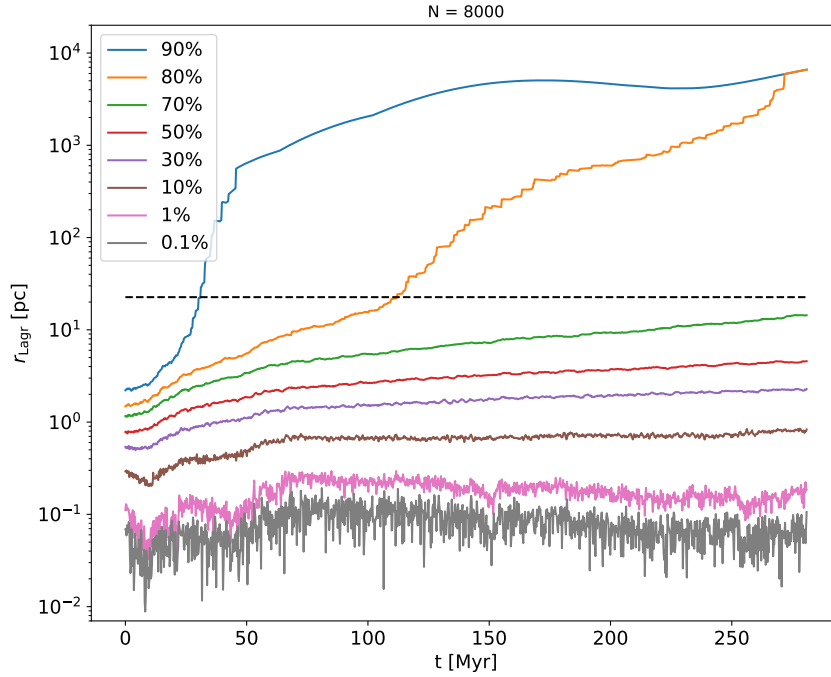


**Fig. 3.2.:** Lagrangian radii  $r_{\text{Lagr}}$  of the 8k star cluster, containing the indicated fraction of mass, as a function of time. The black dashed curve shows the initial tidal radius  $r_{\text{tide}}$ .

Li & Adams (2015) study scattering encounters between Solar system analogues and passing stars (single stars and binary systems) and determine cross-sections for the disruption of these planetary systems. Their planetary systems contain the four Solar system giants Jupiter, Saturn, Uranus, and Neptune with their present-day masses. In the “standard configuration” of Li & Adams (2015), they use the current semimajor axes of the planets but they assign circular and coplanar orbits. Inspired by the Nice model (Gomes et al. 2005), Li & Adams (2015) use two more compact configurations in which the three outer planets are closer to Jupiter. The first one is referred to as “compact configuration”. Although these planetary systems are tightly packed, this configuration is fully stable over 100 Myr. In the second one, the four planets are in mutual mean-motion resonance (MMR), wherefore this configuration is called “resonant configuration”. In this configuration, Jupiter/Saturn and Saturn/Uranus are each in a 3:2 MMR while Uranus and Neptune are in a 5:4 MMR. See Li & Adams (2015) and the references therein for a further discussion of this initial state. The initial orbital angles in this configuration play a key role in the question whether not only this system is stable for a certain period of time but also the resonance angles librate for similar period of time. In our simulations, we can fulfil the stability and resonance criterion usually long enough until the first encounters of neighbouring stars start to disturb the planetary systems and break the resonances between the planets. However, it should

**Tab. 3.2.:** Initial orbital parameters of our planetary systems in the different configurations from [Li & Adams \(2015\)](#).

Config.	Common param.		Jupiter	Saturn	Uranus	Neptune
Standard	$e = 0$	$i = 0^\circ$	$a = 5.20$ au	$a = 9.54$ au	$a = 19.19$ au	$a = 30.08$ au
Compact	$e = 0$	$i = 0^\circ$	$a = 5.20$ au	$a = 8.67$ au	$a = 14.4$ au	$a = 24.1$ au
Resonant	$e = 0$	$i = 0^\circ$	$a = 5.88$ au	$a = 7.89$ au	$a = 10.38$ au	$a = 12.01$ au
Eccentric #1		$i = 0^\circ$	$a = 5.20$ au $e = 0.049$	$a = 9.54$ au $e = 0.057$	$a = 19.19$ au $e = 0.045$	$a = 30.08$ au $e = 0.011$
Eccentric #2	$e = 0.1$	$i = 0^\circ$	$a = 5.20$ au	$a = 9.54$ au	$a = 19.19$ au	$a = 30.08$ au
Massive	$e = 0$	$i = 0^\circ$	$a = 5.20$ au	$a = 9.54$ au	$a = 19.19$ au	$a = 30.08$ au
	$m_{\text{pl}} = 1 M_{\text{Jup}}$					

be mentioned that this resonant configuration is generally highly unstable due to its compactness, and usually at least one of the outer planets is ejected rapidly when the initial orbital parameter are not chosen properly.

Furthermore, [Li & Adams \(2015\)](#) use two eccentric configurations (referred to as “Eccentric #1” and “Eccentric #2”). In the first eccentric case, the planets start again at their current semimajor axes but with their actual eccentricities (instead of circular orbits as in the standard configuration). In the second eccentric configuration, all four planets have initial eccentricities of  $e = 0.1$ . While the first eccentric configuration is fully stable over 100 Myr, Neptune is ejected in the second eccentric configuration after 5 Myr if we place the system in isolation. Therefore, the second eccentric as well as the resonant configuration both contain an internal instability leading to a higher vulnerability against external perturbations. The sixth investigated configuration in [Li & Adams \(2015\)](#) is referred to as “massive configuration” in which all planets have Jovian masses instead of their actual masses. Despite the large masses of all four planets, the configuration is stable for at least 100 Myr.

For all these six configurations, we distribute 200 identical planetary systems around those stars in the cluster whose masses are closest to  $1 M_\odot$ . The host stars within one cluster simulation are therefore the same for each configuration. This allows us to work out the differences in vulnerability in the clustered environment between those initial configurations due to the different positions of the host stars in the cluster. The number of 200 planetary systems per cluster and per configuration is a compromise between computational costs and the possibility to do proper statistics about our sample. Since we simulate 200 planetary systems in six different configurations in all four star clusters, we have a total number of 4800 different planetary system simulations. On grounds of efficiency, our simulations are therefore carried out using the simulation monitor SiMon ([Qian et al. 2017](#)).

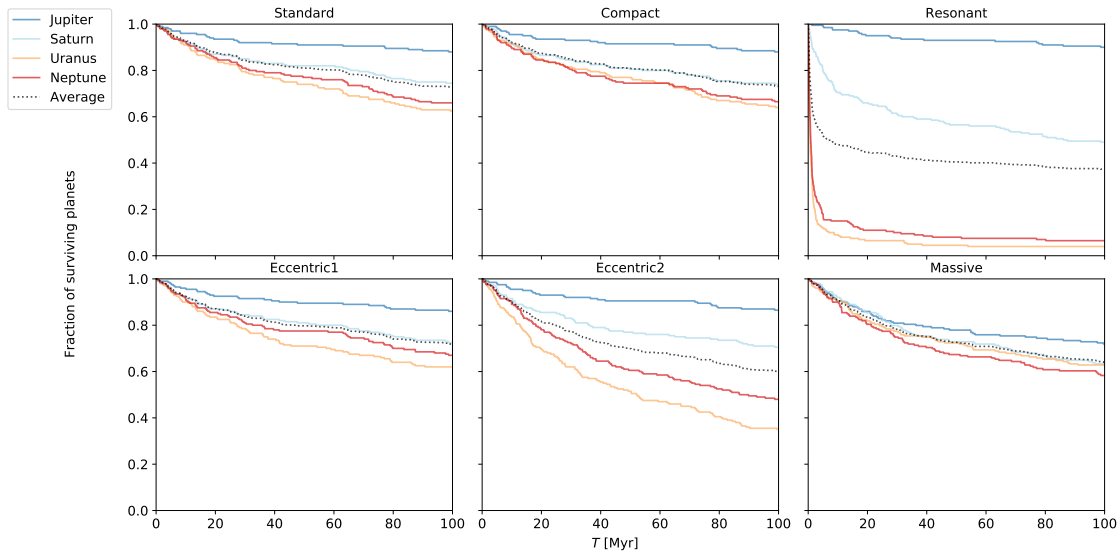


**Fig. 3.3.:** The survival fractions for the Solar system giant planets as a function of time for the six different initial configurations in a 16k Plummer model star cluster. The black dotted curves represent the overall survival fraction averaged over the four planets.

Each planetary system is integrated for 100 Myr (as discussed in Sec. 3.2.2). Planets that are excited to an eccentricity  $e > 0.99$  are considered as having been ejected from the system and are removed from the simulation. The mass-loss of the  $\sim 1 M_{\odot}$  host stars is negligible during the main-sequence phase and especially during the first 100 Myr which is why it is not taken into account for the dynamical evolution of the planetary systems.

## 3.3 Results

### 3.3.1 Fractions of Surviving Planets

For each configuration, we simulate 200 identical planetary systems and distribute them around  $\sim 1 M_{\odot}$  host stars. As we do not include primordial mass segregation in our clusters the positions of the host stars (and therefore the stellar densities the planetary systems experience) in our clusters are random. However, to ensure comparability between the different initial configurations we use the same 200 host stars for all planetary systems of the same cluster.

In this work we define a planet having “survived” when it has not been ejected from the planetary system during the course of the simulation. This means that the planet’s eccentricity has been

$e \leq 0.99$  for at least 100 Myr. For the determination of the survival fraction of a certain kind of planet we average over all 200 planets of the same type in the same star cluster.

An inspection of the survival fraction as a function of time for the four different planets in our systems reveals large differences between the initial configurations. Figure 3.3 shows the survival fraction for all six configurations as a function of time for the 16k cluster. In Fig. 3.4, the fraction of surviving planets after 100 Myr is plotted against the number of stars,  $N$ , in the host star cluster, for the six initial orbital configurations.

In all of our simulations, Jupiter is the planet with the highest survival probability. The reason for this is two-fold: Jupiter is not only the most massive planet (in five of our six configurations) but it is also the innermost planet, so that its binding energy is by far the largest. The same reasoning explains why Saturn is usually the second most resistant planet. Although Neptune is the outermost planet, its binding energy is somewhat larger than that of Uranus due to its larger mass. This is why in most of our simulations Neptune is slightly more likely to survive than Uranus.

The survival fractions after 100 Myr for the planets in standard configuration in the 16k cluster are 88.0%, 74.5%, 62.5%, and 66.0% for Jupiter, Saturn, Uranus, and Neptune, respectively. Starting the planets in the 16k cluster in a more compact configuration does not change these values significantly as can be seen in Fig. 3.3. Also the first eccentric configuration in which the planets were assigned their true eccentricities does not differ significantly from the standard and compact case. The overall survival fraction (averaged over all four planets) is around 72% for these three configurations in the 16k cluster.

While the differences in the survival fractions of the standard and compact configurations are negligible, the survival fractions in the resonant case differ significantly from those in the compact configuration. Only the fraction of surviving Jupiters is comparable to the other configurations and is 90.0% in the 16k cluster. For Saturn, the survival fraction decreases from 74.5% in the standard case to 49.0% in the resonant configuration. However, the percentage of surviving Uranus- and Neptune-like planets is much lower and is only 4.0% and 6.5%, respectively. The overall survival fraction in the resonant case is only 37.4% which is the lowest value for all six configurations in the 16k cluster. Although all planets have initially circular orbits, the effect of planet–planet interaction in this configuration is very destructive. Due to the compactness of the planetary system, the system is only long-term stable on timescales of several ten thousand years. The first encounters have usually already occurred at that time, removing the system from resonances and exciting the orbital parameters of some or all planets. Uranus and Neptune are the most vulnerable planets in this configuration. In none of our simulations, all four planets

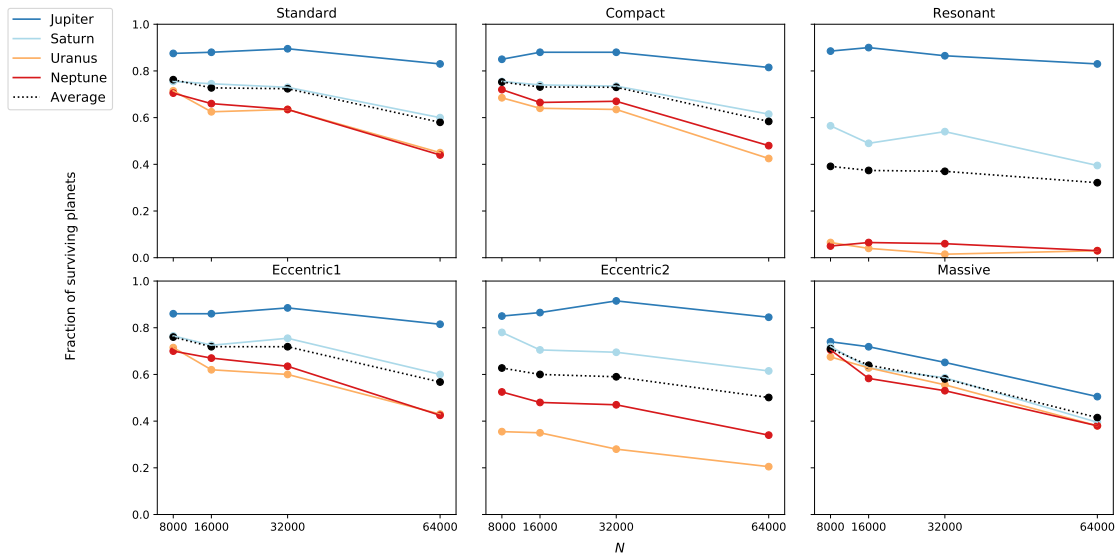


**Fig. 3.4.:** The survival fractions for the Solar system giant planets as a function of the number of stars,  $N$ , in the host star cluster at  $t = 100$  Myr.

survived. Usually either Uranus or Neptune (or both) is ejected latest after several million years. Only in 2 out of 800 simulations of the resonant case, Uranus and Neptune survived together. In both cases, Saturn is ejected within the first two million years.

In the second eccentric configuration, the survival fractions of Jupiter and Saturn are relatively unaffected by the larger initial eccentricities of all four planets. Only for Uranus and Neptune, the differences are significant compared to the standard, compact, and first eccentric case. In the 16k cluster, the survival fractions after 100 Myr drop down to 35% and 48% for Uranus and Neptune, respectively. Although Neptune is the outermost planet, it has a significant higher chance to survive in this eccentric planetary system than Uranus. In this configuration, Uranus' fate is mainly determined by secular evolution. Since the planets already have an initial eccentricity of  $e = 0.1$ , it requires less angular momentum transfer to another star to trigger destructive interactions between the planets. Due to its position between Saturn and Neptune and the fact that it has the smallest mass, Uranus is easily excited to highly eccentric orbits which often leads to the ejection of the planet.

The fractions of surviving planets in the massive configuration reveal not only the importance of the planetary mass during stellar encounters but also its role during secular evolution. The overall survival fraction in the 16k cluster drops from 72.8% in the standard configuration to 63.9% in the massive configuration. While Jupiter had by far the largest likelihood for survival in the other configurations, the differences between the planets in the massive configuration are significantly

smaller. The survival fraction for Jupiter in the 16k cluster is 88.0% in the standard and compact case, but only 71.9% in the massive configuration. For Saturn, Uranus and Neptune the survival rates in the massive configuration are all around 60% in the 16k cluster.

Our simulated clusters all have the same initial half-mass radius but differ in central density. Therefore, the survival fractions for the different configurations also depend on the number of stars in the host cluster. In general, the survival fractions for the different planets decrease with increasing stellar density due to an increasing number of close encounters between cluster members. However, the effect of an increasing stellar density is larger on the outer planets of the system since they are more easily liberated by another star due to their smaller gravitational binding energy. While the survival fractions for Jupiter, Saturn, Uranus, and Neptune in the standard configuration in the 8k cluster are 87.5%, 75.5%, 71.5%, and 70.5%, respectively, these values decrease to 83.0%, 60.0%, 45.0%, and 44.0%, respectively, in the 64k cluster (see Fig. 3.4).

### 3.3.2 Comparison of the Survival Fractions with Previous Studies

In table 2 in [Li & Adams \(2015\)](#), the authors provide their ejection cross-sections in units of  $\text{au}^2$ . In order to normalize this to obtain an escape or survival fraction, one needs to know the maximum impact parameter chosen in their models. However, their maximum impact parameter is variable, depending on parameters (e.g. 10 times the semimajor axis of a stellar binary which encounters a planetary system, but not more than 1000 au). To be able to compare our results with those of [Li & Adams \(2015\)](#), we adopt  $p_{\text{max}} = 1000 \text{ au}$  for the normalization of their cross-sections. Table 3.3 lists our survival fractions in percentage after integrating the planetary systems in the 8k cluster in four of the six different initial configurations for 100 Myr. We assume that our smallest cluster is most similar to the cluster environment simulated in [Li & Adams \(2015\)](#). However, our models are different in three aspects — (1) the distribution of impact parameters and relative velocities of encounters is very different to the one assumed in Monte Carlo simulations of encounters as they did; (2) [Li & Adams \(2015\)](#) stop the planetary system model after the encounter, while we continue all planetary systems for the entire simulation time of 100 Myr and find many delayed unstable systems, which reduce the survival fraction; (3) our simulations take into account the cumulative effect of several encounters. Due to these differences, we find much more ejections of planets in our simulations and have significantly smaller survival fractions for each planet type than [Li & Adams \(2015\)](#).

**Tab. 3.3.:** Survival fractions (in percent) at  $t = 100$  Myr in the 8k cluster, in comparison to the results of Li & Adams (2015).

	Jupiter	Saturn	Uranus	Neptune	Jupiter	Saturn	Uranus	Neptune
	8k				Li & Adams (2015)			
Standard	87.5	75.5	71.5	70.5	98.5	96.6	92.8	88.7
Compact	85.0	75.5	68.5	72.0	98.2	96.7	94.3	90.6
Resonant	88.5	56.5	6.50	5.0	97.6	96.0	93.9	94.0
Massive	74.0	72.0	67.5	70.5	97.6	96.2	92.2	89.5

**Tab. 3.4.:** Fractions of prompt and delayed ejections in the standard configuration of the 16k cluster for the different planet types.

Planet	Prompt ejection	Delayed ejection
Jupiter	88%	12%
Saturn	61%	39%
Uranus	52%	48%
Neptune	59%	41%

The ejection of one or several planets can occur either during or directly after the encounter (prompt ejection), or at a later time due to secular evolution (delayed ejection). For the standard case in the 16k cluster, we find a fraction of  $\sim 60\%$  prompt ejections and  $\sim 40\%$  delayed ejections (see Table 3.4 for a distinction between the different planet types). However, both events (but especially the latter case) are not well defined in our simulations since the planetary systems are continuously perturbed by other stars. In many cases, where planetary systems are already moderately or highly excited, the true source for a planet’s ejection — secular evolution or the next external perturbation — cannot be clearly identified. The mentioned fraction for the delayed ejection should therefore be treated with caution. We often see a strong planet–planet interaction subsequent to an encounter which leaves the system in a highly vulnerable state. It then only requires a very weak perturbation by another star to eject some of the planets which would not have been strong enough to disrupt the planetary system without the previous excitation. Those events are counted as delayed ejection even though they result from the combined effect of secular evolution and (another) prompt ejection due to the next encounter.

Fujii & Hori (2019) perform  $N$ -body simulations of different cluster types and use a semi-analytical approach for the calculation of the fraction of ejected planets. The cluster model which is closest to one of our clusters is a high-density King-model cluster (King 1966) with  $N = 2048$  and  $W_0 = 3$ . Using the power-law function from eq. 10 in Fujii & Hori (2019) and the corresponding best-fitting parameter for G-type stars, one obtains survival fractions  $[1 - f_{\text{ejc}}(a)]$  for the standard configuration of 93% (Jupiter), 90% (Saturn), 82% (Uranus), and 76% (Neptune).

**Tab. 3.5.:** Fractions of planetary systems in which at least one planet is ejected during the simulation.

Configuration	8k	16k	32k	64k
Standard	34%	42%	42%	62%
Compact	34%	38%	38%	63%
Resonant	100%	100%	100%	100%
Eccentric #1	35%	44%	43%	67%
Eccentric #2	83%	82%	83%	90%
Massive	40%	52%	60%	77%

These values are higher than the results for our smallest cluster. The important difference between our work and [Fujii & Hori \(2019\)](#) is not so much the different cluster models but the fact that we also take into account delayed ejections due to planet–planet scattering (for which the multiplicity of our planetary systems plays a crucial role) and the possibility of several strong encounters.

In the standard configuration of our 16k cluster the fraction of systems in which at least one planet is immediately ejected after an encounter (regardless of the intruder’s mass) is 26%. This value is comparable to the study of [Malmberg et al. \(2011\)](#) where they find fractions between 15% and 31% for a mass range of 0.6 – 1.5  $M_{\odot}$  for the intruder star. [Malmberg et al. \(2011\)](#) also determine the fractions of systems from which at least one planet has been ejected within 100 Myr after the encounter and find fractions of 47–69% for flybys of stars with masses of 0.6 – 1.5  $M_{\odot}$ . We find a corresponding value of 42% in the standard configuration of the 16k cluster (see Tab. 3.5 for other configurations and other cluster sizes). The lower value likely stems from the shorter integration time. Although we simulate the planetary systems for 100 Myr, the remaining simulation time after the first strong encounter is shorter wherefore our values cannot be directly compared with those from [Malmberg et al. \(2011\)](#).

Although [Malmberg et al. \(2007\)](#) use  $N$ -body simulations, a direct comparison is also difficult as they only study encounters between stars but do not explicitly analyze planetary systems. Furthermore, their studied clusters are rather small in terms of stellar members. They define a star that has never been part of a binary system or has never undergone any close encounters with other stars as “singleton”. We calculate the fraction of singletons in our simulations and obtain values of 50% (8k cluster), 32% (16k cluster), 20% (32k cluster), and 6% (64k cluster). [Malmberg et al. \(2007\)](#) provide the fraction of singletons for different half-mass radii and different numbers of cluster members. Taking their largest cluster ( $N = 1000$ ) as reference, our results are most similar to the range of initial half-mass radii of 0.38–1.69 pc.

The most consistent simulations of star clusters with planetary systems so far have been performed by [van Elteren et al. \(2019\)](#). They adopted the initial conditions from earlier simulations that tried

to match the mass and size distributions of circumstellar discs in the Orion Trapezium cluster (Portegies Zwart 2016). In the follow-up calculations by van Elteren et al. (2019), the discs were replaced by planetary systems, selected according to the Oligarchic growth model (Kokubo & Ida 1998). The parameter search was limited to a cluster of 1500 stars. The initial conditions were generated from the simulation of a star cluster with circumstellar discs of 400 au each for 1 Myr during which the discs were truncated and harassed by passing stars. In that time frame, the cluster evolved and the discs were affected by passing stars but not by internal processes. After 1 Myr, a total of 977 stars remained bound in the cluster, 512 of which received a planetary system. The calculation was performed with 2522 planets with a total mass of 3527 Jovian masses. At an age of 11 Myr, 10 Myr after the birth of the cluster, 2165 planets were still bound to their host star: 16.5% of the planets became unbound. The majority ( $\sim 80\%$ ) of the ejected planets promptly escaped the cluster, the rest lingers around for at least half a million years before escaping the cluster potential.

### 3.3.3 Distribution in $a$ - $e$ Space

We plot the eccentricity as a function of the semimajor axis of the planets for the different cluster sizes in Fig. 3.5 for the 8k cluster, and in Figs. B.1, B.2, and B.3 in the appendix for the 16k, 32k, and 64k clusters, respectively. These figures clearly show a trend with increasing cluster size. In the 8k cluster most planets are only excited in eccentricity and just a few of them migrate into wider (or sometimes tighter) orbits. The fraction of highly eccentric orbits and planets that undergo significant orbital migration increases with increasing cluster density. The planets' distribution in the  $a$ - $e$  space is therefore wider for our larger clusters.

Having a look on the different initial orbital configurations reveals large differences in the  $a$ - $e$  space at the end of our simulations. In the 8k cluster (see Fig. 3.5), the standard and compact configuration look similar. Most planets roughly retain their initial semimajor axis for 100 Myr. Only a few have migrated to larger semimajor axes and even less to tighter orbits (mainly Jovian-like planets, but there is also one Uranus-like planet in the standard case with  $a < 2$  au). Especially the outermost planets tend to migrate to very wide orbits of more than 100 au. In the standard configuration of the 8k cluster, even one Saturn-analogue can be found beyond  $a > 100$  au. Due to the initially smaller semimajor axis of the outer three planets in the compact configuration, we observe a smaller number of planets on orbits with  $a > 50$  au. In the compact configuration of the 16k cluster (see Fig. B.1 in the appendix) we can find in general more wide-orbit planets than in the 8k cluster but also wide-orbit planets with eccentricities  $e < 0.4$  which are missing

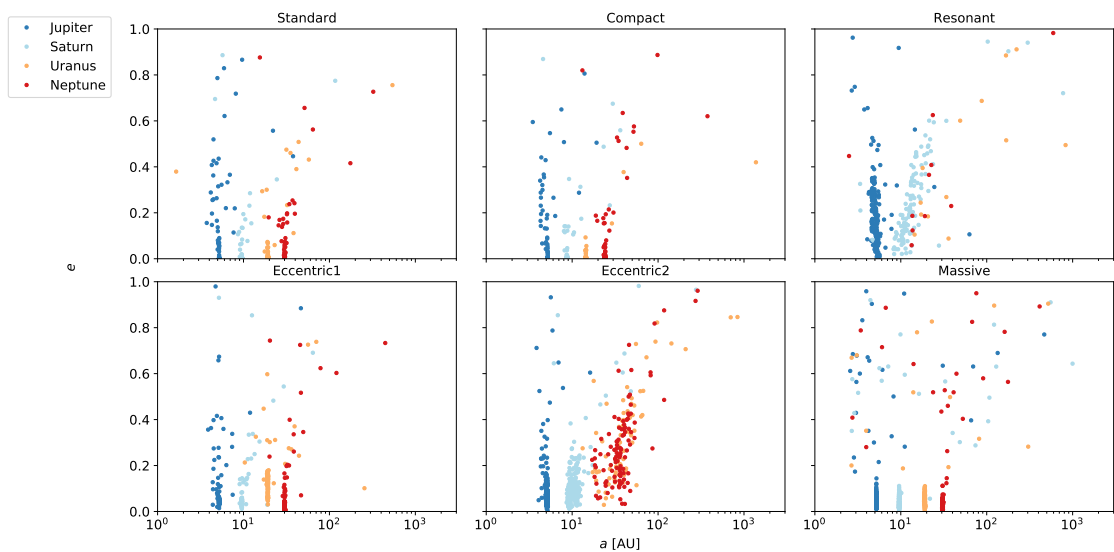


**Fig. 3.5.:** The  $a$ - $e$  space for all planets in the 8k star cluster which are not ejected from their host planetary system at  $t = 100$  Myr, for the six different initial configurations. A video showing the  $a$ - $e$  space for the course of the simulation is available on our Silkroad project team webpage: [http://silkroad.bao.ac.cn/silkroad-save/a\\_e\\_space\\_N8k.mp4](http://silkroad.bao.ac.cn/silkroad-save/a_e_space_N8k.mp4).

in the standard configuration. The fraction of planets which remains unaffected in their orbital parameters is lower in the 32k and 64k clusters.

The distribution of planets in the  $a$ - $e$  space looks different for the resonant configuration. In the 8k cluster, most Jovian-like planets were at least excited in eccentricity and some also migrated within the system (mainly to wider orbits). None of the Saturn-like planets can retain its initial semimajor axis and eccentricity, and a clear trend towards wide, eccentric orbits is observable. The few Uranus-like planets which survived for 100 Myr all have wide and/or eccentric orbits. Four of these planets have  $a > 100$  au and one even has  $a > 800$  au. All of these four planets have eccentricities of  $e \gtrsim 0.5$ . While all Uranus-like planets failed to keep their initial semimajor axis, three of the Neptune-like planets succeeded in doing so. However, all of them were at least slightly excited in eccentricity (as well as the Uranus-like planets). In all of these three systems Uranus was ejected during the first few tens of thousands of years after a relatively short interaction with Neptune before the first strong encounter happened. Due to the encounters with Neptune, all three Uranus's migrated to an orbit with a semimajor axis smaller than that of Jupiter which led to the ejection of Uranus within the subsequent tens of thousands of years. This fortunate circumstance made the planetary system robust enough to withstand the gravitational perturbations by other stars during the remaining 99 Myr.

The three orbital parameters  $a$ ,  $e$ , and  $i$  of one of these three planetary systems as a function of time are shown in Fig. 3.6. The time is plotted in logarithmic scale to highlight the planet-planet scattering during the first 100 000 yr. We additionally plot the distance of the host star to the cluster centre and the distance to the next stellar perturber in grey in the top and middle panel to illustrate the interaction with the cluster. The cumulative gravitational effects of several neighbours in distances between 13 000 and 23 000 au remove the resonance of Uranus and Neptune within the first 10 000 yr which causes them to slightly interact with each other and to change their orbital position for a few hundred years. After migrating back to the second outermost position Uranus is already excited in eccentricity. The subsequent interaction with Jupiter and Saturn and the simultaneous close approach of a neighbouring star leads to the prompt ejection of Uranus and the removal of the remaining resonances in the system. Due to this circumstance, the remaining three planets form a stable system and stay relatively unperturbed for the rest of the simulation even though neighbouring stars closely approach the system several times.

The  $a$ - $e$  space for the first eccentric configuration in the 8k cluster looks similar to the standard and compact configuration but there are slight differences. On the one hand, the number of Jupiters that have high eccentricities is reduced. On the other hand, the number of Uranus- and Neptune-like planets with high eccentricities is larger in the first eccentric configuration. While Jupiter, Saturn, and Uranus all start at eccentricities of  $e \approx 0.05$  there are Jupiters and Saturns that end up at nearly-circular orbits. However, this is not the case for Uranus. While some of them keep their initial eccentricity, there are no Uranus-like planets that have reduced it after 100 Myr. Most of them are significantly excited in eccentricity.

Increasing the initial eccentricity of all planets to  $e = 0.1$  makes a large difference in the outcome of our simulations. Especially Uranus and Neptune cover a much wider range in the  $a$ - $e$  space after 100 Myr compared to the first eccentric configuration. On the other hand, most of our Jupiters and Saturns “fall back” to circular or almost circular orbits during the simulation which can be explained by the exchange of angular momentum between the planets during close encounters. This effect can be seen in Fig. 3.7 where Neptune is ejected at  $t = 22$  Myr. A  $6.9 M_{\odot}$  star approaches the planetary system down to a distance of 310 au and ejects Neptune out of the system by “kicking” it to the inner regions of the planetary systems where it transfers angular momentum to Jupiter and Saturn. The eccentricity of both planets subsequently decreases.

The massive configuration is more difficult to be excited in orbital parameters which can be seen the right bottom panel of Fig. 3.5. There is a clear distinction between those planets that are only slightly perturbed, which are those with eccentricities below 0.2, and those which have been sufficiently perturbed to trigger fatal planet-planet scattering. Due to the equal mass of all planets in this configuration, the number of highly eccentric planets that have undergone orbital

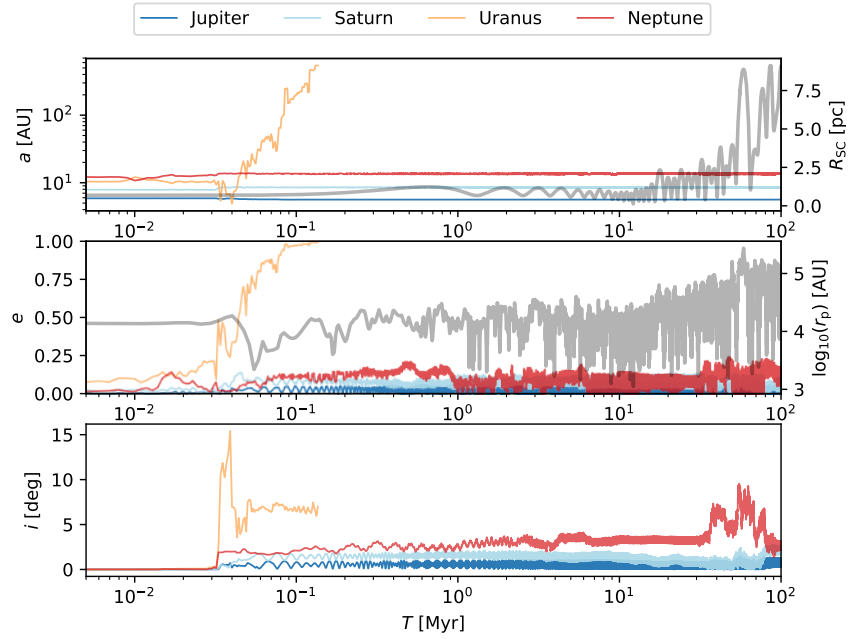


**Fig. 3.6.:** The orbital parameters  $a$  (top),  $e$  (middle), and  $i$  (bottom) of a resonant planetary system from the 8k cluster as a function of time. The time is plotted in logarithmic scale. The scales on the right side correspond to the grey lines in the plots which represent the distance of the host star to the cluster centre (top) and the distance to the closest perturber (middle).

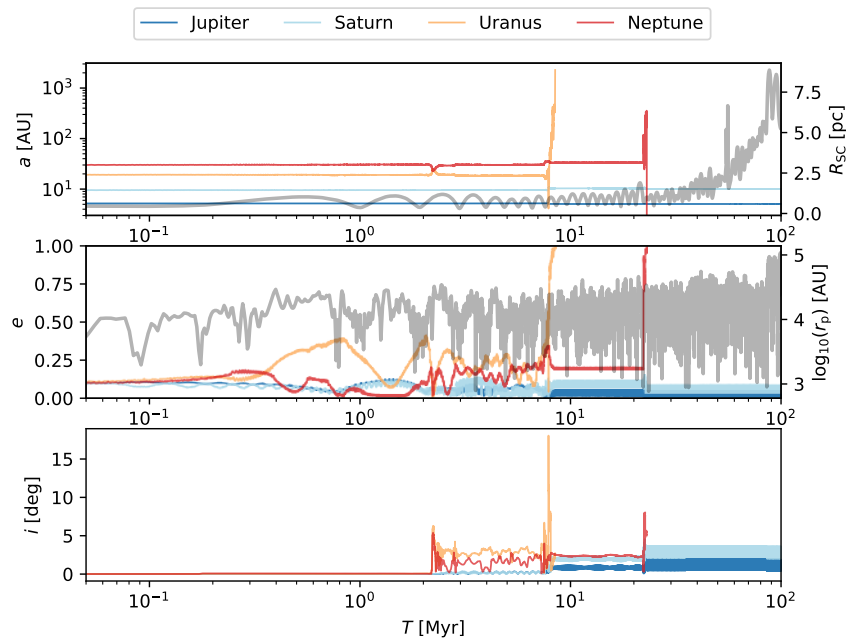


**Fig. 3.7.:** Same as in Fig. 3.6 but for a planetary system with initial eccentricities of  $e = 0.1$  from the 8k cluster.

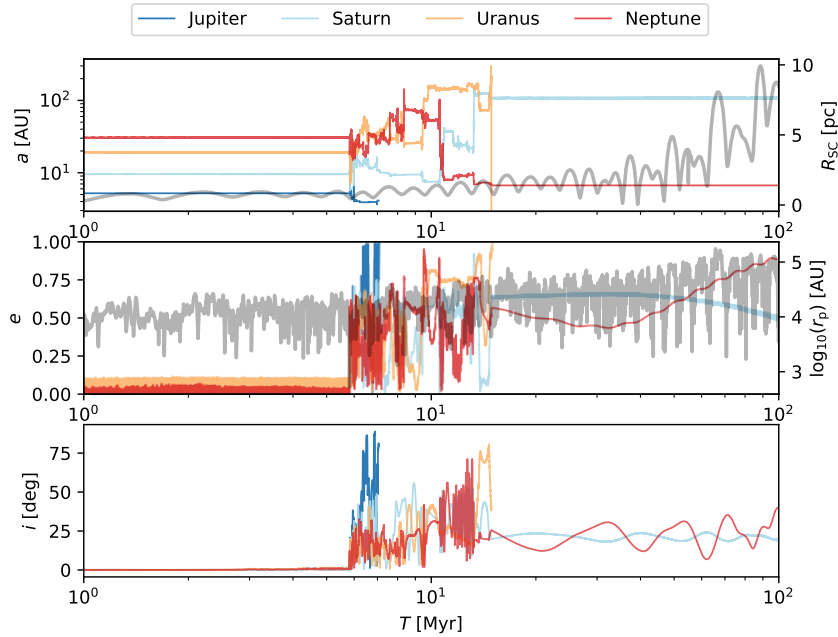


**Fig. 3.8.:** Same as in Fig. 3.6 but for a massive planetary system from the 8k cluster.

migration is almost comparable for all kind of planets. The numbers of almost unexcited planets is only slightly larger for the inner planets due to their smaller semimajor axis. Figure 3.8 shows the orbital elements of a planetary system in which the planets are mostly unaffected for the first few million years despite several encounters. At  $t = 5.8$  Myr a red dwarf with a mass of  $0.3 M_{\odot}$  approaches the system closer than 240 au causing a transfer of energy and angular momentum from Neptune to the perturber. Due to the inwards migration of Neptune on an orbit with an eccentricity of around 0.5, a fatal chain reaction with strong planet–planet scattering is triggered in which the eccentricity of the three other planets is excited as well. After a very short change of position with Saturn, Jupiter migrates inwards and reaches twice an eccentricity of more than 0.9 before it is finally ejected at  $t = 7.1$  Myr. During that time and in the following 7 Myr the remaining planets Saturn, Uranus, and Neptune change their order several times. Due to that strong interaction, Uranus migrates outwards to a very wide and eccentric orbit. Saturn follows at  $t = 13.3$  Myr which finally leads to the ejection of Uranus at  $t = 14.9$  Myr. For the remaining 85 Myr, Saturn retains its wide orbit of  $a \approx 107$  au while Neptune remains at  $a = 6.7$  au.

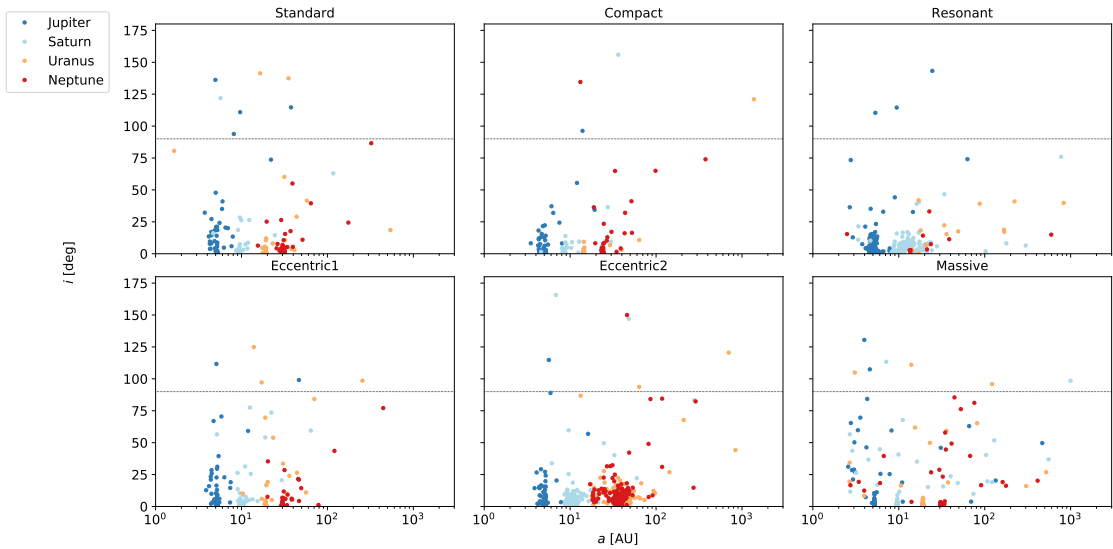


**Fig. 3.9.:** The  $a$ - $i$  space for all planets in the 8k star cluster which are not ejected from their host planetary system after a simulation time of 100 Myr for the six different initial configurations. The dotted black line shows the threshold of  $i = 90^\circ$ . Planets near that value have polar orbits while those above it have retrograde orbits.

### 3.3.4 Distribution in $a$ - $i$ Space

A change in eccentricity is often directly related to a change in inclination since both result from the transfer of angular momentum. By looking on the  $a$ - $i$  space of the planets after 100 Myr for the different cluster sizes in Figs. 3.9, B.4, B.5, and B.6, we can again see a wide distribution in that parameter space, although all planets started on coplanar, prograde orbits (Figs. B.7, B.8, B.9, and B.10 show the  $e$ - $i$  space after 100 Myr for comparison). Those planets that get excited to polar orbits ( $i \approx 90^\circ$ ) or retrograde orbits ( $i > 90^\circ$ ) are of special interest.

In 2006, Remijan & Hollis (2006) found first evidence that parts of the protoplanetary disc around the binary system IRAS 16293–2422 are counterrotating which means that planets that form in that region would have a retrograde orbit. The first two detected planets for which a retrograde or polar orbit is assumed are WASP-17b (Anderson et al. 2010) and HAT-P-7b (Winn et al. 2009).

We find planets with inclined orbits of more than  $90^\circ$  in all of our simulations, independent of the initial configuration and stellar density of the host cluster. Some planets switch to a retrograde orbit for only a few million years but some also keep their highly inclined orbit for the rest of the simulation. An example of the latter case is shown in Fig. 3.10. At 71 Myr, the encounter of a  $1.9 M_\odot$  star of less than 600 au causes Uranus (the outermost planet at that time) to switch from a prograde orbit (inclined by  $23^\circ$ ) to a retrograde orbit with  $i = 164^\circ$ . Despite several additional

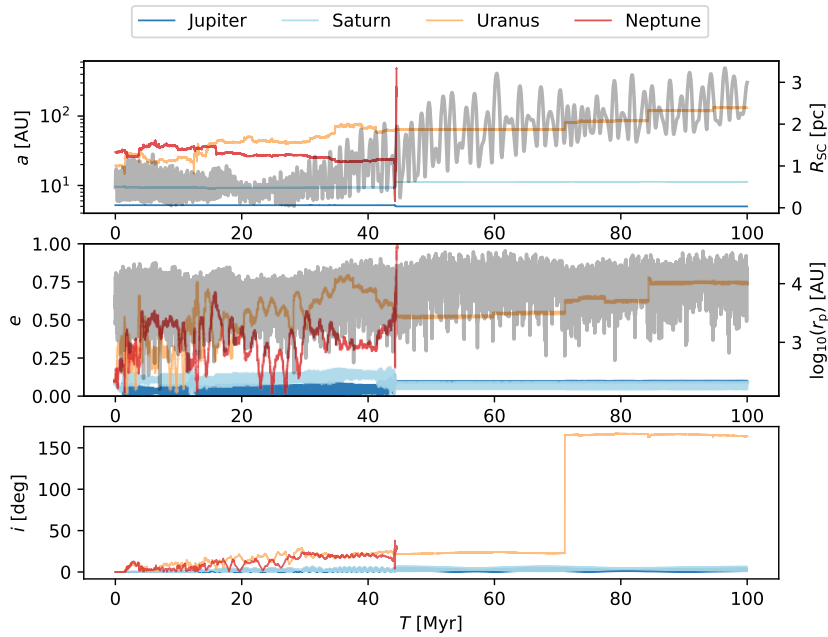


**Fig. 3.10.:** Same as in Fig. 3.6 but for a planetary system with initial eccentricities of  $e = 0.1$  from the 32k cluster. The time is plotted in linear scale.

encounters during the remaining 29 Myr with periastron distances of less than 1000 au, Uranus keeps its retrograde orbit until the end of the simulation.

There is no clear trend visible in which configuration or with which cluster density we can expect the highest fraction of retrograde orbits. However, in all four cluster simulations, the massive configuration results in the largest number of highly inclined orbits with  $i > 50^\circ$  after 100 Myr. We can therefore conclude that retrograde orbits mainly occur due to strong external perturbation while planet–planet scattering especially seems to be an additional source for the excitation of planetary orbits to the range of  $i \approx 50^\circ - 80^\circ$ .

### 3.3.5 Dynamical Evolution of a Planetary System in Different Initial Configurations

In the previous sections, we have shown the differences between the initial configurations averaged over identical 200 planetary systems. However, from this we can only have a rough estimate of how the dynamical evolution of one planetary system looks like if we put it in different initial configurations. Therefore, we show the dynamical evolution of planetary system #15 from the 32k cluster in all six different configurations in Fig. 3.11 as an example. While in the standard

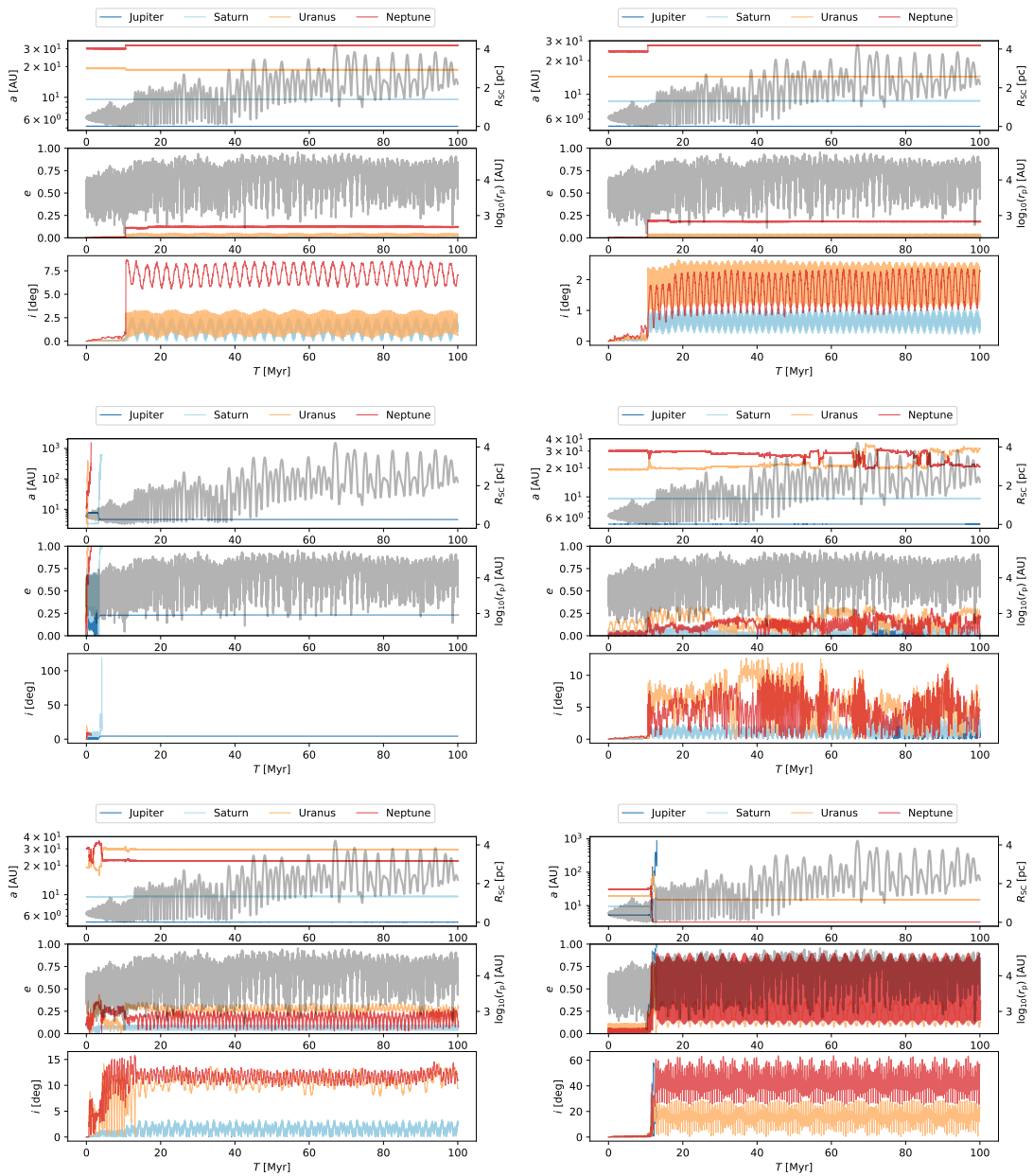


**Fig. 3.11.:** Comparison of the dynamical evolution of one planetary system in the 32k cluster around the same host star in all six different initial configurations. *Top left:* Standard configuration. *Top right:* Compact configuration. *Middle left:* Resonant configuration. *Middle right:* Eccentric#1 configuration. *Bottom left:* Eccentric#2 configuration. *Bottom right:* Massive configuration.

case Jupiter and Saturn only get slightly excited in eccentricity and inclination due to an encounter at  $t = 10$  Myr, Uranus migrates inwards by  $\sim 0.5$  au and Neptune outwards by  $\sim 2$  au. Neptune's increase in eccentricity and inclination is the largest of all four planets.

There is almost no difference in the dynamical evolution of Jupiter, Saturn, and Uranus between the standard and compact configuration. However, instead of migrating inwards, Uranus keeps its semimajor axis in the compact configuration unlike Neptune which now migrates outwards by 3.5 au due to the same encounter as in the standard configuration. Neptune is also more excited in eccentricity but less in inclination.

In the resonant configuration, Saturn, Uranus, and Neptune do not even survive until the first very close encounter at  $t = 10$  Myr which is the only encounter in the standard and compact configuration which affects the system significantly. Uranus and Neptune are both ejected within the first 1.3 Myr, whereas Saturn migrates to  $a = 3.4$  au and strongly oscillates in eccentricity within the following millions of years. Jupiter, which migrates outwards to a semimajor axis of 7.8 au, and Saturn cross their orbits after an additional stellar encounter at  $t = 3.3$  Myr which causes the ejection of Saturn at  $t = 4.2$  Myr. Due to that interaction, Jupiter migrates back to a smaller orbit of  $a = 4.6$  au and stays completely unaffected during additional encounters within the rest of the simulation.

The dynamical evolution of the first eccentric configuration is characterized by the interaction between Uranus and Neptune. The same encounter that affected the standard and compact configuration causes a first close orbital approach of Uranus and Neptune after roughly 10 Myr. Due to that, their initially small eccentricities increase as well as their inclinations. Additional encounters, especially during the last 50 Myr of our simulation cause steady interaction and switch of orbital positions between the two outermost planets. Jupiter and Saturn stay relatively unaffected in this simulation.

The higher initial eccentricity in the second eccentric configuration leads to a quicker interaction between Uranus and Neptune than in the previous case. After a switch of positions the whole planetary system stays stable for the rest of the simulation.

The massive configuration reveals the increasing risk for the innermost planets if all planets in the system have the same mass. In all of the previous configurations, Jupiter survived without facing any serious dangers for its orbital stability while Saturn survived in four configurations. In the massive configuration, these two planets are the only planets that get ejected while Uranus and Neptune survive. The external perturbation that leads to the ejection of Jupiter and Saturn is the same stellar encounter which is the formative encounter in the dynamical evolution of the system in the standard, compact and first eccentric configuration.

## 3.4 Discussion and Conclusions

We have explored the stability and vulnerability of 4800 planetary systems, which are exposed to repeated stellar encounters in the star cluster in which they formed. In each of our four star clusters, we distribute 200 identical planetary systems in six different initial configurations, which were inspired by the Monte Carlo simulations of [Li & Adams \(2015\)](#). All planetary systems were Solar system analogues (with host star masses of  $\sim 1 M_{\odot}$ ) consisting of the solar system's gas giant planets Jupiter, Saturn, Uranus, and Neptune. In the standard configuration, the planets have their current semimajor axes but circular orbits. Two other configurations are more compact versions of that case which are called the compact and resonant configurations (due to mutual MMRs between the planets). In two additional configurations, the eccentricities of the standard case are increased to the planets' present-day values and to larger values of  $e = 0.1$  (the first and second eccentric configurations). The sixth configuration differed from the standard configuration only in the equal planetary masses of one Jovian mass.

Our results for the cluster simulation can be summarized as follows: after 100 Myr the star clusters have undergone the phases of mass segregation, stellar mass-loss and core collapse, and re-expand again after a time of maximum central density. The maximum central density reaches about 10 times the initial central density; after mass segregation and core collapse the cluster generally re-expands and reaches a quasi-stationary state, where the central density is about equal to its initial value, and the average density inside the half-mass radius has dropped by a factor of approximately 10. We observe that at that stage most of the dynamical interactions between planetary systems and passing stars are over, so for the current pilot study we stop our models at 100 Myr.

Generally, the most stable planetary systems are the standard and compact ones, and the configuration with small (current) eccentricities. The results for the standard, compact, and first eccentric configuration are comparable in fractions of surviving planets and final distribution in  $a - e$  and  $a - i$  space. However, a trend is observable that the compact system becomes slightly more resistant and the eccentric one slightly more vulnerable with increasing stellar density relative to the standard case.

We note that the compact system relative to the standard system shows very little differences — one would expect that it experiences less strong interactions under the effect of the same encounters as the standard system; our result of very similar survival fractions can only be explained by stronger internal interactions, which destabilize the system even after relative weak

perturbations. Furthermore, small initial eccentricities seem to not significantly change the vulnerability of a planetary system.

Due to its innermost position and highest mass, Jupiter is generally the planet with the highest chance to survive a perturbation by a stellar encounter of another cluster member, followed by Saturn. The exact order of the survival fraction of the two outermost planets Uranus and Neptune depends on the initial configuration and cluster density. However, usually Uranus is slightly more likely to be ejected from the planetary system due to an encounter or secular evolution. Even though Uranus is not the outermost planet, its lower mass makes the planet slightly more vulnerable to gravitational perturbations from the host cluster due to its lower gravitational binding energy compared to Neptune. This difference can especially be seen in the survival fractions for the second eccentric configurations. In all four clusters, Uranus has by far the lowest chance to survive in the system if all planets are started with their true semimajor axes but with an eccentricity of 0.1. If all planets have equal masses, the differences in survival fractions shrink significantly. Due to its smallest semimajor axis, Jupiter still has a slightly higher chance for survival while the rates for Saturn, Uranus, and Neptune are almost equal. From this, we can deduce that a planet's mass (compared to the other planets in the system) plays a more crucial role for the estimation of its vulnerability than its semi-major axis.

The fourth most stable system is the massive configuration in the 8k and 16k cluster but the system with initial eccentricities of  $e = 0.1$  is instead more resistant in the 32k and 64k cluster. In all clusters, the resonant system is the one with the highest vulnerability. However, the system is a special case and very interesting for a certain reason. Our integrations show that without perturbations by passing stars it is generally very short lived, getting unstable after about  $10^5$  yr, around that time Uranus and Neptune are inevitably ejected from the planetary system. However, embedded in a star cluster, the system tends to be more stable. We believe that this is due to a process where stellar encounters detune or break the resonances and thus render the systems more stable. In many of the simulated systems, this is achieved by only ejecting one of the outer planets (Uranus or Neptune), and then the remaining three-planet system survives much longer than in the isolated case.

In [van Elteren et al. \(2019\)](#), the authors find that the probability of a star to lose a planet is independent of the planet mass and independent of its initial orbital separation. As a consequence, the mass distribution of free-floating planets would be indistinguishable from the mass distribution of planets bound to their host star. Our results do not confirm this. The discrepancy may result from the larger number of stars in the clusters in our simulations, the longer evolutionary timescales (we integrated for 100 Myr whereas in [van Elteren et al. 2019](#), they integrated up to 10 Myr), and finally they adopted the Oligarchic growth model for planetary systems. In the latter

model, planet mass increases further away from the host star. This has interesting consequences for the stability of the planetary systems from perturbations from inside as well as for external perturbations. A small perturbation from another star may render an entire planetary system catastrophically unstable, whereas if the outer most planets have low mass, such a system survives more easily in a dense stellar environment.

The survival fractions for the different planet types in our simulations are generally smaller than those of [Li & Adams \(2015\)](#). This is due to the different approaches. First, [Li & Adams \(2015\)](#) randomly select their encounter parameter equally from the available phase space that is not realistic (see figs. 1 and 2 in [Spurzem et al. 2009](#)). Secondly, [Li & Adams \(2015\)](#) only focus on the prompt ejections of planets while we continue the integration of the planetary systems long enough to account for secular evolution. Thirdly, our planetary systems are exposed to the cumulative effect of several encounters over a significant fraction of the host star cluster's lifetime. From the reduced survivability of the planets, which we see in our results compared to [Li & Adams \(2015\)](#), we can conclude that the effects of secular evolution and cumulative encounters are not negligible.

We find that passing stars excite mutual inclinations between planets in our planetary systems; quite some cases lead to high values of relative inclination and even to counter-rotating planets. It is quite impossible to excite significant inclinations by internal evolution of planetary systems, they are a tell-tale sign of the important role of stellar encounters in shaping the planetary system. While this effect has been mentioned in previous studies (such as in [Spurzem et al. 2009](#)), there is not yet a more quantitative study of this process.

Our simulations could be and will be refined in future work in many ways. Planetary systems around more massive stars are subject to orbital changes when the host star becomes a red giant and finally loses significant mass. The presence of many initial binaries, which is expected from star and cluster formation, will be an interesting issue — including S- and P-type planetary systems.

The Monte Carlo models of [Li & Adams \(2015\)](#) give some information about encounters between planetary systems and binary stars. Finally, in this work we have only presented a limited set of star clusters. A wider parameter study may be required to predict the impact of stellar encounters on the final planetary population in the Galactic field. Other processes shaping planetary systems in the formation process inside a star cluster have also not been taken into account here.

We have, however, clearly shown that encounters of passing stars in star clusters have a considerable effect and contribute to the diversity of planetary systems in all respects.

# Birth Cluster Simulations of Planetary Systems with Multiple Super-Earths: Initial Conditions for White Dwarf Pollution Drivers

” *In the Atacama, I saw the future, when the Sun eats up the last of its hydrogen and burns into its red-giant phase, big enough to cook life and clouds and oceans off this naked orb. It wouldn't be a fast process, not by our standards. Millions of years in the execution, our sky would finally be half filled by a Sun the color of a red-hot moonrise. After that, the Sun would probably collapse into a white dwarf, meanwhile blasting away its outer shells of gas into an explosive planetary nebula. I imagine that all of our minerals will pay off as we make a rainbow streak flaring off into space. We will be beautiful. — from the book "Apocalyptic Planet"*

— **Craig Childs**  
(American writer)

**Details of authorship:** *The content of this chapter is entirely based on the manuscript of [Stock et al. \(2022\)](#), which has been submitted to MNRAS. The manuscript as well as all scientific work, calculations and conclusions contained therein have been prepared by me. Before submission and during the review process, I incorporated suggestions for improvement and corrections from the co-authors and the reviewer. For this thesis, I have slightly adjusted the format of the figures*

*and tables to better fit the single-column layout of this thesis. The appendix of this publication has been moved to the appendix of this thesis.*

## 4.1 Introduction

Over 99% of all known exoplanet host stars will eventually evolve into white dwarfs (WDs). This fact emphasises the importance of being able to connect planetary architectures around WDs to their previous incarnations around giant branch and main-sequence stars, and to the processes which occurred in their nebular birth clusters.

One way to pursue this connection is to consider the observations of known planetary systems around WDs. [Veras \(2021\)](#) partitions these observations into four classes: (i) major planets, (ii) minor planets (such as asteroids, comets or moons, but also the remnants of larger planets), (iii) discs and rings, and (iv) chemical pollution by metals in the WD's atmosphere from accreted planetary debris. The largest category is by far the last, which includes over 1 000 systems ([Dufour et al. 2007](#); [Kleinman et al. 2013](#); [Kepler et al. 2015, 2016, 2021](#); [Coutu et al. 2019](#)). The smallest category is the first, with just five examples of major planets known ([Thorsett et al. 1993](#); [Sigurdsson et al. 2003](#); [Luhman et al. 2011](#); [Gänsicke et al. 2019](#); [Vandenburg et al. 2020](#); [Blackman et al. 2021](#)). Nevertheless, both categories are connected, despite this observational gulf, because planets can dynamically drive this debris or their progenitor asteroids, moons or comets into WDs.

The accreted debris is ubiquitous, appearing in between 25% and 50% of Milky Way WDs ([Zuckerman et al. 2003, 2010](#); [Koester et al. 2014](#)). The debris has also been observed to occur at cooling ages (the time since becoming a WD) up to 8 Gyr ([Hollands et al. 2018](#); [Blouin & Xu 2022](#)).

Identifying the planetary architectures which can allow planets to perturb smaller bodies towards the WD in a manner that mimics the distribution of accretion rate with cooling age is an ongoing challenge and is subject to a large number of degeneracies. The currently known exoplanets orbiting main-sequence stars will predominately be engulfed by their parent stars upon leaving the main sequence ([Maldonado et al. 2020a,b, 2021](#)), and sub-Saturn sized planets remain largely hidden from view at separations where such planets would survive.

However, such distant super-Earths is a class of planets shown to be particularly efficient at polluting WDs at a wide variety of cooling ages ([Frewen & Hansen 2014](#); [Mustill et al. 2018](#)),

particularly because such planets meander with their orbits in continuous motion (Veras & Gänsicke 2015; Veras et al. 2016). In contrast, a Jupiter-mass planet acts more like a sledgehammer on a fixed orbit, dissipating the system and polluting the WD in short bursts (Veras et al. 2021). One key feature of these super-Earth polluters is that they are on eccentric orbits (as e.g. for  $\beta$  Pictoris; Beust & Morbidelli 1996), because a single planet on an exactly circular orbit cannot perturb minor bodies sufficiently close towards a WD (Antoniadou & Veras 2016). Also helpful for pollution is when planets reside in multiple-planet systems, because otherwise perturbing minor bodies onto star-grazing orbits is challenging (Bonsor et al. 2011) and may require asteroid reservoirs several orders of magnitude more massive than the Solar Systems’ (Debes et al. 2012). WD pollution due to secular chaos in multiplanetary systems has been previously investigated in Smallwood et al. (2018, 2021) and O’Connor et al. (2021).

The vast majority of WD pollution investigations which contain perturbing planets (see Fig. 6 of Veras 2021 for an extensive list) use initial conditions for their planetary systems which are not outputs from birth cluster simulations. In a first attempt to bridge this gap, Veras et al. (2020) connected the outcomes of stellar cluster simulations involving outer Solar system analogues with their future evolution across different stellar phases. However, partly because their setup was limited to giant planets on nearly circular orbits, that architecture is not necessarily representative of those found in chemically polluted WD systems<sup>1</sup>.

Here, we perform stellar cluster simulations with a wider variety of planetary architectures which are more likely to pollute the eventual WDs over long cooling times. We also use more representative progenitor WD masses ( $1.5 M_{\odot} - 2.5 M_{\odot}$ ; Tremblay, Cummings, Kalirai, Gänsicke, Gentile-Fusillo, & Raddi 2016; Cummings, Kalirai, Tremblay, Ramirez-Ruiz, & Choi 2018; McCleery, Tremblay, Gentile Fusillo, Hollands, Gänsicke, Izquierdo, Toonen, Cunningham, & Rebassa-Mansergas 2020) rather than  $1.0 M_{\odot}$  Sun-like stars. A key result of this study is publicly-available sets of post-cluster initial conditions that modellers could use as starting points for their simulations of post-main-sequence planetary systems.

Given the computational expense and complexity of stellar cluster simulations which contain multiplanetary systems, we devote Sec. 4.2 towards describing our methods. In Sec. 4.3 we report the results, and we state our conclusions in Sec. 4.4. Our output data tables are available as supplementary material in the online version of this paper. The full simulations are available on Zenodo at [doi:10.5281/zenodo.5883613](https://doi.org/10.5281/zenodo.5883613) in time steps of 2 000 years.

---

<sup>1</sup>The fate of the Sun itself appears to be one of a polluted white dwarf (Li et al. 2021), which helps to highlight the importance of considering different reservoirs of minor body material when evolving these Solar system analogues (Veras et al. 2020).

## 4.2 Methods and Initial Conditions

### 4.2.1 Computational Approach

Stars form predominantly in groups, like stellar associations or star clusters (Lada & Lada 2003; Portegies Zwart et al. 2010), and due to the close connection between star and planet formation, planets are accordingly born into these clustered environments. However, the simulation of multiplanetary systems in star clusters is challenging due to various reasons and requires different computational approaches depending on the underlying scientific question. One challenge for the numerical integration of the motions of the planets around the stars and the motion of the host star through the cluster are the completely different dynamical timescales. While the dynamical evolution of planets takes place on timescales of days and years, for star clusters it is typically in the range of several million years. Another aspect is the hierarchical nature of stars with (multi-)planetary systems. In principle, planetary systems can be treated and regularized similar to binary systems. Spurzem et al. (2009), who studied single-planetary systems in a star cluster in a fully coupled dynamical simulation, used this approach, as well as van Elteren et al. (2019), who studied multiplanetary systems in star clusters using the *Nemesis* module in *AMUSE* (Portegies Zwart 2011; Portegies Zwart & McMillan 2018). However, we want to be able to accurately trace resonant and secular effects in the dynamical evolution of the planetary systems. For this reason, we use a hybrid approach and simulate star cluster and planetary systems separately by using encounter information from the star cluster simulation for the integration of the planets. This approach is possible under the assumption that the motion of individual stars and the evolution of the whole star cluster can influence the dynamical evolution of the planets, but not vice versa.

As a first step in this approach, the star cluster is simulated using *NBODY6++GPU* (Aarseth 2003; Wang et al. 2015c, 2016, and references therein), where the motions of the stars are integrated using the Hermite scheme (e.g. Aarseth 2003; Aarseth et al. 2008). All necessary information is stored in high temporal resolution in the HDF5<sup>2</sup> format. Then, using the *LonelyPlanets* Scheme (LPS; Cai et al. 2015, 2017, 2018, 2019; Flammini Dotti et al. 2019; Stock et al. 2020), which is based on the *AMUSE* framework, all encounters of the selected host stars with each of the five nearest stars during the cluster simulation are calculated and stored, including the first and second time derivatives of the perturbers, in order to reconstruct the details of an encounter for the subsequent integration of the planetary systems. LPS uses *REBOUND* (Rein & Liu 2012) for the actual integration of the planetary systems, as well as additional features from *REBOUNDx* (Tamayo et al. 2020b). For our simulations, we use *REBOUND*'s high-order, adaptive-step size

---

<sup>2</sup><https://www.hdfgroup.org/>

integrator IAS15 (Rein & Spiegel 2015) to obtain accurate integration results of systems with close encounters between the planets.

## 4.2.2 Initial Conditions for the Star Cluster Simulation

We simulate an open star cluster consisting of 8 000 stars whose masses follow a Kroupa (2001) initial mass function (IMF) in the mass range of  $0.08 - 20 M_{\odot}$ . The total cluster mass is  $M_{\text{cl}} = 4073.4 M_{\odot}$ . The star's initial positions and velocities in the cluster are drawn from a Plummer (1911) model. The star cluster is initially in virial equilibrium ( $|U| = 2T$ , where  $U$  is the total potential energy of the Plummer sphere and  $T$  is the total kinetic energy of the cluster stars). The virial radius, which is defined as  $r_{\text{vir}} = GM_{\text{cl}}^2/(2|U|)$  (with  $G$  being the gravitational constant), is 1 pc for our cluster, while the initial half-mass radius is  $r_{\text{hm}} \approx 0.78$  pc. The star cluster is assumed to be on a Solar-like orbit around the Galactic centre which is why the tidal forces of the Galaxy acting on the cluster are assumed to be equal as for the Solar neighbourhood (Heisler & Tremaine 1986). The cluster's initial tidal radius  $r_{\text{tid}} = R_{\text{G}}(M_{\text{cl}}/M_{\text{G}})^{1/3}$  (with  $R_{\text{G}}$  being the distance to the Galactic centre and  $M_{\text{G}}$  being the Galaxy's mass contained inside  $R_{\text{G}}$ ) is 22.6 pc. Stellar evolution is implemented (see e.g. Spera et al. 2015; Khalaj & Baumgardt 2015), but the mass loss is negligible for the host stars whose planetary systems are only simulated during a period when their host star is still on the main sequence. Primordial binary systems are not included, however, binaries can form during the course of the simulation. We also do not assume primordial mass segregation, but we observe the onset of mass segregation during the first few million years when the cluster experiences a short phase of core collapse.

According to eq. 3 in Malmberg et al. (2007), encounters below  $r_{\text{min}} = 1000$  au between our host stars and an average-massed star ( $M_{\star} \sim 0.51 M_{\odot}$ ) in the cluster take place on timescales of  $\tau_{\text{enc}} \approx 0.6 - 1.2$  Myr. This corresponds to encounter rates of  $0.8 - 1.7$  encounters per star and per Myr for the host-star mass range used in our simulation.

We want to integrate the planetary systems until the cluster has sufficiently dissolved. Here, however, a compromise must be found between the computational costs of the planetary system simulations and the complete dissolution of the cluster. A good compromise for the 8 000 star cluster we simulate is a period of 100 Myr. Although only about 20% of the stars have completely escaped the cluster's gravitational field by then, the cluster has already expanded significantly to  $r_{\text{vir}} = 3.87$  pc, so that encounters between stars outside the dense core are very rare after more than 100 Myr. The median distance of the host stars to the cluster centre after 100 Myr is around 8 pc for the lowest and highest host star mass range, while the median distance to the nearest star

is 1.1 pc and 1.4 pc, respectively, and has increased by a factor of 11 and a factor of 15 compared to the beginning of the simulation. Thus a maximum integration time of 100 Myr for the planetary systems seems to be adequate. An optical comparison between the star cluster at the beginning of the simulation and after 100 Myr is shown in Fig. 4.1.

### 4.2.3 Initial Conditions for the Planetary System Simulations

In this work we provide the results of 1224 planetary systems embedded in an open star cluster whose properties were described in Sec. 4.2.2. The host stars to be simulated are the typical progenitor stars of polluted WDs on the main sequence, which typically have masses of  $1.5 - 2.5 M_{\odot}$  (see, for example, Tremblay et al. 2016; Cummings et al. 2018; El-Badry et al. 2018; McCleery et al. 2020; Barrientos & Chanamé 2021).

However, using a continuous mass spectrum for the host stars, as would be the case in a real star cluster, would reduce the comparability between the individual simulated planetary systems. For this reason, we divide the host stars into three different mass ranges,  $1.25 - 1.75 M_{\odot}$ ,  $1.75 - 2.25 M_{\odot}$  and  $2.25 - 3.25 M_{\odot}$ , and search for those stars whose masses lie in one of these mass ranges. Since the IMF drops off very steeply towards higher masses and the number of available stars is limited in the range around  $2.5 M_{\odot}$ , the upper limit of the third mass range is deliberately chosen to be higher. We then calculate the encounters of all these stars with each of the nearest five stars in the cluster and store this information. For the subsequent integration of the planetary systems, the masses of the host stars are set to  $1.5 M_{\odot}$ ,  $2.0 M_{\odot}$  and  $2.5 M_{\odot}$  to ensure the comparability of the planetary systems within these three mass ranges and to be able to work out the pure effect of the cluster environment on the dynamical evolution of the individual systems. According to the number of stars present in the three mass ranges, we have a total of 408 host stars available (193 stars with  $M_{\star} = 1.5 M_{\odot}$ , 114 stars with  $M_{\star} = 2.0 M_{\odot}$  and 101 stars with  $M_{\star} = 2.5 M_{\odot}$ ).

The planetary systems around these 408 host stars are then started in three different initial orbital configurations, while the host star and its trajectory through the cluster remain the same for all three different planetary system models. All planetary systems solely consist of super-Earths, each having a mass of  $0.01 M_{\text{Jup}} (\approx 3.2 M_{\oplus})$ . Due to the variety in multiplicity of actual observed planetary systems, we aim to simulate two bounding cases of systems consisting of three and seven planets. However, the compactness of a 7-planet system crucially determines its dynamical evolution, especially if it is externally perturbed (by stellar flybys).

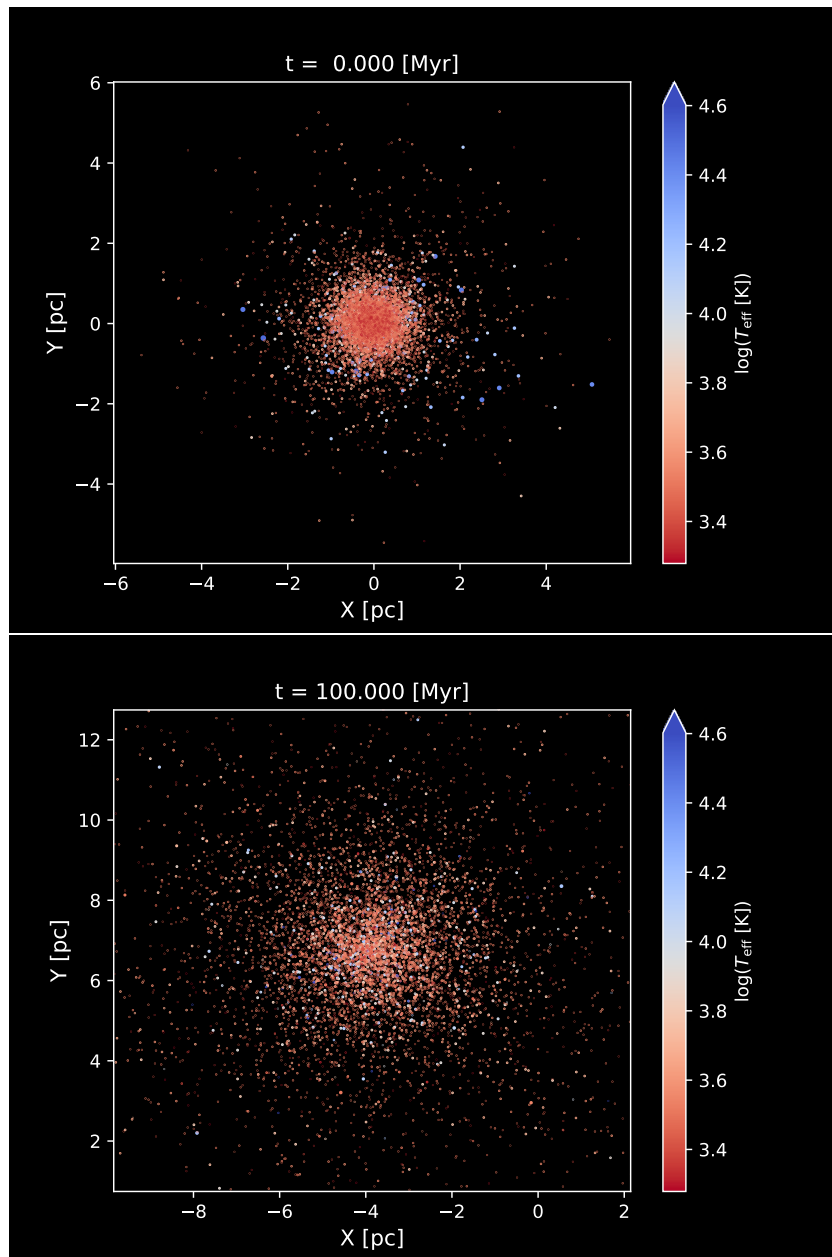


**Fig. 4.1.:** The simulated star cluster at the beginning of the simulation ( $t = 0$  Myr,  $r_{\text{vir}} = 1.0$  pc; top panel) and at the time  $t = 100$  Myr ( $r_{\text{vir}} = 3.9$  pc; bottom panel). The star cluster has visibly expanded and is in the process of dissolving. Although the cluster's centre of mass and its density centre moves, which means that the plotted axes range must be adjusted with increasing simulation time, the physical scale (a total of 12 pc on x- and y-axis) for both plots remains the same.

**Tab. 4.1.:** The planet’s initial semimajor axes (in au) for the three different planetary system models. All orbits are initially circular, coplanar and aligned. The mass of each individual planet is  $M_{\text{pl}} = 0.01 M_{\text{Jup}}$ .

Model	P1	P2	P3	P4	P5	P6	P7
3P	2.00	6.10	18.63				
7PC	2.00	2.90	4.21	6.10	8.86	12.85	18.63
7PW	2.00	3.49	6.10	10.67	18.63	32.55	56.87

Therefore, we simulate the following three scenarios in which all planets are equally separated in terms of mutual Hill radii ( $R_{\text{H,m}} = (a_1 + a_2)/2 \cdot ((M_1 + M_2)/(3M_\star))^{1/3}$ ): (i) a system consisting of only three planets (called “3P model”) between 2.0 and 18.63 au, (ii) a rather tightly packed system of seven planets, called “7PC model”, within the same orbital boundaries as model 3P, and (iii) a wider system of seven planets, called “7PW model”, in which the five innermost planets are placed in the same orbital range as in the previous two cases, with two additional planets on wider orbits (the outermost planet has  $a = 56.87$  au, resulting from the fixed number of mutual Hill radii).

The orbital configurations of the three models and the number of mutual Hill radii used for the orbital spacing are listed in Table 4.1 and Table 4.2, respectively. In all three models the planetary orbits are initially circular ( $e = 0$ ) and coplanar ( $i = 0^\circ$ ). Furthermore, all systems are long-term stable if they are placed in isolation. The argument that the planetary systems should be stable in isolation over time was also decisive for outwardly increasing spacings between the planets, which we achieve by using mutual Hill radii instead of using similar orbital spacings according to the peas-in-a-pod theory (e.g. Millholland et al. 2017; Weiss et al. 2018) based on findings from the Kepler mission.

The inner boundary of 2.0 au is chosen as a minimum semimajor axis to account for the potential engulfment of the innermost planet due to the expansion of the host star during the giant branch phase. As a basis for the outer boundary in the first two cases, we take into account that core accretion during planet formation becomes inefficient at larger semimajor axes, although it is not impossible for super-Earths to form at wider orbits (see, for example, fig. D.3 in Schlecker et al. 2021) which is why we additionally consider the possibility of a more extended planetary system in the third scenario.

**Tab. 4.2.:** The number of mutual Hill radii  $R_{H,m}$  between the planets in each model.

Model	1.5 $M_{\odot}$	2.0 $M_{\odot}$	2.5 $M_{\odot}$
3P	62.6	68.9	74.2
7PC	22.7	25.0	26.9
7PW	33.6	37.0	39.8

## 4.3 Results and Discussion

### 4.3.1 Fraction of Surviving Planets

If the eccentricity of a planet is excited to more than  $e > 0.99$ , we assume that the planet is close to ejection and remove it from the simulation. These ejected planets would, depending on their escape velocity, either continue to move through the cluster as free-floating planets, which may even allow re-capture by other cluster members, or they would directly escape not only the gravitational field of the host star, but also that of the star cluster.

For technical reasons, we do not trace the motion of the planets through the cluster after their ejection from a planetary system. However, the fraction of ejected planets  $f_{ej}$  gives an estimate for the expected number of free-floating planets in open clusters with similar properties to the one we simulated. The fraction of surviving planets  $f_{surv} = 1 - f_{ej}$  is plotted in Fig. 4.2 for all three planetary models as a function of simulation time. The model with the highest  $\bar{f}_{surv}$  (dotted black line in Fig. 4.2), averaged over all planets in the system, is the 3P model with a value of 0.76. The 7PC model shows little difference with  $\bar{f}_{surv} = 0.74$ , indicating that despite the higher planet density in this system compared to the 3P model, which in principle leads to more planet-planet interaction and to higher ejection rates, the orbit width of the outer planets is the more important factor for the averaged survival fraction. Consequently, the planets in the 7PW model have on average the lowest survival probability with a value of  $\bar{f}_{surv} = 0.71$ . The fraction of escapers that arise in our simulations are slightly higher than e.g. in [van Elteren et al. \(2019\)](#), who obtained  $\bar{f}_{ej} \approx 0.14$ . However, the difference can be explained by the significantly shorter simulation time and the considerably smaller number of stars in the host star cluster in [van Elteren et al. \(2019\)](#).

However, when considering the survival probability for the individual planets, the exact configuration of the planetary system, especially its multiplicity and consequently its compactness, does play a role. While in the 3P model the planet's probability for being ejected correlates with its initial semimajor axis, this is not consistent with the 7PC and 7PW models, as can be seen in Fig. 4.2.

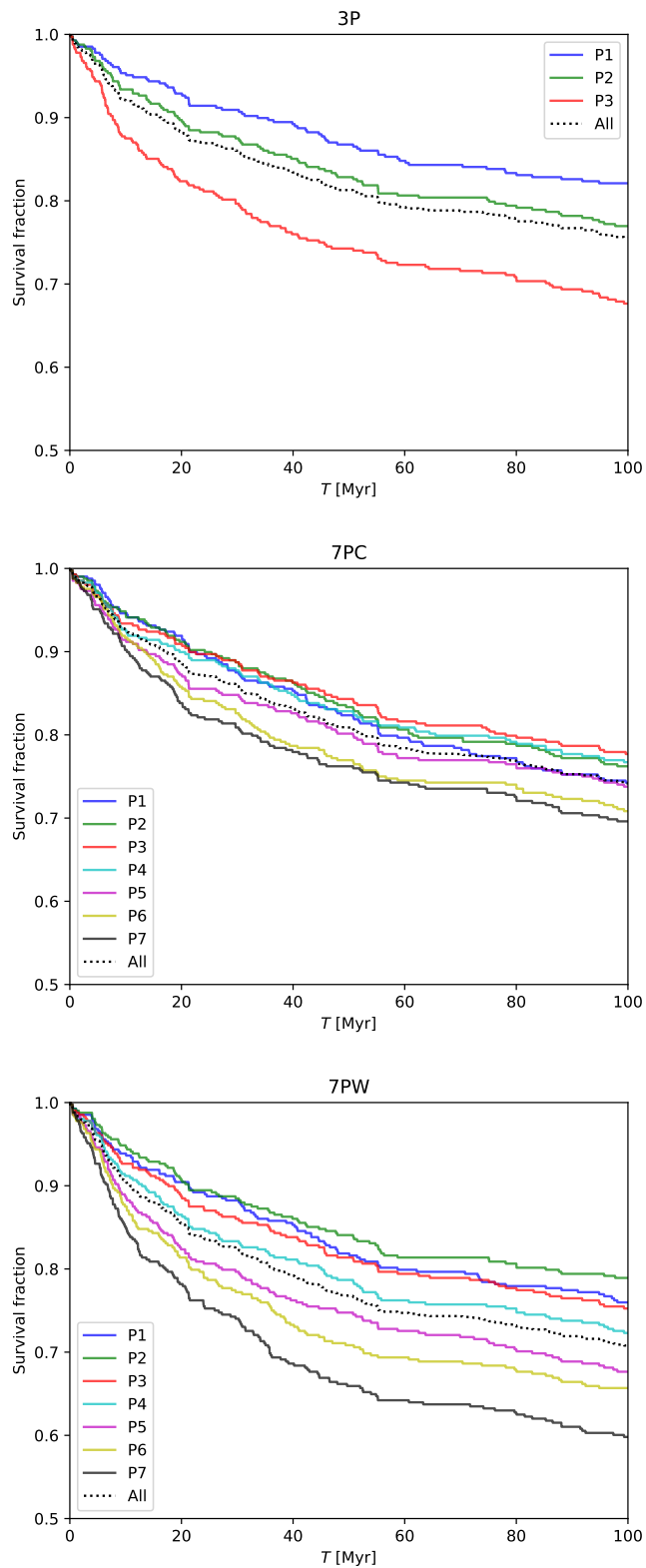


**Fig. 4.2.:** Fractions of surviving planets for the 3P, 7PC, and 7PW model. The dotted black line represents the average survival fraction for each model.

The planet with the highest survival fraction in the 7PC model is P3 ( $f_{\text{surv}} = 0.78$ ), followed by P4 ( $f_{\text{surv}} = 0.77$ ), P2 ( $f_{\text{surv}} = 0.76$ ) and P1 ( $f_{\text{surv}} = 0.74$ ), so the survival rate increases slightly for the middle planets and only decreases from the fifth planet towards the outer planets P7 (which has  $f_{\text{surv}} = 0.70$ ). The spread in survivability for the 3P model is only slightly larger and ranges from  $f_{\text{surv}} = 0.68$  to  $f_{\text{surv}} = 0.82$ . The reason for the changed order in the survival fraction of the planets in the 7PC model is the higher planetary density at constant orbital expansion of the system. Due to increased interactions among the planets after an external gravitational perturbation, the inner planets can experience delayed ejection from the system indirectly as a result of an earlier flyby of a neighbouring star. These delayed ejections have also been observed in [van Elteren et al. \(2019\)](#) and [Stock et al. \(2020\)](#).

As expected, for a system with wider orbits but the same number of planets, as in the 7PW model, the spread in the individual planet's survival rate is larger than for the more compact case. Here the values are between  $f_{\text{surv}} = 0.60$  (P7) and  $f_{\text{surv}} = 0.79$  (P2). As in the 7PC model, the second innermost planet in the 7PW model has a slightly larger survival fraction than the innermost planet P1 ( $f_{\text{surv}} = 0.76$ ), but here the planets' survival probability decreases beyond the second planet as expected with increasing initial semimajor axes.

### 4.3.2 Semimajor Axis and Eccentricity Distribution and Possible Engulfment during Red Giant Phase

The fraction of planetary systems whose dynamical evolution is considerably perturbed by passing stars (directly or indirectly by delayed planet-planet scattering) depends on the one hand on the planetary model used, but also on the host star mass. For the 3P model and a host star mass of  $1.5 M_{\odot}$ , we generally observe the lowest effect of the stellar environment on the dynamical evolution of the individual planets. In this scenario, 83% of the planets remain largely unperturbed. As a criterion for a considerable perturbation, we look at whether the semimajor axis deviates by more than 5% from the initial value by the end of the simulation, or whether the eccentricity increases to more than 0.1. The fraction of planets that are significantly perturbed in their dynamics increases for the models with more planets per star, the orbital separation of the outermost planet, and the host star mass. For the 7PW model and a host star mass of  $2.5 M_{\odot}$ , the fraction of perturbed planets increases from 17% to 29%. The distribution in  $a$ - $e$  space is wide for those planets that were considerably perturbed, as we demonstrate in [Fig. 4.3](#), and comparable to results from previous studies (see e.g. [fig. 10 in Malmberg et al. 2011](#)). We observe inward migration for the perturbed planets in a few cases, but outward migration in the vast majority of cases. Almost 1% of all planets have wide orbits of more than 100 au at the end of the simulation

Model	$a > 100$ au	$a > 1000$ au	$e > 0.5$	$i \geq 90^\circ$
3P	0.49	0.00	6.54	1.72
7PC	0.49	0.04	6.1	1.09
7PW	1.58	0.0	6.27	1.47
1.5 $M_\odot$	0.67	0.00	4.94	1.31
2.0 $M_\odot$	0.98	0.00	6.24	1.29
2.5 $M_\odot$	1.40	0.06	8.68	1.51

**Tab. 4.3.:** Fraction of planets (in per cent) with wide ( $a > 100$  au), very wide ( $a > 1000$  au), very eccentric ( $e > 0.5$ ) or retrograde ( $i \geq 90^\circ$ ) orbits for the different planetary models (independent of the host star mass) and for the different host star masses (independent of the planetary system model used).

and one planet out of a total of 6936 planets is even scattered to an orbit of more than 1000 au. More than 6% of all planets are excited to high eccentricities ( $e > 0.5$ ). The fractions vary depending on the planetary system model and host star mass and are listed in Table 4.3 for all the different scenarios.

For the question of whether the planetary system model used or the mass of the host star (and thus the stellar density in the vicinity of a planetary system) has a stronger influence on the formation of high eccentricities, we plot in Fig. 4.4 the cumulative distribution of eccentricities after 100 Myr. We distinguish between the three planetary system models (independent of the host-star mass) and the host-star mass (independent of the used planetary system model). For those systems that orbit a 2.5  $M_\odot$  host star, it can be clearly seen that the host star mass, and thus the position in the cluster, which in turn is related to the stellar density in the vicinity, plays a more important role in exciting planets to high eccentricities than the exact orbital configuration and multiplicity of the planetary system.

Many studies have investigated the critical engulfment distance during the giant branch phases at different levels of detail and with different underlying theories (Mustill & Villaver 2012; Adams & Bloch 2013; Nordhaus & Spiegel 2013; Villaver et al. 2014; Madappatt et al. 2016; Privitera et al. 2016; Ronco et al. 2020). We use the critical engulfment distances along the asymptotic giant branch phases for Earth-mass planets from figs. 2–4 in Mustill & Villaver (2012) and calculate for how many planets the periastron distance ( $r_p = (1 - e)a$ ) would be below this limit. For the planets around a 1.5  $M_\odot$  star, the critical distance is about 1.9 au. About 5% of our planets around such a star would be engulfed during the giant branch phases. The critical distance for 2.0 and 2.5  $M_\odot$  stars is 2.2 and 2.3 au, respectively. In these cases, 16% and 15% of the planets would be engulfed, respectively. Although the possibility of being engulfed by the host star mainly affects the innermost planet P1, it is not exclusive, since an external perturbation combined with internal

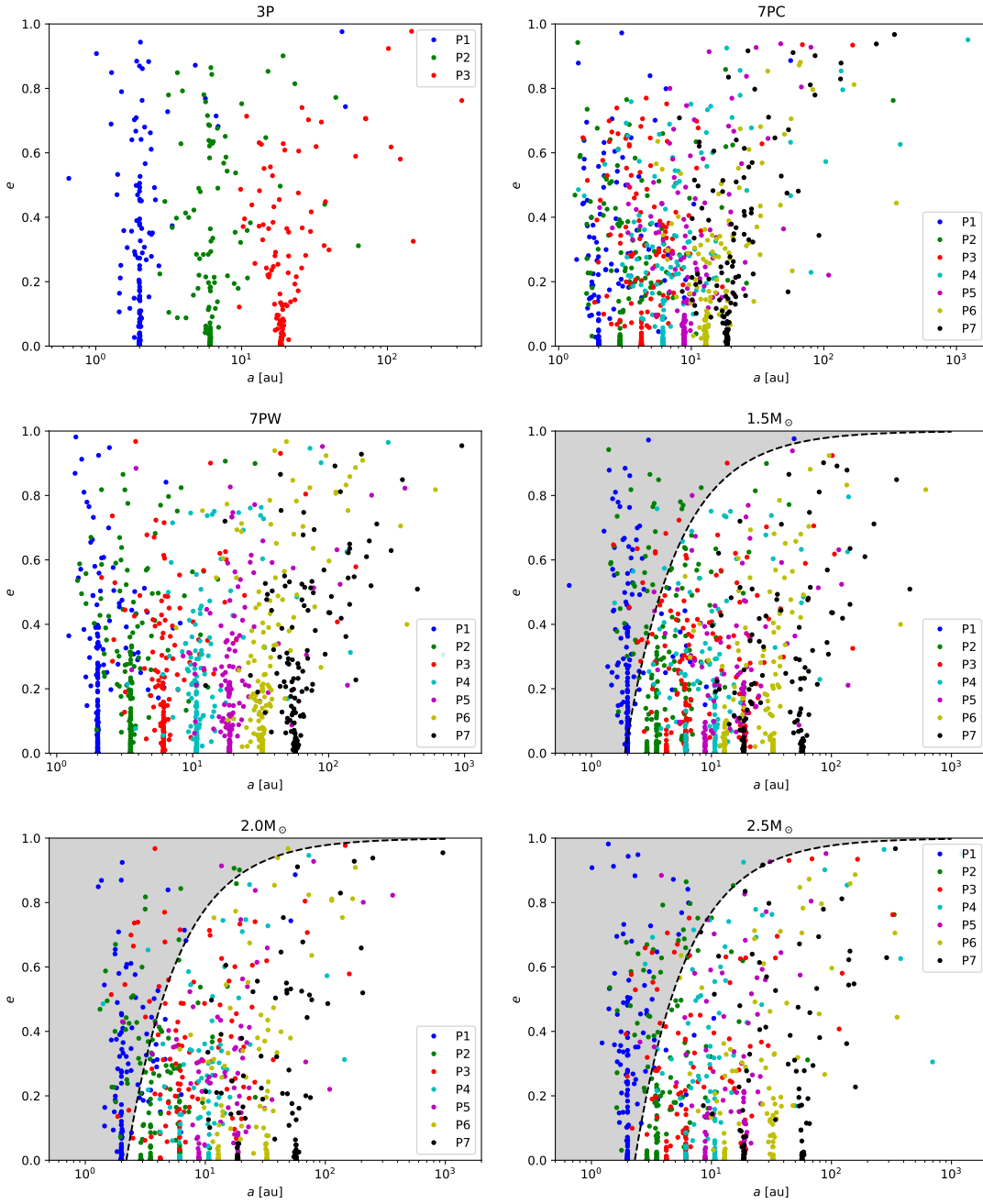


**Fig. 4.3.:** The  $a$ - $e$  space for the 3P, 7PC and 7PW model as well as for the different host star masses. The grey shaded area shows which planets would be engulfed by the star during the red giant phase.

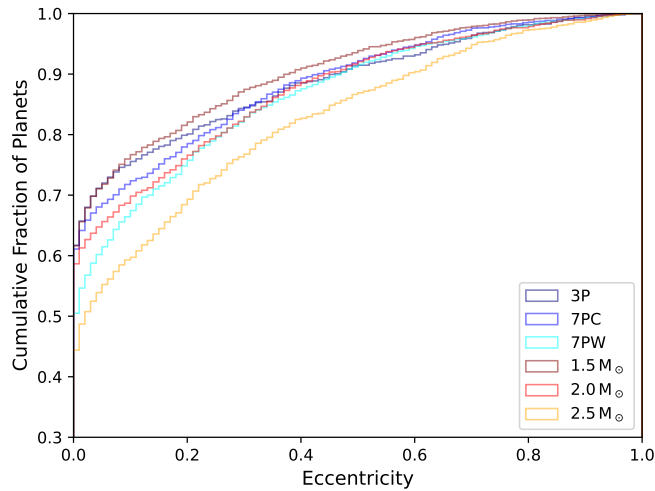


**Fig. 4.4.:** Cumulative, normalized histogram showing the distribution of eccentricities sorted by planetary model (bluish colors) and host star mass (reddish colors). The bin size is 0.02.

planet-planet scattering can cause even the initially outermost planet to migrate to a small or highly eccentric orbit, causing its periastron distance to fall below the critical value. This can be seen in the bottom panels of Fig. 4.3, where we additionally plot the critical engulfment distance for each host-star mass.

### 4.3.3 Inclination and Retrograde Orbits

The first exoplanets thought to have a polar or retrograde orbit ( $i \geq 90^\circ$ ) were HAT-P-7 b (Winn et al. 2009) and WASP-17 b (Anderson et al. 2010; Bayliss et al. 2010). Since the number of confirmed retrograde planetary orbits is still small, the statistical abundance of these peculiar orbits is still uncertain. In addition to the expected clustering of prograde orbits, Albrecht et al. (2021) recently found a further clustering of polar orbits in a sample of 57 systems rather than a scattering over the entire range of possible obliquities. Since all planets in our simulations are initially coplanar, most planetary orbits are still only slightly inclined at the end of the simulations.

The distribution of planetary orbits in the  $a$ - $i$  space for all three planetary system models at the end of the simulation is shown in Fig. 4.5.

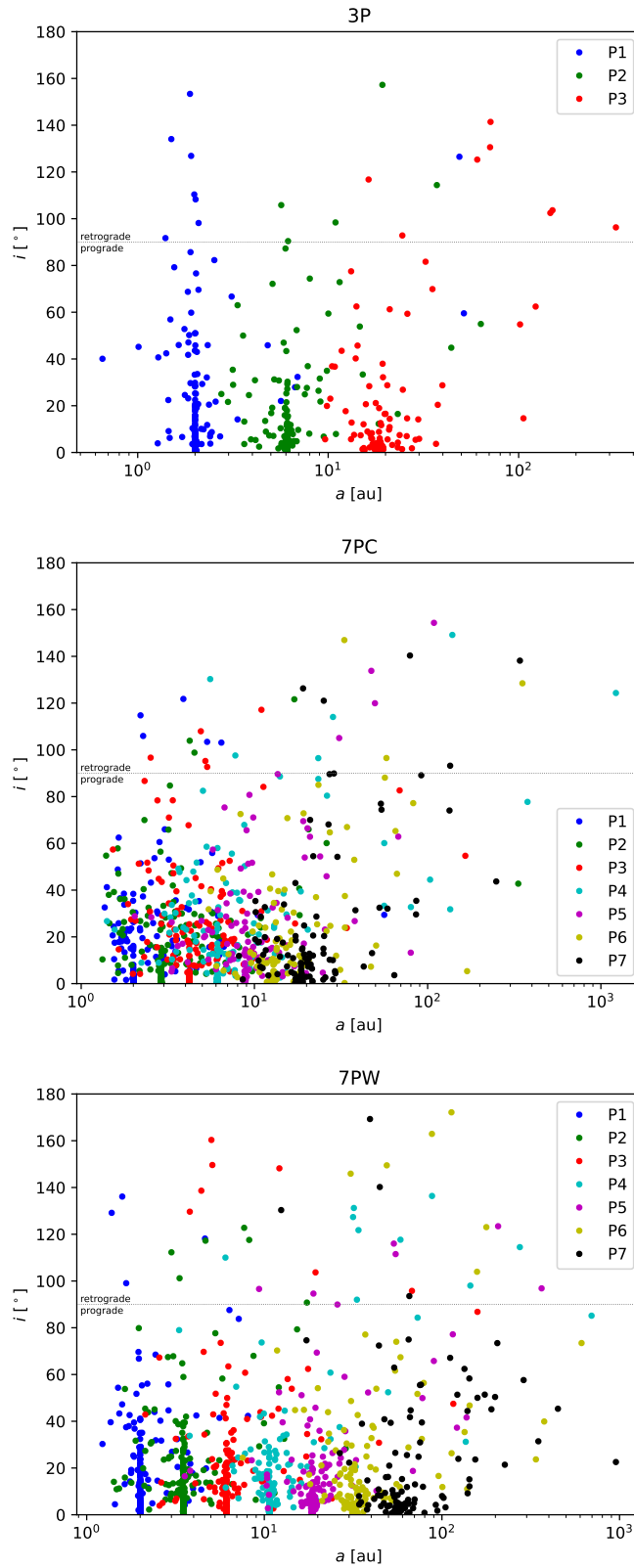


**Fig. 4.5.:** The  $a$ - $i$  space for the 3P, 7PC, and 7PW model. Planets above the dotted grey line are on a retrograde orbit.

The averaged fraction of planets with a retrograde motion at the end of the simulation is 1.4%, with values ranging from 0.5–2.2% for the different system models (the fraction of retrograde orbits for each scenario used in this work are listed in Table 4.3). This is somewhat higher but still in good agreement with the values in [Stock et al. \(2020\)](#), where we used variations of the Solar System around Sun-like host stars and found, depending on the initial planet configuration and the star cluster size, 0.1–1.6% of all planets to be on a retrograde orbit after the same simulation time of 100 Myr. The subtle differences can be explained by the higher multiplicity in the 7PC and 7PW models as well as by the generally larger host star masses used in this study. This agreement, and the circumstance that we cover a wide range of possible planetary systems in this work and in [Stock et al. \(2020\)](#), leads us to the rough estimate that in open star clusters similar to the one simulated in this work and those simulated in [Stock et al. \(2020\)](#), about 1–2% of all planets could be on stable retrograde orbits.

The number of planets that flip to a retrograde orbit for at least one integration step at some time during the simulation is significantly larger and gives an indication that unstable retrograde orbits are not uncommon in environments with frequent external gravitational perturbation. “Unstable retrograde orbit” in this context means that the planet does not remain permanently on a retrograde orbit, either because it changes back to a prograde orbit or because it is ejected from the planetary system at a later time. In 33% of all systems we find at least one planet which flips to a retrograde orbit for at least one (stored) time step of 1 000 years during the simulation. This fraction of systems is generally lowest for the 3P model and 1.5  $M_{\odot}$  stars, and highest for the 7PW model and 2.5  $M_{\odot}$  stars.

Since inclined orbits, just like eccentric orbits, from through angular momentum exchange, and close stellar encounters are particularly good at introducing an angular-momentum deficit into the planetary system, it is especially the systems around 2.5  $M_{\odot}$  stars which have inclined orbits, as can be seen in Fig. 4.6. Again, the mass of the host star and thus the frequency and strength of the encounters with other cluster members is more important than the exact planetary configuration for the formation of inclined planetary orbits.

#### 4.3.4 Mean-Motion Resonances

Resonances in planetary systems can be a source for WD pollution, because the orbits of asteroids can increase in eccentricity due to planets near a secular or mean-motion resonance (MMR) ([Debes et al. 2012](#); [Smallwood et al. 2018, 2021](#); [Antoniadou & Veras 2019](#); [Veras et al. 2021](#)). Finding MMRs in simulations is very challenging in view of the large number of

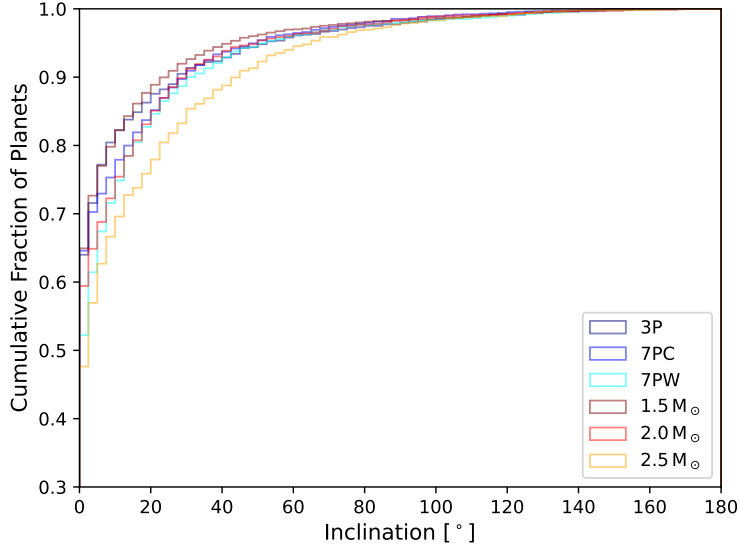


**Fig. 4.6.:** Cumulative, normalized histogram showing the distribution of inclinations sorted by planetary model (bluish colors) and host star mass (reddish colors). The bin size is  $2.5^\circ$ .

simulated planetary systems, the long integration time, but especially because of the often chaotic dynamical evolutions of the planetary systems due to the steady external perturbation from the cluster. This type of dynamical evolution can lead to transitory resonances which may endure over just a handful of output time steps, or even within two consecutive outputs of the simulations.

We use the FAIR method of [Forgács-Dajka et al. \(2018\)](#) which allows the fast identification of MMRs between planets without any prior knowledge about the MMR to be searched. The method is based on plotting the difference of the mean orbital longitudes for two planets ( $\lambda' - \lambda$ , if  $a < a'$ ) against the mean anomaly  $M$  of the inner planet. The mean longitude is defined as  $\lambda = M + \varpi = M + \omega + \Omega$ , where  $\varpi$  is the longitude of the periastron and  $\omega$  the argument of periastron. When the planets have a mean-motion ratio of  $n/n' = (p + q)/p$  throughout the period under consideration, there will be  $q$  centres on the x-axis and  $p + q$  centres on the y-axis, which in turn means that only the number of crossings of the stripes present in the plot with the horizontal and vertical axes must be counted to obtain  $q$  and  $p + q$ , respectively. Subsequently, the necessary criteria for the presence of an MMR, the period ratios and the libration of the resonance variables

$$\theta_1 = (p + q)\lambda' - p\lambda - q\varpi, \quad (4.1)$$

$$\theta_2 = (p + q)\lambda' - p\lambda - q\varpi', \quad (4.2)$$

around a mean value, need to be tested. This value is not necessarily always  $0^\circ$  or  $180^\circ$ .

In principle, we find MMR in our simulations at arbitrary times (except at the beginning), but they only rarely survive for longer times (i.e. several million years) due to the constant gravitational perturbation of the neighbouring stars. Only with increasing simulation duration and the expansion of the host star cluster, when the frequency and strength of the encounters with neighbouring stars decrease, can the planets actually remain in MMR for several million years. In particular, we therefore investigate how many and which MMRs are found in the last 1 million years of our simulations that are stable until the end of the simulation at  $t = 100$  Myr, since these can also persist once the cluster has completely dissolved. If we consider only planetary pairs that were direct neighbours at the beginning of the simulation, we find six planetary pairs that are in stable MMR at the end of the simulation and list them in Table 4.4.

For the 2:1 MMR in system 122 from the 7PC model with a  $1.5 M_\odot$ , we show the FAIR plot for the time range  $t = 99$ – $100$  Myr in Fig. 4.7 and, in addition, also plot the orbital elements as well as the resonance angle of the 2:1 MMR as a function of the total simulation time in Fig. 4.8. This makes it possible to see whether a system was excited into this resonance by chance only at the end of the simulation or whether the planets were already close to resonance for a long time.

As can be seen in Fig. 4.8, planets 6 and 7 both migrate outwards to eccentric crossing orbits with  $a \sim 23$ – $24$  au as a result of a close encounter ( $r_p < 231$  au) at  $t = 8.4$  Myr with a  $0.2 M_\odot$  star. After another encounter at time  $t = 11.8$  Myr, both planets are thrown to orbits of  $a = 66$  au and  $a = 91$  au, and thus happen to be near 2:1 MMR. Due to several further, but weak perturbations, they first enter 2:1 MMR at  $t = 54.2$  Myr, which does not completely resolve until  $t = 66.2$  Myr (however, the libration amplitude is very large in the interim). Due to subsequent weak perturbations, the planets re-enter 2:1 MMR at  $t = 80$  Myr. The angle around which the resonance angle librates changes during the remaining simulation time, but in principle the planets remain in 2:1 MMR until the end of the simulation. That both planets are in stable resonance over the last one million years can be seen in Fig. 4.7.

Planet-planet scattering as a cause of MMRs is often disregarded. Yet they can be particularly responsible for the higher-order resonances (Raymond et al. 2008), as these cannot arise so easily through migration (Papaloizou & Szuszkiewicz 2005; Tadeu dos Santos et al. 2015; Xu et al. 2018). In our simulations, however, star-planet interactions seem to be more important than planet-planet interactions. In addition to four first-order resonances, we find a third-order resonance and a seventh-order resonance, and plot the resonances (Figs. C.1, C.3, C.5, C.7, C.9 in

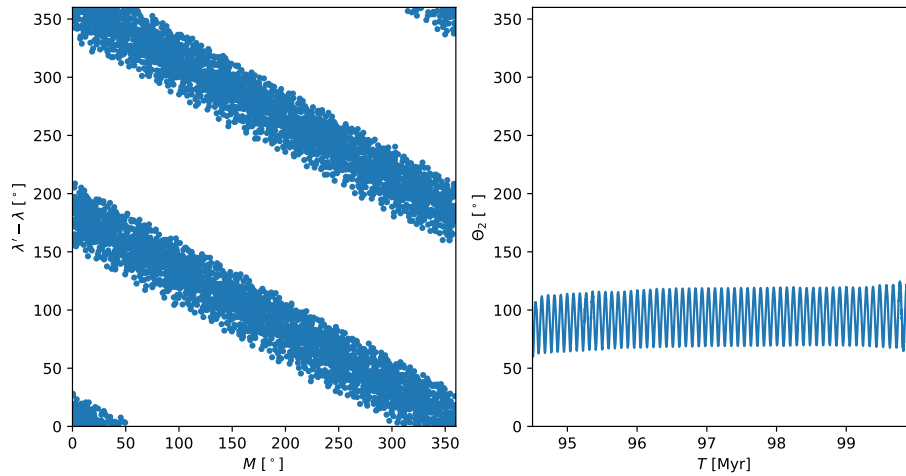


**Fig. 4.7.:** 2:1 MMR in planetary system 122 (7PC model,  $1.5 M_{\odot}$  host star) between planet 6 and 7 for  $t = 94.5\text{--}100$  Myr.

the appendix) and the overall dynamical evolution of the systems including perturber information (Figs. C.2, C.4, C.6, C.8, C.10 in the appendix) for each of these systems. However, some librating resonance angles show a long-term trend that cannot be resolved in time. Whether the systems are in actual — and stable — resonance cannot be said with certainty in these cases. In all systems, one or several encounters with neighbouring stars lead to a migration of the planetary pairs near a certain MMR. Further weaker stellar perturbations, usually millions of years later, drive the planetary pair into actual resonance. Only in the case of system 192 from the 7PW model around a  $2.5 M_{\odot}$  star (see Fig. C.10 in the appendix) a resonance is created directly by the first strong stellar perturbation, but this resonance is repeatedly perturbed by stellar neighbours at later times without breaking it completely.

Our results are only partially comparable to Raymond et al. (2008), since the instability in our simulations has an external rather than an internal origin. In most cases, the external perturbation completely outweighs internal effects. In cases where planet-planet scattering may play an additional role in the origin of the resonance, the effects of external and internal perturbation cannot be separated clearly enough. However, our simulations confirm that most of the resonances that arise are low-order and that higher-order resonances can also arise in a few cases. Furthermore, an important difference from the simulations in Raymond et al. (2008) is the mass distribution within the planetary system. While we exclusively simulate planets of equal masses, Raymond et al. (2008) also use mixed systems, in which the interplay of large and small planet plays an important role in the formation of resonances due to planet-planet scattering.

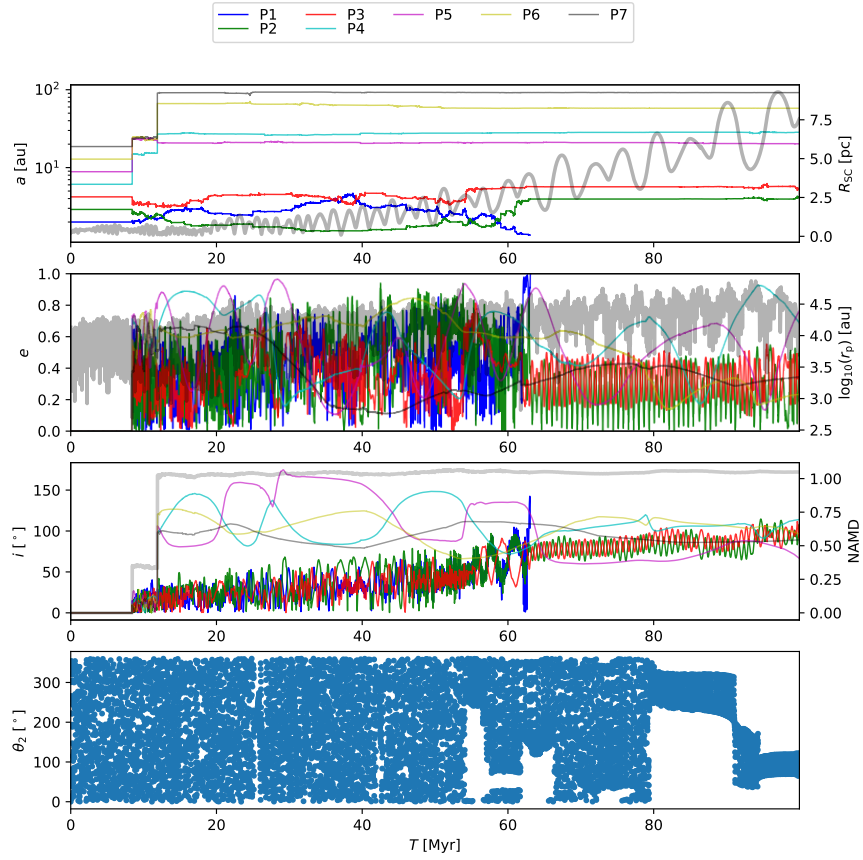


**Fig. 4.8.:** Orbital elements  $a$ ,  $e$  and  $i$  for planetary system 122 (7PC model,  $1.5 M_{\odot}$  host star) and the resonance angle  $\theta_2$  with  $p = q = 1$  (for planet 6 and 7) as a function of the simulation time. The thicker grey lines in the background represent the distance to the cluster centre (top panel), the distance to the closest stellar perturber (top middle panel) and the normalized angular momentum deficit (bottom middle panel), defined as  $\text{NAMD} = \text{AMD} / (\sum_k m_k \sqrt{G m_{\star} a_k})$  (see [Turrini et al. 2020](#), and references therein).

Host Star	Model	System ID	Planet Pair	MMR	$t$ [Myr]
$1.5 M_{\odot}$	3P	177	2/3	10:3	97.0–100
$1.5 M_{\odot}$	7PC	122	6/7	2:1	95.0–100
$2.0 M_{\odot}$	7PW	22	5/6	3:2	99.0–100
$2.0 M_{\odot}$	7PW	45	5/6	3:2	90.0–100
$2.5 M_{\odot}$	7PW	38	4/5	5:2	97.0–100
$2.5 M_{\odot}$	7PW	192	3/4	4:3	98.5–100

**Tab. 4.4.:** Stable MMRs after the end of the simulation.

### 4.3.5 Long-term Stability

The focus of this investigation is to perform stellar cluster simulations including multiplanetary systems, and to present the results as initial conditions which may be used for the simulation community. Nevertheless, we can make some preliminary rapid judgements about the stability of these systems along the main sequence by taking advantage of machine learning.

In order to estimate the long-term stability of each planetary system (with the host star mass remaining constant), we perform a SPOCK test (Tamayo et al. 2020a) for each system. SPOCK is able to predict the long-term stability of compact multiplanetary systems by using the statistics from machine learning training datasets in a fraction of the time compared to actual integration (see Tamayo et al. 2020a, for a detailed description of the training and the model). Since SPOCK requires at least three planets in the system, for those systems where planets have been ejected, we replace the missing planets with massless particles at wide orbits ( $> 100$  au) before performing the SPOCK test. We give the likelihood for the long-term stability of our planetary systems as additional feature in our result tables (see the online version of Stock et al. 2022, or the extracts in Tables C.1 and C.2 in the appendix) for the different planet system models.

## 4.4 Conclusions

We have presented the results from a total of 1224 simulations of planetary systems embedded in a cluster environment, differing in the planetary system model used and in the mass of the host star. We have aimed to publish a comprehensive dataset that contains those planetary systems typically responsible for WD pollutions which, at the same time, have the dynamical imprint of a typical birth star cluster. This data set can now be used for further numerical integration beyond the main sequence to the WD phase.

The three different planetary system models should represent the extreme cases of possible planetary systems regarding their multiplicity and orbital spacing. For this reason we simulate one model with only three planets (3P model), and two models with seven planets each in the system, which differ in their compactness (7PC and 7PW model). As host stars we have chosen those stars from our 8 000 star cluster which are most similar to the masses of  $1.5 M_{\odot}$ ,  $2.0 M_{\odot}$  and  $2.5 M_{\odot}$ . All planetary systems are integrated to  $t = 100$  Myr. By that time the star cluster has expanded considerably and perturbations from neighbouring stars are very rare.

In our simulations, it was not only the number of planets or the compactness of the system that played a role in the average survival rate, but above all the semimajor axes of the outermost planets. The 3P model has an average survival fraction of 76%, the 7PC model has 74% and the 7PW model, with the widest orbits, has only 71%. While the innermost planet has the highest survival probability in the 3P model, it is the third planet in the 7PC model and the second innermost planet in the 7PW model. The spread in survivability has been particularly small in the 7PC model, which is why we conclude that the compactness of the system and thus enhanced internal effects such as planet-planet scattering almost equalizes the planets' probability to survive the star cluster phase.

Given our initial conditions, we found that about 5% of planets around  $1.5 M_{\odot}$  stars, roughly 16% of the planets around  $2.0 M_{\odot}$ , and approximately 15% of the planets around  $2.5 M_{\odot}$  stars would be swallowed by the eventual asymptotic giant branch star's envelope because the planets' periastron distances would be below the critical engulfment distance.

The excitation in eccentricity and inclination correlates with the number of planets in the system and the initial semimajor axis of the outermost planet. In particular it also correlates with the stellar density in the vicinity of the host star, which tends to be larger for higher mass stars due to the effect of mass segregation. On average, 1.4% of all planets are on a retrograde orbit at the end of the simulation, which is, due to the higher host star masses and the higher multiplicity in the 7PC and 7PW model, somewhat higher but still in good agreement with the results from [Stock et al. \(2020\)](#).

Eccentric planets in the super-Earth/mini-Neptune mass regime are thought to be particularly efficient drivers for WD pollution over a wide range of cooling ages ([Frewen & Hansen 2014](#); [Mustill et al. 2018](#)). 30% of the planets in our simulations attained an eccentricity of  $e > 0.1$  and 25% have  $e > 0.17$  after 100 Myr, showing that the birth environment of planetary systems can produce a sufficient distribution in eccentricity to help generate the architectures suitable for dynamical delivery of pollutants to WDs. Even if subsequent increases in eccentricity due to mutual perturbations and along the giant branch phases due to stellar mass loss are negligible ([Veras et al. 2011](#)), the planets' primordial eccentricities will persist into the WD phase.

Furthermore, we find planetary pairs in several planetary systems that are in resonance at the end of the simulation. These systems may also play a role in WD pollution, since asteroids near these resonances may be driven to eccentric orbits and subsequently be tidally disrupted by the WD ([Smallwood et al. 2018, 2021](#)).

# The Effect of Stellar Encounters in Star Clusters on the Formation of Hot Jupiters

” *I could not believe it, I thought there was something not working in the software. I tried to calculate an orbit but knowing nothing, it gave me what I believed being a wacky result.*

— **Didier Queloz**

(one of the discoverer of 51 Peg b)

## 5.1 Hot Jupiters

Of the first exoplanets discovered, such as 51 Peg b (Mayor & Queloz 1995), Upsilon Andromedae b (Butler et al. 1997) and HD 187123 b (Butler et al. 1998), many had very short orbital periods of only a few days and very large (minimum) masses. This finding was surprising and challenged the prevailing planet formation model at that time, which was mainly based on properties and observations of planets in the Solar system. Such gas planets, which are similar in size to Jupiter but have orbital periods of less than 10 days and correspondingly very high surface temperatures, are referred to as *hot Jupiters* (e.g. Wang et al. 2015a; Dawson & Johnson 2018). The reason for the high discovery rate of hot Jupiters was partly due to the observation methods used (such as the radial velocity method, which was predominant in the beginning), which made it particularly likely to detect massive planets in a close orbit around the central star. Today, the occurrence rate of hot Jupiters around Sun-like stars is estimated to be about 1% — around lower-mass stars, the rate is estimated to be much lower (see e.g. Dawson & Johnson 2018, and references therein).

## 5.2 Formation Scenarios for Hot Jupiters

To date, it has not been conclusively clarified how hot Jupiters are formed. The standard planet formation model (see Sec. 1.1.1) predicts that gas giant planets preferentially form beyond the ice line because only there can they accrete sufficient material for their growth on short timescales before the protoplanetary disc dissolves. In contrast to this is the first formation scenario for hot Jupiters, the *in situ* formation. In this scenario, hot Jupiters already form on a very close orbit around the star. Neither the classical core accretion theory from Sec. 1.1.1 nor other theories, such as the disc instability theory, in which parts of the protoplanetary disc fragment into clumps due to gravitational instabilities (e.g. Boss 1997), can sufficiently explain the *in situ* formation scenario (Rafikov 2005, 2006).

Two other scenarios are based on *ex situ* formation, i.e. formation at a larger distance from the star, and subsequent migration of the planet to a short-period orbit. Two mechanisms can in principle be considered as the origin of such migration. The first mechanism is *gas disc migration*, in which the gas giant migrates to a short-period orbit due to torques from the gaseous protoplanetary disc (see e.g. Baruteau et al. 2014, and references therein). This would need to take place during the relatively short protoplanetary disc phase. An alternative explanation to gas-disc migration is *high-eccentricity tidal migration* after the dispersal of the protoplanetary disc (see e.g. Hamers et al. 2017; Hamers & Tremaine 2017, and references therein). In this scenario, angular momentum is transferred from the planet to a perturber, resulting in the planet moving to a highly eccentric orbit with a periastron distance small enough for tidal forces to circularise the planet's orbit.

The high-eccentricity tidal migration scenario due to external stellar perturbation is investigated in the following by simulating multiplanetary systems in star clusters, taking into account tidal star-planet interaction.

## 5.3 The Angular Momentum Deficit

From Eqs. 1.16 and 1.37 we know that the angular momentum, written in Jacobi coordinates, is:

$$L = \mu \sqrt{a(1 - e^2)GM}. \quad (5.1)$$

Through a transformation to Cartesian coordinates (see Sec. 1.2 for the difference between Cartesian and Jacobi coordinates) and assuming a circular orbit, the following expression is

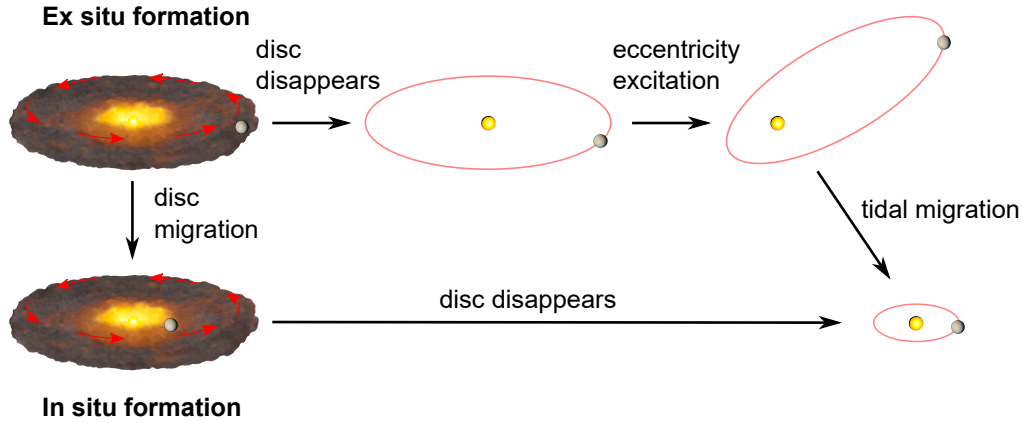


**Fig. 5.1.:** Formation scenarios for hot Jupiters: in situ formation, disc migration and tidal migration.

obtained for the angular momentum of a planet  $k$  with mass  $m_k$  on a circular and coplanar orbit around a central star with mass  $M_\star$ , which is referred to in the following as circular angular momentum (CAM):

$$\text{CAM}_k = m_k \sqrt{a_k GM_\star}. \quad (5.2)$$

This is the maximum angular momentum value for that value of semimajor axis that a planet can acquire. Deviations from a circular or coplanar orbit (i.e. by an increase in eccentricity,  $e$ , or inclination,  $i$ ) reduce the angular momentum by the factors  $\sqrt{1 - e^2}$  and  $\cos(i)$  respectively. In order to describe the deviation from an ideal orbit (in the sense of circular and coplanar) and thus to be able to investigate the stability of the Solar system and later exoplanetary orbits, [Laskar \(1997, 2000\)](#) and [Laskar & Petit \(2017\)](#) introduced the so-called *angular momentum deficit* (AMD), which is defined for an individual planet  $k$  as

$$\text{AMD}_k = m_k \sqrt{a_k GM_\star} \left( 1 - \sqrt{1 - e_k^2} \cos i_k \right). \quad (5.3)$$

The total AMD of a multiplanetary system with multiplicity  $N$  is obtained by the sum of the individual angular momentum deficits over all  $N$  planets ([Laskar 1997, 2000](#); [Laskar & Petit 2017](#)):

$$\text{AMD} = \sum_{k=1}^N \text{AMD}_k = \sum_{k=1}^N m_k \sqrt{a_k GM_\star} \left( 1 - \sqrt{1 - e_k^2} \cos i_k \right). \quad (5.4)$$

A major disadvantage of this quantity is that the total AMDs of planetary systems, which differ considerably in their architecture, cannot be compared among each other. To solve this problem,

Chambers (2001) introduced the normalised angular momentum deficit (NAMD), for which we follow the notation from Turrini et al. (2020), and which is defined as

$$\text{NAMD} = \frac{\text{AMD}}{\text{CAM}} = \frac{\sum_{k=1}^N m_k \sqrt{a_k} \left(1 - \sqrt{1 - e_k^2} \cos i_k\right)}{\sum_{k=1}^N m_k \sqrt{a_k}}. \quad (5.5)$$

In this chapter, the normalised angular momentum deficit will serve as a comparative parameter between different planetary system architectures in order to be able to work out a possible correlation of this parameter with the formation of hot Jupiters.

## 5.4 Modelling the Tidal Star-Planet Interaction

To model the tidal interaction between the central star and the planets and enable tidal orbital migration, the weak friction model as described in Hut (1981) is implemented in LPS using REBOUNDx (Tamayo et al. 2020b; Baronett et al. 2021), a library for adding perturbing conservative forces and dissipative effects to REBOUND simulations.

The weak friction model was first introduced by Darwin (1879) and later discussed in detail by Alexander (1973) and Hut (1981). It assumes that the bodies under consideration consist of a weakly viscous fluid (Bolmont et al. 2015, and references therein). Hut (1981) investigated the model using a binary system in which both stars cause tidal bulges on the surface of the other star through a gradient in the gravitational field. Due to dissipative processes within the perturbed body these tidal bulges are slightly misaligned with respect to the distance vector  $\vec{r}$ , which connects both bodies, resulting in a torque component in the gravitational attraction of the stars (Hut 1981; Heller et al. 2011). While the dissipative processes lead to a loss of orbital and rotational energy, angular momentum is exchanged due to the torque component (Hut 1981). Both effects lead to a change in the orbital parameters of the system (Hut 1981; Heller et al. 2011). The model of Hut (1981) uses a constant time lag,  $\tau$ , for the description of the slight misalignment between the tidal bulge and the distance vector  $\vec{r}$ , which is why the model is also referred to as *constant time lag model*.

According to eq. 8 from Hut (1981), the tidal perturbing force from a star with mass  $m_2$  on another star with mass  $m_1$  is then expressed by

$$\vec{F} = -G \frac{m_1 m_2}{r^2} \left[ \hat{r} + 3 \frac{m_2}{m_1} \left( \frac{R}{r} \right)^5 k_2 \left( \left( 1 + 3 \frac{\dot{r}}{r} \tau \right) \hat{r} - (\Omega - \dot{f}) \tau \hat{f} \right) \right], \quad (5.6)$$

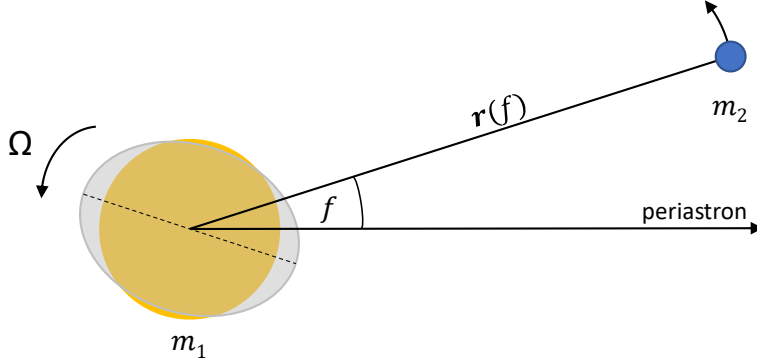


**Fig. 5.2.:** Tidal bulges on the primary, with mass  $m_1$ , caused by the companion, with mass  $m_2$ .

where  $R$  is the physical radius and  $\Omega$  the rotational angular frequency (i.e. the spin) of the perturbed star (with mass  $m_1$ ),  $\dot{f}$  (the time derivative of the true anomaly  $f$ ) is the instantaneous orbital angular velocity of the perturber (with mass  $m_2$ ) and  $\hat{r}$  as well as  $\hat{f}$  are unit vectors in the directions of  $r$  and  $f$ . The parameter  $k_2$  is the *potential Love number* (Love 1911) of degree 2 of the perturbed body, a quantity for the reaction of the body to the perturbing force which depends on the body's density profile. It is defined as

$$k_2 = \frac{3 - \eta(R)}{2 + \eta(R)}, \quad (5.7)$$

where  $\eta$  is a dimensionless parameter which is related to the density distribution of the body via a differential equation (see eq. 9 in Becker & Batygin 2013). It should be noted that this parameter is referred to as “apsidal motion constant”  $k$  in Hut (1981), which is misleading, as the *apsidal motion constant* is nowadays typically defined as  $k_1 = k_2/2$  (see also the short discussion in Baronett et al. 2021).

The mass of a tidal bulge on the primary is given by

$$m_{\text{bulge}} = \frac{1}{2} k_2 m_2 R^3 \sqrt[3]{r(t - \tau)}, \quad (5.8)$$

where  $r$  is the distance between both bodies at time  $t - \tau$  (Bolmont et al. 2015). The tidal bulge lags with respect to the position of the companion if  $\Omega$  is smaller than the orbital angular velocity  $n$  (see Eq. 1.35). In the opposite case (if  $\Omega > n$ ), the tidal bulge is leading compared to  $\vec{r}$  (Hut 1981). The first case ( $\Omega < n$ ) is depicted in Fig. 5.2.

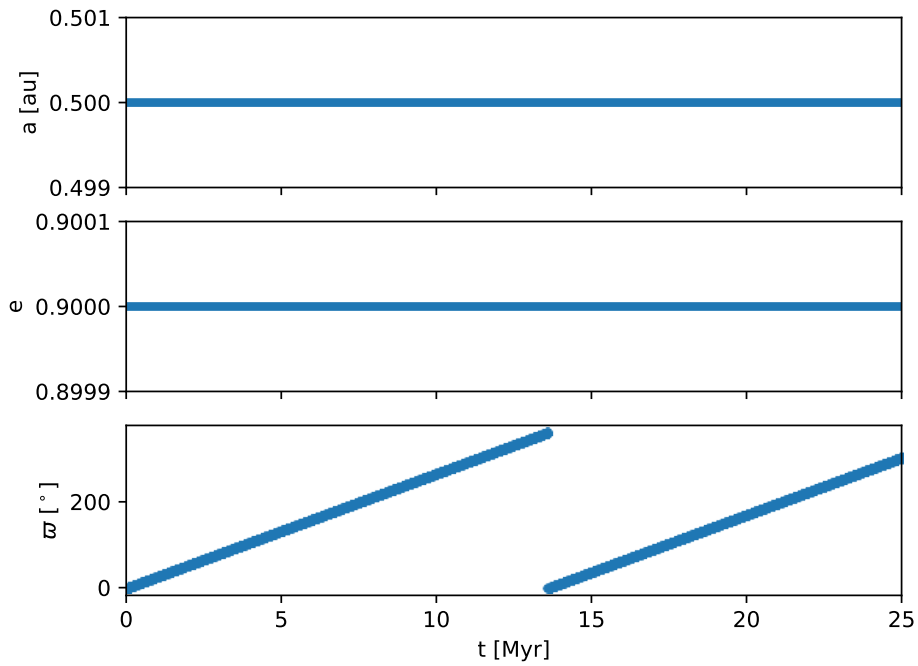
## 5.5 Initial Conditions

The constant time lag model of [Hut \(1981\)](#) can be applied to the simulation of planets around stars within its physical limits (see [Efroimsky & Makarov 2013](#), for a discussion) to model the tidal star-planet interaction. For this purpose, the additional tidal force components from Eq. 5.6 are implemented into LPS using REBOUNDx. [Baronett et al. \(2021\)](#) demonstrate the application of the constant time lag model for a star-planet system using Earth’s physical and orbital parameter around a non-rotating red giant (which is assumed to have a Sun-like main-sequence progenitor star). Due to the large physical extension of the star, the tidal effects and thus the influence on the orbital parameters of the planet are accordingly large (as can be seen in fig. 3 in [Baronett et al. 2021](#)). However, since hot Jupiters are also found around main-sequence stars, this chapter aims to investigate whether the star cluster environment can facilitate the high-eccentricity tidal migration of giant planets onto short-period orbits around Sun-like host stars.

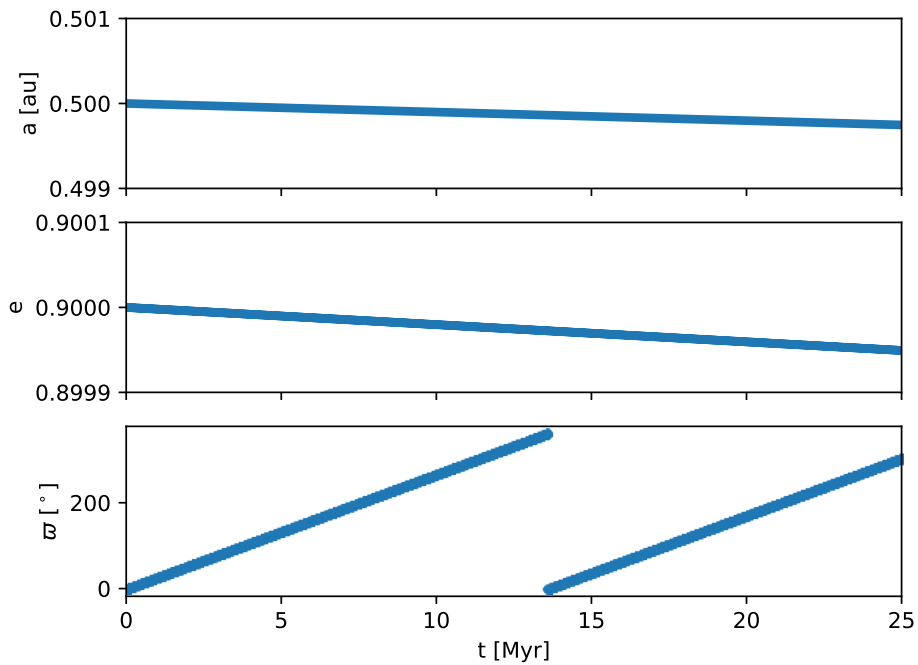
### 5.5.1 Test Runs of Short-Period Planets in Isolation

In order to see whether the implemented tidal effect works and whether the selected parameters are suitable, a short test simulation is carried out below. For this, a planet with Jovian mass is placed on a highly eccentric orbit ( $e = 0.9$ ) with a small semimajor axis ( $a = 0.5$  au) around a Solar-mass star and integrated for 25 million years. The radii used for the star and the planet are the Solar and Jovian radius. The values for the apsidal motion constants from table 1 in [Hamers et al. \(2017\)](#) are chosen and converted to Love number values by doubling them. The Love numbers for star and planet are therefore  $k_{2,\star} = 0.028$  and  $k_{2,\text{pl}} = 0.5$ . [Leconte et al. \(2010\)](#) give conditions of  $k_{2,\text{J}}\tau_{\text{J}} \lesssim 2 - 3 \cdot 10^{-2}$  s and  $k_{2,\star}\tau_{\star} \sim 2 \cdot 10^{-1} - 2 \cdot 10^{-2}$  s for Jupiter-like planets and for a Sun-like star. In order to still fulfil these conditions, but also not to choose the time lag too small,  $\tau_{\text{pl}}$  is set to 0.05 s and  $\tau_{\star}$  to 6.7 s. In this thesis, the stellar and planetary spin,  $\Omega_{\star}$  and  $\Omega_{\text{pl}}$ , are set to zero, to reduce the complexity of the problem. The inclusion of the spins could be subject of future follow-up studies.

Figure 5.3 shows the evolution of the orbital parameters of the test planet over time for two different cases. In the first case (Fig. 5.3a), for demonstration purposes, the time lag  $\tau$  is set to 0 for both the star and the planet. As a result, no evolution of the orbital elements  $a$  and  $e$  takes place. Only  $\varpi$  changes linearly with time, indicating an apsidal precession, i.e. a gradual rotation of the periastron position and thus of the entire orbit. The apsidal motion arises from the non-spherical gravitational field in the perturbed body, which in turn results from the redistribution of mass within the body due to tidal distortions ([Ou et al. 2021](#)). In the second case, the time lags  $\tau_{\text{pl}}$  and



(a)



(b)

**Fig. 5.3.:** The evolution of the orbital parameter  $a$ ,  $e$  and  $\varpi$  of a test planet due to the tidal interaction with the central star. a) The time lags for planet and star are both neglected. b) The time lags for planet and star are set to  $\tau_{\text{pl}} = 0.05$  s and  $\tau_{\star} = 6.7$  s.

$\tau_\star$  are included and set to the respective values discussed above. As can be seen in Fig. 5.3b, the orbit's semimajor axis and eccentricity are gradually decreasing. Since the planet is still very distant from the star over a large portion of its orbit and only comes sufficiently close to the star near its periastron ( $r_p = a(1 - e) = 0.05$  au), the effect on the orbital parameters is small, but not negligible on long timescales. The decrease in  $a$  and  $e$  is due to tidal dissipation that reduces the orbital energy of the planet, while the angular momentum is still conserved (Dawson & Johnson 2018). With a longer integration time (which, however, would be disproportionately computationally intensive due to the small step size), a further shrinking and an increasing circularisation of the orbit would be observed. If the star had been assigned a spin, and the planet's orbital period was longer than the star's rotational period, the orbit would expand. With  $\Omega_\star = 0$ , on the other hand, the planet's orbital period is generally shorter than the star's rotational period, so the planet's orbit would continue to shrink until it is finally tidally disrupted by the star (Dawson & Johnson 2018). The tidal disruption of the planet cannot be properly simulated, so that the planet eventually collides with the star. By taking into account the time evolution of the spins, an equilibrium state could be reached that would be characterised by coplanarity and circularity of the planet's orbit as well as bound rotation. However, this is beyond the scope of this thesis which is why neither the spin nor its time evolution are considered in the simulations presented here.

## 5.5.2 Initial Conditions for the Planetary System Simulations including Stellar Perturbation

For the simulations in this chapter, the 64k star cluster from Chapter 3 serves as the star cluster environment, as it is particularly well suited for an initial quantitative investigation of the hot Jupiter formation rate due to the cluster's high stellar density and large encounter rate. Those 200 stars closest to a mass of  $1 M_\odot$  are again selected as host stars. For the first set of simulation, 200 planetary systems consisting of 5 planets of equal mass ( $1 M_{\text{Jup}}$ ) are created and distributed around the 200 host stars. The planets are placed in the system according to Table 5.1 and all planetary systems are integrated for 100 Myr.

The orbital spacing in the first set of simulation assumes that five massive planets have formed beyond the ice line and that one of them has already migrated to a smaller orbit through disc migration without the influence of the star cluster within the lifetime of the disc. However, this imposes several requirements on the physical and temporal framework of the formation of the planets in the system. In order to be able to neglect these requirements, a second set of simulations

**Tab. 5.1.:** Initial conditions for the first set of planetary system simulations.

Parameter	P1	P2	P3	P4	P5
Semimajor axis $a$	1 au	5 au	10 au	20 au	30 au
Eccentricity $e$	0.0	0.0	0.0	0.0	0.0
Inclination $i$	0°	0°	0°	0°	0°
Mass	1 M <sub>Jup</sub>				

is created for comparison, identical to the first, except that the innermost planet at 1 au is missing, leaving only 4 planets in the system.

## 5.6 Results

### 5.6.1 Tidal Evolution and Hot Jupiter Candidate Criterion

The  $a$ - $e$  phase space for the first set of simulations is shown in Fig. 5.4 for time steps of 10 Myr each. The planets are distributed over a large range of the phase space. It is therefore evident that an AMD introduced by one or more external perturbations affects the entire planetary system, as it is passed on to the inner planets through planet-planet scattering. Of particular interest for the investigations in this chapter are those planets with small semimajor axis and very high eccentricity, as these are candidates to evolve into a hot Jupiter due to tidal evolution.

The timescale for tidal evolution depends strongly on the final semimajor axis ( $a_{\text{final}}$ ) to which the planet migrates during the circularisation process and has the following proportionality in the constant time lag model (Eggleton et al. 1998):

$$\tau_{\text{circ}} \propto \frac{a}{\dot{a}} \propto a_{\text{final}}^8. \quad (5.9)$$

After decoupling from the perturbation that brought a planet into a highly elliptical orbit by transferring angular momentum to the perturber, its final semimajor axis can be calculated from the time evolution of the semimajor axis,  $a(t)$ , and eccentricity,  $e(t)$ , using the expression

$$a_{\text{final}} = a(t)(1 - e(t)^2), \quad (5.10)$$

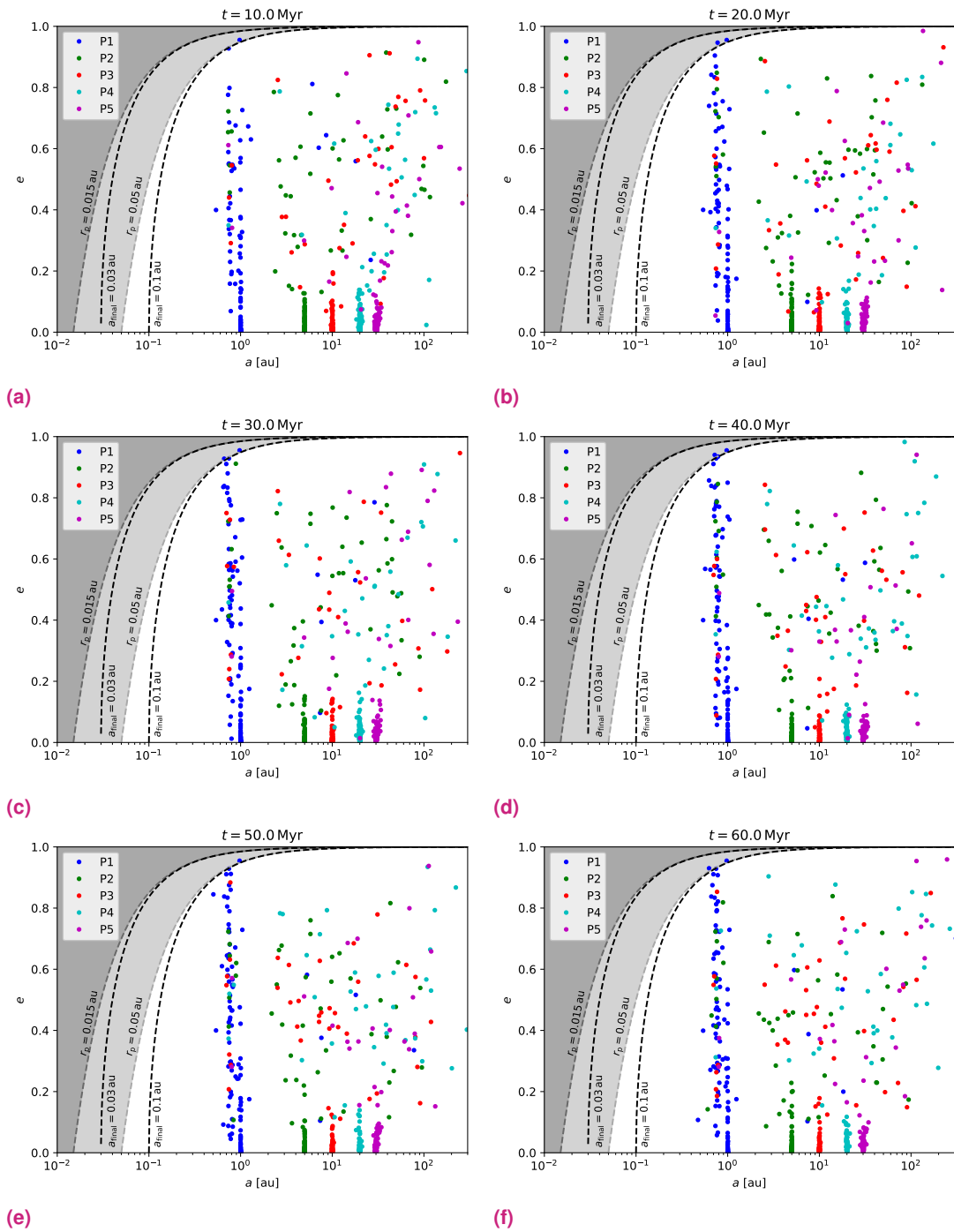


**Fig. 5.4.:** 10 Myr interval snapshots of the  $a$ - $e$  space of the surviving planets from the 200 planetary systems in the first simulation set for the time  $t = 10$ – $60$  Myr. The grey dashed lines represent the lines of equal periastron distance across the  $a$ - $e$  space for  $r_{p,init} = 0.015$  au and  $r_{p,init} = 0.05$  au. The black dashed lines represent the tidal evolution tracks of constant angular momentum for these two initial periastron distances (assuming very high initial eccentricities).

as this is the track of constant angular momentum (Dawson & Johnson 2018). Assuming an initial high-eccentricity orbit, this expression can be simplified to

$$a_{\text{final}} = a(1 - e^2) \approx 2a(1 - e) = 2r_{\text{p,init}} \quad (\text{for } e \rightarrow 1), \quad (5.11)$$

where  $r_{\text{p,init}} = a_{\text{init}}(1 - e_{\text{init}})$  is the initial periastron distance. The tidal evolutionary tracks of two initial periastron distances of 0.015 au and 0.05 au are additionally plotted in Fig. 5.4. Equation 5.9 can be used to estimate that a planet that would circularise within one million years on the first tidal evolutionary track would have a circularisation timescale for the second track that exceeds the age of the Universe. Since Fig. 5.4 only shows snapshots at 10 Myr intervals, not all potential hot Jupiters are visible, as the circularisation timescale can be well below 10 Myr.

Furthermore, planets which are excited to  $e > 0.99$  are removed from the simulation, as they can typically be considered either unbound or destroyed (by collision with the star or by tidal disruption, respectively). In the case of small semimajor axes, however, planets with eccentricities of  $0.99 < e < 1.0$  are also of interest, since the eccentricity can decrease due to tidal dissipation. For numerical reasons, this eccentricity criterion is kept in this chapter and those planets that would have sufficiently approached the star due to an eccentricity of  $0.99 \text{ au} < e < 1.0 \text{ au}$  are examined regarding their fate on the basis of their last orbital parameters.

Following the criterion in Hamers et al. (2017), all planets that reach a semilatus rectum (see Eq. 1.30 in Sec. 1.2.3) value of  $p < 0.091 \text{ au}$  during the simulation are considered as hot Jupiter candidates, as this value corresponds to the semimajor axis of a Jovian-mass planet on a circular 10-day orbit around a Solar-mass star. Such a criterion is necessary because the circularisation timescales of many planets significantly exceed the simulation time, limiting the possibility of observing their tidal evolution. However, not all candidates are completely decoupled from the secular evolution of the remaining planets in the system, as can be seen in the following section, which is why a large fraction of candidates are never expected to become hot Jupiters. There are also cases where further stellar encounters lead to an interaction of the remaining planets in the system with the hot Jupiter even within the simulation time, as a result of which the hot Jupiter would have been tidally disrupted by the star. Regardless of their long-term fate, planets that meet the semilatus-rectum criterion for at least 100 output time steps ( $\hat{=}$ 100 kyr) are considered actual hot Jupiters, as the semilatus-rectum criterion otherwise includes many planets that meet it for a short period of time during their ejection process or as a result of chaotic interaction with neighbouring planets. Since the stellar and planetary spin are not taken into account in the simulations, even those hot Jupiters that are unperturbed on long timescales do not reach a state

of equilibrium. Thus, all hot Jupiters are tidally disrupted on short or long timescales in the simulations presented here.

## 5.6.2 The Formation of Hot Jupiters through Stellar Encounters Based on Individual Systems

Figure 5.5 shows the dynamical evolution of selected hot Jupiters for which a decrease of the semimajor axis and eccentricity is observable within the simulation time and which meet the semilatus-rectum criterion for at least 100 output time steps. However, the evolution timescales are very different for each planet. For example, Planet 2 in Fig. 5.5a has a circularisation timescale of 1.5 Myr, whereas other hot Jupiters have circularisation timescales that far exceed the simulation time of 100 Myr. One reason for this is that the hot Jupiter in Figs. 5.5b–5.5f show a high-frequency oscillation of their eccentricity due to perturbations with the second innermost planet in the system (which, except for Fig. 5.5e, is no longer Planet 2), which significantly increases the circularisation timescale.

In the case of the system in Fig. 5.5b, this high-frequency oscillation is a special phenomenon from secular evolution theory, the so-called Lidov-Kozai mechanism (Lidov 1962; Kozai 1962). It occurs when a third body has an initial inclination in the range  $39.2^\circ$ – $140.8^\circ$  (Fabrycky & Tremaine 2007) to a binary system (either a stellar binary system or, as in this case, a star-planet system). If this is satisfied, the outermost body (if  $e_{\text{out,init}} = 0$ ), in this case a second planet, will periodically increase the eccentricity of the inner planet (if  $e_{\text{in,init}} = 0$ ) to a maximum value of

$$e_{\text{in,max}} = \sqrt{1 - (5/3) \cos^2 i_{\text{init}}}, \quad (5.12)$$

where  $i_{\text{init}}$  is the initial mutual inclination (Fabrycky & Tremaine 2007; Fabrycky 2010). Since inclination and eccentricity are coupled in this high-eccentricity and high-inclination region, the eccentricity of the inner planet and the mutual inclination of the inner and outer planets oscillate periodically. According to Kiseleva et al. (1998), these Kozai cycles occur on timescales of

$$\tau_{\text{LK}} = \frac{2T_{\text{out}}^2}{3\pi T_{\text{in}}} \frac{m_1 + m_2 + m_3}{m_3} (1 - e_{\text{out}}^2)^{3/2}, \quad (5.13)$$

where  $m_1$  is the mass of the central star,  $m_2$  and  $m_3$  are the mass of the inner and outer planet and  $e_{\text{out}}$  is the outer planet's eccentricity.

For the system in Fig. 5.5b, this timescale would be about 0.072 Myr at time  $t = 25$  Myr, which is in good agreement with the actual oscillation timescale, which is about 0.075 Myr. The maximum eccentricity from Eq. 5.12 at  $t = 25$  Myr, which is  $e_{\max} = 0.99$ , is also in good agreement with the actual maximum value of  $e_{\max} = 0.98$  at that time. Note also the similarity of the eccentricity oscillation pattern of the inner planet in Fig. 5.5b compared to fig. 1a in Fabrycky & Tremaine (2007), where a hypothetical progenitor planet of HD 80606b is investigated under the influence of tidal forces and Kozai cycles. The ejection of the inner planet in Fig. 5.5b at time  $t = 61$  Myr occurs due to a close encounter with another star and is independent of its tidal evolution and the Lidov-Kozai mechanism.

After all other planets have been ejected from the system shown in Fig. 5.5c, the orbits of the two outer planets have a mutual inclination that is in principle capable of triggering a Kozai cycle. The Lidov-Kozai timescale for this system according to Eq. 5.13 is about 1.05 Myr at time  $t = 40$  Myr, but the actual oscillation period for the eccentricity is about 1.30 Myr. The maximum eccentricity value for the inner planet of  $e_{\max} = 0.65$  according to Eq. 5.12 is strongly exceeded with an actual value of  $e_{\max} = 0.97$ . Furthermore, since the inclination shows a disturbed oscillation pattern that differs from that of the eccentricity, an unperturbed Kozai cycle cannot be assumed for this system.

In six of the eight presented systems, it is Planet 1, the initially innermost planet, which is sufficiently excited in eccentricity by planet-planet scattering to be affected by tidal dissipation. In Fig. 5.5a, on the other hand, it is Planet 2 which, as a result of an encounter after about 5 Myr and the subsequent planet-planet scattering, loses sufficient energy and angular momentum to become the innermost planet. Due to tidal dissipation and because of its lack of spin, the planet eventually falls into the star. In Fig. 5.5c, it is even Planet 4, the initially second outermost planet in the system, that tidally interacts with the central star as a result of a stellar encounter at roughly 35 Myr.

All systems in which hot Jupiters (candidates) have formed or are in the process of forming at the end of the simulation have in common that at least one planet was ejected from the system immediately before the onset of high-eccentricity tidal migration. In five of the eight presented systems in Fig. 5.5, as many as three planets were ejected as a result of planet-planet scattering. In all cases, at least two planets survived the planet-planet scattering following the external perturbation. Furthermore, in all presented systems, those encounters that were responsible for the onset of planet-planet scattering and the subsequent high-eccentricity tidal migration of one of the surviving planets induced a NAMD  $> 0.6$  into the system.

All eight candidates from Fig. 5.5 that actually became or could have become hot Jupiters (with longer integration times or without ejection by stellar flybys) had highly inclined orbits during the tidal circularisation phase. Planet 2 from Fig. 5.5a is even in a retrograde orbit throughout the period of tidal interaction, whereas Planet 1 from Fig. 5.5b and Fig. 5.5h remain in a near-polar orbit during that process. This clustering of highly inclined orbits may indicate that the detection of hot Jupiters using the transit method tends to miss additional planets in the system. A combination with other observational techniques, such as spectroscopic or astrometric follow-up observations, might therefore be promising.

### 5.6.3 Statistics and Comparison with Second Simulation Set

Since many planets in the simulations that experience tidal interaction with the star have a very high circularisation timescale (partly due to ongoing interaction with other planets in the system), the semilatus-rectum criterion from Hamers et al. (2017) was applied to estimate how many hot Jupiters would form.

However, the criterion was refined as follows:

- If  $p < 0.091$  au for at least 1 snapshot: the planet is a hot Jupiter candidate.
- If  $p < 0.091$  au for at least 100 snapshots: the planet is a hot Jupiter (or becomes one with longer simulation time).

In the first simulation set, a total of 97 hot Jupiter candidates were found in 80 systems according to these criteria. However, only 43 planets from 36 systems fulfil the criterion for hot Jupiters. 37 planets from the hot Jupiter candidates were tidally disrupted by the star during the simulation time of 100 Myr. Whether a planet has been tidally disrupted can be estimated from its minimum periastron distance. For this purpose, the tidal disruption threshold from Guillochon et al. (2011) is adopted, which assumes tidal disruption by the star if the planet's periastron distance falls below the following radius:

$$r_t = 2.7 \cdot R_{\text{pl}} \left( \frac{M_{\star}}{m_{\text{pl}}} \right)^{1/3}. \quad (5.14)$$

For the parameters used in this chapter, this yields  $r_t \approx 0.013$  au.

The results from the second set of simulations, in which the innermost planet is missing in each system, demonstrate the significance of a close-in planet for the formation of hot Jupiters. Without the presence of a planet at 1 au, only 35 candidates and three hot Jupiters were formed. The respective percentages compared to the first simulation set are listed in Table 5.2.

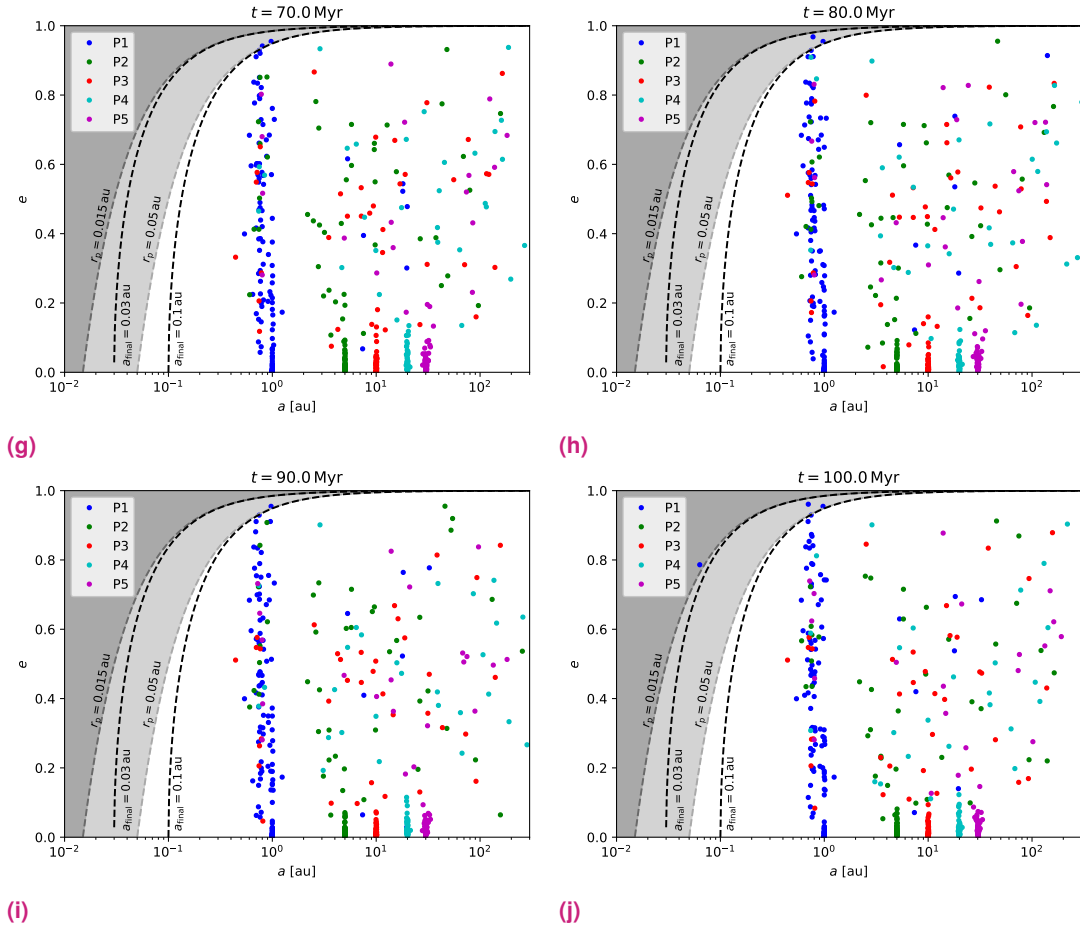
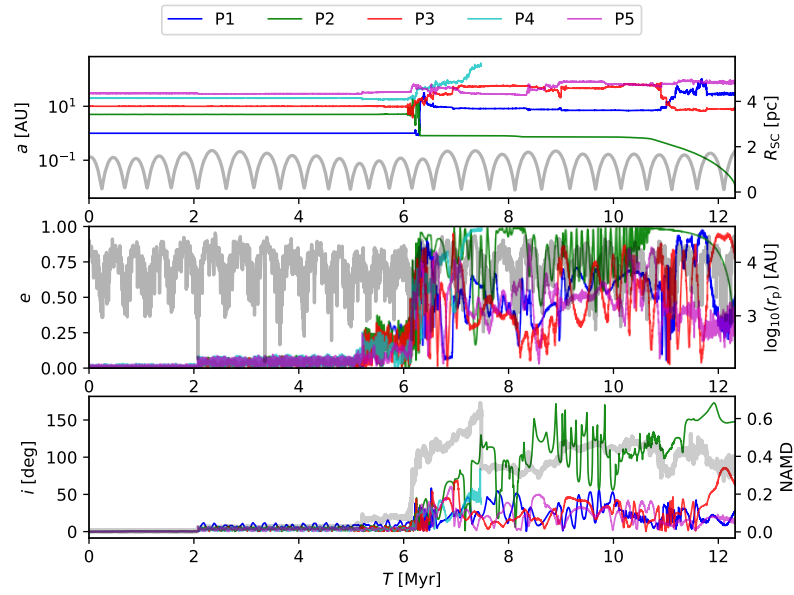


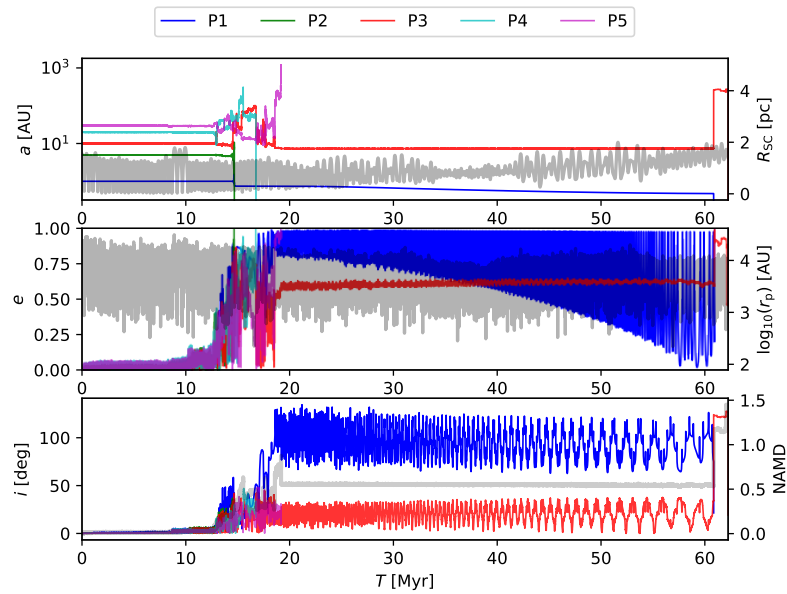
**Fig. 5.4.:** (Cont.) 10 Myr interval snapshots of the  $a$ - $e$  space of the surviving planets from the 200 planetary systems in the second simulation set for the time  $t = 70$ – $100$  Myr. The grey dashed lines represent the lines of equal periastron distance across the  $a$ - $e$  space for  $r_{p,\text{init}} = 0.015$  au and  $r_{p,\text{init}} = 0.05$  au. The black dashed lines represent the tidal evolution tracks of constant angular momentum for these two initial periastron distances (assuming very high initial eccentricities).

**Tab. 5.2.:** Statistics of found hot Jupiter candidates (fourth column), actual hot Jupiters (fifth column) and tidally disrupted planets (sixth column).

Simulation Set	#systems	#planets	$p < 0.091$ au (for $> 1$ step)	$p < 0.091$ au (for $> 100$ steps)	$r_p < r_t$
#1	200	1000	0.097	0.043	0.037
#2	200	800	0.044	0.004	0.0

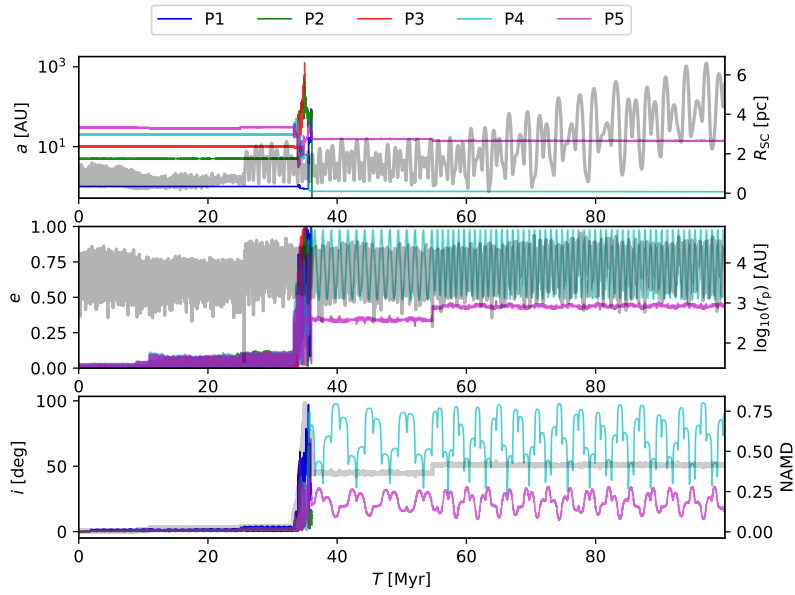


(a)

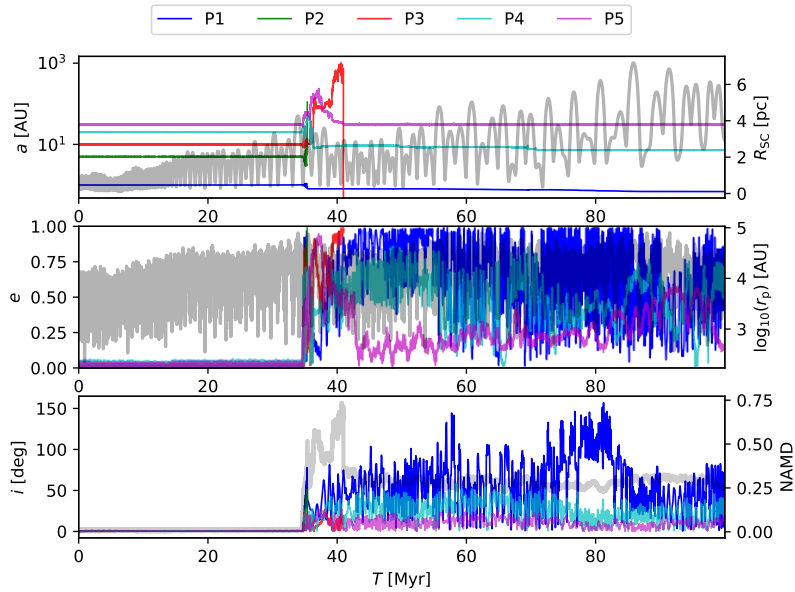


(b)

**Fig. 5.5.:** Tidal evolution of hot Jupiters: (a) The shrinking and circularisation of the orbit of Planet 2 starts at 10.8 Myr. (b) The shrinking and circularisation of the orbit of Planet 1 starts at 17.1 Myr, but the planet eventually never becomes a hot Jupiter because, despite its small semimajor axis of 0.47 au, it is ejected from the system by an encounter with a  $4 M_{\odot}$  star at  $t = 60.1$  Myr. *Background:* The thicker grey lines represent the distance to the cluster centre (top panel), the distance to the closest stellar perturber (middle panel) and the normalized angular momentum deficit (bottom panel).

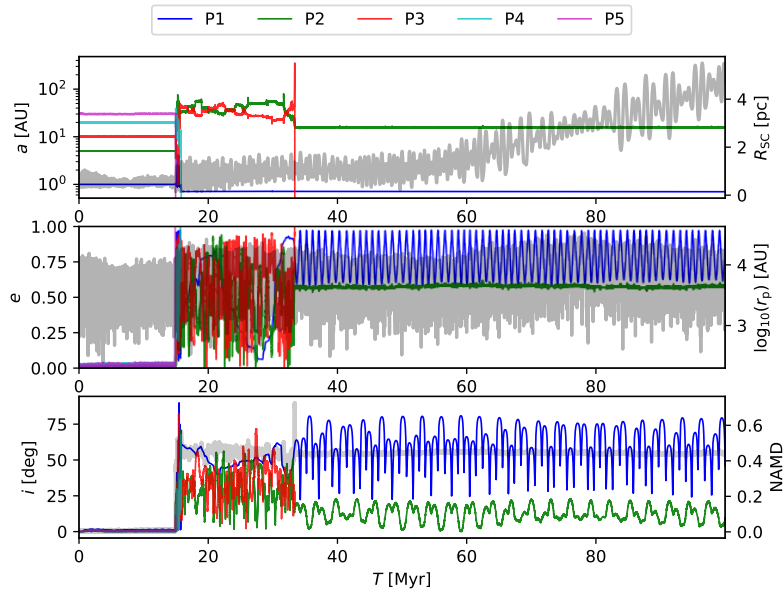


(c)

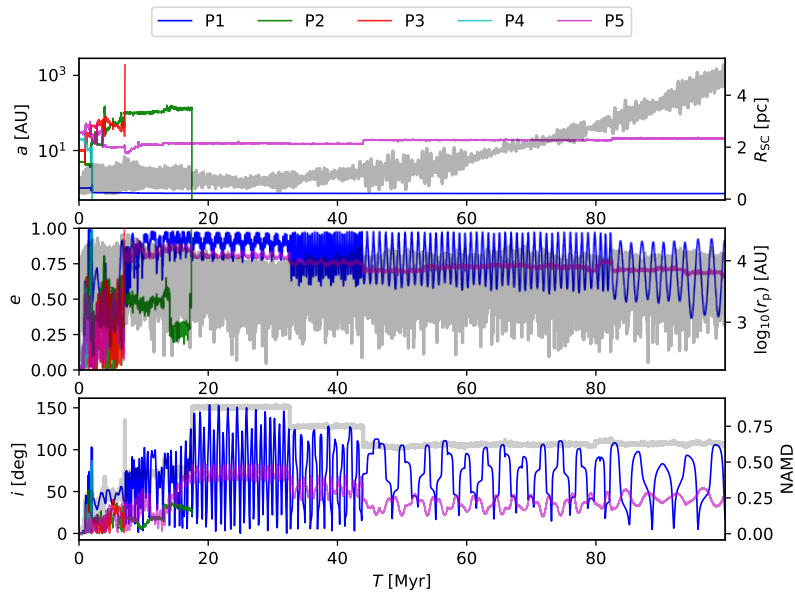


(d)

**Fig. 5.5.:** (Cont.) Tidal evolution of hot Jupiters: (c) The shrinking and circularisation of the orbit of Planet 4, as well as its secular perturbation by Planet 5, starts around 35.6 Myr but is interrupted in phases of lower eccentricity. (d) The shrinking and circularisation of the orbit of Planet 1 starts roughly at 43.5 Myr and is also interrupted in phases of lower eccentricity due to gravitational interaction with Planet 4. *Background:* The thicker grey lines represent the distance to the cluster centre (top panel), the distance to the closest stellar perturber (middle panel) and the normalized angular momentum deficit (bottom panel).

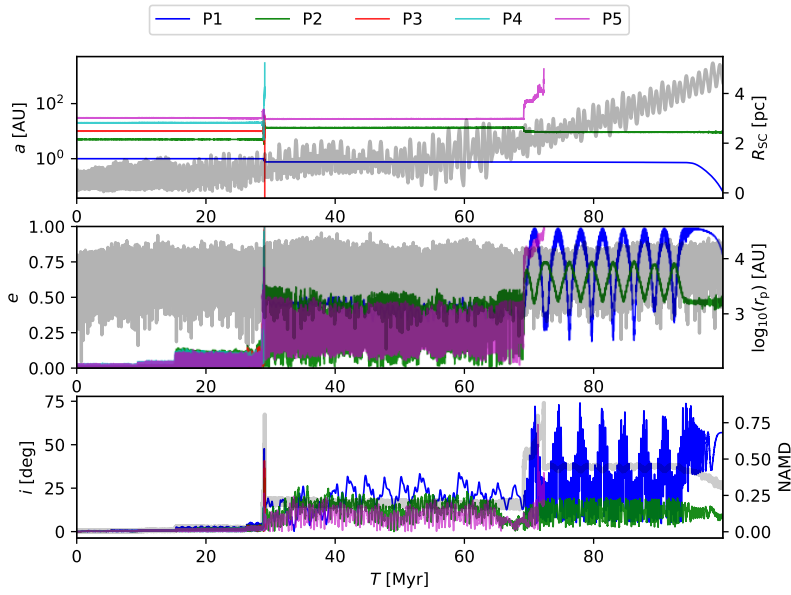


(e)

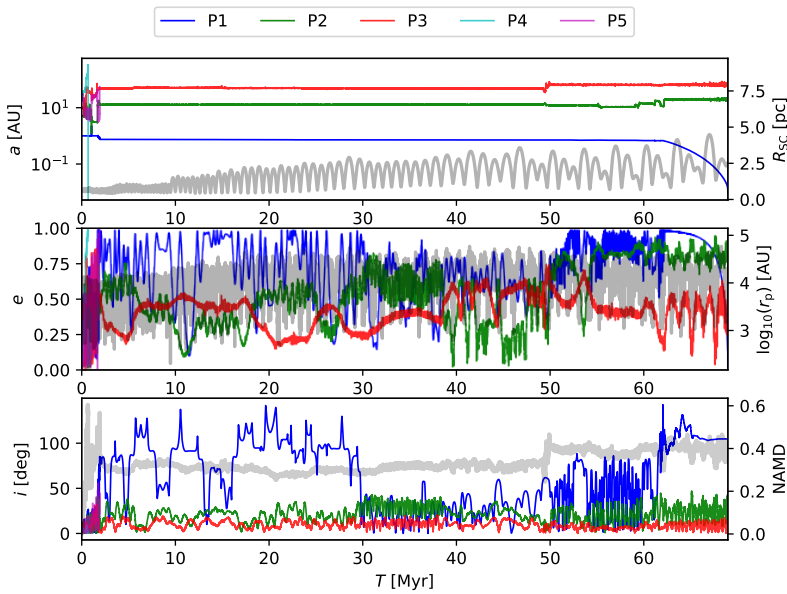


(f)

**Fig. 5.5.:** (Cont.) Tidal evolution of hot Jupiters: (e) The shrinking and circularisation of the orbit of Planet 1, as well as its secular perturbation by Planet 2, starts around 34.2 Myr, shortly after the ejection of Planet 3, but is interrupted in phases of lower eccentricity. (f) The shrinking and circularisation of the orbit of Planet 1 starts roughly at 10.7 Myr, after Planet 3 is kicked out of the system, and is interrupted in phases of lower eccentricity due to gravitational interaction with Planet 5. *Background:* The thicker grey lines represent the distance to the cluster centre (top panel), the distance to the closest stellar perturber (middle panel) and the normalized angular momentum deficit (bottom panel).



(g)



(h)

**Fig. 5.5.:** (Cont.) Tidal evolution of hot Jupiters: (g) Due to high-eccentricity phases after 70 Myr the orbit of Planet 1 is shrinking on long timescales. The abrupt shrinking and the actual circularisation of the orbit of Planet 1 starts around 95.0 Myr. The simulation stopped as scheduled after 100 Myr, which happened to coincide with the circularization phase. (h) Tidal circularisation of Planet 1 starts at 62.2 Myr and is almost complete by the time the planet collides with the star 6.7 Myr later. *Background:* The thicker grey lines represent the distance to the cluster centre (top panel), the distance to the closest stellar perturber (middle panel) and the normalized angular momentum deficit (bottom panel).

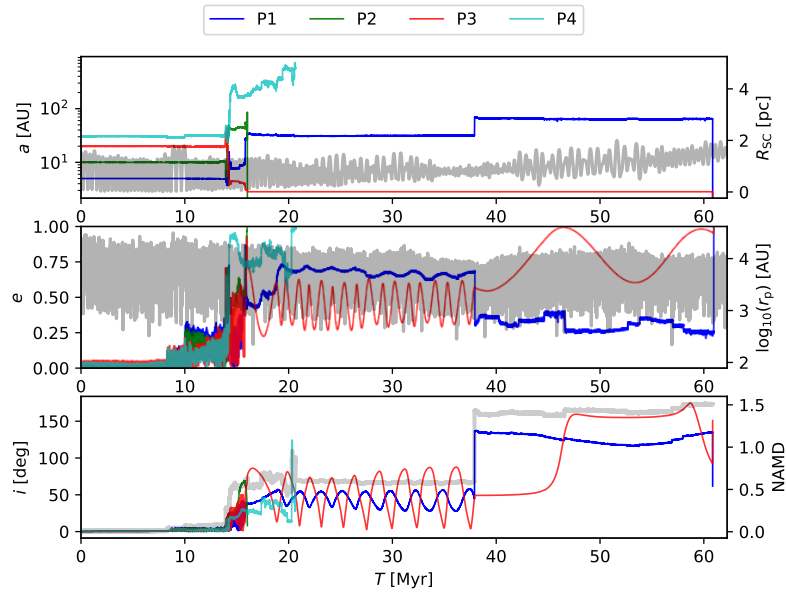


**Fig. 5.6.:** The shrinking and circularisation of the orbit of Planet 3 is only taking place during phases of high-eccentricity as the planet still has a semimajor axis of 2.8 au after  $t = 16$  Myr. Background: The thicker grey lines represent the distance to the cluster centre (top panel), the distance to the closest stellar perturber (middle panel) and the normalized angular momentum deficit (bottom panel).

Figure 5.6 shows the dynamical evolution of one of the three hot Jupiters found in the second set of simulations. Although Planet 3 fulfils the semilatus-rectum criterion for more than 100 000 years (during the phases of maximum eccentricity), it is obvious that its circularisation timescale would be significantly longer than the simulation time. Here, the star cluster environment prevents an unperturbed tidal evolution, as the planet, along with the second remaining planet, is ejected from the system by a close encounter with a  $4 M_{\odot}$  star at  $t = 60$  Myr. The host star (and thus its trajectory through the cluster) is the same as in Fig. 5.5b. In both planetary systems, the same stellar encounter prevents the tidal evolution of the planet into an actual hot Jupiter. However, it should be noted that due to the different initial configuration, a different planet was affected by the tidal evolution in each case. This illustrates the chaotic nature of planet-planet scattering and the stochastic component in the formation of hot Jupiters.

The distribution in  $a-e$  space for the second simulation set in Fig. 5.7 compared to Fig. 5.4 illustrates the orders of magnitude in parameter space that must be overcome by the planets to be subject to significant tidal evolution. Given that the initial semimajor axis of all planets is larger than 5 au, the number of planets that get close to a periastron distance of 0.05 au is nevertheless remarkable. As a result of tidal dissipation, planets with an initial periastron distance of 0.05 au

would circulate to a semimajor axis of 0.1 au. This would correspond to an orbital period of 11.5 d. These planets would then lie on the boundary between hot ( $T < 10$  d) and warm Jupiters ( $T = 10$  d–200 d).

Figure 5.8 shows cumulative histograms of the maximum NAMD in systems with and without hot Jupiter candidates in comparison for both simulation sets. Systems in the first simulation set where hot Jupiter candidates have formed generally have a  $\text{NAMD}_{\text{max}} > 0.45$ , i.e., at least about half of the total angular momentum in the planetary system must be transferred to the stellar perturber. The average maximum value in systems with hot Jupiter candidates is 0.85, which is almost twice as high as in systems without hot Jupiter candidates ( $\langle \text{NAMD}_{\text{max}} \rangle = 0.44$ ).

For the second set of simulations, due to the larger distances to be overcome by the planets in  $a-e$  space, a higher NAMD is required from stellar flybys to produce hot Jupiter candidates. The average value for systems with hot Jupiter candidates here is 0.95, but the average value of 0.55 in systems without hot Jupiter candidates is also higher than in the first simulation set because the absence of the innermost planet results in a slightly higher average ejection rate for all planets in the system, which correlates with a higher NAMD.

## 5.7 Discussion

Figure 5.9 shows the distribution of 4903 exoplanets detected to date in  $a-e$  phase space. Those 536 planets with a mass larger than  $0.1 M_{\text{Jup}}$  and an orbital period shorter than 10 days are hot Jupiters and are marked in brown. Therefore, 11% of the planets discovered so far are hot Jupiters, although this value is expected to considerably exceed the true occurrence rate due to observational bias. The occurrence rate of hot Jupiters around Sun-like stars is estimated to be about 1% (Dawson & Johnson 2018, and references therein). Despite numerous observational and theoretical studies of hot Jupiters, it is not yet entirely understood which is the key process in the formation of these planets.

This chapter has investigated the concatenation of three different processes using numerical simulations of a total of 400 planetary systems embedded in a star cluster environment (of in total 64 000 stars) along with their Sun-like host stars. Encounters with neighbouring stars in the cluster trigger planet-planet scattering in many of these previously stable planetary systems, which in some cases can lead to high-eccentricity tidal migration of one of these planets and thus to the formation of a hot Jupiter.

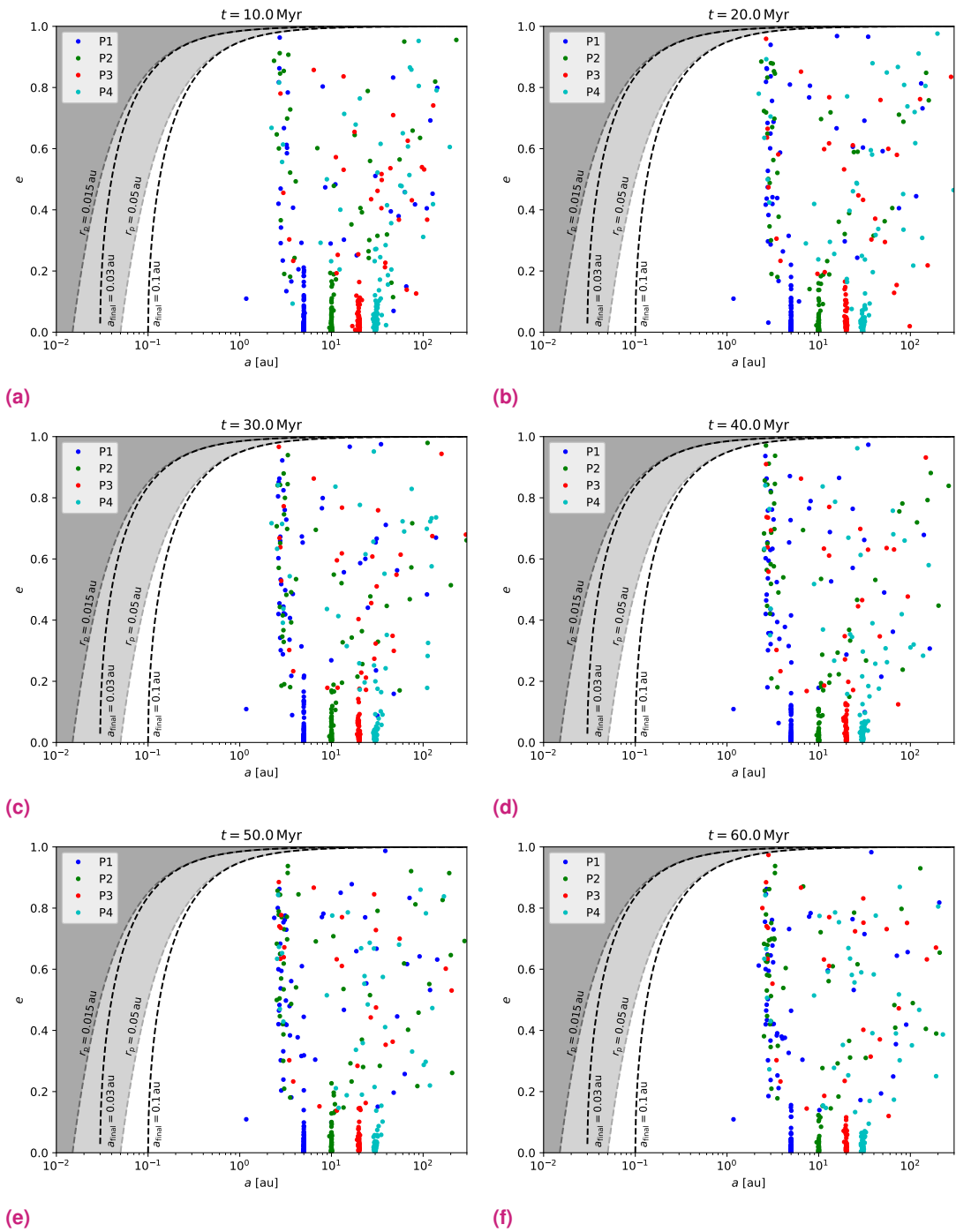


**Fig. 5.7.:** 10 Myr interval snapshots of the  $a$ - $e$  space of the surviving planets from the 200 planetary systems in the second simulation set for the time  $t = 10$ – $60$  Myr. The grey dashed lines represent the lines of equal periastron distance across the  $a$ - $e$  space for  $r_{p,\text{init}} = 0.015$  au and  $r_{p,\text{init}} = 0.05$  au. The black dashed lines represent the tidal evolution tracks of constant angular momentum for these two initial periastron distances (assuming very high initial eccentricities).

In the first simulation set with 200 identical planetary systems, in each of which 5 planets with  $1 M_{\text{Jup}}$  are distributed between 1 au and 30 au, a total of 43 planets in 36 systems have reached a semilatus rectum value of less than 0.091 au over at least 100 000 years. In their simulations, [Hamers et al. \(2017\)](#) consider all planets with a semilatus rectum of less than 0.091 AU to be hot Jupiters, regardless of the duration for which the parameter is below this limit. However, such a criterion does not appear useful without an additional criterion for the duration, as 9.7% of all planets in the first simulation set fulfil this criterion for at least one simulation output time step. A closer look at these planets revealed that many planets fulfil this criterion for a short time as a result of strong planet-planet scattering (and thus in some cases during their ejection phase from the system). This criterion also includes 12 planets that were removed from the simulation for numerical reasons because their eccentricity was too close to an unbound orbit of  $e = 1$ , and 37 planets that would have been tidally disrupted by the star due to their small periastron distance. All planets that met the semilatus-rectum criterion for at least one output time step were referred to as hot Jupiter candidates in this chapter, whereas those planets that met the criterion for at least 100 000 years were considered actual hot Jupiters, regardless of whether they actually met the definition of real hot Jupiters during the simulation period. A longer simulation time of these systems is hardly feasible due to the high computational costs.

In the second simulation set, a total of 35 planets fulfilled the semilatus criterion for at least one output time step and only 3 planets for at least 100 output time steps. Thus, only about 0.4% of the planets could be considered hot Jupiters in the second simulation set, compared to about 4% in the first simulation set. Since in a few systems even two hot Jupiters would have been formed (which is only possible if the first one is already tidally disrupted by that time), the occurrence rate per system for the first planetary system model was 18%, whereas it was only 1.5% for the second model. Compared to the estimated occurrence rate of about 1% around Sun-like stars, this means that the system's orbital architecture and mass distribution in the second simulation set seem to better reproduce reality<sup>1</sup>. The first planetary system model requires a prior disc migration of one of the planets from its formation point beyond the ice line at about 3 au ([Martin & Livio 2012](#)) to a smaller orbit. If the second planetary system model seems to better reproduce the estimated occurrence rate, such a prior disc migration of one of the planets would not be essential. In addition, a smaller number of massive planets would be required in the system. Whether a system consisting of only three massive planets with the innermost gas giant near the ice line would also produce a comparable rate of hot Jupiters could be the subject of future simulations.

---

<sup>1</sup>However, it should be noted that the estimated occurrence rate of 1% around Sun-like stars also includes planetary systems that are not as massive as those simulated in this chapter. A direct comparison is therefore only possible to a limited extent.

Our results are similar in order of magnitude to the simulation results in [Hamers et al. \(2017\)](#), who, among others, simulate systems in isolation consisting of three  $0.3 M_{\text{Jup}}$ -mass planets at initial semimajor axes of 1 au, 6 au, and 12–62 au. While [Hamers et al. \(2017\)](#) find hot Jupiters corresponding to the semilatus-rectum criterion in 32% of their systems, in the first simulation set presented here, which is most similar to the initial conditions of [Hamers et al. \(2017\)](#), hot Jupiters evolved in 40% of all systems.

The large NAMD required to trigger high-eccentricity tidal migration via planet-planet scattering also shows that for hot Jupiters to form, an initial high multiplicity (i.e. a large number of planets in the system) is beneficial, but at the same time this multiplicity cannot be kept up for long due to the high NAMD, as it leads to instability in the system. Thus, if hot Jupiters are formed (primarily) by a concatenation of stellar encounters, planet-planet scattering and high-eccentricity tidal migration, the ejection of other planets in the system is required, as was the case in all systems studied in this chapter.

The simulations presented in this chapter show that star clusters can stimulate and facilitate the formation of hot Jupiters. Flybys of neighbouring stars can induce a sufficiently large AMD in previously stable planetary systems with circular and coplanar orbits, such that high-eccentricity tidal migration is triggered for one of the planets in the system. A high multiplicity as well as a previous disc migration of one of the planets to an orbit within the ice line facilitates hot Jupiter formation. In one case, it could be shown that a stellar encounter stimulated a Lidov-Kozai oscillation, which is also a possible cause of high-eccentricity tidal migration. In no case, however, was the stellar encounter the exclusive cause for the formation of a hot Jupiter. In all systems, additional planet-planet scattering, triggered by the encounter, played a crucial role. The ejection of at least one planet as a result of the planet-planet scattering was in all cases necessary to drive one of the planets (often, but not necessarily, the innermost planet) towards a highly eccentric orbit via angular momentum exchange to trigger high-eccentricity tidal migration.

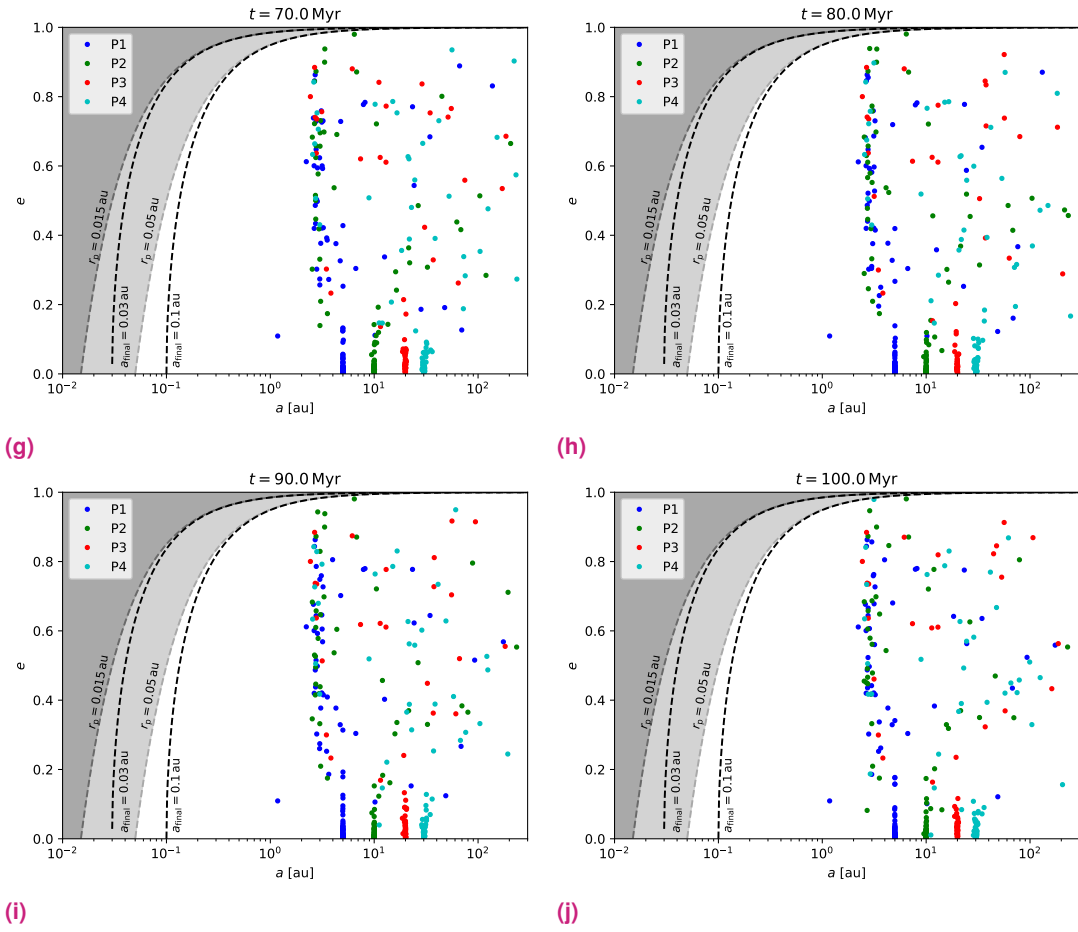


**Fig. 5.7.:** (Cont.) 10 Myr interval snapshots of the  $a$ - $e$  space of the surviving planets from the 200 planetary systems in the second simulation set for the time  $t = 70$ – $100$  Myr. The grey dashed lines represent the lines of equal periastron distance across the  $a$ - $e$  space for  $r_{p,\text{init}} = 0.015$  au and  $r_{p,\text{init}} = 0.05$  au. The black dashed lines represent the tidal evolution tracks of constant angular momentum for these two initial periastron distances (assuming very high initial eccentricities).

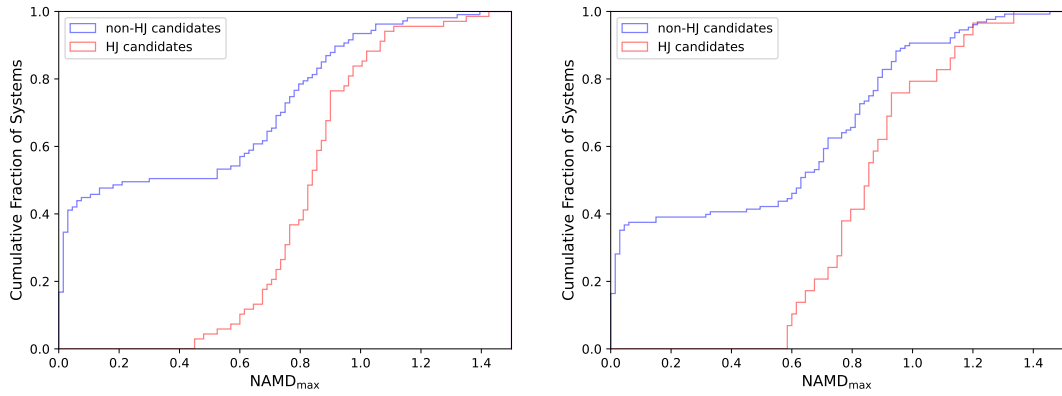


**Fig. 5.8.:** Cumulative histograms for the maximum NAMD induced in hot-Jupiter candidate systems and non-hot-Jupiter candidate systems by stellar encounters in the first (left panel) and second (right panel) simulation set.

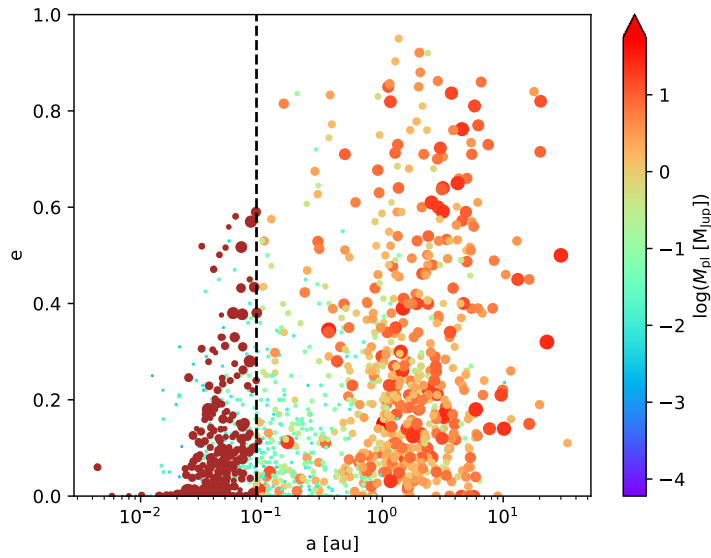


**Fig. 5.9.:** The distribution of detected exoplanets (according to the [NASA Exoplanet Archive](#) as of January 2022) in the  $a$ - $e$  space. The semimajor axis hot Jupiter threshold for a Jovian-mass planet of 0.091 au is marked as dashed line and the hot Jupiters ( $T < 10$  d and  $m_{pi} > 0.1 M_{Jup}$ ) are marked in brown. The size of the dots representing the planets is  $\propto \sqrt{m_{pi}}$ .

## Discussion and Conclusion

” *We are in danger of destroying ourselves by our greed and stupidity. We cannot remain looking inwards at ourselves on a small and increasingly polluted and overcrowded planet.*

— **Stephen Hawking**

In this thesis I have investigated the gravitational influence of the birth environment of stars on the dynamical evolution of planetary systems that have formed around these stars. Today’s prevailing model of star formation assumes a collapse of a giant molecular cloud due to self-reinforcing contractions and a subsequent hierarchical fragmentation into smaller dense clouds, from which single or multiple stars can form (e.g. [Parker 2020](#)). Due to the close connection between star and planet formation, this implies the formation of stars as well as planets in groups of stars or larger clusters which is supported by observations (e.g. [Lada & Lada 2003](#)). Given the high stellar densities in these environments, the process of planet formation that takes place within the protoplanetary disc around a star can be affected. For example, close flybys of neighbouring stars can either completely destroy or truncate the protoplanetary disc (e.g. [Portegies Zwart 2016](#); [Parker 2020](#)). In addition, the high-energy radiation of hot O and B stars in the vicinity can lead to a mass loss of the protoplanetary disc due to photoevaporation (e.g. [Störzer & Hollenbach 1999](#); [Armitage 2000](#)), shortening the lifetime of the disc ([Störzer & Hollenbach 1999](#)) and hampering the formation of larger planets ([Armitage 2000](#)).

The Solar system was formed in an open star cluster with about 2 000–3 000 members ([Portegies Zwart 2009](#); [Portegies Zwart et al. 2018a](#)), which has dissolved over time. Evidence for this is provided by the presumably truncated edge of the Kuiper belt, the slight tilt of the Solar system with respect to the equatorial plane of the Sun, and the enrichment of the protoplanetary disc with particular isotopes (e.g. [Portegies Zwart et al. 2018a](#), and references therein).

While on the one hand the protoplanetary disc can facilitate planetary migration, on the other hand it generally also has a protective effect against external perturbations because the gas in the disc dampens the eccentricities of the planetary orbits (e.g. [Lee & Peale 2002](#); [Kley et al.](#)

2004). However, in larger cluster environments with  $> 10^4$  stars, the protoplanetary discs of the stars typically dissolve two to three orders of magnitude faster than the cluster. Thus, planets born in larger open star clusters or small globular clusters are exposed to the destructive effect of passing stars over timescales in the range of  $10^7$ – $10^8$  years until the star cluster has sufficiently expanded and the encounter timescale has dropped significantly. Most star-forming regions have initial stellar densities of at least  $100 M_{\odot} \text{pc}^{-3}$  (e.g. Parker 2020). Close encounters with other stars in the cluster can significantly alter planetary orbits and even eject planets from the system (e.g. Smith & Bonnell 2001; Davies & Sigurdsson 2001; Hurley & Shara 2002; Spurzem et al. 2009; Cai et al. 2017, 2018; van Elteren et al. 2019; Cai et al. 2019). These ejections can happen both immediately and/or delayed (up to tens of millions of years later) as a result of long-term instabilities.

For this thesis, four different star clusters were simulated. The clusters consisted of 8 000, 16 000, 32 000 and 64 000 stars and had an initial half-mass radius of 0.78 pc each. The initial stellar positions and velocities were drawn from a Plummer model (Plummer 1911). All the clusters showed a short phase of core collapse and expanded rapidly thereafter. After about 100 Myr–250 Myr, their central densities corresponded to those of star clusters observed today and the clusters were in the process of dissolving.

The numerical integration of the planetary systems was carried out subsequent to the star cluster simulation. This hybrid approach is possible under the assumption that the motion of the stars in the cluster has an influence on the dynamical evolution of the planets, but not vice versa. The simulation code, LPS, has been used in previous studies such as Cai et al. (2017, 2018, 2019) and Flammioni Dotti et al. (2019). In contrast to a fully coupled  $N$ -body treatment as done in Hurley & Shara (2002), this approach does not enable to track the motion of free-floating planets in the cluster after their ejection from a planetary system. Instead, the hybrid approach allows the simulation of multiplanetary systems, as well as the simulation of different planetary system architectures assuming the same host star trajectory through the cluster.

## 6.1 The Survival of Solar-System Analogues in Different Star Cluster Environments

In Chapter 3, the 200 stars from all four star clusters whose mass is closest to the Solar mass were selected as host stars. For these stars, as well as for the five nearest neighbouring stars at any given time, the motion through the star clusters was reconstructed and stored. Considering

a maximum of 5 neighbouring stars proved to be sufficient even in the larger and denser star clusters. Because the gravitational force is proportional to  $1/r^2$ , in most cases it is the nearest neighbour that has the largest perturbing effect on the planetary systems, even if the star in the second-nearest position is a very massive one. However, since weak cumulative effects should also play a role for planetary systems close to the instability, the choice of 5 neighbouring stars to be taken into account proved to be a suitable compromise between the accuracy of the simulation and its computational cost.

In order to investigate the behaviour of Solar system analogues in star clusters and to be able to compare the results with previous studies, in Chapter 3 variants of the Solar system were distributed around all 200 Sun-like stars in each of the four clusters. For numerical and dynamical reasons, all variations of the Solar system consisted only of the four massive giant planets Jupiter, Saturn, Uranus and Neptune. All orbits were initially coplanar and six slightly different initial orbital configurations were used which were adopted from [Li & Adams \(2015\)](#).

In the standard configuration, all four planets were placed on circular orbits with their present-day semimajor axes. In the compact configuration, the semimajor axes for Saturn, Uranus and Neptune were reduced compared to the standard configuration. A third, even more compact configuration, placed Jupiter/Saturn and Saturn/Uranus each in a 3:2 mean-motion resonance, and Uranus/Neptune in a 5:4 mean-motion resonance, which is why this configuration was referred to as the resonant configuration. In three further configurations, the semimajor axes were adopted from the standard configuration and a different parameter was changed. Two eccentric configurations placed the planets on eccentric orbits, once with the planets' present-day eccentricities and once with initial eccentricities of  $e = 0.1$  for all four planets. In the sixth configuration, all planetary masses were set to  $1 M_{\text{Jup}}$ . To ensure comparability and to be able to work out the different behaviour of the individual configurations in the star cluster, the same 200 stars per cluster were used as host stars for all six initial orbital configurations.

As the most massive (in five out of six configurations) and innermost planet at the beginning of the simulations, Jupiter had by far the highest average survival rate across all 4 800 simulations performed. Saturn had the second highest survival rate in all orbital configurations, but in the massive configuration (where all planets had the same mass) it was similar to that of Uranus and Neptune.

This shows that in a multiplanetary system it is primarily the mass of a planet (in relation to the masses of the other planets) and only secondarily its position within the system that determines whether it is ejected from the system as a result of stellar encounters.

Since Uranus has only about 85% of the mass of Neptune, it was more easily directly ejected (by stellar encounters) or indirectly ejected (by subsequent instabilities) from the system than the outermost planet Neptune, apart from the configuration with equal masses.

Due to its compactness, the resonant configuration was on average the most unstable planetary system with the highest ejection rate. Within the cluster environments, even the weak cumulative perturbations of distant stars caused the resonances to break up and rapidly reach instability. Long-term stability in the resonant configuration was only reached by a rapid ejection within the first few million years of at least one of the four planets, combined with a low encounter rate during the rest of the simulation.

In terms of resilience to stellar flybys, the standard and compact configurations, as well as the first eccentric configuration (with present-day eccentricities), achieved comparable results regardless of the stellar density in the cluster. The average survival rate of all planets was about 76% in the smallest cluster in all three configurations and decreased with increasing density to about 58% in the largest cluster. Although the stellar density of the environment generally correlated with the average ejection rate, there was only a minor difference in the average survival rate between the clusters with 16 000 and 32 000 stars in all configurations with inhomogeneous mass distributions. The reason for this was a slight redistribution of the survival rates between the planets. In the standard configuration as well as in both eccentric configurations, the survival probability of Jupiter increased at the expense of the two outer planets Uranus and Neptune, respectively, which only marginally decreased the average value (see Fig. 3.4). The reason for this was the increase in direct ejections, which primarily affected the two outer and less massive planets Uranus and Neptune, and the decrease in delayed ejections (by passing on an angular momentum deficit to the inner massive planets) with increasing stellar density. A homogeneous mass distribution between the planets, on the other hand, resulted in an almost linear decrease in the survival rates of all planets with increasing numbers of particles in the cluster at constant half-mass radius.

The survival rates of individual planets in the simulations presented in Chapter 3 were significantly lower than in [Li & Adams \(2015\)](#) and [Fujii & Hori \(2019\)](#). This is due to several reasons. The most important reason is the consideration of delayed ejections due to planet-planet scattering in the simulations presented here. For this, both the multiplicity of the planetary system and the possibility of multiple flybys play a crucial role. Both are neglected in [Li & Adams \(2015\)](#) as well as in [Fujii & Hori \(2019\)](#). Furthermore, the star cluster environments simulated in this thesis are larger and denser than in both previous studies, resulting in limited comparability. Furthermore, the methodology used in this work differs from that in [Li & Adams \(2015\)](#), who perform Monte Carlo scattering experiments. The actual distribution of impact parameters and relative velocities of encounters in star clusters as simulated in this thesis differs significantly from those in [Li](#)

& Adams (2015). Most Monte Carlo approaches assume simple distribution functions in the encounter phase space, such as constant distributions for  $p^2$  (with  $p$  being the impact parameter; see eq. 4 in Spurzem et al. 2009) and Maxwellian-type distributions for the encounter velocities. Figures 1 and 2 in Spurzem et al. (2009) show the distributions of encounter parameters in a real star cluster. In this respect, numerical  $N$ -body simulations are methodologically superior to approaches such as Monte Carlo simulations, but at the same time much more computationally expensive.

In some systems with weak external perturbations, such as in both eccentric configurations in Fig. 3.11, an exchange of the positions of Uranus and Neptune was observed once or even several times. This is an interesting observation because some studies assume that the Solar system was originally much more compact (the so-called Nice model; Gomes et al. 2005; Tsiganis et al. 2005; Morbidelli et al. 2005) and Uranus and Neptune may have swapped positions in the course of their outward migration. Tsiganis et al. (2005) calculated a 50% probability of a swap between Uranus and Neptune based on simulations. This is supported by the study of Desch (2007), who used calculations of the surface density profile of the Solar protoplanetary disc to conclude that the gas and ice giants of the Solar system were formed in order of decreasing mass. The extent to which weak stellar encounters could explain the properties of the Solar system as an alternative or complement to the Nice model should be investigated in further studies.

## 6.2 The Birth Cluster as Potential Origin for White Dwarf Pollution Drivers

In Chapter 4, the formation of eccentric orbits as a result of stellar encounters from initially circular orbits in planetary systems with multiple super-Earths was investigated. Eccentric super-Earths are considered to be the main drivers for the pollution of white dwarf atmospheres, as they are particularly effective at transporting minor bodies (such as asteroids) towards a central white dwarf on long timescales (Frewen & Hansen 2014; Mustill et al. 2018). Since metals in a hydrogen-dominated atmosphere would sink within a few days due to the high density of the white dwarf (e.g. Smallwood et al. 2018), debris must be continuously accreted onto the stellar remnant for atmospheric pollution to be observed, which is the case for 25-50% of all white dwarfs in the Milky Way (Zuckerman et al. 2003, 2010; Koester et al. 2014). More than 99% of all known exoplanet-hosting stars will eventually evolve into white dwarfs<sup>1</sup>. Those

---

<sup>1</sup>As of January 2022, the [NASA Exoplanet Archive](#) lists only 4 exoplanet hosting stars with  $M_{\star} > 7 M_{\odot}$ .

planets that are not engulfed by the expanding stellar envelope during the giant-branch phase can potentially survive until the white-dwarf phase, while maintaining the shape of their orbit, with a simultaneous increase in their semimajor axis due to the host star's mass loss during its post-main-sequence evolution. Due to observational limitations and the planet's long orbital periods, super-Earths around main-sequence stars on orbits of several astronomical units have so far been difficult to detect<sup>2</sup>.

The aim of Chapter 4 was therefore to simulate a possible birth environment for multiplanetary systems containing super-Earths around the typical main-sequence progenitor stars of observed polluted white dwarfs, which typically had masses between  $1.5 M_{\odot}$  and  $2.5 M_{\odot}$  during their main-sequence phase. The smallest cluster ( $N = 8000$ ) from Chapter 3 was used as birth environment and the motion of those stars whose masses were between  $1.25 M_{\odot}$  and  $3.25 M_{\odot}$  was reconstructed from the star cluster simulation output. For the numerical integration of the planetary systems, these 408 found stars were assigned a stellar mass of  $1.5 M_{\odot}$ ,  $2.0 M_{\odot}$  or  $2.5 M_{\odot}$ , depending on which value they were closest to.

As already seen in Chapter 3, the exact orbital configuration of a planetary system is crucial for its dynamical evolution when exposed to external perturbations. Therefore, two extreme cases were constructed in terms of planetary multiplicity and orbital spacing. One configuration with 3 super-Earths (3P model), and two configurations with 7 super-Earths each, one in a compact configuration (7PC model) and one in a wide configuration (7PW model). All planets had masses of  $0.01 M_{\text{Jup}} (\approx 3.2 M_{\oplus})$ . In order to achieve the highest possible stability of the planetary systems in isolation, the planets were distributed in the system according to a fixed number of mutual Hill radii. Assuming that planets form on coplanar and circular orbits, all planets started on orbits with  $e = 0$  and  $i = 0^{\circ}$ . All three different planetary system models were simulated around all three types of host star masses. These 1224 different planetary systems were integrated for a total of 100 Myr until the star cluster had expanded sufficiently so that the probability for close encounters between the stars had significantly decreased (see Fig. 1.10).

In six of the 1224 planetary systems, mean-motion resonances between planets were found at the end of the simulation. In addition to four first-order resonances, one third-order resonance and one seventh-order resonance emerged. In contrast to Raymond et al. (2008), the instabilities as a result of which the resonances arose in the simulations presented in Chapter 4 were of external rather than internal origin. Secular and mean-motion resonances in planetary systems can be an additional source of white dwarf pollution (Debes et al. 2012; Smallwood et al. 2018, 2021; Antoniadou & Veras 2019; Veras et al. 2021). For example, secular resonances can shift

---

<sup>2</sup>As of January 2022, the [NASA Exoplanet Archive](#) lists only 13 exoplanets with  $a > 1$  au and  $m_{\text{pl}} < 10 M_{\oplus}$ .

outwards into previously stable regions of an asteroid belt during stellar evolution (Smallwood et al. 2021). The asteroids in these regions would then experience an increase in their eccentricity and eventually be tidally disrupted by the white dwarf. Resonances that already arise during the star cluster phase, however, do not necessarily survive the mass loss during the giant branch phase (Veras & Hinkley 2021).

Depending on the planetary system model and the host star mass, planets were perturbed to different degrees by the cluster environment. The criterion for a significant perturbation was a deviation of more than 5% from the initial semimajor axis value or an excitation of the eccentricity to  $e > 0.1$ . While for the 3P model around  $1.5 M_{\odot}$  stars only 17% of the planets had experienced significant perturbations, for the 7PW model around  $2.5 M_{\odot}$  stars it was already 29%. The fraction of perturbed planets thus slightly correlated with the multiplicity and the orbital width of the planetary system respectively, as well as with the host star mass. Although the mass of the host star was not a direct cause for the increased perturbation of planets in the system, more massive stars tend to sink towards the cluster centre, where the stellar density and thus the number and impact of encounters with neighbouring stars is generally higher. This effect is known as mass segregation.

More than 6% of all planets experienced an excitation of the orbital eccentricity to values larger than 0.5, while 25% of all planets had an eccentricity of  $e > 0.17$  and 30% had  $e > 0.1$  at the end of the simulation. The spread in eccentricities at the end of the simulations covered in all models the entire parameter space.

In systems where planet-planet scattering occurred as a result of the external stellar perturbations, a significant change in the planetary semimajor axes was observed. The middle planet from one of the 7PC systems was even kicked from its initial semimajor axis at 6.1 au to an orbit with a semimajor axis of more than 1000 au. Especially due to eccentricity excitation, but also due to inward migration, between 5% and 16% of the planets reached a critical engulfment distance, the exact value of which depends on the respective stellar mass. Planets below this periastron distance would be engulfed by the host star during the giant-branch phase. The orbits of the surviving planets would be driven to wider orbits due to the mass loss of the star during subsequent evolutionary phases, while keeping their eccentricities from the cluster and main-sequence phase.

Therefore, in principle, a sufficiently dense natal star cluster can contribute to the evolution of eccentric super-Earths and thus potentially also indirectly to the chemical pollution of the white dwarf's atmosphere hundreds of millions to a few billion years later. However, based on the simulation results presented in Chapter 4, no prediction can be made about which of the

resulting planetary system architectures would be particularly effective in transporting smaller bodies from the system (which were not considered in these simulations) towards the surface of the white dwarf. To allow this question to be addressed in later studies, the simulation outputs from Chapter 4 were made available to the scientific community to serve as input parameters for simulations along the different evolutionary phases of the central stars.

### 6.3 Stellar Flybys as a Trigger for Hot Jupiter Formation

Despite the large number of hot Jupiters discovered so far, their formation is still not fully understood. From today's perspective, the two most promising scenarios are based on the formation of a cold Jupiter (with  $m_{\text{pl}} > 0.1 M_{\text{Jup}}$ ) on an orbit with  $T > 200$  d, followed by further inward migration. Besides disc migration, tidal migration offers a possible explanation for the migration of these planets to orbits with periods of less than 10 days.

In Chapter 5 I investigated whether the flybys of neighbouring stars in a star cluster can trigger a chain process characterised by the creation of an angular momentum deficit in the system's outer planets, the propagation of this angular momentum deficit via planet-planet scattering to inner planets and subsequent high-eccentricity tidal migration of an inner planet leading to the formation of a hot Jupiter. For this purpose, the time-lag model of Hut (1981) was implemented to simulate tidal interaction between star and planet.

The densest star cluster with 64 000 stars was chosen as the star cluster environment in this chapter. Two different planetary system models were distributed around the 200 most Sun-like stars in the cluster and integrated for 100 million years as in the previous chapters. The first planetary system model contained five Jovian-mass planets on orbits with semimajor axes of 1 au, 5 au, 10 au, 20 au and 30 au. Assuming that giant planets form beyond the ice line at about 3 au (Hayashi 1981; Podolak & Zucker 2004), this planetary system model would require the prior migration of a planet to a smaller orbit during the disc phase. To avoid this constraint, a second planetary system model was created for comparison, in which the innermost planet at 1 au is missing.

The criterion from Hamers et al. (2017), which considers planets with a semilatus rectum of  $p < 0.091$  au as hot Jupiters that are in the process of forming, was fulfilled in 40% of all systems for the first planetary system model (which was most similar to the model in Hamers et al. 2017) and was thus slightly above the result of Hamers et al. (2017) of 32%. According to this criterion, almost 10% of all planets would have evolved into hot Jupiters in the first planetary system model

and about 4% in the second planetary system model. However, a closer look at these systems showed that this criterion was insufficient for the simulations carried out in this work without an additional criterion for the duration of  $p$  dropping below this limit. Thus, it also included planets that fell below this limit for a very short period of time during their ejection or due to persistent interactions with other planets in the system, but did not have a sufficient probability of undergoing any significant tidal evolution.

These planets were therefore only referred to as candidates, while all planets that met this criterion for at least 100 000 years during the simulation period were referred to as actual hot Jupiters (regardless of whether they had already achieved an orbital period of less than 10 days by the end of the simulation). This improved criterion was achieved in 18% of all systems for the first planetary system model and in 1.5% for the second planetary system model. Thus, the second planetary system model was significantly closer to the assumed occurrence rate of hot Jupiters around Sun-like stars of about 1% (see e.g. [Dawson & Johnson 2018](#), and references therein). Thus, prior disc migration of one of the planets would not be a requirement for the formation of hot Jupiters as a result of stellar flybys. Similarly, four Jupiter-mass planets in the system appear sufficient to propagate the induced angular momentum deficit inwards via planet-planet scattering. Whether as few as 3 Jupiter-mass planets or 4 giant planets similar to our Solar system would be sufficient could be investigated in future simulations.

In all systems where hot Jupiters were formed or were in the process of formation, at least one planet, but most often two planets (and even three for the first planetary system model) were ejected from the system during planet-planet scattering following the stellar encounter. In the systems where candidates had emerged, the maximum normalised angular momentum deficit was at least 0.45 and 0.6 for the first and second planetary system models, respectively. This means that in these two planetary system models, at least about half of the angular momentum present in the system must be transferred to the passing star during an encounter for a planet in the system to experience tidal interaction with the star.

In addition, all the hot Jupiters presented in Chapter 5 had very inclined and in some cases retrograde orbits. In all of these systems, the orbits of the hot Jupiters were inclined to the remaining planets in the system in such a way that if the hot Jupiter had been detected by the transit method, it was very likely that the remaining planets in the system would not have been discovered. Only in some cases with oscillating inclinations, where the values briefly overlapped, this would have been in principle possible.

This could indicate that for exoplanetary systems with hot Jupiters where no other planets were found using the transit method, it could be promising to search for other planets in the system with spectroscopic or astrometric follow-up observations, for example.

Furthermore, in one case Kozai oscillations (Kozai 1962) of eccentricity and inclination were observed for two surviving planets in a system (one of which showed tidal interaction with the star). These oscillations were triggered by a chain process of stellar flyby and planet-planet scattering. Since the Lidov-Kozai mechanism (Lidov 1962; Kozai 1962) periodically “pumps” the eccentricity of the inner planet to high values, this effect can also facilitate the formation of hot Jupiters. Like for the onset of planet-planet scattering, the Lidov-Kozai mechanism first requires a certain degree of instability in the system, as the orbits of both planets must have a mutual inclination that is within a critical range ( $i_{\text{init}} = 39.2^\circ\text{--}140.8^\circ$ ). For both mechanisms, stellar encounters can serve as triggers, as demonstrated in Chapter 5.

That star cluster environments can facilitate the formation of hot Jupiters is also supported by the observations of Brucalassi et al. (2017), who find a (statistically marginally) higher occurrence rate for hot Jupiters in the Solar-metallicity open star cluster M67 than around field stars.

## 6.4 Comparison of the Simulation Results with the Population of Detected Exoplanets

Statistical evaluations of the exoplanet population show that a considerable proportion of all exoplanets have non-circular orbits. At first glance, however, this contradicts the assumption that planets in a disc form on almost circular, coplanar orbits, as already assumed by Kant (1755) and Laplace & Fourier (1835) and which was supported by observations of the planets in the Solar system. With an increasing number of discovered planets on eccentric orbits during the last 25 years, the suggestion that planet-planet scattering or other gravitational interactions are an important process in the early phase of planetary systems soon emerged (e.g. Cumming 2010).

The simulations presented in this thesis confirm the importance of both aspects and at the same time suggest that the birth environment of the central star, due to gravitational interactions with the planetary system, may be a hitherto largely underestimated aspect in the dynamical evolution of planetary systems. On the one hand, stellar flybys of neighbouring stars can directly and immediately change the orbital architecture of a planetary system to a considerable extent, e.g. by ejecting single or multiple planets. On the other hand, encounters with other stars can trigger a fatal planet-planet scattering process that, by propagating the induced angular momentum deficit

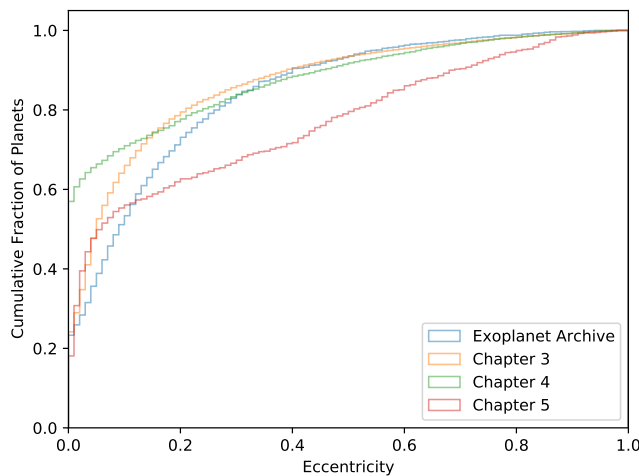


**Fig. 6.1.:** Cumulative histogram for the eccentricity distribution in the simulation results from Chapter 3–5 in comparison to the actual distribution in the exoplanet population discovered so far according to the [NASA Exoplanet Archive](#) (as of January 2022).

inwards, can also significantly affect the orbital parameters and survival probabilities of inner planets.

Figure 6.1 shows the cumulative distribution of eccentricities in the simulations presented in the different chapters compared to the actual observed distribution of eccentricities in the known exoplanet population. It is obvious that the different variations of the Solar system in four different star cluster environments from Chapter 3 most closely represent the actual distribution of eccentricities. This is in agreement with [Ford et al. \(2003\)](#), who showed that an uneven mass distribution in the planetary system produces an eccentricity distribution consistent with the observed one. The planetary system models from Chapter 4, which consist exclusively of equal-mass super-Earths and which were placed in a less dense star cluster environment, show too many nearly circular orbits in direct comparison. The distribution of eccentricities for the planetary system models from Chapter 5, which consisted only of Jupiter-mass planets and which were embedded in the densest star cluster environment, on the other hand shows an almost linear increase towards large eccentricities, suggesting that an unusual large fraction of planets were excited to high eccentricities. This is mainly due to the fact that the aim of this chapter has been to get a first idea of whether star cluster environments can facilitate the formation of hot Jupiters. The star cluster environment and the planetary system model were therefore deliberately chosen in such a way that a particularly large amount of angular momentum exchange between the planets could be expected. The comparison with the actually observed exoplanet population

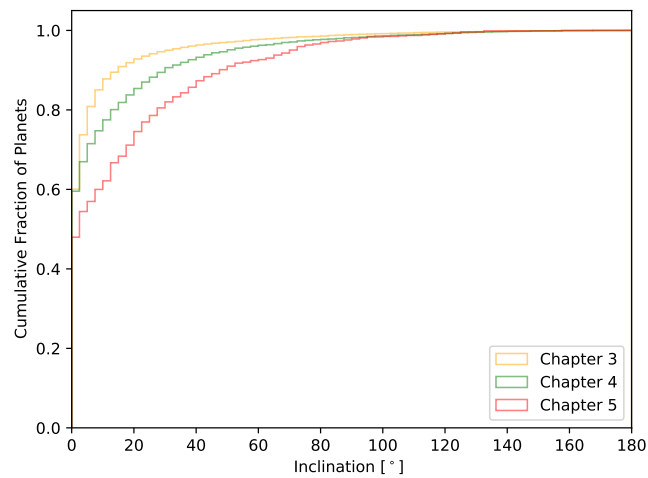


**Fig. 6.2.:** Cumulative histogram for the inclination distribution in the simulation results from Chapter 3–5.

enables a more realistic choice of initial conditions in future simulations, especially regarding the mass distribution in the planetary systems.

Figure 6.2 shows the cumulative distribution of inclinations in the different simulations. Since the orbital inclination for almost all exoplanets is undetermined, no comparison with the observed exoplanet population is possible. There is obviously no direct correlation between the inclination distributions in Fig. 6.2 and the eccentricity distributions from Fig. 6.1. However, in Figs. B.7–B.10 in the appendix, as in [Jurić & Tremaine \(2008\)](#), a correlation between both parameters could be demonstrated for high eccentricities. Figure 6.2 illustrates that stellar encounters can strongly excite the inclinations of the planets with respect to the primordial disc plane. In Chapters 3 and 4, between 0.1% and 2.2% of all planets were in retrograde orbits at the end of the simulation, depending on the planetary system model and star cluster density used. The consistency between the eccentricity distributions from Chapter 3 and the one actually observed suggests that the inclination distributions from Chapter 3 might also resemble the actual distribution of inclinations in the observed exoplanet population. Thus, it can be estimated that about 1–2% of all exoplanets could be on a retrograde orbit. Misalignments between the stellar spin axis and planetary orbits can be measured for transiting planets using the Rossiter-McLaughlin effect<sup>3</sup> (see e.g. [Winn et al. 2005](#); [Ohta et al. 2005](#)). Once reliable statistics are available for a representative sample of the

<sup>3</sup>The Rossiter-McLaughlin effect is caused by the alteration of photospheric line profiles that occurs when the planet temporarily reduces the intensity of the blue- and red-shifted spectral lines during a transit, which result from the rotation of the star.

exoplanet population, future studies can compare these statistics with simulation results such as those presented in this thesis.

## 6.5 Conclusion and Outlook

This thesis has demonstrated that the great diversity of exoplanetary orbits can be explained by the gravitational influence of star cluster, which are the typical birth environments for stars and planets. The role of external perturbations due to stellar flybys in the early phase of planetary systems has often been neglected or underestimated. In particular, the fact that star clusters are usually not spherical, but can have clumpy substructures in which the local stellar density is higher than in the rest of the cluster (e.g. [Lada et al. 1996](#); [Chen et al. 1997](#)), shows that using average stellar densities in star clusters may underestimate the destructive effect on young planetary systems. Furthermore, stellar densities observed in star clusters today are often used as a reference, neglecting the fact that star clusters expand considerably during their lifetime and that today's stellar densities no longer correspond to the original birth environment of planetary systems. In which star cluster environments the exoplanet population observed today typically originated should be the subject of future studies. By extrapolating the results presented in this thesis, it can be deduced that larger star clusters with higher stellar densities than those simulated here, such as globular clusters, would produce a larger fraction of unbound planets. In the clusters with 8 000 or 16 000 stars, depending on the planetary system model used, about one fifth to one quarter of all planets were ejected from the system either directly or delayed by external perturbations. Star clusters in particular could thus be targets for the search for free-floating planets using gravitational microlensing surveys, such as the *Galactic Exoplanet Survey* of the *Nancy Grace Roman Space Telescope* (see [Johnson et al. 2020](#)).

The role of binary systems has been completely neglected in this thesis. Studies such as [Laughlin & Adams \(1998\)](#), [Davies & Sigurdsson \(2001\)](#) and [Li & Adams \(2015\)](#) have investigated encounters of planetary systems with binary stars, but without full  $N$ -body treatment. Future studies could especially investigate the dynamical evolution of planets within binary systems embedded in star clusters, both circumbinary and circumstellar (around one of the two stars). Moreover, a coupling of planet formation simulations and star cluster simulations would be advantageous to obtain a more comprehensive picture of the early evolutionary phases of planetary systems. Furthermore, the simulations from Chapter 5 should be extended and varied in their initial conditions in order to be able to specify the conditions for the formation of hot Jupiters by stellar encounters.

This thesis aimed to provide an overview of the manifold effects of external gravitational perturbations on the dynamical evolution of multiplanetary systems. However, further studies on this subject are needed to improve our understanding of the overall picture of the formation and evolution of planetary systems.

Nevertheless, this thesis has highlighted one aspect: if our Solar system had formed in higher stellar density environments, it could have faced a much more violent fate. We have therefore not only hit the habitable sweet spot for formation in the Galaxy and within the Solar system, but also within our stellar birth environment.

# Bibliography of Own Publications

In accordance with the HGSFP rule, all publications for which I was either first author or co-author are listed here, including a comment on whether they were used in this thesis.

## Bibliography of first-author papers used in this thesis

- **Stock, K.**; Cai, M.; Spurzem, R.; Kouwenhoven, M. B. N.; Portegies Zwart, S.: On the survival of resonant and non-resonant planetary systems in star clusters. – *MNRAS*, 497, 1807, September 2020
- **Stock, K.**; Veras, D.; Cai, M.; Spurzem, R.; Portegies Zwart, S.: Birth cluster simulations of planetary systems with multiple super-Earths: initial conditions for white dwarf pollution drivers. – *MNRAS*, submitted in November 2021

## Bibliography of first-author papers not used in this thesis

- **Reichert, K.**; Reffert, S.; Stock, S.; Trifonov, T.; Quirrenbach, A.: Precise radial velocities of giant stars. XII. Evidence against the proposed planet Aldebaran b. – *A&A*, 625, A22, May 2019

## Bibliography of co-author papers not used in this thesis

- Veras, D.; **Reichert, K.**; Flammini Dotti, F.; Cai, M.; Mustill, A. J.; Shannon, A.; McDonald, C.; Portegies Zwart, S.; Kouwenhoven, M. B. N.; Spurzem, R.: Linking the formation and fate of exo-Kuiper belts within Solar system analogues. – *MNRAS*, 493, 5062, April 2020



# Bibliography

- Aarseth, S. J. 1999, *PASP*, 111, 1333
- Aarseth, S. J. 2003, *Gravitational N-Body Simulations*
- Aarseth, S. J., Tout, C. A., & Mardling, R. A. 2008, *The Cambridge N-Body Lectures*, Vol. 760 (Springer-Verlag Berlin Heidelberg)
- Adams, F. C. & Bloch, A. M. 2013, *ApJ*, 777, L30
- Ahmad, A. & Cohen, L. 1973, *Journal of Computational Physics*, 12, 389
- Albrecht, S. H., Marcussen, M. L., Winn, J. N., Dawson, R. I., & Knudstrup, E. 2021, *ApJ*, 916, L1
- Alexander, M. E. 1973, *Ap&SS*, 23, 459
- ALMA Partnership, Brogan, C. L., Pérez, L. M., et al. 2015a, *ApJ*, 808, L3
- ALMA Partnership, Fomalont, E. B., Vlahakis, C., et al. 2015b, *ApJ*, 808, L1
- Anderson, D. R., Hellier, C., Gillon, M., et al. 2010, *ApJ*, 709, 159
- Anderson, K. R., Adams, F. C., & Calvet, N. 2013, *ApJ*, 774, 9
- Andrews, S. M., Huang, J., Pérez, L. M., et al. 2018, *ApJ*, 869, L41
- Antoniadou, K. I. & Veras, D. 2016, *MNRAS*, 463, 4108
- Antoniadou, K. I. & Veras, D. 2019, *A&A*, 629, A126
- Antonov, V. A. 1985, in *Dynamics of Star Clusters*, ed. J. Goodman & P. Hut, Vol. 113, 525
- Armitage, P. J. 2000, *A&A*, 362, 968
- Banerjee, S., Belczynski, K., Fryer, C. L., et al. 2020, *A&A*, 639, A41
- Baronett, S. A., Ferich, N., Tamayo, D., & Steffen, J. H. 2021, arXiv e-prints, arXiv:2101.12277
- Barrientos, M. & Chanamé, J. 2021, *ApJ*, 923, 181
- Baruteau, C., Crida, A., Paardekooper, S. J., et al. 2014, in *Protostars and Planets VI*, ed. H. Beuther, R. S. Klessen, C. P. Dullemond, & T. Henning, 667

- Bate, R. R., Mueller, D. D., & White, J. E. 2020, *Fundamentals of astrodynamics.*, 2nd edn. (Dover Publications)
- Bayliss, D. D. R., Winn, J. N., Mardling, R. A., & Sackett, P. D. 2010, *ApJ*, 722, L224
- Beck, J. G. & Giles, P. 2005, *ApJ*, 621, L153
- Becker, J. C. & Batygin, K. 2013, *ApJ*, 778, 100
- Bettwieser, E. & Sugimoto, D. 1984, *MNRAS*, 208, 493
- Beust, H. & Morbidelli, A. 1996, *Icarus*, 120, 358
- Birnstiel, T., Dullemond, C. P., & Brauer, F. 2010, *A&A*, 513, A79
- Blackman, J. W., Beaulieu, J. P., Bennett, D. P., et al. 2021, *Nature*, 598, 272
- Blouin, S. & Xu, S. 2022, *MNRAS*, 510, 1059
- Boekholt, T. C. N., Portegies Zwart, S. F., & Valtonen, M. 2020, *MNRAS*, 493, 3932
- Bolmont, E., Raymond, S. N., Leconte, J., Hersant, F., & Correia, A. C. M. 2015, *A&A*, 583, A116
- Bonsor, A., Mustill, A. J., & Wyatt, M. C. 2011, *MNRAS*, 414, 930
- Boss, A. P. 1997, *Science*, 276, 1836
- Brucalassi, A., Koppenhoefer, J., Saglia, R., et al. 2017, *A&A*, 603, A85
- Brucalassi, A., Pasquini, L., Saglia, R., et al. 2014, *A&A*, 561, L9
- Brucalassi, A., Pasquini, L., Saglia, R., et al. 2016, *A&A*, 592, L1
- Butler, R. P., Marcy, G. W., Vogt, S. S., & Apps, K. 1998, *PASP*, 110, 1389
- Butler, R. P., Marcy, G. W., Williams, E., Hauser, H., & Shirts, P. 1997, *ApJ*, 474, L115
- Cai, M. X., Kouwenhoven, M. B. N., Portegies Zwart, S. F., & Spurzem, R. 2017, *MNRAS*, 470, 4337
- Cai, M. X., Meiron, Y., Kouwenhoven, M. B. N., Assmann, P., & Spurzem, R. 2015, *ApJS*, 219, 31
- Cai, M. X., Portegies Zwart, S., Kouwenhoven, M. B. N., & Spurzem, R. 2019, *MNRAS*, 489, 4311
- Cai, M. X., Portegies Zwart, S., & van Elteren, A. 2018, *MNRAS*, 474, 5114
- Carroll, B. W. & Ostlie, D. A. 2007, *An Introduction to Modern Astrophysics*, pearson new international edition, 2 edn. (San Francisco, CA: Pearson, Addison Wesley)

- Chambers, J. E. 2001, *Icarus*, 152, 205
- Chen, H., Tafalla, M., Greene, T. P., Myers, P. C., & Wilner, D. J. 1997, *ApJ*, 475, 163
- Clarke, C. J., Bonnell, I. A., & Hillenbrand, L. A. 2000, in *Protostars and Planets IV*, ed. V. Mannings, A. P. Boss, & S. S. Russell, 151
- Clarke, C. J. & Pringle, J. E. 1993, *MNRAS*, 261, 190
- Cohn, H. 1979, *ApJ*, 234, 1036
- Concha-Ramírez, F., Vaher, E., & Portegies Zwart, S. 2019, *MNRAS*, 482, 732
- Coutu, S., Dufour, P., Bergeron, P., et al. 2019, *ApJ*, 885, 74
- Cumming, A. 2010, in *Exoplanets*, ed. S. Seager, 191–214
- Cummings, J. D., Kalirai, J. S., Tremblay, P. E., Ramirez-Ruiz, E., & Choi, J. 2018, *ApJ*, 866, 21
- Danby, J. M. A. 1988, *Fundamentals of celestial mechanics*
- Darwin, G. H. 1879, *Philosophical Transactions of the Royal Society of London Series I*, 170, 1
- Davies, M. B. & Sigurdsson, S. 2001, *MNRAS*, 324, 612
- Dawson, R. I. & Johnson, J. A. 2018, *ARA&A*, 56, 175
- Debes, J. H., Walsh, K. J., & Stark, C. 2012, *ApJ*, 747, 148
- Delgado Mena, E., Lovis, C., Santos, N. C., et al. 2018, *A&A*, 619, A2
- Desch, S. J. 2007, *ApJ*, 671, 878
- Dufour, P., Bergeron, P., Liebert, J., et al. 2007, *ApJ*, 663, 1291
- Dullemond, C. P., Brauer, F., Henning, T., & Natta, A. 2008, *Physica Scripta Volume T*, 130, 014015
- Duncan, M. J., Levison, H. F., & Lee, M. H. 1998, *AJ*, 116, 2067
- Efroimsky, M. & Makarov, V. V. 2013, *ApJ*, 764, 26
- Eggleton, P. P., Kiseleva, L. G., & Hut, P. 1998, *ApJ*, 499, 853
- El-Badry, K., Rix, H.-W., & Weisz, D. R. 2018, *ApJ*, 860, L17
- Emsenhuber, A., Mordasini, C., Burn, R., et al. 2021, *A&A*, 656, A69
- Ernst, A., Just, A., Spurzem, R., & Porth, O. 2008, *MNRAS*, 383, 897
- Everhart, E. 1985, in *Astrophysics and Space Science Library*, Vol. 115, IAU Colloq. 83: Dynamics of Comets: Their Origin and Evolution, ed. A. Carusi & G. B. Valsecchi, 185

- Faber, N. T., Stibbe, D., Portegies Zwart, S., McMillan, S. L. W., & Boily, C. M. 2010, *MNRAS*, 401, 1898
- Fabrycky, D. & Tremaine, S. 2007, *ApJ*, 669, 1298
- Fabrycky, D. C. 2010, *Non-Keplerian Dynamics of Exoplanets*, ed. S. Seager, 217–238
- Facchini, S., Clarke, C. J., & Bisbas, T. G. 2016, *MNRAS*, 457, 3593
- Farr, W. M., Ames, J., Hut, P., et al. 2012, *New A*, 17, 520
- Flammini Dotti, F., Kouwenhoven, M. B. N., Cai, M. X., & Spurzem, R. 2019, *MNRAS*, 489, 2280
- Ford, E. B., Rasio, F. A., & Yu, K. 2003, in *Astronomical Society of the Pacific Conference Series*, Vol. 294, *Scientific Frontiers in Research on Extrasolar Planets*, ed. D. Deming & S. Seager, 181–188
- Forgács-Dajka, E., Sándor, Z., & Érdi, B. 2018, *MNRAS*, 477, 3383
- Frewen, S. F. N. & Hansen, B. M. S. 2014, *MNRAS*, 439, 2442
- Fujii, M. S. & Hori, Y. 2019, *A&A*, 624, A110
- Gaidos, E., Mann, A. W., Rizzuto, A., et al. 2017, *MNRAS*, 464, 850
- Gänsicke, B. T., Schreiber, M. R., Toloza, O., et al. 2019, *Nature*, 576, 61
- Gladman, B., Duncan, M., & Candy, J. 1991, *Celestial Mechanics and Dynamical Astronomy*, 52, 221
- Glaser, J. P., McMillan, S. L. W., Geller, A. M., Thornton, J. D., & Giovinazzi, M. R. 2020, *AJ*, 160, 126
- Gomes, R., Levison, H. F., Tsiganis, K., & Morbidelli, A. 2005, *Nature*, 435, 466
- Gouliniski, N. & Ribak, E. N. 2018, *MNRAS*, 473, 1589
- Guenther, E. W., Paulson, D. B., Cochran, W. D., et al. 2005, *A&A*, 442, 1031
- Guillochon, J., Ramirez-Ruiz, E., & Lin, D. 2011, *ApJ*, 732, 74
- Gurfil, P. & Seidelmann, P. K. 2016, *Celestial Mechanics and Astrodynamics: Theory and Practice*, Vol. 436 (Springer-Verlag Berlin Heidelberg)
- Hall, S. M., Clarke, C. J., & Pringle, J. E. 1996, *MNRAS*, 278, 303
- Hamers, A. S., Antonini, F., Lithwick, Y., Perets, H. B., & Portegies Zwart, S. F. 2017, *MNRAS*, 464, 688
- Hamers, A. S. & Tremaine, S. 2017, *AJ*, 154, 272

- Hands, T., Dehnen, W., Gration, A., Stadel, J., & Moore, B. 2019, in AAS/Division for Extreme Solar Systems Abstracts, Vol. 51, AAS/Division for Extreme Solar Systems Abstracts, 315.02
- Hao, W., Kouwenhoven, M. B. N., & Spurzem, R. 2013, MNRAS, 433, 867
- Hayashi, C. 1981, Progress of Theoretical Physics Supplement, 70, 35
- Heggie, D. C. & Mathieu, R. D. 1986, Standardised Units and Time Scales, ed. P. Hut & S. L. W. McMillan, Vol. 267, 233
- Heisler, J. & Tremaine, S. 1986, Icarus, 65, 13
- Helled, R. & Morbidelli, A. 2021, Planet Formation, ed. N. Madhusudhan, 12–1
- Heller, R., Leconte, J., & Barnes, R. 2011, A&A, 528, A27
- Hintz, G. R. 2015, Orbital Mechanics and Astrodynamics. (Springer International Publishing Switzerland)
- Hollands, M. A., Gänsicke, B. T., & Koester, D. 2018, MNRAS, 477, 93
- Hurley, J. R., Pols, O. R., Aarseth, S. J., & Tout, C. A. 2005, MNRAS, 363, 293
- Hurley, J. R. & Shara, M. M. 2002, ApJ, 565, 1251
- Hut, P. 1981, A&A, 99, 126
- Ida, S., Larwood, J., & Burkert, A. 2000, ApJ, 528, 351
- J Jeans, J. H. 1902, Philosophical Transactions of the Royal Society of London Series A, 199, 1
- Jílková, L., Hamers, A. S., Hammer, M., & Portegies Zwart, S. 2016, MNRAS, 457, 4218
- Johnson, S. A., Penny, M., Gaudi, B. S., et al. 2020, AJ, 160, 123
- Jurić, M. & Tremaine, S. 2008, ApJ, 686, 603
- Just, A., Berczik, P., Petrov, M. I., & Ernst, A. 2009, MNRAS, 392, 969
- Kant, I. 1755, Allgemeine Naturgeschichte und Theorie des Himmels, 1st edn. (Königsberg; Leipzig: Petersen)
- Kenyon, S. J. & Bromley, B. C. 2004, Nature, 432, 598
- Kepler, S. O., Koester, D., Pelisoli, I., Romero, A. D., & Ourique, G. 2021, MNRAS, 507, 4646
- Kepler, S. O., Pelisoli, I., Koester, D., et al. 2015, MNRAS, 446, 4078
- Kepler, S. O., Pelisoli, I., Koester, D., et al. 2016, MNRAS, 455, 3413
- Khalaj, P. & Baumgardt, H. 2015, MNRAS, 452, 924

- Khalisi, E., Wang, L., & Spurzem, R. 2016, NBODY6++: Manual for the Computer Code, Tech. rep., Astronomisches Rechen-Institut
- King, I. 1962, *AJ*, 67, 471
- King, I. R. 1966, *AJ*, 71, 64
- Kiseleva, L. G., Eggleton, P. P., & Mikkola, S. 1998, *MNRAS*, 300, 292
- Klahr, H. & Schreiber, A. 2020, *ApJ*, 901, 54
- Kleinman, S. J., Kepler, S. O., Koester, D., et al. 2013, *ApJS*, 204, 5
- Kley, W., Peitz, J., & Bryden, G. 2004, *A&A*, 414, 735
- Koester, D., Gänsicke, B. T., & Farihi, J. 2014, *A&A*, 566, A34
- Kokubo, E. & Ida, S. 1998, *Icarus*, 131, 171
- Kouwenhoven, M. B. N., Goodwin, S. P., Parker, R. J., et al. 2010, *MNRAS*, 404, 1835
- Kozai, Y. 1962, *AJ*, 67, 591
- Kroupa, P. 2001, *MNRAS*, 322, 231
- Krumholz, M. R., McKee, C. F., & Bland-Hawthorn, J. 2019, *ARA&A*, 57, 227
- Kustaanheimo, P., Schinzel, A., Davenport, H., & Stiefel, E. 1965, *Journal für die reine und angewandte Mathematik*, 1965, 204
- Lada, C. J., Alves, J., & Lada, E. A. 1996, *AJ*, 111, 1964
- Lada, C. J. & Lada, E. A. 2003, *ARA&A*, 41, 57
- Lada, E. A., Strom, K. M., & Myers, P. C. 1993, in *Protostars and Planets III*, ed. E. H. Levy & J. I. Lunine, 245
- Laplace, P.-S. & Fourier, J.-B.-J. 1835, *Exposition du système du monde*, 1st edn. (Paris: Bachelier)
- Laskar, J. 1997, *A&A*, 317, L75
- Laskar, J. 2000, *Phys. Rev. Lett.*, 84, 3240
- Laskar, J. & Petit, A. C. 2017, *A&A*, 605, A72
- Laughlin, G. & Adams, F. C. 1998, *ApJ*, 508, L171
- Leconte, J., Chabrier, G., Baraffe, I., & Levrard, B. 2010, *A&A*, 516, A64
- Lee, M. H. & Peale, S. J. 2002, *ApJ*, 567, 596
- Li, D., Mustill, A. J., & Davies, M. B. 2021, arXiv e-prints, arXiv:2110.12660

- Li, G. & Adams, F. C. 2015, MNRAS, 448, 344
- Lidov, M. L. 1962, Planet. Space Sci., 9, 719
- Livingston, J. H., Dai, F., Hirano, T., et al. 2019, MNRAS, 484, 8
- Love, A. E. H. 1911, Some Problems of Geodynamics
- Luhman, K. L., Burgasser, A. J., & Bochanski, J. J. 2011, ApJ, 730, L9
- Lynden-Bell, D. & Eggleton, P. P. 1980, MNRAS, 191, 483
- Lynden-Bell, D. & Wood, R. 1968, MNRAS, 138, 495
- Madappatt, N., De Marco, O., & Villaver, E. 2016, MNRAS, 463, 1040
- Makino, J. 1996, ApJ, 471, 796
- Makino, J. & Aarseth, S. J. 1992, PASJ, 44, 141
- Malavolta, L., Nascimbeni, V., Piotto, G., et al. 2016, A&A, 588, A118
- Maldonado, R. F., Villaver, E., Mustill, A. J., Chavez, M., & Bertone, E. 2020a, MNRAS, 497, 4091
- Maldonado, R. F., Villaver, E., Mustill, A. J., Chavez, M., & Bertone, E. 2020b, MNRAS, 499, 1854
- Maldonado, R. F., Villaver, E., Mustill, A. J., Chávez, M., & Bertone, E. 2021, MNRAS, 501, L43
- Malmberg, D., Davies, M. B., & Hoggie, D. C. 2011, MNRAS, 411, 859
- Malmberg, D., de Angeli, F., Davies, M. B., et al. 2007, MNRAS, 378, 1207
- Mann, A. W., Gaidos, E., Mace, G. N., et al. 2016, ApJ, 818, 46
- Mann, A. W., Gaidos, E., Vanderburg, A., et al. 2017, AJ, 153, 64
- Mann, A. W., Vanderburg, A., Rizzuto, A. C., et al. 2018, AJ, 155, 4
- Martin, R. G. & Livio, M. 2012, MNRAS, 425, L6
- Mayor, M. & Queloz, D. 1995, Nature, 378, 355
- McCleery, J., Tremblay, P.-E., Gentile Fusillo, N. P., et al. 2020, MNRAS, 499, 1890
- McMillan, S. L. W. 1986, The Vectorization of Small-N Integrators, ed. P. Hut & S. L. W. McMillan, Vol. 267, 156
- Miller, A. A., Irwin, J., Aigrain, S., Hodgkin, S., & Hebb, L. 2008, MNRAS, 387, 349
- Miller, R. H. 1964, ApJ, 140, 250

- Millholland, S., Wang, S., & Laughlin, G. 2017, *ApJ*, 849, L33
- Mohr, P. J., Newell, D. B., & Taylor, B. N. 2016, *Journal of Physical and Chemical Reference Data*, 45, 043102
- Morbidelli, A., Levison, H. F., Tsiganis, K., & Gomes, R. 2005, *Nature*, 435, 462
- Murray, C. D. & Dermott, S. F. 1999, *Solar system dynamics*
- Mustill, A. J. & Villaver, E. 2012, *ApJ*, 761, 121
- Mustill, A. J., Villaver, E., Veras, D., Gänsicke, B. T., & Bonsor, A. 2018, *MNRAS*, 476, 3939
- Newton, I. 1687, *Philosophiae Naturalis Principia Mathematica* (London)
- Nordhaus, J. & Spiegel, D. S. 2013, *MNRAS*, 432, 500
- Obermeier, C., Henning, T., Schlieder, J. E., et al. 2016, *AJ*, 152, 223
- O'Connor, C. E., Teyssandier, J., & Lai, D. 2021, arXiv e-prints, arXiv:2111.08716
- Ohta, Y., Taruya, A., & Suto, Y. 2005, *ApJ*, 622, 1118
- Olczak, C., Pfalzner, S., & Spurzem, R. 2006, *ApJ*, 642, 1140
- Ormel, C. W. & Klahr, H. H. 2010, *A&A*, 520, A43
- Ou, J.-W., Yu, C., Yang, M., et al. 2021, *ApJ*, 922, 37
- 'Oumuamua ISSI Team, Bannister, M. T., Bhandare, A., et al. 2019, *Nature Astronomy*, 3, 594
- Papaloizou, J. C. B. & Szuszkiewicz, E. 2005, *MNRAS*, 363, 153
- Parker, R. J. 2014, *MNRAS*, 445, 4037
- Parker, R. J. 2020, *Royal Society Open Science*, 7, 201271
- Parker, R. J. & Quanz, S. P. 2012, *MNRAS*, 419, 2448
- Perets, H. B. & Kouwenhoven, M. B. N. 2012, *ApJ*, 750, 83
- Perryman, M. A. C. 2011, *The exoplanet handbook* (Cambridge [u.a.]: Cambridge Univ. Press), X, 410 S.
- Pfalzner, S. & Bannister, M. T. 2019, *ApJ*, 874, L34
- Plummer, H. C. 1911, *MNRAS*, 71, 460
- Podolak, M. & Zucker, S. 2004, *Meteoritics & Planetary Science*, 39, 1859
- Pollack, J. B., Hubickyj, O., Bodenheimer, P., et al. 1996, *Icarus*, 124, 62
- Portegies Zwart, S. 2011, *AMUSE: Astrophysical Multipurpose Software Environment*

- Portegies Zwart, S. & McMillan, S. 2018, *Astrophysical Recipes; The art of AMUSE*
- Portegies Zwart, S., Pelupessy, I., van Elteren, A., Wijnen, T. P. G., & Lugaro, M. 2018a, *A&A*, 616, A85
- Portegies Zwart, S., Torres, S., Pelupessy, I., Bédorf, J., & Cai, M. X. 2018b, *MNRAS*, 479, L17
- Portegies Zwart, S. F. 2009, *ApJ*, 696, L13
- Portegies Zwart, S. F. 2016, *MNRAS*, 457, 313
- Portegies Zwart, S. F. & Jílková, L. 2015, *MNRAS*, 451, 144
- Portegies Zwart, S. F., McMillan, S. L. W., & Gieles, M. 2010, *ARA&A*, 48, 431
- Privitera, G., Meynet, G., Eggenberger, P., et al. 2016, *A&A*, 591, A45
- Prša, A., Harmanec, P., Torres, G., et al. 2016, *AJ*, 152, 41
- Qian, P. X., Cai, M. X., Portegies Zwart, S., & Zhu, M. 2017, *PASP*, 129, 094503
- Quinlan, G. D. & Tremaine, S. 1992, *MNRAS*, 259, 505
- Quinn, S. N., White, R. J., Latham, D. W., et al. 2012, *ApJ*, 756, L33
- Quinn, S. N., White, R. J., Latham, D. W., et al. 2014, *ApJ*, 787, 27
- Rafikov, R. R. 2005, *ApJ*, 621, L69
- Rafikov, R. R. 2006, *ApJ*, 648, 666
- Raymond, S. N. 2015, *Hill Radius/Sphere*, ed. M. Gargaud, W. M. Irvine, R. Amils, H. J. J. Cleaves, D. L. Pinti, J. C. Quintanilla, D. Rouan, T. Spohn, S. Tirard, & M. Viso (Berlin, Heidelberg: Springer Berlin Heidelberg), 1110–1111
- Raymond, S. N., Barnes, R., Armitage, P. J., & Gorelick, N. 2008, *ApJ*, 687, L107
- Rein, H. & Liu, S. F. 2012, *A&A*, 537, A128
- Rein, H. & Spiegel, D. S. 2015, *MNRAS*, 446, 1424
- Remijan, A. J. & Hollis, J. M. 2006, *ApJ*, 640, 842
- Rizzuto, A. C., Vanderburg, A., Mann, A. W., et al. 2018, *AJ*, 156, 195
- Ronco, M. P., Schreiber, M. R., Giuppone, C. A., et al. 2020, *ApJ*, 898, L23
- Sato, B., Izumiura, H., Toyota, E., et al. 2007, *ApJ*, 661, 527
- Schlecker, M., Mordasini, C., Emsenhuber, A., et al. 2021, *A&A*, 656, A71
- Seager, S. & Lissauer, J. J. 2010, *Introduction to Exoplanets*, ed. S. Seager, 3–13

- Sheldon, J. W., Zondek, B., & Friedman, M. 1957, *Mathematical Tables and Other Aids to Computation*, 11, 181
- Sigurdsson, S., Richer, H. B., Hansen, B. M., Stairs, I. H., & Thorsett, S. E. 2003, *Science*, 301, 193
- Smallwood, J. L., Martin, R. G., Livio, M., & Lubow, S. H. 2018, *MNRAS*, 480, 57
- Smallwood, J. L., Martin, R. G., Livio, M., & Veras, D. 2021, *MNRAS*, 504, 3375
- Smith, K. W. & Bonnell, I. A. 2001, *MNRAS*, 322, L1
- Spera, M., Mapelli, M., & Bressan, A. 2015, *MNRAS*, 451, 4086
- Spurzem, R. 1999, *Journal of Computational and Applied Mathematics*, 109, 407
- Spurzem, R., Berentzen, I., Berczik, P., et al. 2008, *Parallelization, Special Hardware and Post-Newtonian Dynamics in Direct N - Body Simulations*, ed. S. J. Aarseth, C. A. Tout, & R. A. Mardling, Vol. 760, 377
- Spurzem, R., Giersz, M., Heggie, D. C., & Lin, D. N. C. 2009, *ApJ*, 697, 458
- Stock, K., Cai, M. X., Spurzem, R., Kouwenhoven, M. B. N., & Portegies Zwart, S. 2020, *MNRAS*, 497, 1807
- Stock, K., Veras, D., Cai, M. X., Spurzem, R., & Portegies Zwart, S. 2022, *MNRAS*, submitted on 17/11/2021, re-submitted on 26/01/2022
- Störzner, H. & Hollenbach, D. 1999, *ApJ*, 515, 669
- Tadeu dos Santos, M., Correa-Otto, J. A., Michtchenko, T. A., & Ferraz-Mello, S. 2015, *A&A*, 573, A94
- Tamayo, D., Cranmer, M., Hadden, S., et al. 2020a, in *AAS/Division of Dynamical Astronomy Meeting*, Vol. 52, AAS/Division of Dynamical Astronomy Meeting, 300.01
- Tamayo, D., Rein, H., Shi, P., & Hernandez, D. M. 2020b, *MNRAS*, 491, 2885
- Thorsett, S. E., Arzoumanian, Z., & Taylor, J. H. 1993, *ApJ*, 412, L33
- Toomer, G. J. 1998, *Ptolemy's ALMAGEST* (Princeton University Press)
- Torres, S., Cai, M. X., Brown, A. G. A., & Portegies Zwart, S. 2019, *A&A*, 629, A139
- Tremblay, P. E., Cummings, J., Kalirai, J. S., et al. 2016, *MNRAS*, 461, 2100
- Tsiganis, K., Gomes, R., Morbidelli, A., & Levison, H. F. 2005, *Nature*, 435, 459
- Turrini, D., Zinzi, A., & Belinchon, J. A. 2020, *A&A*, 636, A53
- van Elteren, A., Portegies Zwart, S., Pelupessy, I., Cai, M. X., & McMillan, S. L. W. 2019, *A&A*, 624, A120

- Vanderburg, A., Rappaport, S. A., Xu, S., et al. 2020, *Nature*, 585, 363
- Veras, D. 2021, *Planetary Systems Around White Dwarfs*, 1
- Veras, D. & Gänsicke, B. T. 2015, *MNRAS*, 447, 1049
- Veras, D., Georgakarakos, N., Mustill, A. J., et al. 2021, *MNRAS*, 506, 1148
- Veras, D. & Hinkley, S. 2021, *MNRAS*, 505, 1557
- Veras, D., Mustill, A. J., Gänsicke, B. T., et al. 2016, *MNRAS*, 458, 3942
- Veras, D., Reichert, K., Flammini Dotti, F., et al. 2020, *MNRAS*, 493, 5062
- Veras, D., Wyatt, M. C., Mustill, A. J., Bonsor, A., & Eldridge, J. J. 2011, *MNRAS*, 417, 2104
- Villaver, E., Livio, M., Mustill, A. J., & Siess, L. 2014, *ApJ*, 794, 3
- Wang, J., Fischer, D. A., Horch, E. P., & Huang, X. 2015a, *ApJ*, 799, 229
- Wang, L., Kouwenhoven, M. B. N., Zheng, X., Church, R. P., & Davies, M. B. 2015b, *MNRAS*, 449, 3543
- Wang, L., Spurzem, R., Aarseth, S., et al. 2016, *MNRAS*, 458, 1450
- Wang, L., Spurzem, R., Aarseth, S., et al. 2015c, *MNRAS*, 450, 4070
- Weigert, A., Wendker, H. J., & Wisotzki, L. 2010, *Astronomie und Astrophysik*, 5th edn., Lehrbuch Physik (Weinheim: Wiley-VCH)
- Weiss, L. M., Marcy, G. W., Petigura, E. A., et al. 2018, *AJ*, 155, 48
- Weldrake, D. T. F. 2008, in *Astronomical Society of the Pacific Conference Series*, Vol. 398, *Extreme Solar Systems*, ed. D. Fischer, F. A. Rasio, S. E. Thorsett, & A. Wolszczan, 133
- Winn, J. N., Johnson, J. A., Albrecht, S., et al. 2009, *ApJ*, 703, L99
- Winn, J. N., Noyes, R. W., Holman, M. J., et al. 2005, *ApJ*, 631, 1215
- Xu, W., Lai, D., & Morbidelli, A. 2018, *MNRAS*, 481, 1538
- Zapatero Osorio, M. R., Béjar, V. J. S., Martín, E. L., et al. 2000, *Science*, 290, 103
- Zapatero Osorio, M. R., Gálvez Ortiz, M. C., Bihain, G., et al. 2014, *A&A*, 568, A77
- Zheng, X., Kouwenhoven, M. B. N., & Wang, L. 2015, *MNRAS*, 453, 2759
- Zuckerman, B., Koester, D., Reid, I. N., & Hünsch, M. 2003, *ApJ*, 596, 477
- Zuckerman, B., Melis, C., Klein, B., Koester, D., & Jura, M. 2010, *ApJ*, 722, 725



## Appendix for Chapter 1

### A.1 Additional Material for Sec. 1.2.2

The full derivation of Eq. 1.22 is:

$$\begin{aligned} -\frac{GM}{r^3}(\vec{r} \times \vec{h}) &= \frac{GM}{r^3}(\vec{h} \times \vec{r}) = \frac{GM}{r^3}(\vec{r} \times \vec{v}) \times \vec{r} = \frac{GM}{r^3}(\vec{v}(\vec{r} \cdot \vec{r}) - \vec{r}(\vec{r} \cdot \vec{v})) \\ &= \frac{GM}{r}\vec{v} - \frac{GM\dot{r}}{r^2}\vec{r} = GM\left(\frac{\vec{v}}{r} - \frac{\dot{r}\vec{r}}{r^2}\right) = GM\frac{d}{dt}\left(\frac{\vec{r}}{r}\right). \end{aligned} \quad (\text{A.1})$$

### A.2 Additional Material for Sec. 1.2.3

In polar coordinates, the position and acceleration vectors can be written as

$$\vec{r} = r\vec{e}_r \quad (\text{A.2})$$

and

$$\dot{\vec{r}} = \dot{r}\vec{e}_r + r\dot{\theta}\vec{e}_\theta, \quad (\text{A.3})$$

where  $\vec{e}_r$  and  $\vec{e}_\theta$  represent unit vectors along and perpendicular to  $\vec{r}$ , respectively. The specific angular momentum in polar coordinates is then:

$$\vec{h} = r^2\dot{\theta}\vec{e}_z, \quad (\text{A.4})$$

where  $\vec{e}_z$  is a unit vector perpendicular to the plane of the orbit. Therefore,

$$h = r^2\dot{\theta}. \quad (\text{A.5})$$



## Appendix for Chapter 3

# B

### B.1 Additional Material

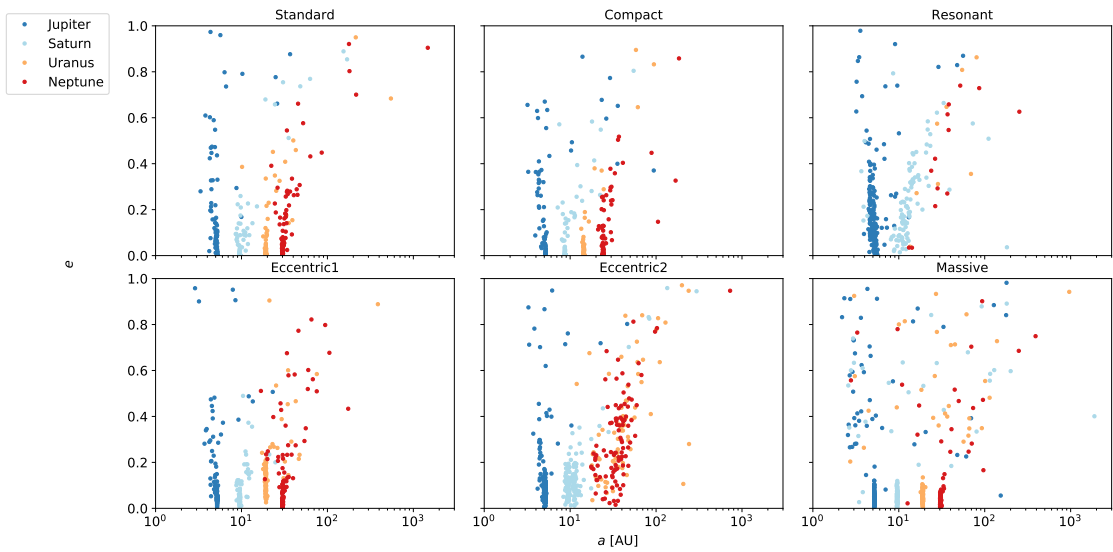


**Fig. B.1.:** Same as Fig. 3.5 but for the 16k cluster.

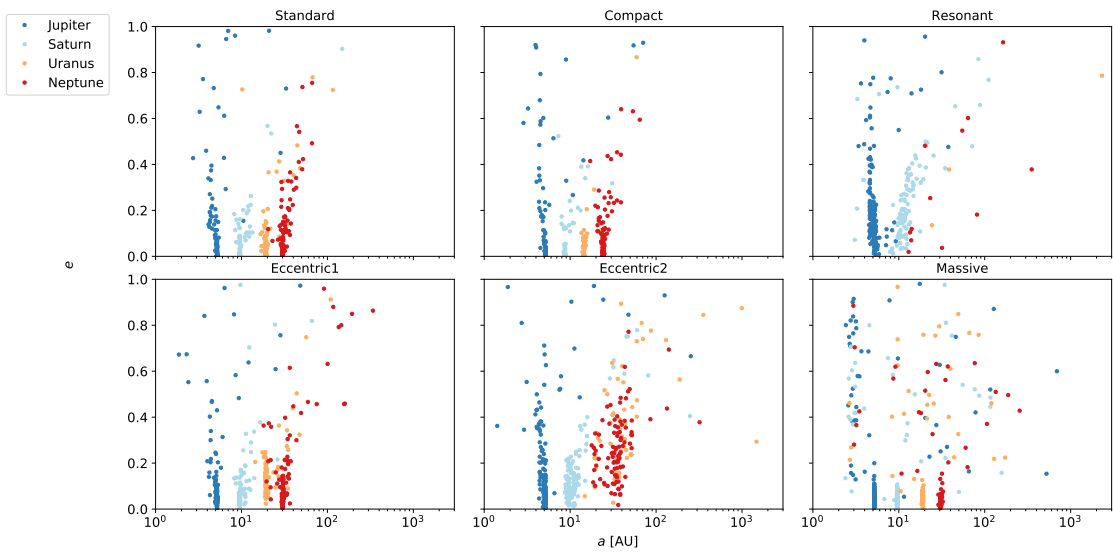


**Fig. B.2.:** Same as Fig. 3.5 but for the 32k cluster.

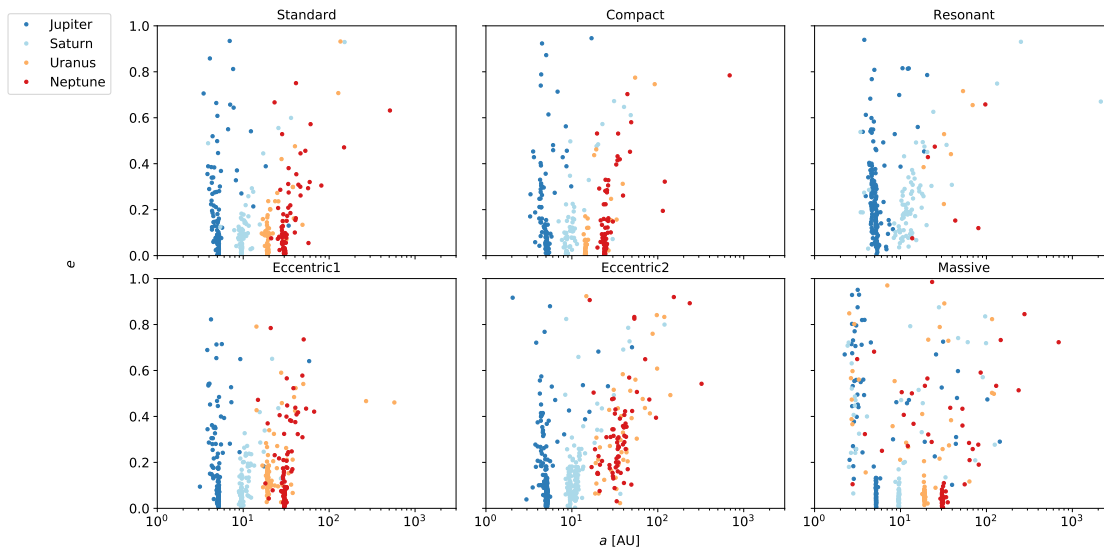


Fig. B.3.: Same as Fig. 3.5 but for the 64k cluster.

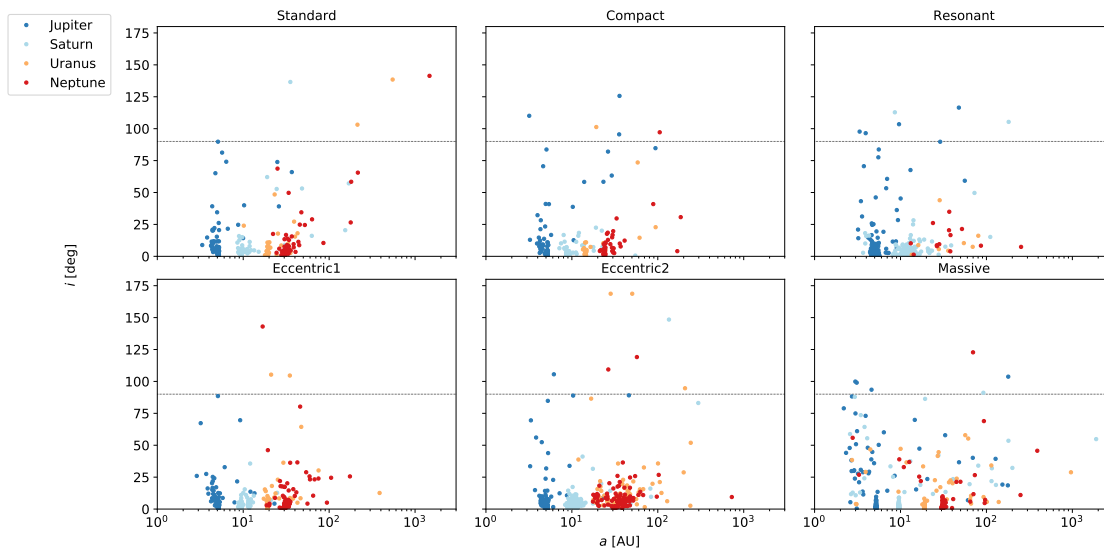


Fig. B.4.: Same as Fig. 3.9 but for the 16k cluster.

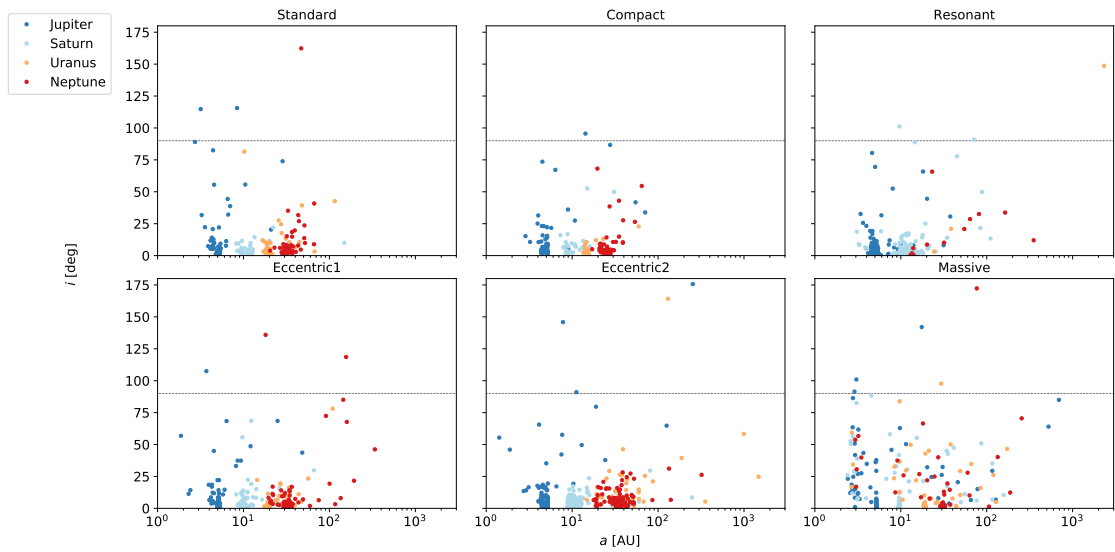


Fig. B.5.: Same as Fig. 3.5 but for the 32k cluster.

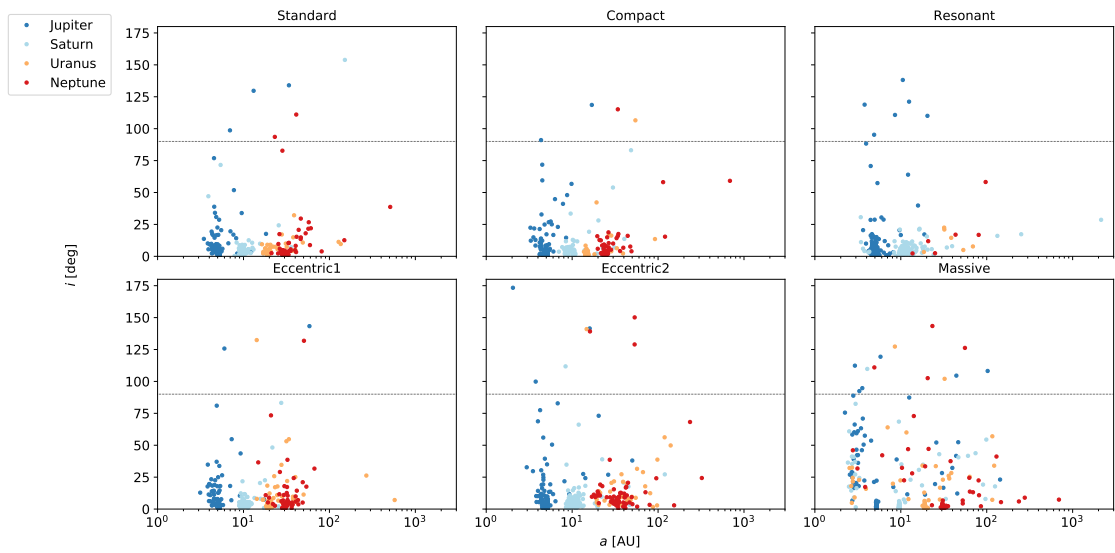
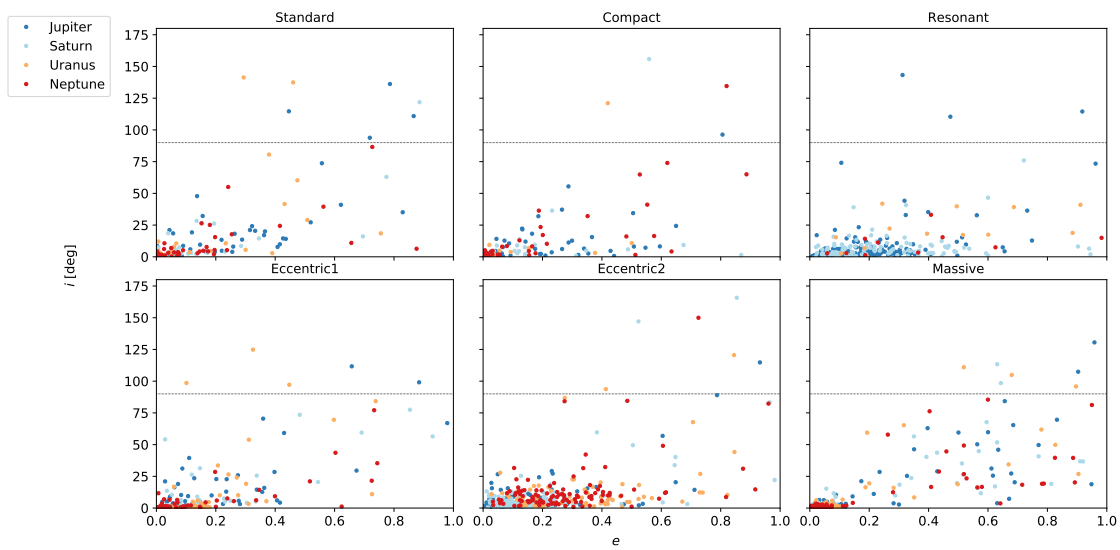
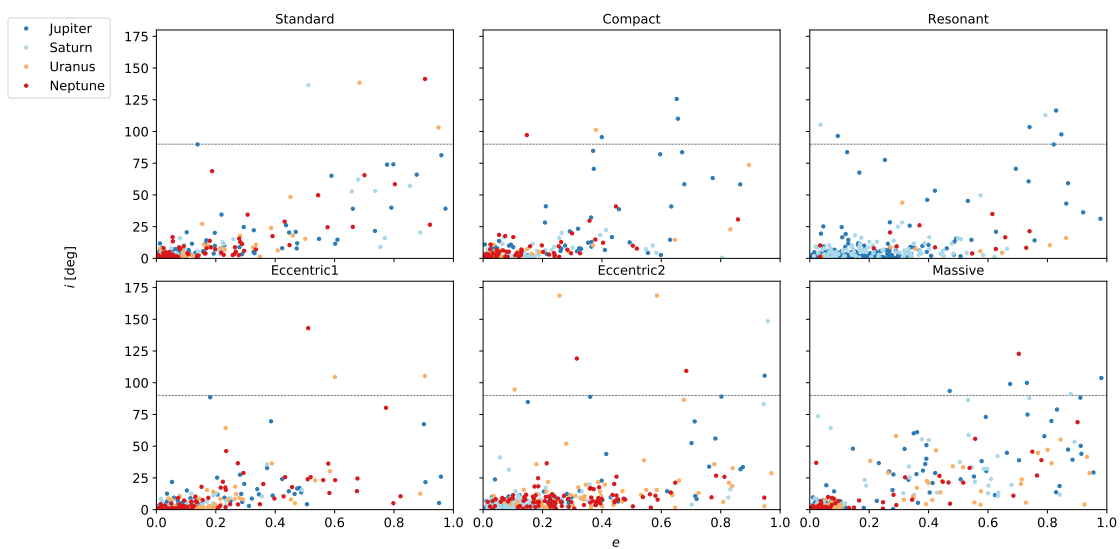


Fig. B.6.: Same as Fig. 3.5 but for the 64k cluster.



**Fig. B.7.:** The  $e$ - $i$  space for all planets in the 8k star cluster which are not ejected from their host planetary system after a simulation time of 100 Myr for the six different initial configurations. The dotted black shows the threshold of  $i = 90^\circ$ . Planets near that value have polar orbits while those above it have retrograde orbits.



**Fig. B.8.:** Same as in Fig. B.7 but for the 16k cluster.

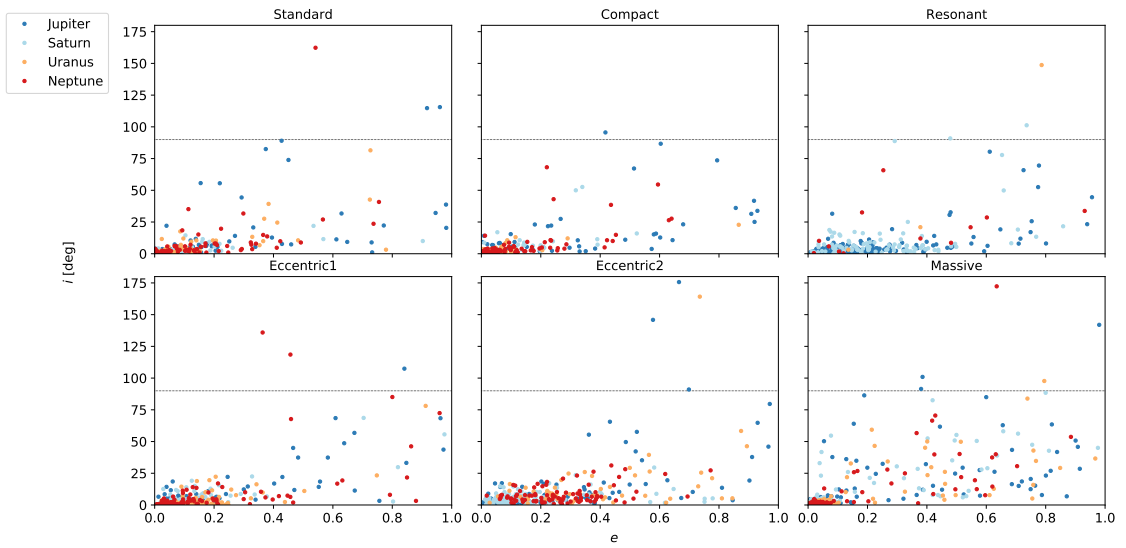


Fig. B.9.: Same as in Fig. B.7 but for the 32k cluster.

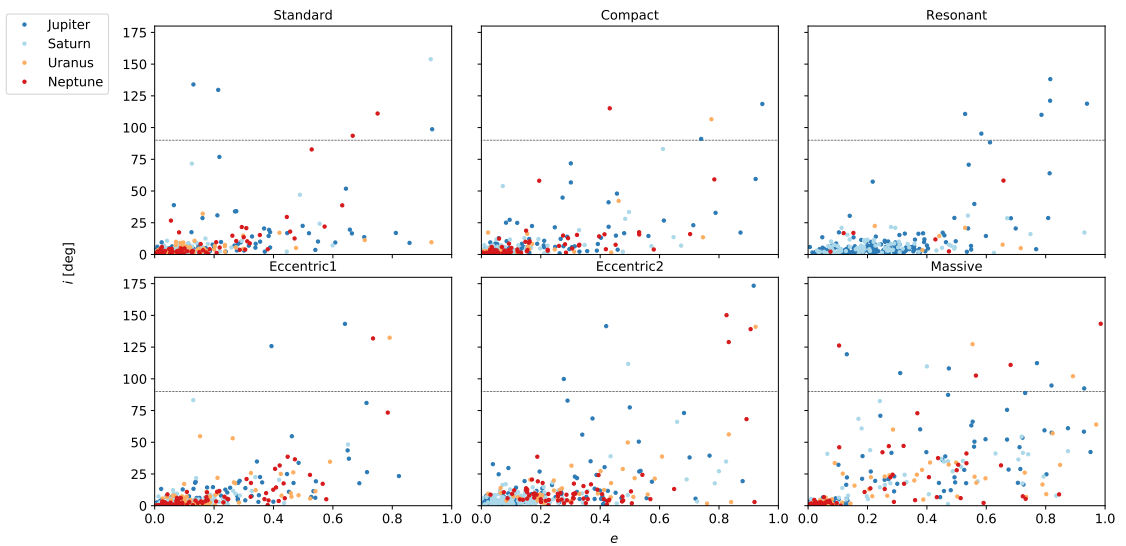
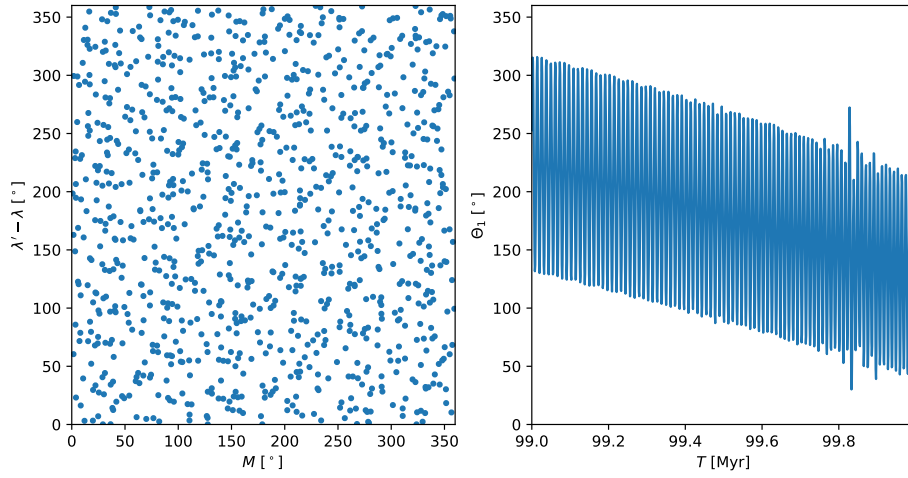


Fig. B.10.: Same as in Fig. B.7 but for the 64k cluster.

## Appendix for Chapter 4

# C

### C.1 Additional Material



**Fig. C.1.:** 10:3 MMR between planet 2 and 3 in planetary system 177 (3P model,  $1.5 M_{\odot}$  host star) between 99–100 Myr.

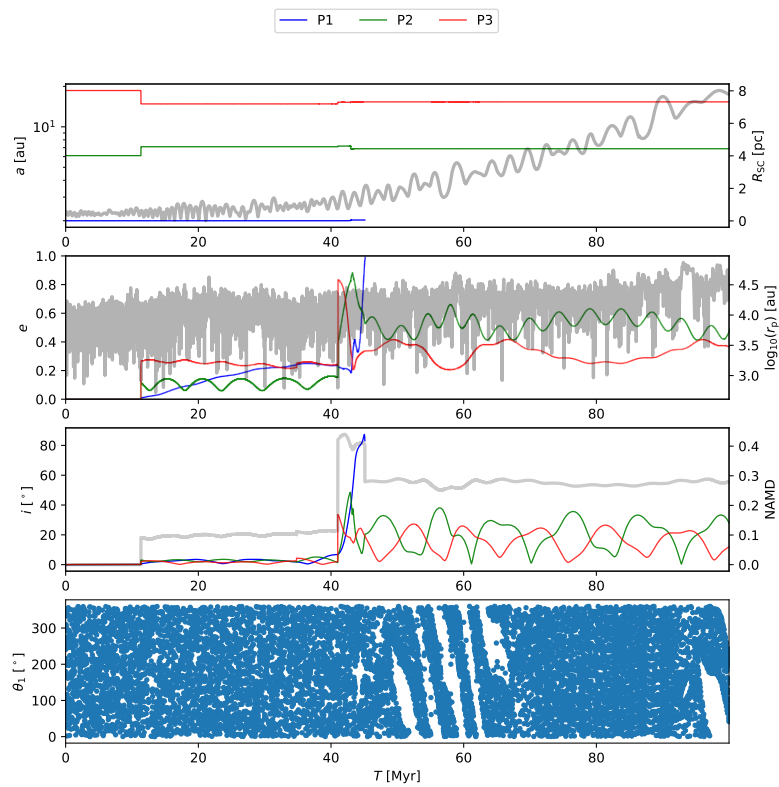


**Fig. C.2.:** As Fig. 4.8 but for planetary system 177 (3P model,  $1.5 M_{\odot}$  host star). The resonance angle is shown for  $p = 3$ ,  $q = 7$  and planet pair 2/3.

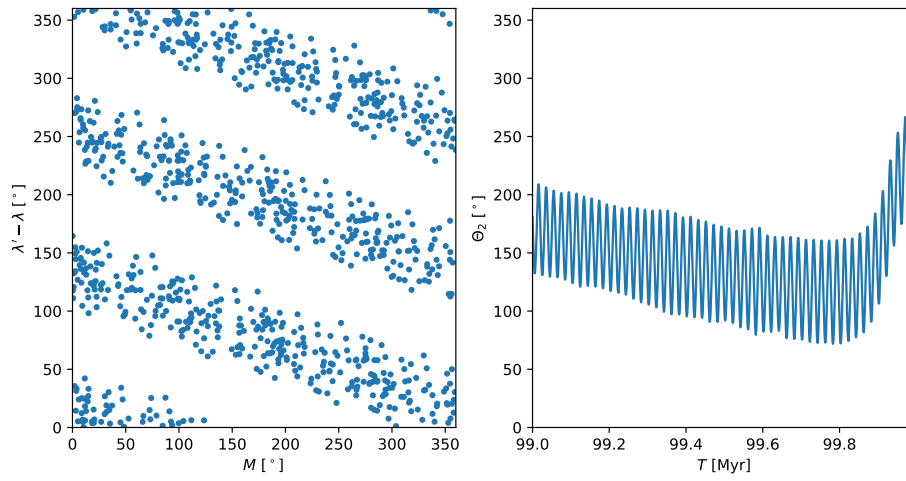


**Fig. C.3.:** 3:2 MMR between planet 5 and 6 in planetary system 22 (7PW model,  $2.0 M_{\odot}$  host star) between 99–100 Myr.

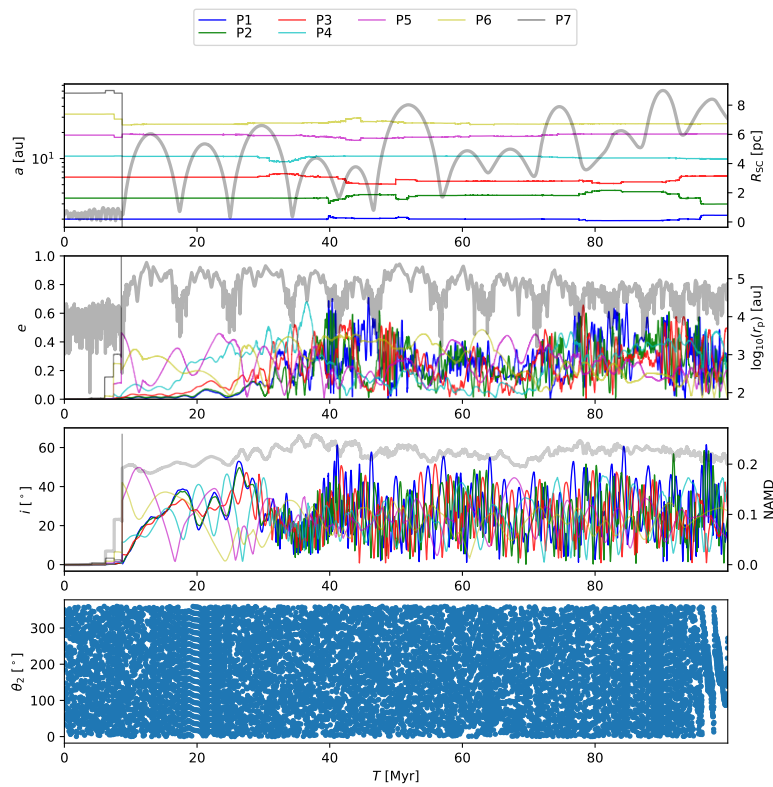


**Fig. C.4.:** As Fig. 4.8 but for planetary system 22 (7PW model,  $2.0 M_{\odot}$  host star). The resonance angle is shown for  $p = 2$ ,  $q = 1$  and planet pair 5/6.

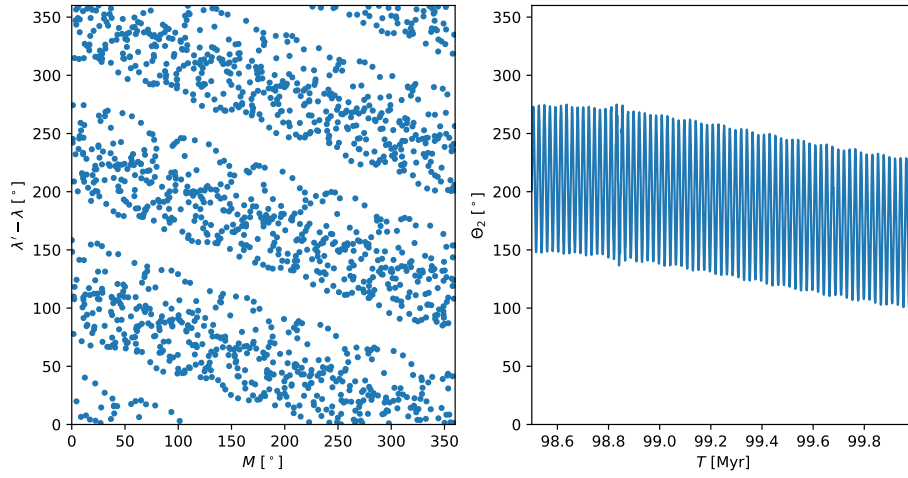


**Fig. C.5.:** 3:2 MMR between planet 5 and 6 in planetary system 45 (7PW model,  $2.0 M_{\odot}$  host star) between 98.5–100 Myr.

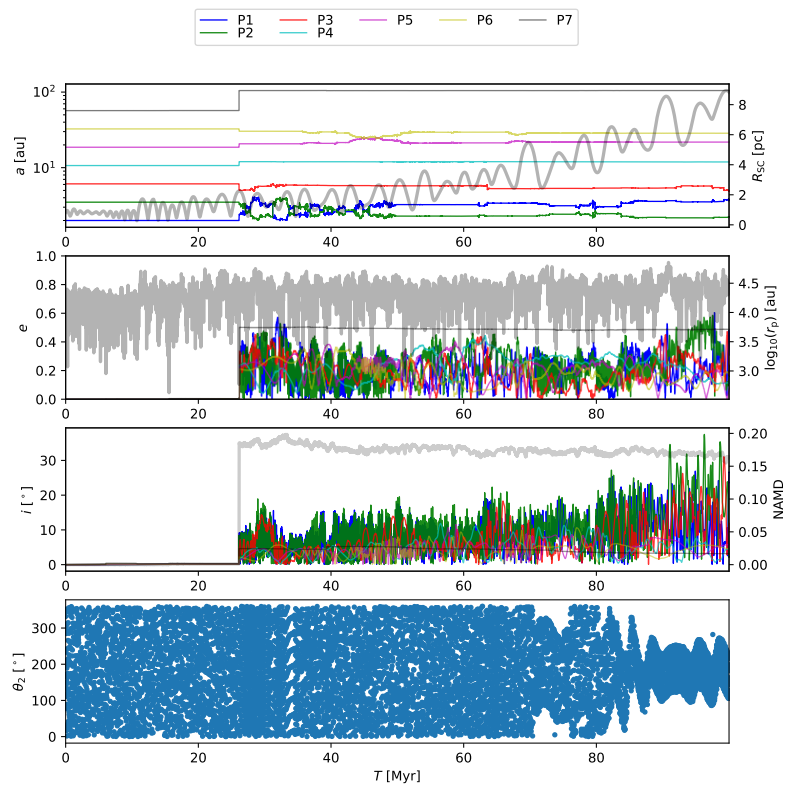


**Fig. C.6.:** As Fig. 4.8 but for planetary system 45 (7PW model,  $2.0 M_{\odot}$  host star). The resonance angle is shown for  $p = 2$ ,  $q = 1$  and planet pair 5/6.

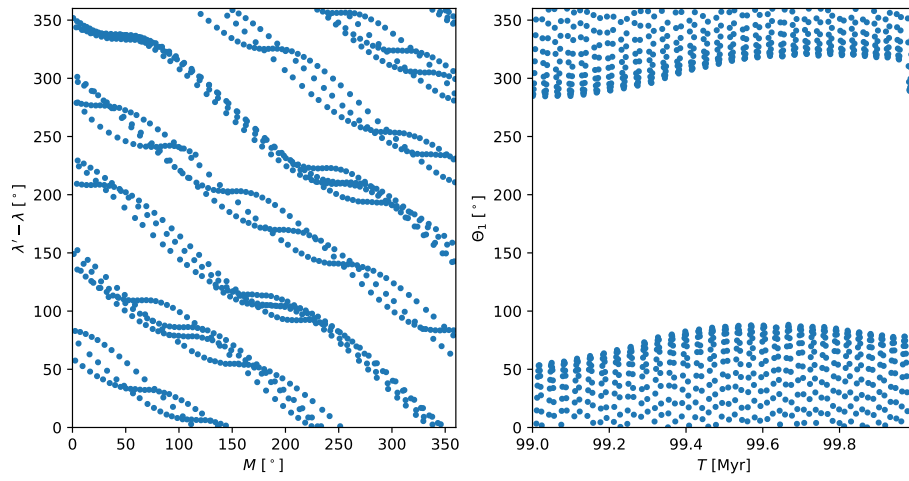


**Fig. C.7.:** 5:2 MMR between planet 4 and 5 in planetary system 38 (7PW model,  $2.5 M_{\odot}$  host star) between 99–100 Myr.

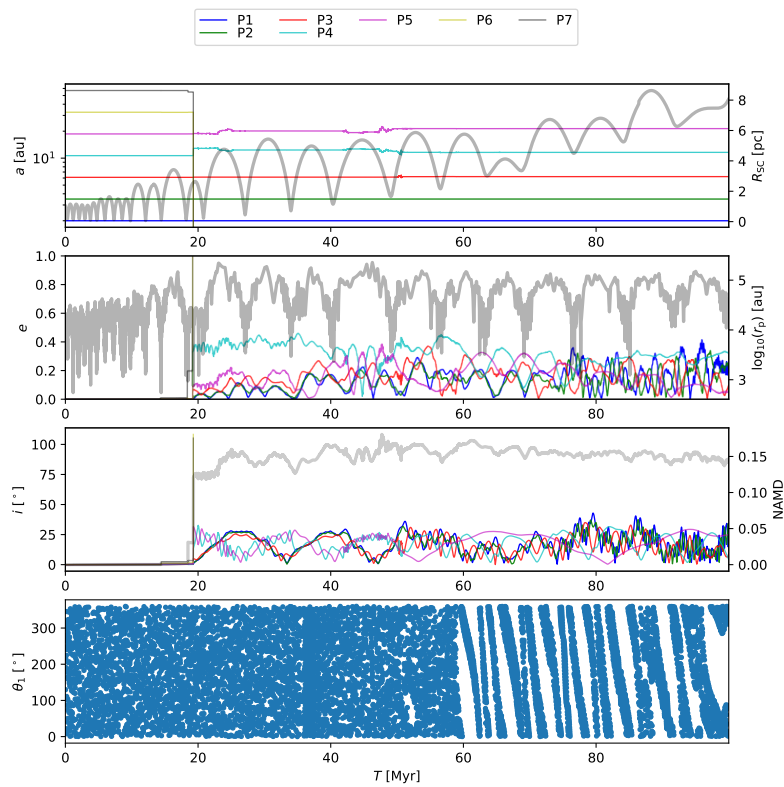


**Fig. C.8.:** As Fig. 4.8 but for planetary system 38 (7PW model,  $2.5 M_{\odot}$  host star). The resonance angle is shown for  $p = 2$ ,  $q = 3$  and planet pair 4/5.

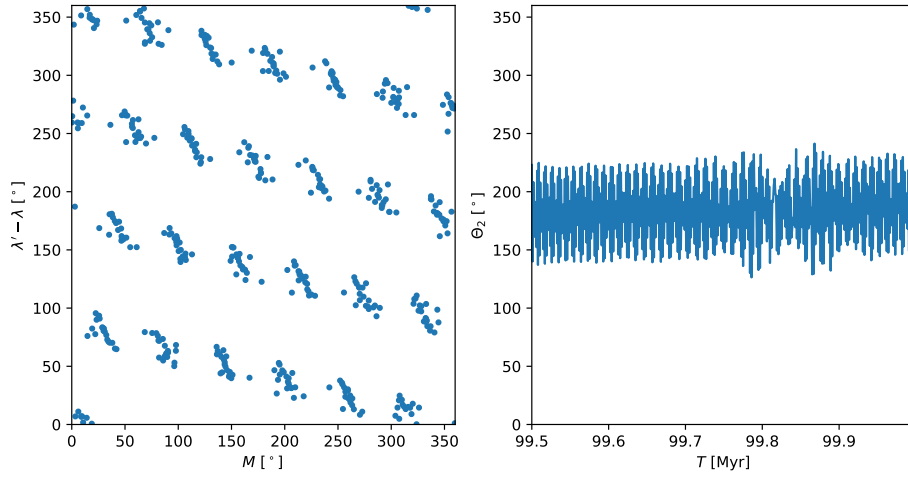


**Fig. C.9.:** 4:3 MMR between planet 3 and 4 in planetary system 192 (7PW model,  $2.5 M_{\odot}$  host star) between 99.5–100 Myr.

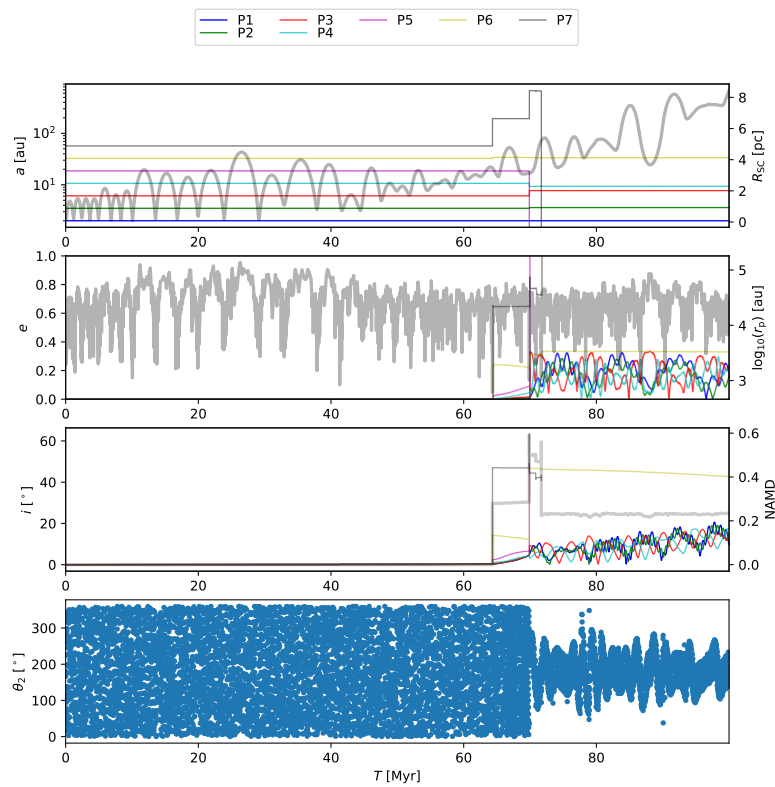


**Fig. C.10.:** As Fig. 4.8 but for planetary system 192 (7PW model,  $2.5 M_{\odot}$  host star). The resonance angle is shown for  $p = 3$ ,  $q = 1$  and planet pair 3/4.

**Tab. C.1.:** Extract from the simulation results for the 3P planetary system model around  $1.5 M_{\odot}$  host stars. A particle ID equal to 0 corresponds to the system's central star. Ejected planets were omitted, as were systems where no planets remained.

Sys. ID	Part. ID	a [au]	e	i [rad]	x [au]	y [au]	z [au]	vx [au/d]	vy [au/d]	vz [au/d]	Particle Mass [ $M_{\odot}$ ]	Stability
0	0	nan	nan	nan	-0.000	-0.001	-0.001	-0.000	0.000	-0.000	1.500E+00	0.91
0	1	2.00	0.17	0.26	-1.641	-1.167	0.201	0.011	-0.010	0.003	9.546E-06	0.91
0	2	6.12	0.17	0.53	-5.786	-2.263	3.397	0.004	-0.006	0.001	9.546E-06	0.91
1	0	nan	nan	nan	-0.186	-0.052	-0.267	-0.000	-0.000	-0.000	1.500E+00	0.94
1	1	2.00	0.00	0.00	-1.667	-1.396	-0.267	0.010	-0.011	-0.000	9.546E-06	0.94
1	2	6.10	0.00	0.00	5.907	0.325	-0.267	-0.001	0.009	-0.000	9.546E-06	0.94
1	3	18.63	0.00	0.00	1.978	18.454	-0.266	-0.005	0.001	-0.000	9.546E-06	0.94
2	0	nan	nan	nan	0.005	-0.003	-0.005	0.000	0.000	-0.000	1.500E+00	0.89
2	1	2.00	0.03	0.06	-2.023	-0.287	0.011	0.002	-0.014	0.001	9.546E-06	0.89
2	2	6.10	0.05	0.05	-5.413	-2.626	0.248	0.003	-0.008	0.000	9.546E-06	0.89
2	3	17.09	0.29	0.06	16.191	13.060	-0.809	-0.003	0.003	0.000	9.546E-06	0.89
3	0	nan	nan	nan	-0.001	0.001	0.001	-0.000	0.000	-0.000	1.500E+00	0.94
3	1	2.00	0.01	0.04	-1.089	-1.686	0.059	0.013	-0.008	0.000	9.546E-06	0.94
3	2	6.11	0.01	0.04	-3.369	5.146	-0.249	-0.007	-0.005	0.000	9.546E-06	0.94
3	3	19.11	0.05	0.02	-18.023	-8.944	-0.187	0.002	-0.004	0.000	9.546E-06	0.94
4	0	nan	nan	nan	0.057	0.476	-0.537	0.000	0.000	-0.000	1.500E+00	0.93
4	1	2.00	0.08	0.28	0.501	2.328	-0.990	-0.015	0.002	-0.002	9.546E-06	0.93
4	2	8.01	0.22	1.30	-2.771	0.292	8.495	0.003	-0.005	0.000	9.546E-06	0.93
5	0	nan	nan	nan	-0.013	-0.021	0.010	-0.000	-0.000	0.000	1.500E+00	0.93
5	1	2.00	0.00	0.01	1.927	-0.508	0.012	0.004	0.014	0.000	9.546E-06	0.93
5	2	6.10	0.00	0.01	5.687	-2.214	0.005	0.003	0.008	0.000	9.546E-06	0.93
5	3	18.64	0.00	0.01	-6.518	-17.419	-0.069	0.005	-0.002	0.000	9.546E-06	0.93
6	0	nan	nan	nan	0.004	0.004	-0.001	0.000	-0.000	-0.000	1.500E+00	0.94
6	1	2.00	0.00	0.00	0.069	2.003	-0.002	-0.015	0.000	0.000	9.546E-06	0.94
6	2	6.10	0.00	0.00	5.518	2.622	-0.004	-0.004	0.008	-0.000	9.546E-06	0.94
6	3	18.63	0.00	0.00	13.892	-12.414	0.047	0.003	0.004	-0.000	9.546E-06	0.94
7	0	nan	nan	nan	0.015	-0.007	0.004	0.000	-0.000	0.000	1.500E+00	0.93
7	1	2.00	0.00	0.00	-1.805	0.821	0.000	-0.006	-0.014	0.000	9.546E-06	0.93
7	2	6.10	0.00	0.00	4.142	4.493	0.010	-0.006	0.006	-0.000	9.546E-06	0.93
7	3	18.63	0.00	0.01	10.357	-15.517	0.053	0.004	0.003	0.000	9.546E-06	0.93
8	0	nan	nan	nan	0.000	0.000	0.001	-0.000	0.000	0.000	1.500E+00	0.90
8	1	1.94	0.47	0.06	-0.246	-0.996	0.017	0.024	-0.006	0.002	9.546E-06	0.90
8	2	6.96	0.06	0.17	2.961	-5.973	-0.340	0.007	0.003	-0.001	9.546E-06	0.90
8	3	28.75	0.70	0.09	-35.177	-30.718	4.088	0.002	-0.001	-0.000	9.546E-06	0.90
9	0	nan	nan	nan	0.025	0.029	-0.006	0.000	0.000	-0.000	1.500E+00	0.92
9	1	2.00	0.00	0.00	1.884	0.768	-0.006	-0.006	0.014	0.000	9.546E-06	0.92
9	2	6.10	0.00	0.00	2.725	5.504	-0.006	-0.008	0.004	0.000	9.546E-06	0.92
9	3	18.63	0.00	0.00	-12.550	13.786	0.013	-0.004	-0.003	0.000	9.546E-06	0.92
10	0	nan	nan	nan	0.019	0.014	0.003	0.000	0.000	0.000	1.500E+00	0.93
10	1	2.00	0.00	0.00	-0.421	-1.937	0.004	0.015	-0.003	-0.000	9.546E-06	0.93
10	2	6.10	0.00	0.00	4.214	4.448	-0.000	-0.006	0.006	0.000	9.546E-06	0.93
10	3	18.63	0.00	0.00	4.954	17.982	0.032	-0.005	0.001	0.000	9.546E-06	0.93
11	0	nan	nan	nan	0.002	0.006	-0.007	-0.000	0.000	-0.000	1.500E+00	0.92
11	1	2.00	0.00	0.00	-1.238	-1.572	-0.005	0.012	-0.009	0.000	9.546E-06	0.92
11	2	6.11	0.00	0.01	5.810	-1.883	-0.049	0.003	0.008	-0.000	9.546E-06	0.92
12	0	nan	nan	nan	0.000	-0.000	0.000	-0.000	-0.000	0.000	1.500E+00	0.93
12	1	2.00	0.00	0.00	0.136	-1.995	-0.001	0.015	0.001	0.000	9.546E-06	0.93
12	2	6.10	0.00	0.00	1.587	-5.895	-0.003	0.008	0.002	0.000	9.546E-06	0.93
12	3	18.63	0.00	0.00	-1.078	18.600	0.029	-0.005	-0.000	-0.000	9.546E-06	0.93
13	0	nan	nan	nan	0.003	-0.001	-0.004	-0.000	-0.000	-0.000	1.500E+00	0.93
13	1	2.00	0.00	0.00	1.722	-1.023	0.001	0.008	0.013	-0.000	9.546E-06	0.93
13	2	6.10	0.00	0.00	-6.078	0.536	-0.008	-0.001	-0.008	0.000	9.546E-06	0.93
13	3	18.63	0.00	0.00	6.921	-17.302	0.008	0.005	0.002	0.000	9.546E-06	0.93
15	0	nan	nan	nan	0.004	0.042	-0.133	-0.000	0.000	-0.000	1.500E+00	0.92
15	1	2.00	0.00	0.00	1.974	0.384	-0.133	-0.003	0.015	0.000	9.546E-06	0.92
15	2	6.10	0.00	0.00	5.116	-3.294	-0.133	0.005	0.007	0.000	9.546E-06	0.92
15	3	18.64	0.00	0.00	-16.439	-8.721	-0.170	0.002	-0.004	-0.000	9.546E-06	0.92
⋮	⋮	⋮	⋮	⋮	⋮	⋮	⋮	⋮	⋮	⋮	⋮	⋮

**Tab. C.2.:** Extract from the simulation results for the 7PW planetary system model around  $2.5 M_{\odot}$  host stars. A particle ID equal to 0 corresponds to the system's central star. Ejected planets were omitted, as were systems where no planets remained.

Sys. ID	Part. ID	a [au]	e	i [rad]	x [au]	y [au]	z [au]	vx [au/d]	vy [au/d]	vz [au/d]	Particle Mass [ $M_{\odot}$ ]	Stability
0	0	nan	nan	nan	-0.001	-0.001	0.001	-0.000	-0.000	0.000	2.500E+00	0.16
0	1	1.23	0.36	0.53	-1.112	-0.953	0.062	0.015	-0.009	-0.010	9.546E-06	0.16
0	2	9.36	0.16	0.51	-4.971	8.082	5.173	-0.006	-0.005	0.001	9.546E-06	0.16
0	3	3.20	0.19	0.12	3.415	0.233	-0.273	-0.003	0.014	0.001	9.546E-06	0.16
0	4	7.12	0.72	0.43	8.489	-1.473	1.580	0.006	0.004	0.003	9.546E-06	0.16
0	5	26.48	0.59	0.38	-16.714	28.949	4.355	-0.002	-0.003	-0.001	9.546E-06	0.16
0	6	37.90	0.20	0.51	38.351	22.718	-3.512	-0.002	0.003	0.002	9.546E-06	0.16
0	7	139.55	0.62	0.16	223.221	-2.257	-32.354	-0.000	0.001	0.000	9.546E-06	0.16
1	0	nan	nan	nan	-0.075	-0.039	0.036	-0.000	-0.000	0.000	2.500E+00	0.90
1	1	2.00	0.02	0.09	0.111	1.989	0.188	-0.019	0.002	-0.001	9.546E-06	0.90
1	2	3.49	0.03	0.09	-2.978	-1.795	-0.268	0.008	-0.013	-0.000	9.546E-06	0.90
1	3	6.10	0.05	0.09	0.129	-6.055	-0.339	0.011	-0.000	0.001	9.546E-06	0.90
1	4	10.70	0.12	0.09	-9.250	-2.138	-0.685	0.002	-0.009	-0.000	9.546E-06	0.90
1	5	18.54	0.18	0.08	8.254	14.019	1.340	-0.007	0.003	-0.000	9.546E-06	0.90
1	6	34.84	0.13	0.07	7.110	-30.189	0.744	0.005	0.002	0.000	9.546E-06	0.90
2	0	nan	nan	nan	-0.000	0.000	0.000	-0.000	-0.000	0.000	2.500E+00	0.93
2	1	2.00	0.00	0.06	-0.365	-1.964	0.098	0.019	-0.003	0.001	9.546E-06	0.93
2	2	3.49	0.00	0.06	-0.493	3.453	-0.206	-0.014	-0.002	-0.000	9.546E-06	0.93
2	3	6.10	0.00	0.06	5.546	-2.536	0.306	0.005	0.010	-0.000	9.546E-06	0.93
2	4	10.67	0.00	0.06	10.500	1.926	0.188	-0.001	0.008	-0.001	9.546E-06	0.93
2	5	18.63	0.00	0.06	-18.587	0.176	-0.459	-0.000	-0.006	0.000	9.546E-06	0.93
2	6	32.63	0.00	0.06	-26.068	-19.737	0.814	0.003	-0.004	0.000	9.546E-06	0.93
2	7	61.95	0.12	0.05	-14.436	53.361	1.607	-0.004	-0.001	0.000	9.546E-06	0.93
5	0	nan	nan	nan	-0.012	-0.006	0.005	-0.000	-0.000	0.000	2.500E+00	0.89
5	1	2.00	0.00	0.04	1.984	-0.003	-0.058	0.000	0.019	0.000	9.546E-06	0.89
5	2	3.49	0.00	0.04	-3.199	-1.437	0.072	0.006	-0.013	-0.001	9.546E-06	0.89
5	3	6.10	0.00	0.05	2.113	5.739	0.114	-0.010	0.004	0.000	9.546E-06	0.89
5	4	10.70	0.01	0.07	10.740	0.963	-0.348	-0.001	0.008	0.000	9.546E-06	0.89
5	5	18.87	0.06	0.10	-13.367	-13.405	-0.398	0.004	-0.005	-0.001	9.546E-06	0.89
5	6	32.69	0.08	0.08	-15.408	26.436	2.387	-0.005	-0.002	-0.000	9.546E-06	0.89
5	7	50.95	0.28	0.07	-37.901	-3.118	1.144	-0.000	-0.005	-0.000	9.546E-06	0.89
6	0	nan	nan	nan	-0.002	0.002	0.002	-0.000	-0.000	-0.000	2.500E+00	0.00
6	1	2.05	0.56	0.97	1.795	0.736	-0.952	0.009	0.014	0.006	9.546E-06	0.00
6	3	6.06	0.37	0.72	5.220	6.275	0.430	-0.004	0.004	0.005	9.546E-06	0.00
6	4	23.56	0.69	1.06	0.258	-34.796	-18.666	0.001	0.001	-0.002	9.546E-06	0.00
6	5	17.11	0.15	0.10	18.423	-2.285	-1.782	0.001	0.006	-0.000	9.546E-06	0.00
6	6	26.71	0.17	0.30	-6.645	20.310	5.730	-0.006	-0.002	-0.001	9.546E-06	0.00
6	7	133.92	0.36	1.09	104.096	66.677	-36.169	-0.001	0.001	0.002	9.546E-06	0.00
7	0	nan	nan	nan	0.002	-0.001	-0.002	-0.000	0.000	0.000	2.500E+00	0.62
7	1	1.85	0.49	0.69	-1.359	-2.317	-0.208	0.007	-0.006	-0.008	9.546E-06	0.62
9	0	nan	nan	nan	0.000	-0.000	0.001	0.000	-0.000	0.000	2.500E+00	0.31
9	2	3.30	0.57	0.24	3.111	2.797	-0.723	-0.002	0.011	-0.003	9.546E-06	0.31
9	5	90.06	0.95	1.15	-33.978	153.282	-75.976	-0.000	0.000	-0.000	9.546E-06	0.31
9	6	100.61	0.60	0.21	-47.834	-145.928	10.892	0.001	0.000	0.000	9.546E-06	0.31
10	0	nan	nan	nan	-0.000	0.000	0.000	0.000	0.000	0.000	2.500E+00	0.91
10	1	2.00	0.00	0.00	0.492	1.939	-0.001	-0.019	0.005	-0.000	9.546E-06	0.91
10	2	3.49	0.00	0.00	-1.407	3.198	-0.009	-0.013	-0.006	-0.000	9.546E-06	0.91
10	3	6.10	0.00	0.00	2.755	5.447	0.005	-0.010	0.005	-0.000	9.546E-06	0.91
10	4	10.67	0.00	0.00	-9.761	-4.294	-0.037	0.003	-0.008	0.000	9.546E-06	0.91
10	5	18.64	0.00	0.00	-18.001	4.714	-0.070	-0.002	-0.006	-0.000	9.546E-06	0.91
10	6	32.52	0.00	0.01	32.360	-3.619	0.148	0.001	0.005	0.000	9.546E-06	0.91
10	7	56.91	0.01	0.01	27.626	-49.813	-0.455	0.003	0.002	0.000	9.546E-06	0.91
⋮	⋮	⋮	⋮	⋮	⋮	⋮	⋮	⋮	⋮	⋮	⋮	⋮

## Colophon

This thesis was typeset with L<sup>A</sup>T<sub>E</sub>X 2<sub>ε</sub>. It uses the *Clean Thesis* style developed by Ricardo Langner. The design of the *Clean Thesis* style is inspired by user guide documents from Apple Inc.

Download the *Clean Thesis* style at <http://cleanthesis.der-ric.de/>.



# Declaration

I hereby declare that this thesis is my own work and that I have used no other than the stated sources and aids.

Ich versichere, dass ich diese Arbeit selbstständig verfasst habe und keine anderen als die angegebenen Quellen und Hilfsmittel benutzt habe.

*Heidelberg, February 07, 2022*

---

Katja Verena Stock

